

Validation Data and Model Development for Fuel Assembly Response to Seismic Loads

Nuclear Energy Advanced Modeling & Simulation

Philippe M. Bardet
George Washington University

In collaboration with:
None

Rob Versluis, Federal POC
David Pointer, Technical POC

Final Report:
Validation data and model development for fuel assembly response to seismic loads

Project Number:
NEUP Project 12-3549, DE-NE00126902

PICSNE Workpackage:
NU-12-DC-GWU -0401-02
Workscope:
NEAMS-2

Lead Organization
Philippe M. Bardet^{*1}, Elias Balaras¹, Majid T. Manzari²
The George Washington University
Washington, DC
*: Principal Investigator
¹: Mechanical and Aerospace Engineering Department
²: Civil and Environmental Engineering Department

No-Cost Collaborators:
Dr. W. Dave Pointer
Oak Ridge National Laboratory

Dr. Guillaume Ricciardi
Commissariat à l'énergie atomique (CEA) - France

Total Funding:
\$862,435

Duration:
07/26/2012 – 12/31/2015

Federal Manager:
Dan Funk

Technical Point of Contact:
Dr. W. Dave Pointer

Executive Summary:

Vibrations are inherently present in nuclear reactors, especially in core and steam generators of pressurized water reactor (PWR). They can have significant effects on local heat transfer and wear and tear in the reactor and often set safety margins. The simulation of these multiphysics phenomena from first principle requires the coupling of several codes, which is one of the most challenging tasks in modern computer simulation. Here an ambitious multiphysics multidisciplinary validation campaign is conducted. It relied on an integrated team of experimentalists and code developers to acquire benchmark and validation data for fluid-structure interaction codes. Data are focused on PWR fuel bundle behavior during seismic transients.

Earthquakes and Loss of Coolant Accidents can damage nuclear power plant cores, which is a major safety concern and set safety margins. Of both types of commercial light water reactor operational in the U.S., PWR cores are especially sensitive to seismic transients. During an earthquake, the fuel assembly spacer grids can collide, which may in turn result in buckling of guide tubes - preventing control rods insertion. Additionally, plant data show very strong reactivity excursions during seismic events that cannot be simulated with the current set of numerical tools.

To provide a first set of answers to these questions and develop tools that can further address these transients, an integrated team of experimentalists and code developers (both structural and fluid dynamicists) worked closely together. The project resulted in a complete dataset for validation and benchmark of fluid structure interaction numerical codes. Having the three teams involved in the project at a single institution offered a symbiotic relationship and close integration of all aspects of this project, which started at the conception and definition of the scope. Collaboration and integration of the expertise were also crucial at the design phase of the facility and definition of the matrix of experiments. Having simulations performed in parallel to the experiment enabled to periodically check experimental data quality and redefine experimental matrix as necessary.

The successful completion of the project relied on several key achievements: scaling strategies for surrogate fuel bundles for FSI studies, design of a flexible and modular experimental facility, development and refinement of experimental techniques, advancement of FSI code, and development of validation schemes

The design of the surrogate fuel bundle had to adhere to strict constraints. The structural components had to be index matched to our working fluid to enable the deployment of optical diagnostics, while preserving dynamic similarities. This led us to:

- Scaling analysis for surrogate bundle design. We were fortunate in recognizing that solid acrylic rods have the same natural frequency than zircaloy tube filled with UO₂ pellets, as

long as the rod diameter is increased by 50%. This led to a surrogate fuel bundle with similar dynamic characteristics than prototypical.

- Use of simulation to inform scaling analysis. To confirm our analytical scaling analysis and assist in optimizing the surrogate bundle design, we performed a series of finite element simulations of the bundle and defined an optimal spacing of the spacer grids to have a model bundle that match prototypical conditions.
- Open source spacer grids. Since it was necessary to increase the fuel rod diameter by 50% to satisfy the scaling criteria, we had to design custom spacer grids. In these grids, we had also scaled the contact force between rod and spring, resulting in a bimetallic spacer grid. It should be noted that our design is open, which simplifies its use for validation.
- Inexpensive spacer grid manufacturing for laboratory testing. We developed an inexpensive manufacturing process and have now been approached by other research groups to manufacture spacer grids for them.
- A posteriori validation of bundle design. Analysis of results show that our surrogate bundle has vibration characteristics that are very similar to the prototypical fuel bundle with matching in natural frequency, damping coefficient, etc.

We have designed and fabricated a *major experimental facility* that will be reused for future DOE funded project. Operating the facility on an earthquake shake table involved addressing several major challenges, it can be stipulated with confidence that if we had relied on an engineering firm to do the design, the facility would have cost several times its current cost and design would also have taken longer.

- Pilot facility prototype. To enable the safe design and learn about operating procedures of the proposed system, we first built a pilot facility at a reduced scale (1:20 in length). This approach is good engineering practice and enabled us to anticipate and address potential challenges with the final facility.
- Full height, environment controlled, index matched facility. The facility is designed to house one full height fuel bundle and sits nearly 7 m tall. An intricate structure had to be designed and built to support the test section and prevent its deflection during shaking. The great height of the facility coupled with small temperature gradients in the room resulted in establishment of natural convection in the test section, which perturbed our initial conditions. These issues were resolved by improving the temperature control of the room. Additionally, the working fluid temperature had to be precisely controlled to guarantee adequate index matching.
- First operating flow loop on a shake table. It is the first time to the authors' knowledge that a flow loop was operated on an earthquake shake table, and here it is index matched and capable of 2,000 gpm flow... To mitigate fluid leak that could have irreparably damaged the shake table, the flow loop and test section were designed with "defense in depth" philosophy; i.e. the test section sits inside a secondary containment, which sits in a ternary containment. Another unconventional measure to save on cost and minimize risks of leaks was to use a simple channel design with minimal intrusion for probes or windows and to rely on an exoskeleton for rigidity and to connect the bracing structure to the test section.

- Modular facility for future growth. We took advantage of our need for a secondary containment to design a modular facility that can house up to 3 full height fuel bundles in the future.
- Precise control of inflow conditions. The inlet nozzle to the test section was designed following best practices in low speed water tunnel designs to provide an initial flow with high uniformity and low level of disturbances.
- Pumping power. As another cost saving strategies, two pumps were employed in parallel instead of a single larger pump (1/3 of the price). With modern variable frequency drives, we were able to conveniently control them in a master/slave configuration. A custom manifold was designed to minimize instabilities coming from the pumps mixing.
- One of the largest index matched facilities. The resulting facility is one of the three largest and most capable refractive index matched facilities. It can reach flow rate up to 2,000 gpm in highly controlled and flexible manner. Special strategies were developed to improve the refractive index matching and increase dissolution of fluorescent dyes in the working fluid. It should be mentioned that solid associated with this refractive index matched fluid, acrylic, is readily available and that future models can be constructed at reasonable costs even for very complex geometries. Finally, the working fluid, paracymene mixtures, has a low viscosity, which enables to reach high Reynolds number flow.

To successfully conduct this project one had to develop and adapt several advanced diagnostics, pushing the state of the art in “traditional” tabletop laser based diagnostics and deploying them “in-situ”. We deployed a broad variety of non-intrusive diagnostics that we specifically designed for this project. Such suite of diagnostics is not commercially available and would have been prohibitively expensive to acquire from an instrumentation vendor (if at all possible). A brief list of accomplishments is given below:

- Timing uncertainty in PIV lasers. While operating our PIV, which was custom made for our needs, we noticed inconsistencies in timing of the laser that can introduce bias error in PIV measurements up to several percent of the mean velocity. We tested a broad range of lasers and found that this is due to laser architecture and that most laser manufacturers did not correct this effect in their lasers till we talked to them.
- Coupling of optical fiber to PIV laser. This was key to safely and precisely delivering laser light to the test section for conducting velocity measurement with particle image velocimetry (PIV). While this was attempted in the past by other groups, we are the only one to report, and share details, of a beam delivery with high beam quality and thin laser investigation plane allowing to measure turbulent velocity fields. This task required an in depth knowledge of optics.
- In-situ flying PIV. In addition to coupling the PIV laser to optical fibers, we deployed an intricate PIV planes configuration to monitor laser planes vibrations. The latter were minimized to a fraction of the laser beam thickness through custom opto-mechanical mounts. This combined with mounting of PIV optical fibers and cameras on remotely operated stages enabled us to deploy PIV in situ, while this technique is typically used in carefully controlled laboratory environments.
- Three dimensional time-resolved velocity field. We used the flexibility offered by our PIV system combined with its precise synchronization and integration with the rest of the

diagnostics (described below) to conduct the first ever volumetric phase averaged velocity fields measurement in a fuel bundle.

- High-Power optical multiplexer for PIV in 6 planes. The flying PIV system relies on two intersecting laser planes. This required to split the laser beam into two independently controllable beamlets in a first phase. In a second phase, we further split the laser into 6 beamlets, which enables us to take PIV data in 6 independent planes, the maximum ever achieved to the authors' knowledge.
- Long recording time time-resolved PIV. We invested in new type of cameras that enable to acquire time-resolved data (kiloHertz range) with recording length of up to 20 min. Hence we could resolve velocity fields during long transients, capturing both the temporal evolution of the flow structures and the flow statistics, which has not been accomplished to date. This could not be envisioned at the start of the experimental campaign.
- Non-intrusive monitoring of bundle oscillations. We relied on optical techniques (Digital Image Correlation or DIC) to measure bundle displacement, instead of displacement probes, such as linear variable differential transformer (LVDT), has the advantages of being non-intrusive (and not perturbing the flow), not adding mass to the overall bundle, and not requiring the introduction of feedthrough (with risk of leaks) in the wall of the test section.
- DIC hardware and software optimization. To monitor the bundle oscillations, we deployed up to 11 high-speed high-resolution cameras and had to rely on a set of low cost CMOS cameras. After careful selection of the cameras, we obtained a resolution of 5 μm and 4 ms with this system, which is on par, or better, than LVDT used in previous tests. To make data processing time reasonable, we developed our own very efficient Digital Image Correlation (DIC) code that was further optimized for operation on GPU processor.
- Instrument synchronization. In additions to the 14 cameras mentioned above, the facility was instrumented with accelerometers, pressure transducers, flow meter, temperature probes, all of which had to be synchronized and monitored precisely. We developed protocols based on time delay generator and GPS clock to do so. In the end, we were able to combine all the data with a resolution better than 100 ns.

In parallel to the experimental campaign, two sets of simulation were performed to validate several aspects of the codes: finite element analysis and high performance high fidelity fluid-structure interaction simulation. For these the codes were further developed and adapted to the experiment conditions. Main accomplishments are reported below.

- Developed a highly effective optimization technique to compute the damping associated with dominant modes of the dynamic response of the dry specimen as well as the specimen with standing fluid and fluid with axial flow. This enabled excellent matching of the measured response of the dry specimen. Additional efforts are ongoing to do the same for the standing fluid and axial flow cases.
- Development of hybrid FSI algorithms: To introduce the seismic ground acceleration, both sets of equations governing the fluid and structural systems are written on a non-inertial reference frame. The use of a non-inertial frame simplifies numerical treatment, providing better computational efficiency. A novel immersed boundary method was developed within this framework to impose boundary conditions on the fuel rods. The resulting scheme is efficient, since it utilizes block-structured Cartesian solvers and at the same time dramatically simplifies grid generation.

- Parallel efficiency on leadership HPC platforms: One of the challenges in such immersed boundary computations is the exchange of information between the Eulerian (fluid) and Lagrangian (structure) grids, which are handled by different data-structures. To overcome these challenges we have developed a bitmap based neighborhood knowledge base, that can be duplicated on all processors for general unstructured communications, and is the basis of our solution to the scaling problem. Strong scaling tests of the overall incompressible flow solver were also performed on the Mira BG/Q system at Argonne National Laboratory for a variety of turbulent flow configurations. Overall we obtained close to 92% parallel efficiency for grids involving up to 43 billion nodes.
- LES of the 6x6 fuel bundle: The above algorithms and computational tools enabled us to conduct LES of the full 6x6 array, considered in the experiment, albeit at a reduced high. The computations, are ongoing and reproduce the phenomena observed in the experiment.

The symbiotic integration of experimental and numerical teams led to many invaluable interactions regarding facility design, operation, instrument selection and resolution requirement, but also on the validation methodology. This last aspect has not been fully developed due to lack of time and resources but shows promising prospects. However, preliminary analysis indicate that:

- Under normal conditions, vibrations of fuel bundle while of small amplitude are sufficient to affect CFD results.

In addition to creating large validation and benchmark datasets, data have given us insights into mechanisms for flow induced damping and stiffening of fuel bundles that are not represented in current models. While, this was beyond the stated scope of the project, these insights have enabled us to reinterpret the flux sensor data of the North Anna Power Plant during the 2011 Virginia earthquake and provided a different explanation for the large reactivity excursion observed there.

Funds from this project enabled to support two PhD students who are now looking for academic positions. We have 16 peer-reviewed publications to date and are working on developing several others.

Finally, over the duration of this project we were awarded several awards and gained recognition inside and outside of the nuclear thermal hydraulics community. Dr. Noah Weichselbaum won the ANS Thermal Hydraulics Division Young Professional competition. We have also been invited by other communities (such as Aerospace Engineering communities) to give invited talks at conferences on our instrumentation development. We were also awarded a 34 million CPU hours through an ALCC award this Fall. We are using these resources to perform high fidelity FSI simulations.

Table of contents

Executive Summary:	2
Table of contents	7
1. Facility design	10
Task 1-1: Scaling analysis:	10
Task 1-2: Inlet plenum and test section:	26
Task 1-3: Flow Loop	31
Task 1-4: Material selection	35
Task 1-5: Spacer Grids Design and fuel bundle	35
Task 1-6: Fuel bundle tension control	37
2. Instrumentation development	38
Task 2-1: Particle image velocimetry – PIV: Fiber optics coupling to laser and camera testing	38
Task 2-2: Laser induced fluorescence tomography - LIFT	51
Task 2-3: Digital image correlation - DIC	53
Task 2-3-2: Stereoscopic Digital image correlation - SDIC	54
Task 2-4: Sample test section design to validate instrumentation and optical configuration	55
Task 2-5: Pressure Measurement	56
Task 2-6: Integration of instruments	56
3. Structural analysis	62
Numerical (Finite Element) Simulations for Design of the Assembly	62
Finite element analysis of one single bundle under seismic loads	62
Finite element analysis of the simplified full length model under seismic loads	63
Finite element analysis of the full model and designing the bracing structure.	64
Finalizing the design of bracing structure, preparing the final drawings and ordering the steel structure.	68
Change in boundary condition of the fuel rods and new finite element analysis.	69
Preliminary experiments on the shake table.	69
Estimation of damping ratios	70
4. CFD validation	72
Task 4.1: FSI solver validation	72

Task 4.2: FSI solver testing on MIRA (BG/Q):	75
LES of 2×2 Spacer Grid – fuel rod system:	80
5. Experimental and Numerical Results.....	82
Background: bundle behavior.....	82
5.1.1 1 D model of bundle	82
Simple model of fluid forces.....	83
Oscillating bundle in stagnant fluid	83
Experiment: bundle behavior.....	84
Experiment: frequency sweeps.....	87
Experiment: Test Cases in Air and Modification of Boundary Conditions	87
Shake Table Tests, Series 1 (Prior to BC modification).....	87
Shake Table Tests, series 2 (After BC modification)	90
Revised analytical model based on new boundary conditions.....	92
Experiment: Initially stagnant water: flow induced by bundle oscillation	93
Experiment: Initially stagnant binary mixture: flow induced by bundle oscillation	101
Experiment: 3D data of velocity in the bypass.....	103
Experiment: 1m/s axial water flow: secondary flow induced by bundle oscillation.....	105
Experiment: 2m/s axial water flow: secondary flow induced by bundle oscillation.....	121
Experiment: Initial conditions characterization.....	122
Experiment: Characterization of Uncertainty.....	124
CFD results	127
6. List of Experimental Runs	155
Tests in air (dry conditions):.....	155
Tests in Water:.....	157
Test conducted in dry environment between water and oil testing	165
Tests conducted in index matched fluid	167
7. Publications.....	173
Journal publications.....	173
Journal publications in preparation.....	173
Conference Proceedings	173
Presentations	174

Invited Talks	175
8. Honors and Awards.....	176
9. Student Involvement	177
10. Conclusions	178
11. References:	184

1. Facility design

Task 1-1: Scaling analysis:

For this seismic study, measurements that elucidate the FSI and acquire validation data are the primary goals. To allow optical access for fluid velocity measurements both in the bypass and within the fuel bundle, a RIM facility is necessitated that dictates the materials that can be utilized for the surrogate fuel rod and working fluid. This difference in material properties mandates a rigorous scaling methodology to ensure data garnered from the model experimental facility is applicable and relevant to a full-scale prototype. This scaling identifies and prioritizes dimensionless similarity groups that are maintained as close to unity as possible for the highest priority groups. Scaling is applied to the full bundle height, and then applied at subsystem levels to the height of the rod between spacer grids and to the design of the spacer grid for constraining the rods.

The working fluid in a prototypical PWR is high temperature (325° C) high pressure (15.6 MPa) water operating at a constant flow rate. For the surrogate fuel bundle used here, solid acrylic rods are utilized with the working fluid P-cymene at room temperature and atmospheric pressure. The geometry of the fuel bundle is maintained as close to unity as possible, by using full height rods, L , maintaining the P/D geometry, and L/D between spacer grids. Comparative values between a prototypical bundle and the surrogate bundle used here can be seen in Table 2.1

Table 2.1: Scaling of Surrogate Fuel Bundle

Parameter	Prototype	Surrogate
Fuel Rod Length (m)	4.000	4.000
Fuel Rod Diameter (mm)	9.500	14.25
P/D	1.333	1.333
L/D	53.47	53.47

For the fuel rod diameter it can be seen that for the surrogate fuel bundle the rod diameter is $1.5D$. This has benefits to two scaling parameters; 1- the first mode resonant frequency of the structure, and 2- the Reynolds number of the axial flow. For the structural response, to consider the fuel bundle as an Euler Bernoulli beam [1] with clamped-clamped constraints, and considering that the majority of the momentum will be absorbed in the first mode, Eq. 2.1 can be used to approximate first mode resonance.

$$f_{model} = \frac{4.73^2}{2\pi L^2} \sqrt{\frac{EI}{m_s + m_f}} \quad (2.1)$$

Where E is the modulus of elasticity, I the moment of inertia, and m_s and m_f the linear mass of the structure and added mass of the fluid respectively. Comparison between the prototype zircaloy tubes with UO₂ pellets inside with the solid acrylic rods can be seen in Table 2.2.

Table 2.2: Prototypical Bundle Geometry Compared with Surrogate Bundle Geometry

Material	Prototype	Parameter	Material	Surrogate
zircaloy	9.5	D_o (mm)	acrylic	14.25
	8.2	D_i (mm)		
	0.51	L_{BG} (m)		0.75
	9.72×10^{10}	E (Pa)		3.30×10^9
	1.76×10^{-10}	I (m^4)		2.02×10^{-9}
UO_2	6570	ρ (kg/m)	P-cymene	1190
	10970	ρ (kg/m)		
	0.699	m_s (kg/m)		0.190
Coolant Water	726	ρ (kg/m)	P-cymene	856
	0.0515	m_f (kg/m)		0.137

From Eq. 2.1 and values from Table 2.2 two more dimensionless properties are obtained, the added mass and the dimensionless frequency of the structure, Table 2.3. The discrepancy in added mass is due to the much closer proximity in density between the fluid and structure in the surrogate bundle, however, this will be accounted for in the scaling for the hydrodynamic forcing from the axial flow, which is the W component of the fluid velocity.

Table 2.3: Dimensionless Parameters for Scaling of Fuel Bundle

Parameter	Equation	Prototype	Surrogate
Added Mass	$m/\rho D^2$	14	2.4
Frequency	$f_{model} L/W$	1.06	1.01

A more rigorous method is then applied to ensure the behavior of the structure will behave similar to a prototypical one. A finite element model of the 6×6 fuel bundle is analyzed in SAP by the collaborators in the Civil Engineering Department, where the following assumptions are made:

- the distance between rods at the spacer grid level are fixed, ie. there is a zero displacement constraint at this level so the displacements of the nodes are identical
- at the extremities the bundle is clamped-clamped
- mass of the spacer grid is applied as a concentrated mass at nodes at the respective levels
- damping ratio in the analysis is conducted at 5% and 15%.

Results from this analysis can be seen in Table 2.4.

Table 2.4: FEA Results for Structure Response to Seismic Forcing

Seismic Forcing Parameters	Prototype (d/D)	Surrogate (d/D)
$a_B = 0.15$ g w/ 5% damping	2.67	3.01
$a_B = 0.30$ g w/ 5% damping	5.36	6.02
$a_B = 0.15$ g w/ 15% damping	1.21	1.31
$a_B = 0.30$ g w/ 15% damping	2.42	2.62

Where the displacement reported, d , is non-dimensionalized by the difference in rod diameter from the surrogate bundle to a prototypical one. Mode shapes from this analysis can be seen in Fig. 2.1 where it can be observed that the mode shapes match even with the reduced number of spacer grids in the surrogate bundle.

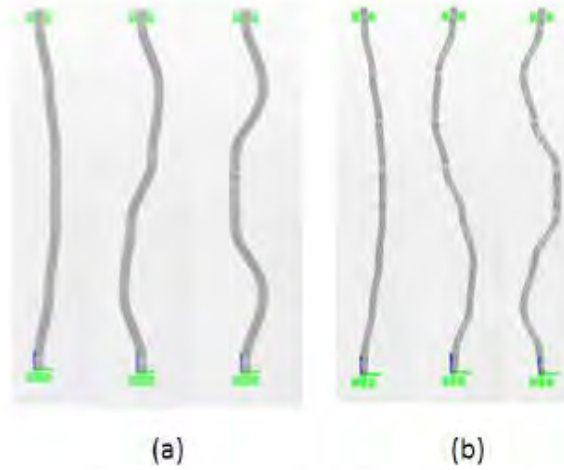


Figure 2.1: Resonant Mode Shapes for first three modes of Fuel Bundle, (a) Surrogate Bundle with 6 spacer grids (b) Prototypical Bundle with 8 spacer grids

Earlier it was discussed that the increase in diameter by $1.5D$ has benefits for the scaling to reach a Reynolds number of the same order of magnitude as a prototypical reactor. As this is an experiment focused on the FSI, the effects of the hydrodynamic loading on the structure need to be properly scaled in addition to the Reynolds number.

The typical Reynolds number in fuel bundles is based on the hydraulic diameter of a rod [2]:

$$Re = \frac{4W(P^2 - \frac{\pi}{4}D^2)}{\pi D\nu} \quad (2.2)$$

Where W is the mean axial liquid velocity, P the pitch, D the rod diameter, and ν the kinematic viscosity. For a mean axial velocity in the bundle of 6 m/s for a prototype this corresponds to $Re = 5 \times 10^5$ in the bundle.

The longitudinal component of drag from the axial flow on the fuel rod per unit length can be modeled with the following equation [3]:

$$F_h = \frac{1}{2} \rho D C_T W^2 \quad (2.3)$$

Where C_T is the friction coefficient, and F_h is the hydrodynamic force on the bundle from the axial flow.

To determine the proper scaling for the axial velocity that corresponds to the hydrodynamic loading on the structure the following steps are taken. Replacing F_h in $F_s = F_h + m_f a_b$

with Eq. 2.3, and F_s with $m_s a_b$, and taking the ratio of the prototype to the surrogate bundle.

$$\frac{(m_s + m_f)_{sur} a_{b,sur}}{(m_s + m_f)_{pro} a_{b,pro}} = \frac{1/2 \rho_{sur} D_{sur} C_{T,sur} W_{sur}^2}{1/2 \rho_{pro} D_{pro} C_{T,pro} W_{pro}^2} \quad (2.4)$$

Rearranging Eq. 2.4 to find the ratio for the axial velocity:

$$\frac{W_{sur}}{W_{pro}} = \sqrt{\frac{(m_s + m_f)_{sur} a_{b,pro} \rho_{pro} D_{pro} C_{T,pro}}{(m_s + m_f)_{pro} a_{b,sur} \rho_{sur} D_{sur} C_{T,sur}}} \quad (2.5)$$

To determine the scaling for the acceleration imposed by the shake table, a true replica model is considered. In earthquake modeling, true replica models simultaneously duplicate inertial, gravitational, and restoring forces [4]. For scaling models for shake table studies, the time history of stress components $\sigma_{ij}(r, t)$ for a true replica model subjected to a time history of vector imposed acceleration $a(t)$, the following dimensionless relationships can be used [5].

$$\frac{\sigma}{E} = f\left(\frac{r}{L}, \frac{t}{L}, \sqrt{\frac{E}{\rho}}, \frac{a}{g}, \frac{gL\rho}{E}, \frac{\sigma_o}{E}, \frac{r_o}{L}\right) \quad (2.6)$$

A true replica model is near impossible to construct, the gravity term in Eq. 2.6 requires the ratio of acceleration between the model and prototype to be $a_r/g_r = 1$. When this is combined with the dimensionless product $gL\rho/E$, it results in the following relationship.

$$\left(\frac{E}{\rho}\right)_r = L_r \quad (2.7)$$

This places a severe restriction on the materials that can be used, for this case where the length ratio for the height of the fuel bundle is unity, this would require the same material to be used in the bundle. However, the hydrodynamic drag force on the bundle is nearly equivalent to the acceleration of gravity and gravity can be neglected. When gravitational effects can be decoupled from the seismic effects, the similitude laws from Eq. 2.6 become more relaxed particularly for the material constraints. Moncarz & Krawinkler [5] provide a new set of similitude laws for using different materials with gravity forces neglected where L , E , and ρ are the independent quantities which are applicable to this case.

The use of solid acrylic rods in place of zirconium-alloy tubes needs to be accounted for in the scaling which can be done by including the moment of inertia, and modifying the independent quantities to be L , EI , and ρ [6], resulting in a reduced value for the acceleration to induce the same displacement of the fuel bundle.

The results for the shake table scaling can be seen in Table 2.5

Table 2.5: Shake Table Scaling Results

Independent Quantity	Relation	Ratio
length	L_r	1.000
time	$\frac{L_r^2}{\sqrt{E_r I_r / m_r}}$	1.054
frequency	$\frac{\sqrt{E_r I_r / m_r}}{L_r^2}$	0.948
acceleration	$\frac{E_r I_r / m_r}{L_r^3}$	0.900
displacement	L_r	1.000

Relating the acceleration term in Table 2.5 back to Eq. 2.5 combining this scaled value with the value for the increased rod diameter in the surrogate bundle Eq. 2.5 can be reduced to:

$$\frac{W_{sur}}{W_{pro}} = \sqrt{\frac{(m_s + m_f)_{sur} \rho_{pro} C_{T,pro}}{1.35(m_s + m_f)_{pro} \rho_{sur} C_{T,sur}}} \quad (2.8)$$

From Eq. 2.8 for an average axial velocity corresponding to $Re = 5 \times 10^5$ for a prototypical bundle, it is found that $W_{sur} = 2.00$ m/s. For a surrogate fuel bundle this corresponds to $Re_{sur} = 3.75 \times 10^4$.

Now from the integral scale, considering the whole domain of the primary channel with the fuel bundle inside, the pressure drop from the axial flow in the surrogate fuel bundle is considered. First to determine the flow rate at the entrance to the fuel bundle, Q_T , the geometry of a cross section of the fuel bundle in the acrylic channel is considered, Fig. 2.2, where subchannels A have been defined and parameters from Table 2.1 and Table 2.2 are used to define the geometry. The unobstructed flow area of each subchannel are determined with Eq. 2.9 - Eq. 2.11 [7].

$$A_1 = P^2 - \frac{\pi}{4}D^2 \quad (2.9)$$

$$A_2 = \frac{A_1}{2} - gap \quad (2.10)$$

$$A_4 = \frac{A_1}{4} - gap \quad (2.11)$$

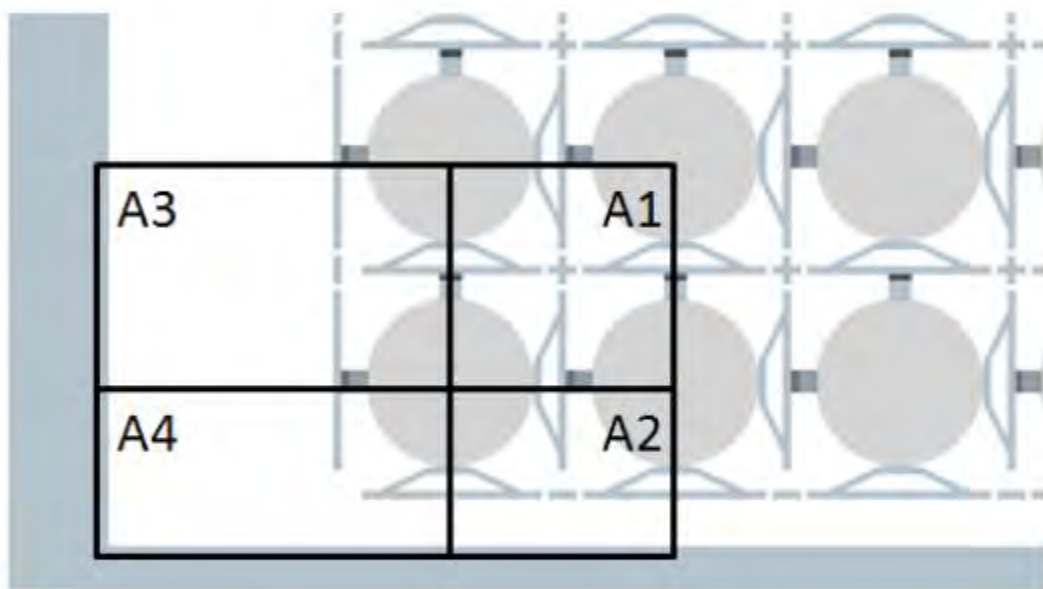


Figure 2.2: Velocity Measurements Inside Static Bundle - 2 m/s Axial Flow Vector Field with Vorticity in Background

Then the hydraulic diameter D_e of the subchannels are determined with Eq. 2.12 - Eq. 2.13:

$$D_{e1} = \frac{4A_1}{\pi D} \quad (2.12)$$

$$D_{e2} = \frac{4A_2}{P + \frac{\pi D}{2}} \quad (2.13)$$

$$D_{e4} = \frac{4A_4}{P + \frac{\pi D}{4}} \quad (2.14)$$

Where equations for A_2 and D_{e2} are the same for A_3 and D_{e3} but with a different value for the gap geometry. The total volume flow rate Q_T is defined with

$$\begin{aligned} Q_T &= \sum W_i A_i = \left(\frac{2g_c \Delta P_r}{L f_w} \right)^{1/2} \sum A_i D_{e,i}^{1/2} \\ &= \left(\frac{2g_c \Delta P_r}{L f_w} \right)^{1/2} A_1 D_{e1}^{1/2} \left(n_1 + n_2 \frac{A_2 D_{e2}^{1/2}}{A_1 D_{e1}^{1/2}} + n_3 \frac{A_3 D_{e3}^{1/2}}{A_1 D_{e1}^{1/2}} + n_4 \frac{A_4 D_{e4}^{1/2}}{A_1 D_{e1}^{1/2}} \right) \end{aligned} \quad (2.15)$$

With Eq. 2.15 the total flow rate can be determined for a desired velocity within A_1 which is considered the axial velocity within the fuel bundle. This flow rate that accounts for the geometry of the primary channel is used in place of the velocity in the following equations to determine the pressure drop through the fuel bundle and spacer grids respectively, Eq. 2.16 - Eq. 2.17.

$$\Delta P_{rod} = f_w \frac{L}{D_{e1}} \frac{\rho W_1^2}{2} \quad (2.16)$$

$$\Delta P_{sg} = C_s \frac{\rho W_1^2}{2} \frac{A_s}{A_1} \quad (2.17)$$

Where A_s is the spacer projected area per unit cell and is determined with $A_s = 2(Pt - t_w^2/2)$. Then the ratio of the pressure drop from the bare rods and from the spacer grids are determined for varying cases in the surrogate bundle and for a prototypical bundle and are reported in Table 2.6.

Table 2.6: Pressure Drop in Integral Scale Fuel Bundle

	Re	W (m/s)	ΔP_{rod} (kPa)	ΔP_{sg} (kPa)	$\Delta P_{rod}/\Delta P_{sg}$	C_s	f_w
Surrogate	10.0×10^3	0.533	0.900	0.169	0.533	1.9	0.0296
	20.0×10^3	1.07	0.317	0.622	0.511	1.75	0.0261
	37.5×10^3	2.00	1.00	2.19	0.456	1.75	0.0233
	100×10^3	5.32	5.95	15.1	0.393	1.7	0.0195
Model	500×10^3	5.52	6.52	16.4	0.396	1.7	0.0150

Where the friction factor f_w is determined for a single interior channel, where it assumed for all cases the flow is fully turbulent inside the bundle, with Eq. 2.18.

$$f_w = \frac{C_f}{Re^{0.18}} \quad (2.18)$$

In Eq. 2.18 C_f is found with the coefficients for a bare rod in a square array with a $P/D = 1.33$ with $a = 0.09059$, $b_1 = 0.02681$, and $b_2 = -0.03411$ with Eq. 2.19.

$$C_f = a + b_1(P/D - 1) + b_2(P/D - 1)^2 \quad (2.19)$$

In Table 2.6 it can be observed that above $Re = 20.0 \times 10^3$ the drag coefficient C_s becomes essentially Reynolds number independent. Furthermore the pressure drop through the spacer grid is always the more prominent pressure drop in relation to the pressure drop from the bare rods. The nominal values for the pressure drop are found to correlate best for $Re = 100 \times 10^3$ for the surrogate bundle to the prototypical bundle at $Re = 500 \times 10^3$. However, the ratio of the pressure drop from the bare rods to the pressure drop through the spacer grid stays fairly constant above $Re = 20.0 \times 10^3$.

Hence $Re = 37.5 \times 10^3$ in the surrogate bundle is representative of $Re = 500 \times 10^3$ in a prototypical bundle for the relationship between the hydrodynamic forces and the structural response of the bundle to external seismic forcing. It will be shown in Section that this scaling is done properly as the center of the first mode shape is skewed to a higher elevation as in prototypical bundles from the $Re = 500 \times 10^3$ axial flow [8].

2.2 Scaling of Surrogate Spacer Grid

The scaling for utilization of surrogate materials defined the number of spacer grids required to match fuel bundle resonant characteristics. However, prototypical spacer grids cannot be used for

this surrogate fuel bundle due to the increased rod diameter and an incorrect spring contact force for the reduced weight of the surrogate fuel rod. This is an important characteristic, as to properly capture the non-linearity of the structure the inclination of the rod in the spacer grid can change the number of contact points and this needs to be modeled properly. To address these constraints, a custom spacer grid is designed.

2.2.1 Design of Scaled Spacer Grid

The current design utilizes geometry from a non-mixing vane spacer grid that was used in a study on subchannel flow for the PSBT benchmark test [9], but is increased by 50% to ensure proper scaling of bundle natural frequency. However, the spring design is modified, while maintaining the other proportions to ensure an appropriate P/D, flow area, and pressure drop through the grid as discussed in Section 2.1

Comparing the spring from Fig. 2.3 with that from the PSBT benchmark test, the primary difference is that a bi-metallic spring design is utilized where the geometry and the material are changed. The justification for these changes, is due to the difference in weight and diameter of the surrogate material for the fuel rod being used, Table 2.7, with more details on the design to follow.

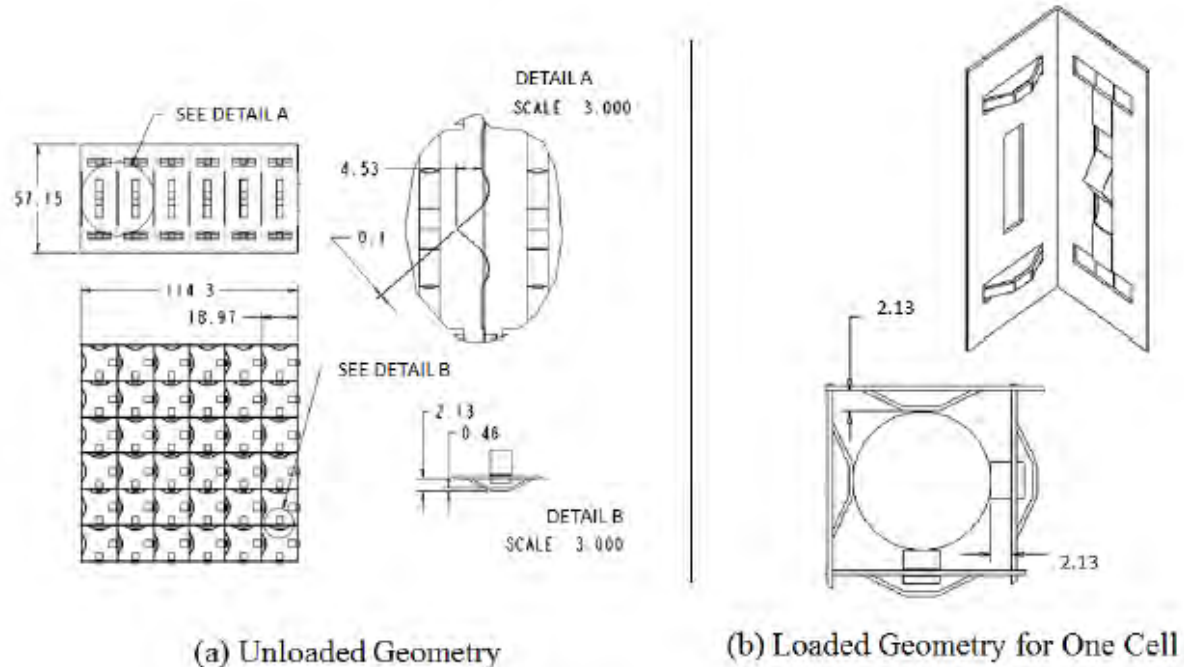


Figure 2.3: Scaled Spacer Grid Geometry for spacer grid A, reported dimensions are in units of mm

Table 2.7: Fuel Bundle Parameters [10] and [11]

	Fuel do(m)	Rod di(m)	L	Spacer Grids	Rod Sect. Weight in Air (N)	Spring Contact Force (N)	Non Dim. Force	Spring Stiff. (N/mm)
Prototype	0.0095	0.008	4	8	3.484	25	5.62	152.9
Model	0.0143	n/a	4	6	1.386	9.8	5.62	4.2

A total of 6 spacer grids are selected for the bundle. The four intermediate grids are SG-A type, Fig. 2.4 and these are free to deflect during testing. The end spacer grids are rigidly fixed to the wall of the test section and have stronger springs to prevent eventual drop of a rod during bundle excitation. These grids are labeled SG-B. This spacer grid configuration is modeled after a prototypical PWR fuel assembly where Inconel spacer grids are used at top and bottom due to the materials high strength and corrosion resistance, while Zircaloy spacer grid are used in the intermediary because of its better neutron economy [12]. The material properties for the two types of spacer grids used in this facility can be seen in Table 2.8.

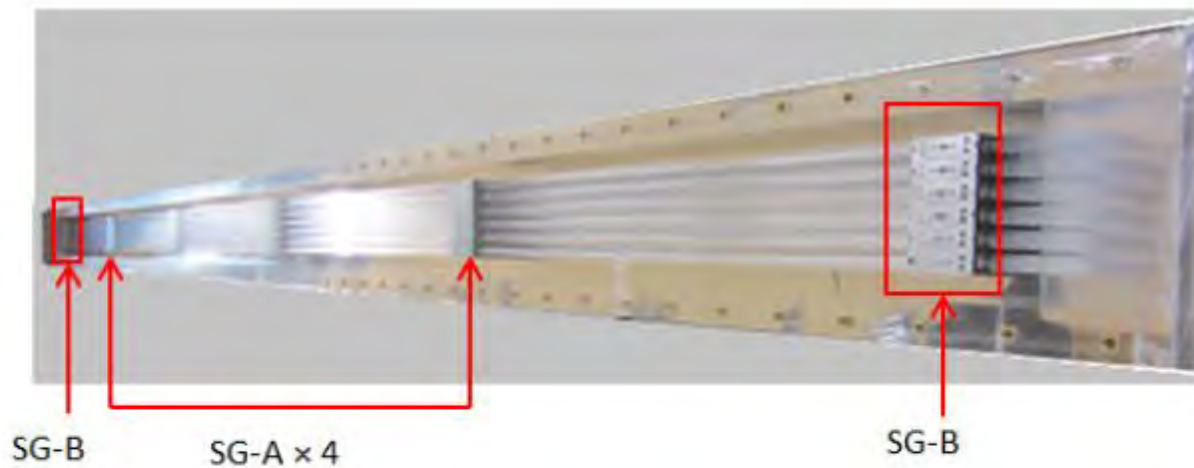


Figure 2.4: Final Rod Bundle. End spacer grids (SG-B) are rigidly fixed to the test section, while the four center one (SG-A) are free to deflect

Table 2.8: Model Spacer Grid Properties

	Material	Strap Thick. (m)	Surface Rough. (m)	Material	Spring Thick. (m)	Surface Rough. R_a (m)
SG-A	26 AWG 304 S.S.	4.6×10^{-4}	8×10^{-7}	Spring Tempered	1.02×10^{-4}	4×10^{-7}
SG-B	25 AWG 304 S.S.	5.3×10^{-4}	8×10^{-7}	301 S.S.	2.03×10^{-4}	4×10^{-7}

The pertinent information for the design of the spacer grids is the geometry and material for the fuel rods, as well as the number of grids utilized for the model. With this information, it is possible to determine a dimensionless contact force to properly model the spring of SG-A. Per fuel rod, each pair of springs in a spacer grid has to be able to hold the weight of the unsupported span of the rod between grids in air. Typically fuel assemblies are designed with a spring contact force that enables the bundle to withstand loads during shipping and installation into the reactor, which leads to a contact force of about 25 N [11]. The dimensionless contact force is the ratio of the weight of the unsupported rod span between grids in air, to the normal force that is a product of the spring contact force and coefficient of friction. For the model parameters, to match the dimensionless contact force, the spring contact force is 9.80 N.

A spring was initially designed that maintained both this scaled contact force and a scaled spring constant based on a published value of 153 N/mm [10]. The deflection of this scaled spring when the rod is placed in contact is at the sub-millimeter scale. During the design of the model rod bundle, it became apparent that this small a deflection would lead to high uncertainty in the spring contact force due to a non-uniformity of the rod diameter. Therefore to produce a spring with an appropriate contact force and acceptable uncertainty level, the scaled spring constant could not be maintained.

2.2.2 Spacer Grid Design and Manufacture Uncertainty Analysis

A geometrical model of a rod in a spacer grid cell is used to predict analytically the overall uncertainty, u_F , on contact force, $F=kx$, see Fig. 2.5 for the model. The latter is due to uncertainties both in spring displacement and stiffness, u_x and u_k , respectively. This enables optimization of the spacer grid and spring design to minimize uncertainty on contact force in static environment. The methodology takes into account tolerances of each manufacturing process, which are summarized in Table 2.9.

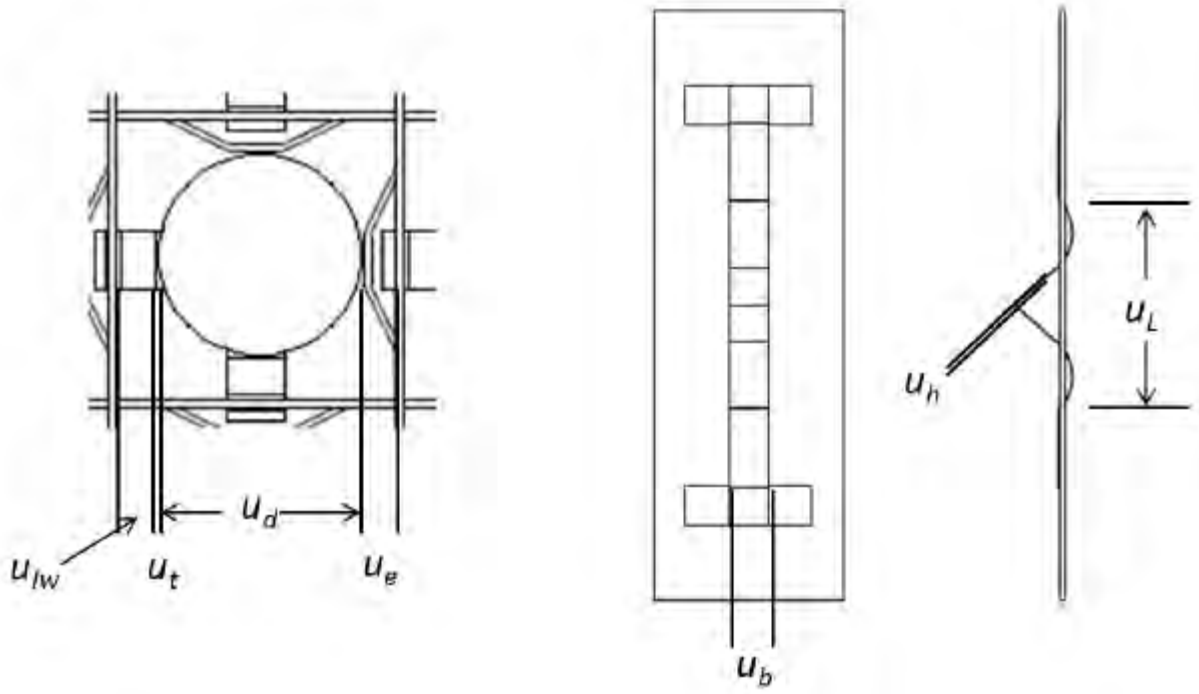


Figure 2.5: Uncertainty values applied to model geometry

Table 2.9: Tolerances for manufacturing of spacer grid strap. u_i are identical for SG-A and B

	Rod Diam. (u_d)	Thick. of strap (u_t)	Laser weld (u_{lw})	Laser Cut (u_{lc})	Embossed Feat. (u_e)
Manufac. Unc. (m)	2.54×10^{-4}	3.81×10^{-5}	2.03×10^{-4}	2.03×10^{-4}	3.81×10^{-4}
Measured Unc. (m)		1.0×10^{-5}	1.3×10^{-4}	2.0×10^{-4}	1.1×10^{-4}

For a process y with an analytical relation $f(x_i)$ relating it to its input variables, x_i :

$$y = f(x_i) \quad (2.20)$$

the design stage uncertainty is [13]:

$$u_c(y) = \sqrt{\sum_i \left(\frac{\partial f}{\partial x_i} u_{x_i} \right)^2} \quad (2.21)$$

The uncertainty in the spring initial displacement is based on the absolute tolerances of the manufacturing processes and materials which are fixed, Fig. 2.5 and Eq. 2.22. In order to keep this uncertainty value in the same order of magnitude as the uncertainty in the spring stiffness, the displacement needs to be in the millimeter scale and a value of 2.3 mm is selected.

$$u_x = k \sqrt{u_d^2 + u_t^2 + u_{tw}^2 + u_e^2} \quad (2.22)$$

With data reported in Table~\ref{tab:gridTol}, the uncertainty on initial displacement for an initial displacement of 2.3 mm is 21.5\% based on tolerances. However, once received the straps have been carefully measured, and the tolerance on the fabricated grids are reported in the last row of Table~\ref{tab:gridTol}. With these values the uncertainty on initial spring compression is 13.1\%.

For the spring stiffness more flexibility is introduced in minimizing the uncertainty as the stiffness is estimated with the Euler Bernoulli beam theory for a rectangular beam clamped at both ends with a concentrated load at its center (\cite{AISC}). It is therefore possible to optimally select its materials (and therefore Young's modulus, E), its thickness, h , width, b , and length, L . Here a spring tempered thin gauge stainless steel is selected for the springs and the uncertainty on Young's modulus is neglected. Based on Eq.~\ref{eq:3.2.2}, the overall uncertainty on spring stiffness reduces to:

$$u_k = k \sqrt{\left(\frac{u_b}{b}\right)^2 + \left(3\frac{u_h}{h}\right)^2 + \left(-3\frac{u_L}{L}\right)^2} \quad (2.23)$$

With current materials and manufacturing tolerance reported in Table 2.9, u_k is 27.3%. With the measured uncertainties for stiffness, u_k is 1.0%, and the overall uncertainty on contact force is the root of the sum of the square (RSS) of u_x and u_k and is 13.2%.

The uncertainties with a spring displacement of 2.3 mm are tabulated in Table 2.10 for SG-A grids utilized in the experimental facility that has the dimensional contact force stipulated in Table 2.7.

Table 2.10: Calculated Relative Uncertainties

Spring	Param.			Measured	Uncertainty	(m)
b (mm)	h (mm)	L (mm)	E (Pa)	u_b	u_h	u_L
1.91	0.457	20.2	1.93×10^{11}	2.0×10^{-5}	1.0×10^{-5}	2.0×10^{-5}

The second type of spacer grid (SG-B) has a contact force that is three times higher, and is made with both thicker gauge straps and springs, the values of which are reported in Table 2.8. The relative uncertainty on contact force in these grids is 13.2% as well.

2.2.3 Characterization of Spring Element

The uncertainty analysis for SG-A defined the distance the spring needs to deflect from the unloaded position, prior to when the fuel rod is inserted, to the final position with the fuel rod in place, this forces use of a spacer grid with bimetallic springs. This feature was taken advantage of to design springs that have constant spring stiffness over the whole allowable displacement. This leads to a linear contact force, which simplifies simulations of this system and is different than prototypical grids, where the spring stiffness strongly depends on deformation. To estimate the rod deflection from a unit load (ie. 1 N), first an analytical analysis utilizing the Euler Bernoulli Beam theory described above is employed. However, while this methodology is acceptable to estimate design stage uncertainty, it does not provide adequate confidence to estimate the actual contact force. Thus a finite element analysis is performed.

The FEA is conducted in ANSYS R15.0. The geometry for the spring from Fig. 2.3 can be seen in Fig. 2.6 with the associated boundary conditions from the grid strap, which is assumed rigid.

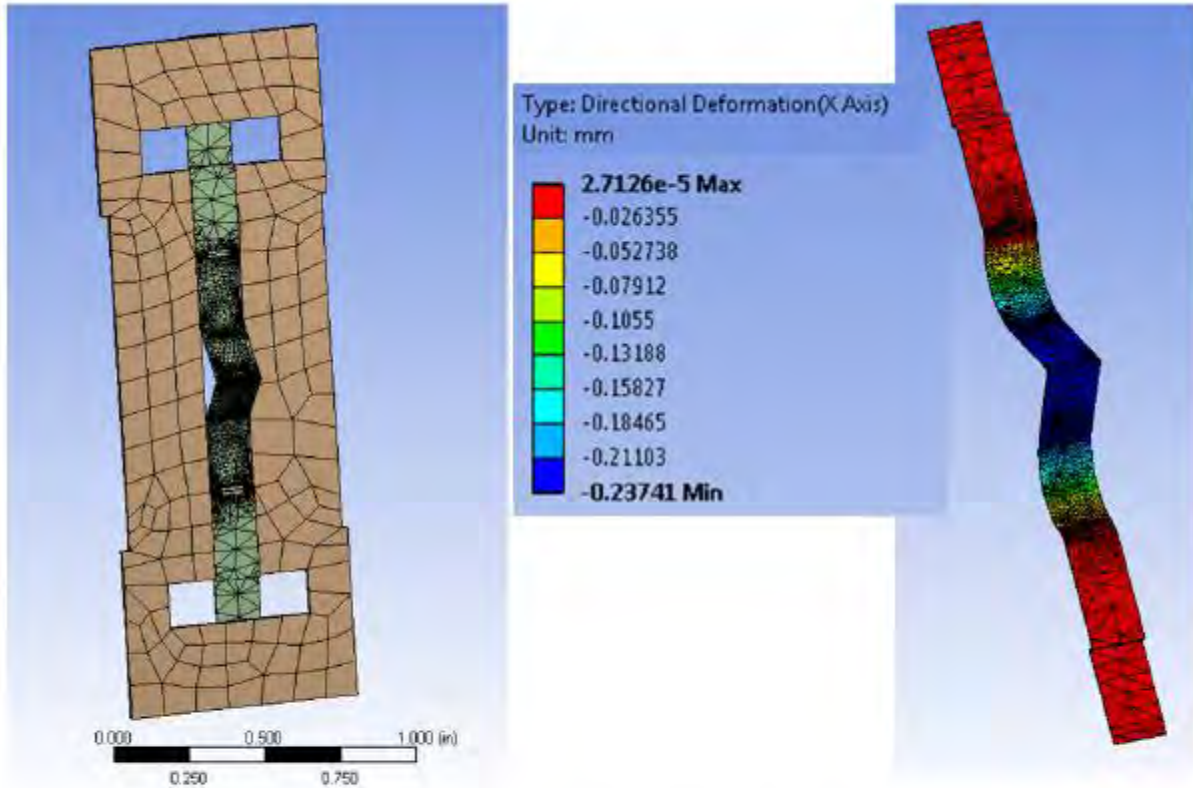


Figure 2.6: FEA boundary conditions and results for unit load analysis with strap geometry hidden for display purposes

For the first analysis material properties for spring tempered stainless steel are defined, Table 2.11, and a unit load is applied at the point where the fuel rod is in contact with the spring, Fig. 2.6.

Table 2.11: Calculated Relative Uncertainties

$\rho(kg/m^3)$	Poission Ratio	E (Pa)	Tensile Str. (Pa)	Yield Str. (Pa)
7,880	0.457	1.93×10^{11}	1.89×10^9	1.55×10^9

The analysis is conducted with an iterative method in which a 5% allowable change is stipulated for the deformation of the spring. A coarse mesh is used in the first analysis, and locations that are identified as being pertinent to the analysis are refined for the ensuing steps. For the unit load analysis, five iterations with a maximum node count of 44309 are required to reach the specified criteria for deformation, with a max deformation at the center of the spring of 0.237 mm, Fig. 2.6. This value is less than that predicted with the analytical analysis, but is at the same order of

magnitude which lends confidence to the FEA analysis. The spring constant can then be determined from $F=kx$ to be 4.2 N/mm.

With the spring constant defined, the contact force can be determined for the deflection of the spring when the rod is inserted which is designed to be 2.33 mm. At this deflection, the contact force is 9.8 N.

To ensure the spring will not experience plastic deformation if the rod vibrations cause the spring to deflect past the designed distance, a second set of analyses are conducted in ANSYS. A prescribed displacement is utilized in place of the unit load in this set of simulations. The maximum distance the spring can deflect is 4.52 mm, which is the distance if the spring is deformed all the way against the strap. Five points are analyzed between the loaded spring displacement value and the maximum deflection, Fig. 2.7.

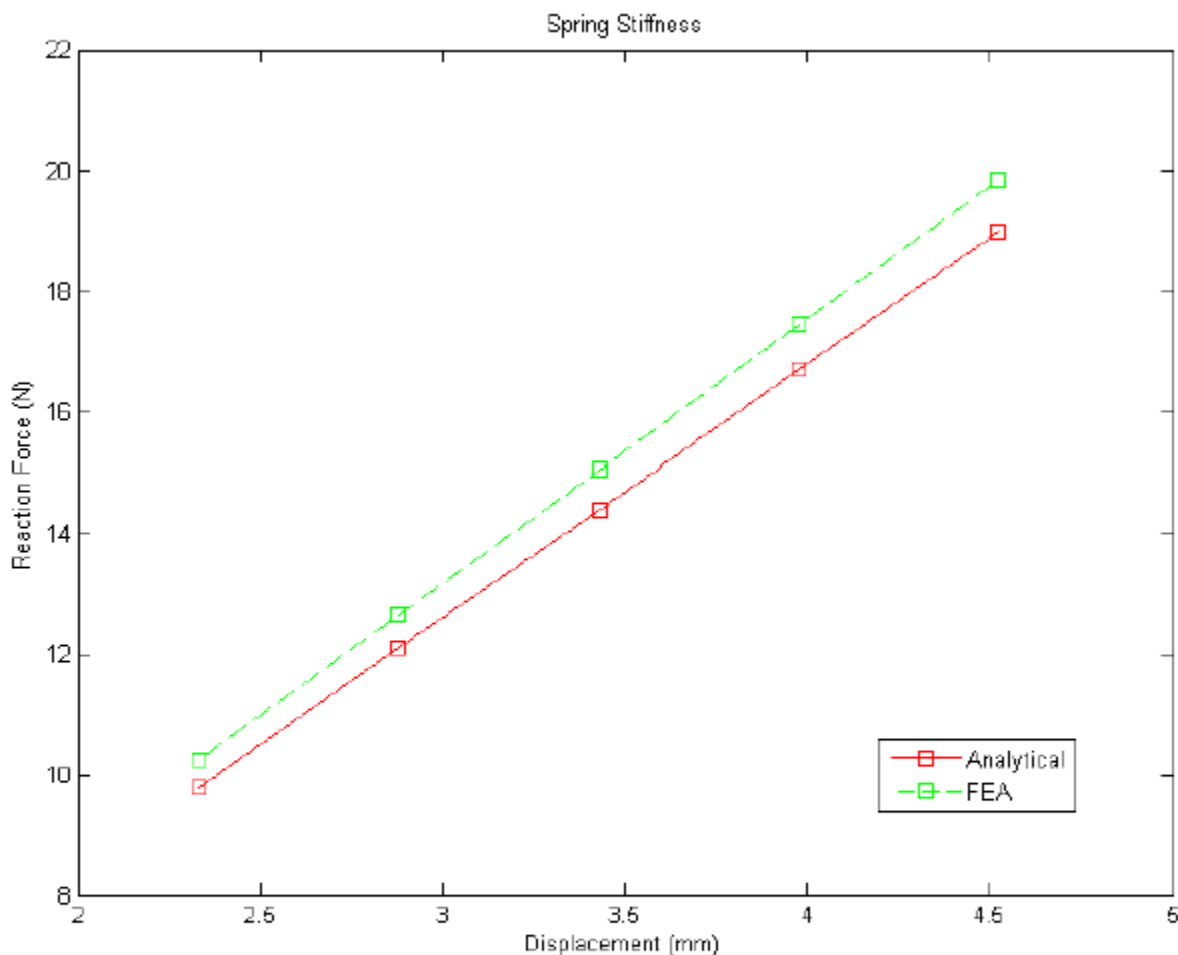


Figure 2.7: Contact force vs. displacement for both calculated and FEA results for SG-A

The contact force is found to have a linear relationship within the possible displacement values for the spring within the spacer grid ensuring they will not plastically deform during testing and spring stiffness of 4.2 N/mm. The maximum von-Mises stress is found to be of 1.35 GPa at the maximum allowable displacement which is 20% less than the yield stress of the material.

Task 1-2: Inlet plenum and test section:

The overall design of the test section, plenums, and support structure were completed in third quarter of FY 2013, Fig. 1.1. The test section was completed in mid-August 2014, see figure 1.1 with the PIs standing in front of it. The facility parameters are given in Table 1.1 and are published in ASME Journal of Nuclear Engineering & Radiation Science.

The overall designed facility is 7 m tall and has a footprint of 3 m × 3 m and weights 6 metric tons, which is half of the capacity of the GW shake table. Details of the facility dimensions are given in Table 1.1.



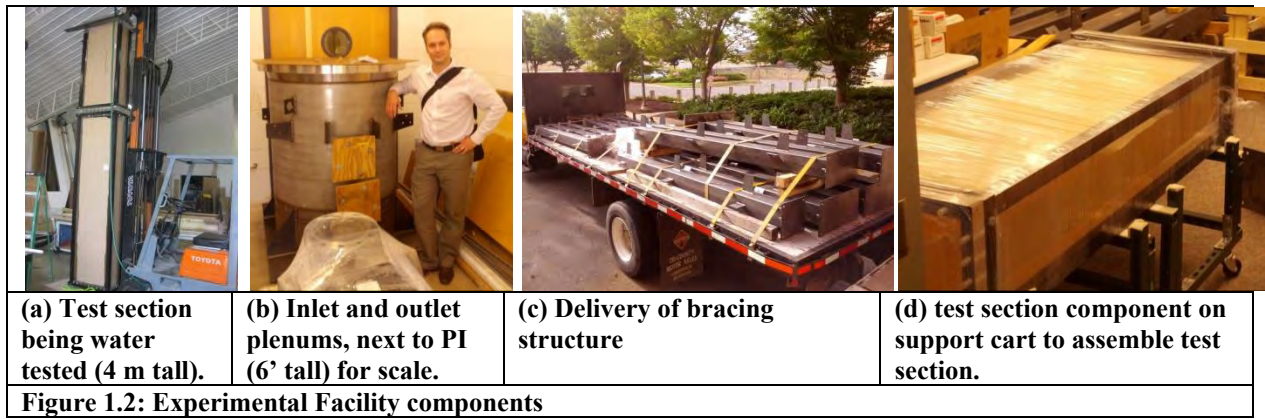
Fig. 1.1. Final facility design with bracing structure, inlet and outlet plenums, and test section

Table 1.1. Facility parameters.			
Sub assembly			6 × 6
Rod diameter (D)		(mm)	14.25
Pitch (P)		(mm)	19.00
P/D			1.333
Test section dimension	Base	(m)	0.216
	Width	(m)	0.559
	Height	(m)	4.22
Shroud dimension	Base	(m)	0.123
	Width	(m)	0.153
	Height	(m)	4.22
Pump			Goulds 50Hp (×2)
Flowmeter			Rosemount Vortex Flow Meter Accuracy: ± 0.65% of reading
Flow rate (max)		(l/s)	120.
Mean velocity (max)		(m/s)	6.0

Because this facility will be used on a shake table, special precautions had to be taken when designing it, in particular to prevent and mitigate leaks. The flow channel is an inner shroud that is inside a sealed test section. If the shroud leaks, the outer test section will act as a secondary containment. Outside of the inlet plenum a tertiary containment will also be built. We have tried this concept on the small scale experiment, see Task 2-4 and validated our design made of thin gauge metal sheets, rivets, and para-cymene resistant epoxy.



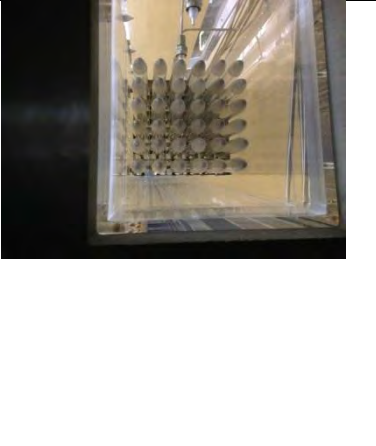
The main components of the experimental facility were delivered on the following dates: test section (June-2013), inlet and outlet plenums (Sept.-2013), and bracing structure (Sept.-2013), see Fig. 1.2. The plenums are made of stainless steel 304 with 3/8" wall thickness and are rated for 8 atmospheres following the guidelines from ASME pressure vessel standards. Pumps and vortex flowmeter were also received during FY 2013.

The test section was assembled on its side (horizontally) and closed with support plates of inlet and outlet plenums before being hoisted on top of the inlet plenum. The various components were positioned in place with support carts, see Fig. 1.2.d. Construction of the fuel bundle and inner channel spanned the 3rd and 4th quarter of FY 2014.



Once construction of the test section was complete, a group of skilled structural workers were hired to erect the test section and bracing system under supervision of the structural and mechanical engineering groups. The procedure was completed in one and half day and everything lined up perfectly. The following photos in figure 1.3 show some steps of assembling the structure.

Advanced flow conditioning elements are integrated in the inlet plenum to guarantee smooth initial flow entering the test section. Details are given on figure 1.4. In short, series of perforated plates, honeycomb, screens, and contraction section are used to generate an initial flow with high uniformity and low level of initial disturbances. Hence the numerical domain can start at the entrance of the test section. To further simplify the simulations, the boundary layers issuing from the nozzle are tripped to make them turbulent, therefore it is not necessary to capture the complex transition from laminar to turbulent boundary layers when simulating this flow.

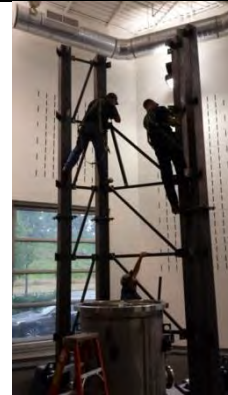
		
<p>Built sub-assembly in inner shroud</p>	<p>Closed inner shroud getting ready for test section construction</p>	<p>Test section being constructed</p>
		
<p>Assembled test section</p>	<p>Bottom of fuel assembly</p>	<p>Top of fuel assembly</p>



Installation of first columns. Inlet plenum is already in place



Construction of 1st column



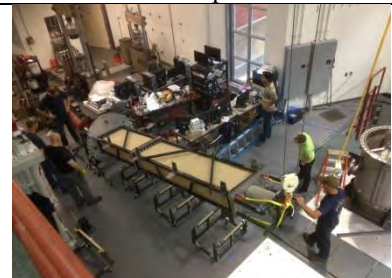
Construction of quarter frame to hold test section in place



Preparation of test section, which is resting horizontally on carts



Lifting of 4m long test section



Lifting of test section



Lifting of test section



Moving of test section towards inlet plenum



Fine tuning of test section on inlet plenum; they are aligned within 0.005"



Test section is installed!



Securing on test section on columns



Bracing structure construction continues



Construction is nearly complete

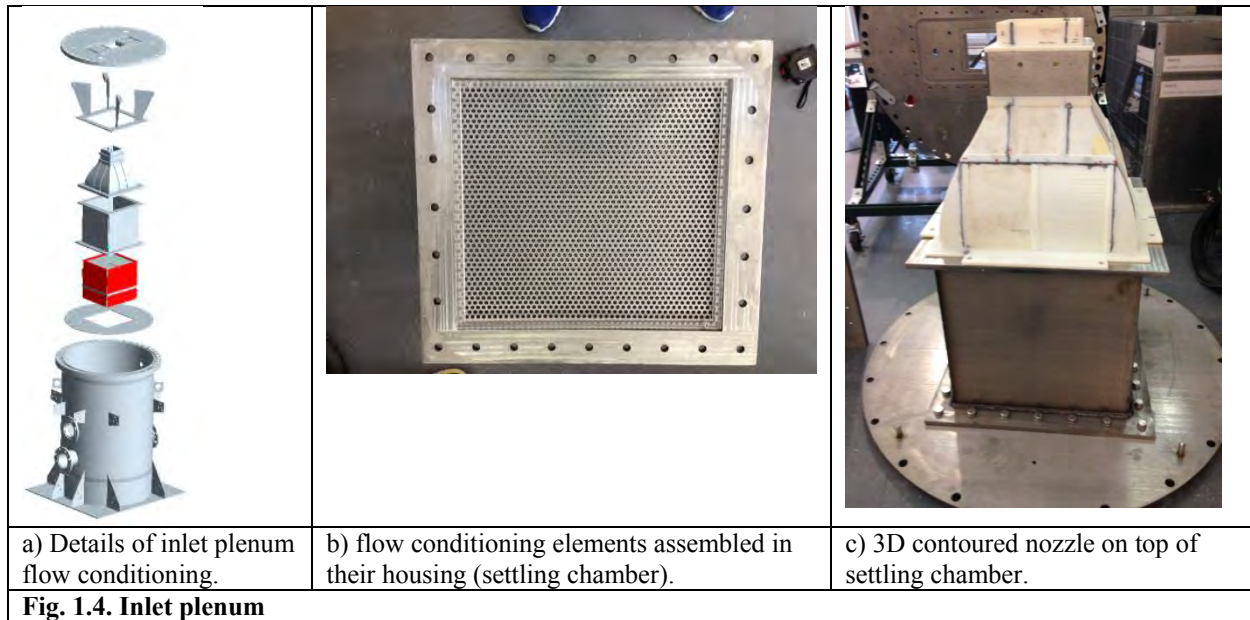


Final tightening of nearly 600 bolts!



Final structure

Figure 1.3. Construction of the test section



Task 1-3: Flow Loop

The flow loop construction was completed and extensively tested with a flow rate equivalent of up to 4 m/s with water during the 2nd quarter of FY 2015. Initial conditions data and extensive shake testing data were acquired both with axial flow and with stagnant water. In this fluid-structure interaction problem, published data indicate that it is critical to reproduce an axial flow with mean velocity on the order of these encountered in nuclear reactors. For our geometry, this corresponds to nearly 120 l/s (~1700 gpm). To deliver this flow rate with sufficient head, a large 100 Hp pump was necessary. This type of pump is prohibitively expensive and instead two 50 Hp pumps were bought. However, with this configuration, the flow is more susceptible to having large scale oscillations due to instabilities between the pumps. Furthermore, we planned on minimizing the volume of fluid as well. As a result, a special return tank had to be designed. It incorporates sets of baffles to guarantee a steady flow. It also has a built in heat exchanger to control the fluid temperature while the loop is operated. The heat exchanger is connected to a 20 tons chiller.

Pumps and return tank are mounted on a custom support frame, Fig. 1.5. The pumps are connected to the return tank with vibration isolation expansion joints that are chemically compatible with para-cymene. They are also mounted on vibration isolation feet. Pumps are controlled with variable frequency controllers. The latter are connected as a master/slave configuration and are computer controlled via a specially developed labview virtual instrument, vi. This same vi is also used for recording measurements from the accelerometers, pressure transducers, thermocouples, and flow meter. Hence a single file contains all the critical information on each dataset is acquired. The pumps are connected together with a custom manifold designed with flow conditioning elements to break down potential sources of instability

as the two streams merge. Finally, a custom made chemically resistant flexible hose connects the manifold to the test section, the completed flow loop can be seen in Fig. 1.6.

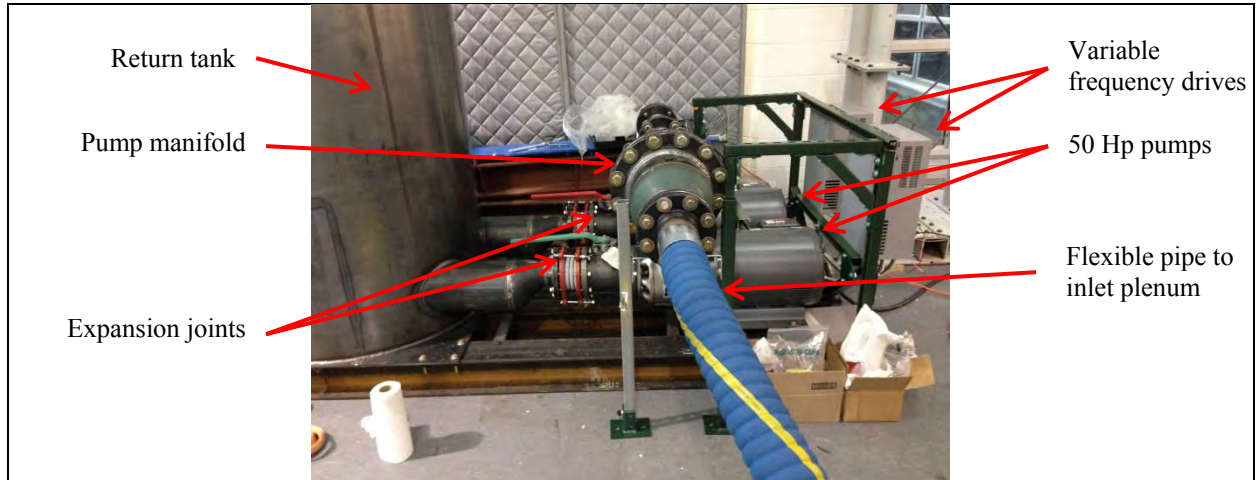


Fig. 1.5. Mounting of pumps and return tank.



Fig. 1.6. Completed flow loop.

A schematic of the flow loop is given in figure 1.7. In this figure we also define the naming convention for the spacer grids. The spacer grids that are free to oscillate are labeled 1 through 4, with 1 being the highest.

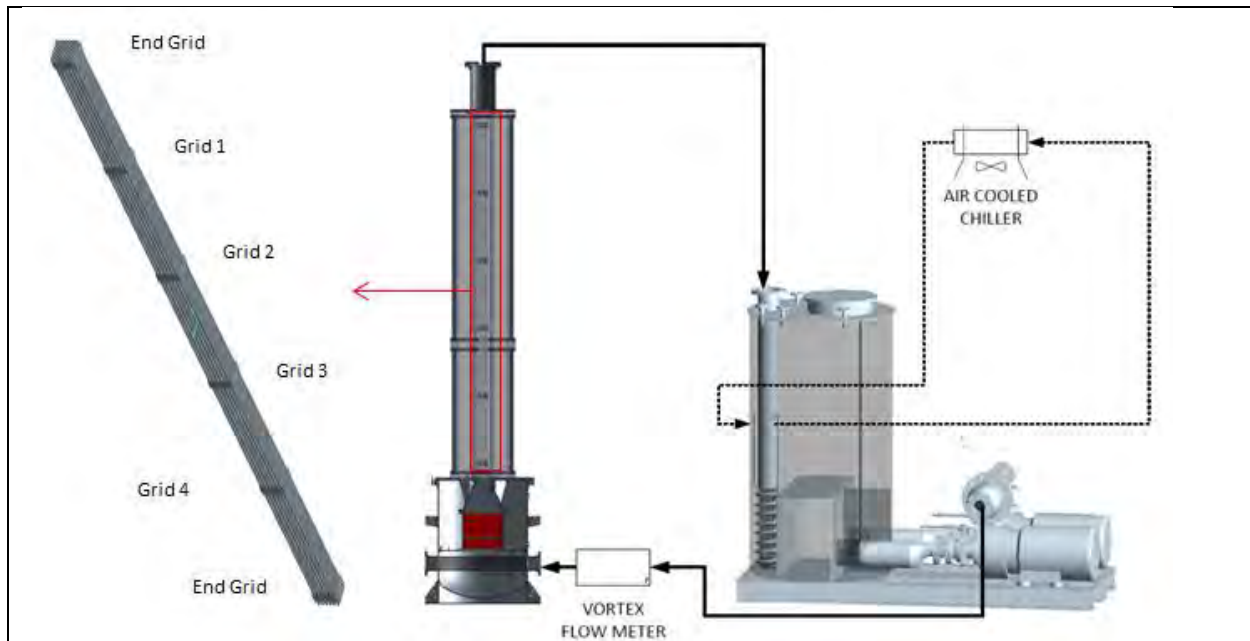


Figure 1.7. Flow loop with nomenclature for the bundle. The two end spacer grids are fixed, while the 4 middle spacer grids are free to deflect. The latter are named 1-4, with # 1 being the highest.

During the 4th quarter of FY 2015 the flow loop was significantly modified to enable operation with paracymene. First the loop was dried for several weeks to prevent contamination of water into the oil. Additionally, many gaskets were replaced with chemically compatible ones. To clean the oil if contaminated, a large inline filter was installed as a bypass loop that can be isolated from the primary loop with the 3 ball valves seen in Fig. 1.8.a. Additionally to fill the stagnant fluid in the secondary tanks, a smaller flow loop with a $\frac{3}{4}$ Hp pump controlled with a vfd was needed to push 4 meters of hydrostatic head. These upgrades were performed on funds of the University.



Figure 1.8. (a) large flow capacity filter installed in the loop (b) pump & vfd for stagnant fluid
The flow loop was leak tested incrementally, first testing components in static conditions prior to turning the pumps on. The primary and secondary channels can be seen being filled with the index matched fluid in Fig. 1.9 where below the fluid line the profile of the rods is not easily discerned due to the near index match with P-cymene.

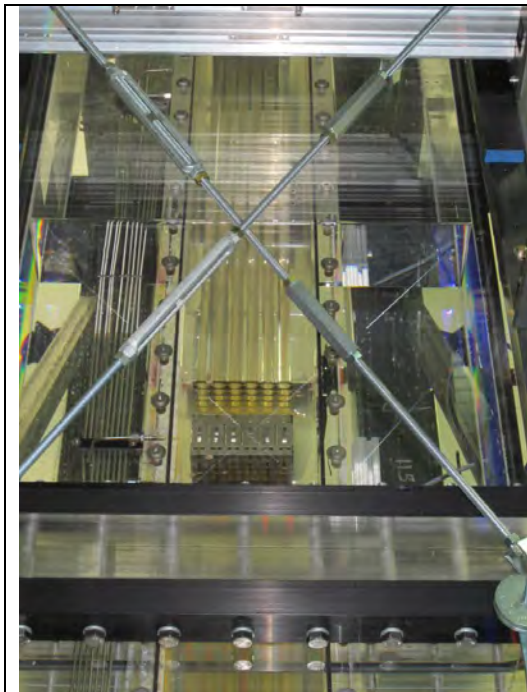
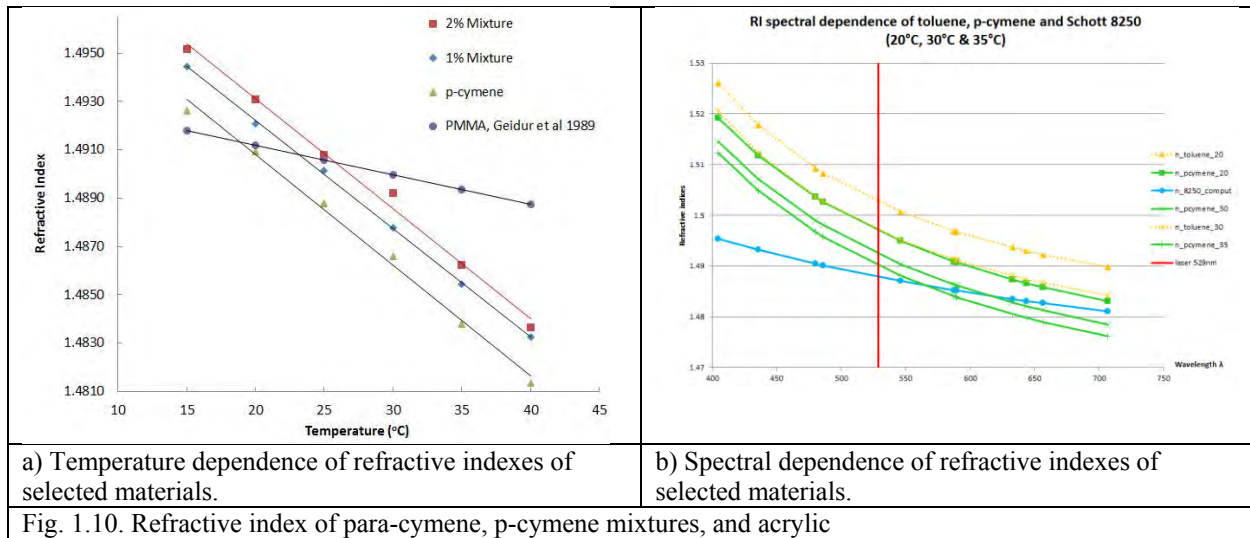


Fig. 1.9. Primary channel being filled with index matched fluid.
Shake tests in still p-cymene were conducted, after which to improve the index matching at room temperature cinnamic aldehyde was added to the working fluid to create the binary mixture that

is further discussed in Task 1-4 and 2-2. With this binary mixture the extensive testing is conducted both with still fluid and with axial flow up to velocities of 2 m/s.

Task 1-4: Material selection

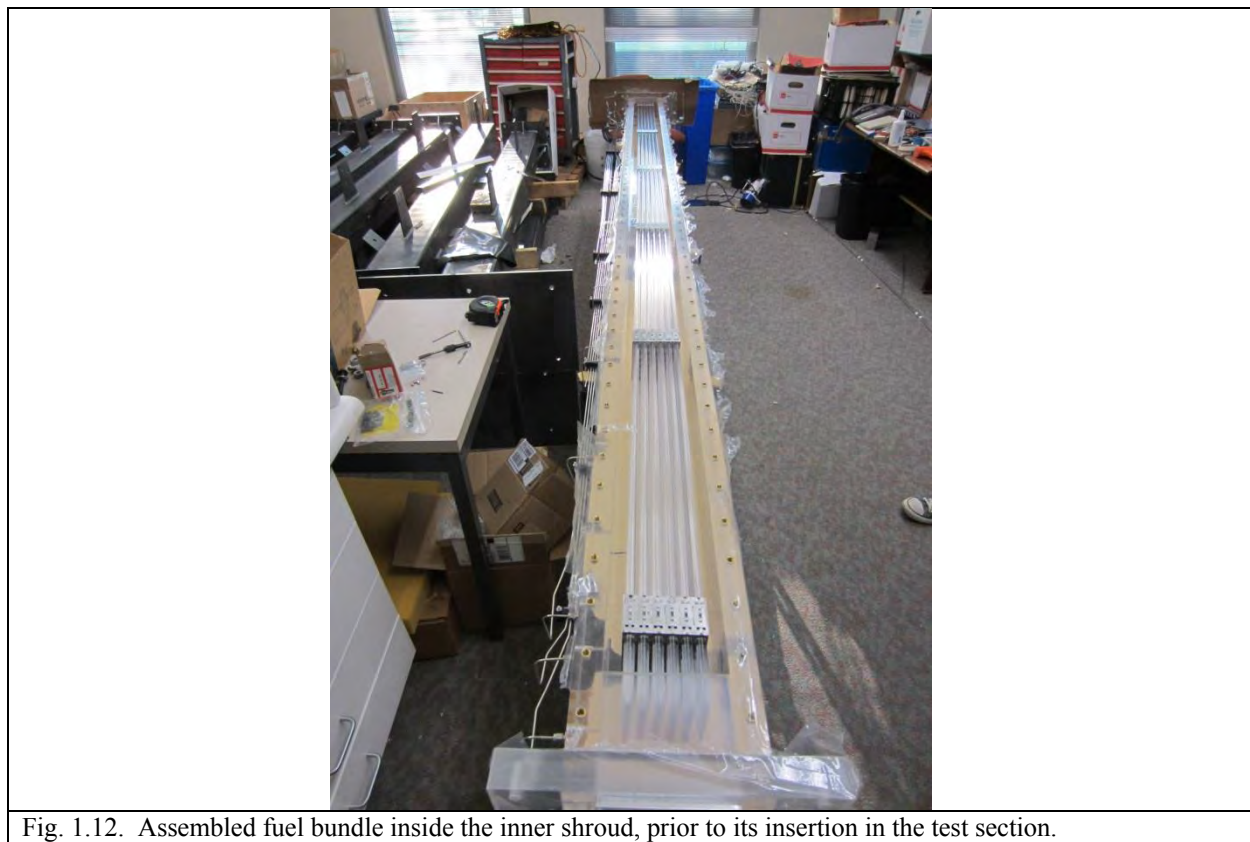
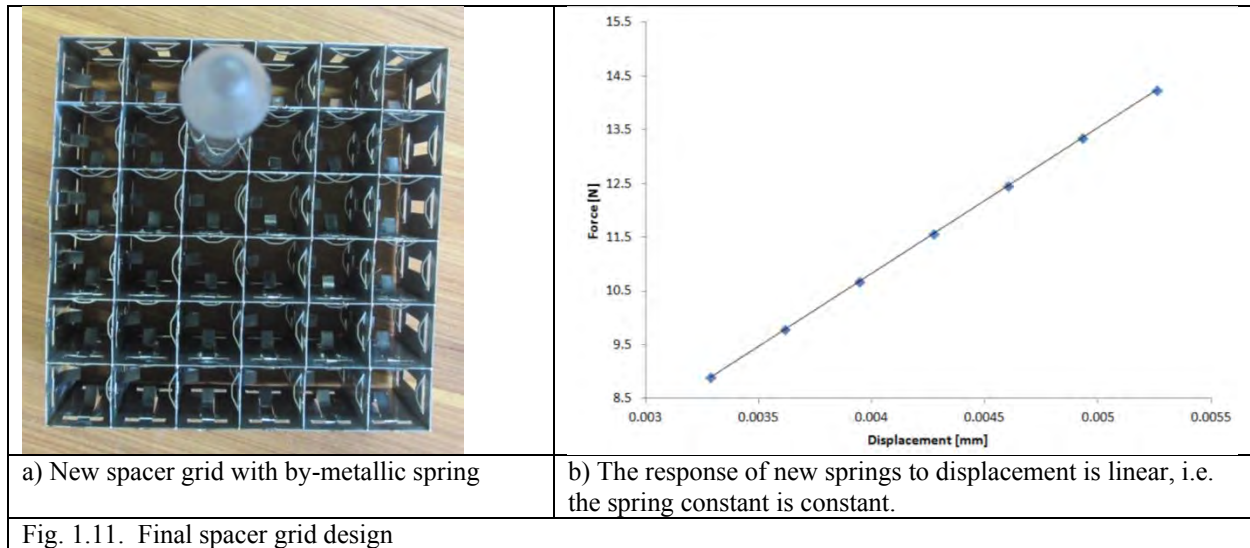
This task is completed. For para-cymene and para-cymene-cinnamaldehyde mixtures, we measured the temperature dependence of density, viscosity, refractive index, Fig 1.10. We found that p-cymene was matched to acrylic at 18°C, which is not practical for our application. By adding a small concentration of cinnamaldehyde, we can increase the working temperature to have a good matching between the liquid and the solid. With 1% and 2%, they are index matched at 23°C and 27°C, respectively. A manuscript summarizing these results has been accepted for publication in Experiments in Fluids.



Task 1-5: Spacer Grids Design and fuel bundle

This task is completed. We have submitted a NURETH 16 manuscript on our design. In brief they have bi-metallic springs that are laser welded onto the straps. The straps follow a standard egg crate design and were laser cut out of thicker gage stainless steel. One added benefit of this new design is that the spring constant is constant, in other words, the contact force exerted by the spring (kx , with k the spring constant and x the spring displacement) is linear, which will simplify modeling the springs and interpret the experimental data, see figure 1.11.

Once all the springs were received we built the fuel bundle prior to inserting it in the test section and building the latter. Figure 1.12 shows the fuel bundle assembled in the inner shroud.



By having custom spacer grids, we can show several effects of spacer grids on bundle oscillations and damping. Figure 1.13 presents such results.

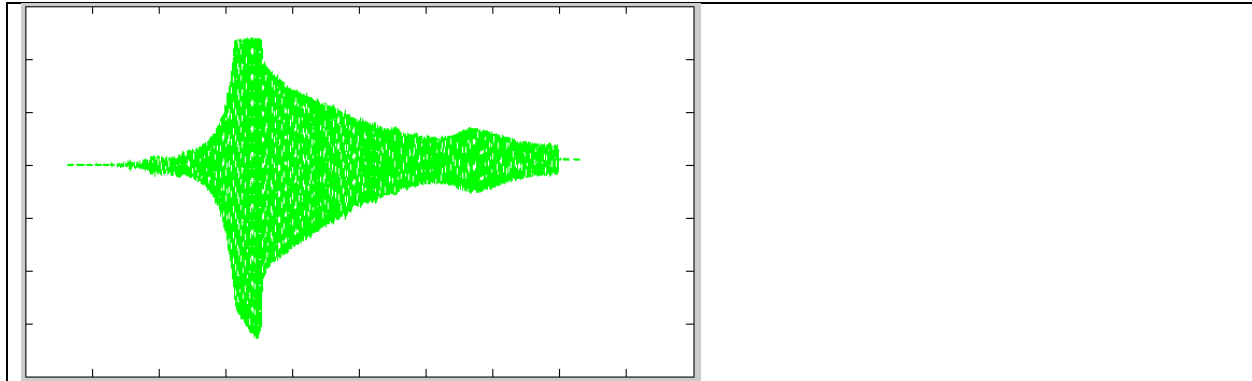


Fig. 1.13. Spacer grid and bundle dynamic response. frequency sweep of bundle between 0 and 6 Hz. Asymmetrical shape is linked to effect of springs on the bundle dynamics.

Task 1-6: Fuel bundle tension control

After the test section was erected, we found that the fuel bundle was sagging slightly. To allow simulating the geometry with confidence it is also necessary to have access to the axial force exerted on the bundle. For these reasons a new task was created: install a force balance connected to the fuel bundle. This required modifying the manner in which the bundle is fixed at the top, in the initial design, it was fixed to the inner shroud with hydrofoils. The upper foils were removed and a replaced with a custom designed force balance that was inserted in place. The main elements of the force balance can be seen in figure 1.14.a (it is missing structural components to rigidify the structure). A bracing structure was made to rigidly support the spacer grid, figure 1.14.b. The force balance also allows correcting the shape of the assembly. As preliminary results show, see section 5, this enables modifying the natural frequency of the bundle. This task was supported by the startup fund of the PI.

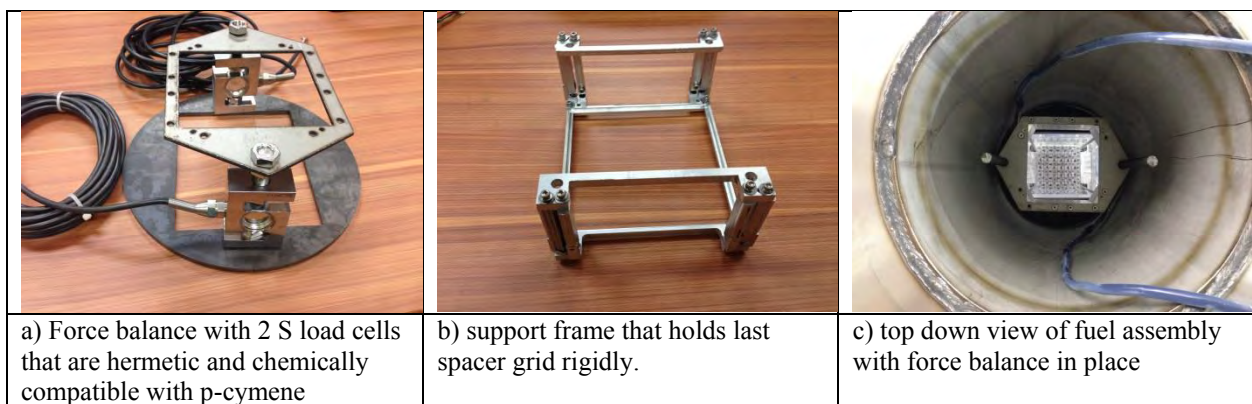


Fig. 1.14. Force balance designed to measure axial force on the bundle.

2. Instrumentation development

Task 2-1: Particle image velocimetry – PIV: Fiber optics coupling to laser and camera testing

The optical fibers that were determined to be best suited for PIV on the shake table were received in the 3rd quarter of FY 2013. These fiber optics with a 600 μm diameter were tested to full power with success. The laser and fiber optics launch are mounted on a granite vibration isolation optical table. The granite table was retrofitted for this project: it was fitted with a compressor to float in the Earthquake Lab and with casters to allow moving the laser between the Thermo-Fluids Lab of Prof. Bardet and the Earthquake Lab of Prof. Manzari. The laser cavities of our Nd:YLF laser have been separated to simultaneously perform either two PIV planes, or PIV and LIFT (see Task 2-2) and we measured a coupling efficiencies greater than 87% into each fiber, Fig. 2.1.

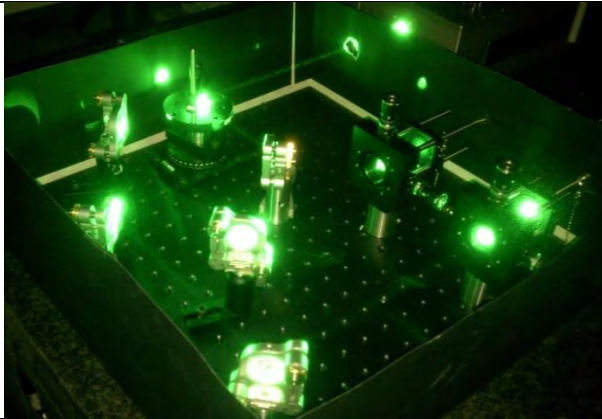


Fig. 2.1. Splitting of the laser cavities and launch into two independent cavity. In essence, we created two lasers out of our Nd:YLF laser.

The flying PIV technique described here is a unique system that has been developed specifically for this experiment for fluid measurements, but has potential for use in numerous applications requiring laser based measurements in harsh environments. The coupling of hydrodynamic forces and external acceleration on the fuel bundle in this experiment require high spatial resolution to resolve flow features in this confined and shaking environment. Hence, the optical magnification must be high, on the order of 0.2 -- 1, which sets stringent constraints on laser beam thickness, wandering, and imaging optics. Even for one dimensional forcing, shake tables have out of plane motions, which if they exceed a fraction of the laser sheet thickness can be detrimental to the measurement. Furthermore, due to the size of the table, measurement from the inertial-laboratory floor would require special telephoto optics with limited aperture; and, therefore, signal strength. Hence, the desired resolution is best obtained with the cameras mounted directly to the moving test section, which provides a fixed interrogation station in the moving reference frame and simplifies data reconstruction. Pseudo-forces affect the measured

fluid and structural dynamics in this non-inertial reference frame. Moreover, beam wandering must be minimized to know with confidence the location of the investigation plane. Pertinent to this constraint, laser sheets used for velocity field measurements must be thin, focusable at a large distance within the test section, and not be affected by table motion. High-power optical fibers are selected as the most appropriate beam delivery mechanism. They offer a flexible beam delivery scheme with very large degrees of freedom. In addition, a special arrangement of PIV planes is employed to reconstruct the velocity in this challenging environment, Fig. 2.2

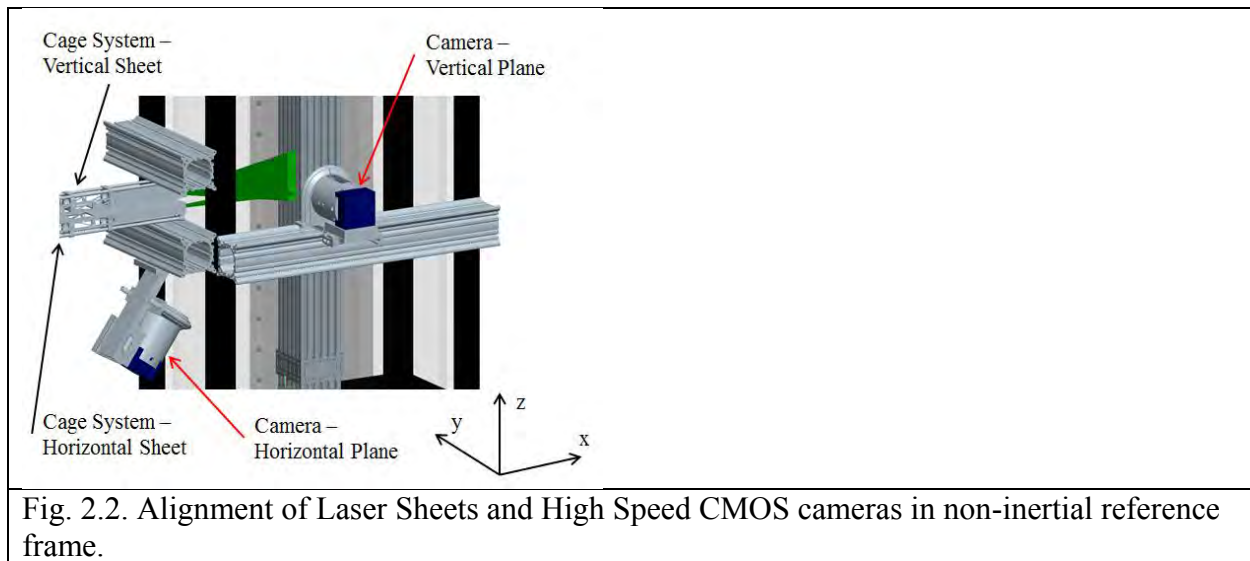


Fig. 2.2. Alignment of Laser Sheets and High Speed CMOS cameras in non-inertial reference frame.

The other constraint on this system, are the limited run time of the shake table and runs that can last several minutes set constraints on operating procedures. Thus to obtain statistically meaningful data on the flow, velocity fields need to be recorded with both high temporal resolution and long recording times. The ability to conduct time-resolved lengthy experimental trials, beginning with a static environment and then imposing external forcing, provides information during transient events that are earthquakes. It is also necessary to have efficient data recording protocol that does not limit the number of tests that can be conducted with the finite time available for operating the shake table. CMOS cameras with limited on board memory require too much time between runs to save the data to external computers. To allow for multiple testing runs while the table is operating, high-speed high-resolution CMOS cameras relying on new CoaXpress transfer protocol are employed; they allow recording directly to computer, hence avoiding the lengthy data transfer step.

In the following subsections the design of the laser delivery system will be described with the reasoning behind the selection of high powered multi-mode step index fiber optics. Then the method for launching laser light into the fiber will be discussed as well as how the light at the exit is recollimated to take measurements at a non-trivial distance from the exit of the fiber. The

design for mounting light sheet optics to a moving test section will then be described with the associated methodology for ensuring the laser planes are aligned and have minimal beam wandering. Last the CMOS cameras will be described in further detail in addition to the method for mounting to minimize camera vibrations that primarily have their source in the micro lens used for high magnification imaging.

Design of fiber laser delivery system

The innate challenge of acquiring high resolution PIV data on a large shake table (and at significant elevations) is the ability to precisely deliver a thin laser sheet to the area of interest in a safe and stable manner.

In high-acceleration environments, vibrations might misalign, and even damage, the PIV laser; as a result, this sensitive and expensive instrument must be installed away from the shaking platform, which forces the laser light to be delivered remotely with great flexibility. For very thin laser planes - needed for turbulent flows in confined environments, or multi-dimensional vibrations - great precision is also needed in the delivery of the laser light.

Mechanical arms with first surface mirrors or prisms in the articulations are good candidates for such laser delivery; they allow transmitting powerful laser beams while maintaining high beam quality with minimal wandering. However, they are complex, somewhat difficult to precisely align, prohibitively expensive if more than one beam is desired, have limited degrees of freedom, and commercially available systems were not judged flexible enough for the high forcing frequency and amplitude applied here.

Instead, a variety of fiber optics were assessed for use in the experimental facility here. A typical laser delivery system with optical fiber consists of a laser, coupler, fiber, and collimator. The three types of fibers for this type of system considered were; 1- single-mode fibers, 2- hollow core fibers, 3- multi-mode fibers.

Single-mode step index fiber optic with a core diameter of 3 μm have been used for laser delivery by [1] with power up to 500 mW for laser Doppler velocimetry measurements. With this type of fiber, the coherence, phase, and polarization are preserved along with a high beam quality. The first application of single-mode fibers for PIV was by Koga et al. [2], who were able to deliver 2 W from a CW Argon-ion laser through a 20 m long fiber. However, short pulses with high peak power are required for the PIV technique used here, and they exceed the LDT of small diameter single mode fibers, thus this type of fiber was not pursued.

For high peak power and beam quality, hollow core fibers have the highest capacity compared to solid core fibers [3]. In fact, very high beam quality ($M^2 \sim 10$) and peak power (100 mJ at nanosecond pulse) has been obtained with large bore (1000 μm) hollow core glass waveguide [4]. However, the power loss at 0.3 m bending radius is nearly three orders of magnitude greater than in solid core fibers [5] [6]. This restriction on bend radius is an issue for two reasons pertaining to the experiment conducted here, 1- to warm up the shake table low frequency high

amplitude cycles are conducted, typically in the range of 0.5 Hz with 80 mm displacements, 2- when the shake table is activated it rises 20 cm from the rest position. Also these fibers are limited in length, which is not adequate for this experiment as to reach certain heights within the test section a 10 m length fiber is needed.

Therefore 10 m-long, high-power, multi-mode, step-index optical fibers are selected for this experiment. Quality and reliability of fibers have improved significantly over the last 20 years, and with careful mounting can offer a wandering-free beam with acceptable beam quality. Long fibers have large degrees of freedom, are affordable, readily available, and enable safe and sustained operation. Nevertheless, there must be a compromise between beam quality and delivered power, and beam collimation requires special care.

The challenge in implementation of multi-mode fibers is a much reduced beam quality in comparison to hollow core fibers with the same core diameter, and balancing the power requirements with the beam quality becomes a significant challenge. \cite{hsu2013a} utilized a large diameter (600 μm) fused-silica step-index fiber optic to simultaneously introduce light to a combustion chamber for combined planar laser induced fluorescence (PLIF) and PIV. However, the larger diameters resulted in degradation of the beam quality, limiting the attainable sheet thickness at the output of the fiber (~ 2 mm) and the pulse energy was only ~ 1.7 mJ. Anderson et al. [7] saw improved results with 600 μm diameter fibers through optimization of the lens elements used to couple the laser and the fibers. They reported peak energy of 5 mJ at 10 Hz with 6-7 ns pulse lengths, and with a single cylindrical lens at the fiber output were able to achieve a light sheet thickness of 1-3.5 mm directly behind the lens.

Here the laser light needs to travel through a minimum of 260 mm of acrylic and liquid that make up the low pressure boundary before it reaches the inner wall of the primary acrylic channel, which is the edge of the measurement region, Fig. 2.2 and a light sheet thickness at the sub millimeter scale is desired. This becomes significantly more difficult than the setup by Anderson et al. [7], and this is due to the relation between the beam thickness ($2\omega_f$) and the spherical lens used to focus the beam at a distance of 260 mm, Eq. 2.1. For a lens of focal length f , the beam waist radius depends on the laser beam quality, or M^2 , aberrations introduced by the lens (A), wavelength of the laser (λ), and the waist of the incident beam (ω_o) [8]:

$$\omega_f = M^2 A \frac{\lambda f}{\pi \omega_o} \quad \text{Eq. 2.1}$$

The Rayleigh range also depends on the same parameters:

$$z_r = \frac{\pi \omega_f^2}{AM^2 \lambda} \quad \text{Eq. 2.2}$$

In a spherical-cylindrical lenses combination, the cylindrical lens generates the laser sheet, while thickness of the latter is set by the spherical. To select the appropriate spherical lens for a higher order Gaussian beam, the beam waist radius at the focal point, ω_f , and Rayleigh range, z_r , must be considered together. The Rayleigh range is the distance from the beam waist where the beam radius has expanded by $\sqrt{2}$. The Rayleigh range is half the confocal parameter or depth of focus of the beam, which is directly related to the PIV investigation domain.

Hence beam quality and type of lens used have direct effects on attainable beam waist and depth of focus. In particular, high order beams and/or strong aberrations in the lens will limit how thin the laser beam can be made as well as its depth of focus. Aberrations introduced by the lenses depend on ω_o and can be minimized if careful design rules are utilized in selecting the lens element. By first expanding the incident beam, it is possible to reduce the beam waist at the price of a shorter depth of focus, and a satisfactory compromise must be found between ω_f and z_r . Beams that are too thick can lead to unsatisfactory "volumetric" illumination if the depth of field of the PIV camera imaging optics is not sufficiently narrow, which is typically the case for most applications, except for magnification greater than one like in micro-PIV.

For multi-mode step index fiber, the M^2 at the fiber output is directly proportional to fiber core radius, r_{fiber} . Eq. 2.3 gives a conservative estimate of it, that is also independent of initial beam quality, Hunter et al. [9], where NA is the numerical aperture of the fiber:

$$M^2 = 0.86 r_{\text{fiber}} \arcsin(NA) \frac{\pi}{\lambda} \quad \text{Eq. 2.3}$$

Hence large core diameter significantly deteriorates the laser beam quality. This makes it challenging to obtain a collimated beam of acceptable characteristics since the beam quality directly affects the smallest spot size that can be attained at the output of the fiber.

In parallel to the desired M^2 , the power handling capability of the fiber must be considered for selecting the optimal system. LDT of the fiber core and cladding materials set requirements on the fiber optics core diameter and materials for launching the beam into the fiber. LDT is the maximal peak fluence that can be accepted by the system; it has units of J/cm^2 . In its calculation, the intensity distribution in the beam profile (which depends on the laser and focusing optics M^2 must be considered. It is a function of pulse length, beam diameter, wavelength, as well as manufacturing processes, such as surface quality and material imperfections.

For the damage mechanisms relevant here, these thresholds can be scaled to lasers with similar pulse lengths with the empirical relations given by Eq. 2.4-2.6 [10]. τ is the pulse length, subscript L refers to laser of interest, while R to reference laser system.

$$LDT_{\omega_L} = LDT_{\omega_R} \left(\frac{2\omega_L}{2\omega_R} \right)^2$$

Eq. 2.4

$$LDT_{\lambda_L} = LDT_{\lambda_R} \left(\frac{\lambda_L}{\lambda_R} \right)^{1/2}$$

Eq. 2.5

$$LDT_{\tau_L} = LDT_{\tau_R} \left(\frac{\tau_L}{\tau_R} \right)^{1/2}$$

Eq. 2.6

High-repetition rate, frequency doubled, continuous pump, Q-switched Nd:YLF lasers in use here have rather long pulses (~150-350 ns) compared to low repetition rate, pulsed pump, Q-switched Nd:YAG lasers (~10 ns), which relaxes the requirements on laser damage threshold, Eq. 2.6. LDT has different threshold values both at the surface of the fiber and in the bulk. Hsu et al. [11] and Allison et al. [12] found that the core-clad interface tended to be the limiting factor for LDT for plastic-clad silica fiber. Here, fused silica core and clad fibers are used; they have some of the highest LDTs for high power applications in the visible. Particularly, they have high LDT for the core-clad interface and surface damage is found to be the limiting constraint for laser power. In fact, our tests showed that the facet of a fiber was damaged when this LDT was exceeded with small core multi-mode step index fibers for well aligned optics. It should be noted that a misaligned beam with respect to optical fiber induces high thermal energy deposition locally, especially for high repetition rate lasers, and leads to large thermal stresses and ultimately fiber failure.

Reported threshold values for the surface damage of fused silica, to be used with Eq. 2.4-2.6, are 150 J/cm² at 1064 nm and 15 ns pulse length [13]. Comparatively bulk thresholds in the core are one order of magnitude higher with measured threshold values of 3,854 +/- 85 J/cm² at 1064 nm and 8 ns pulse lengths [14].

Once the fiber diameter and type are selected, the coupler needs to be designed. Its focusing optics is controlled by Eq. 2.1 and 2.2 and the numerical aperture of the fiber. The beam diameter at the input of the fiber should not exceed 70% of the core diameter per recommendation of the manufacturer. Some authors reduced this to 50% at the cost of coupling efficiency, Hand et al. [15]. It is also recommended that the beam waist of the coupling optics is located before the fiber entrance, i.e., the beam is diverging when entering the fiber. To maximize the coupling efficiency at the input of the fiber, the input cone of light cannot exceed the fiber numerical aperture. OZ Optics recommends maintaining the numerical aperture of the focused rays between 30-90% of the fiber numerical aperture.

The numerical aperture of fiber depends on the materials constituting the core (n_{co}) and cladding (n_{cl}); for step index fiber optics it is defined as:

$$NA = \sqrt{n_{co}^2 - n_{cl}^2}$$

Eq. 2.7

The PIV laser used here is a frequency doubled, double cavity Nd:YLF laser with a dual pulse option per cavity (Photonics Industries DM-527-DH); it is mounted on a vibration isolation granite table positioned on the ground floor next to the shake table. Each cavity is rated for up to 30 mJ per pulse at 1 kHz, has a repetition rate adjustable from 0 to 10 kHz with $\lambda = 527$ nm wavelength, and an M^2 of 15-18. Pulse length varies between 150 and 350 ns and depends on laser repetition rate and power. By design, the cavities of this laser are orthogonally polarized. Here two independent beams are needed for conducting PIV in this challenging environment. With a creative optical setup three sets of independent beams are created resulting in six light sheets. First a polarizing beam splitter is used to separate the cavities. Then for cavity one three 50:50 non-polarizing beam splitters are used to separate the single beam into four beams with equal power, one beam is sent into a beam dump while the other three are directed into 600 μm fibers. For cavity 2 the beam from the polarizing beam splitter is first split with a 70:30 non-polarizing beam splitter, and then with a 50:50 beam splitter to direct the light into three 100 μm fibers. Each fiber is coupled to the laser with air-gap style SMA connectors on either end. The SMA connectors can be mounted in cage system components. The optics for separating the cavities and launching them in the fibers are visible on Fig. 2.3.

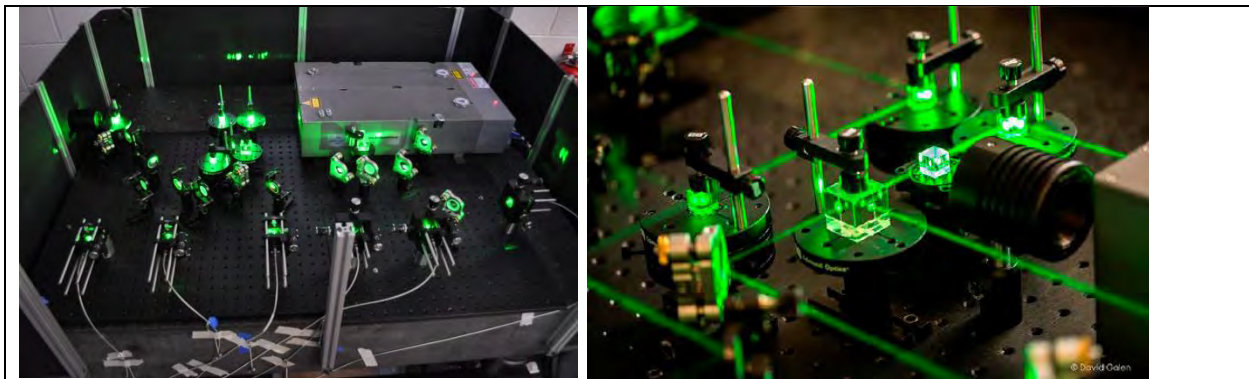


Figure 2.3. Beam splitters arrangement to launch high-power PIV laser into 3 independent optical fibers. This enables to conduct PIV in 3 independent planes simultaneously. We have power to spare on the laser and could launch it more fibers in the future.

Three different fiber core diameters are analyzed and tested to determine the most suitable for the particular application.

Due to requirements on laser sheet thickness, 600 μm and 200 μm fibers are of primary interest, Table 2.1. They reach their respective LDTs with a safety factor of 3.5 (calculated based on pulse energy divided by the beam cross sectional area) at 3.5 mJ/pulse and 14.1 mJ/pulse at 1 kHz. A Gaussian beam would have required a safety factor of 2. 600 μm fibers can handle the maximum energy density the laser is capable of.

Table 2.1 Effect of fiber core diameter on beam quality with 200 mm focal lens

Fiber \varnothing (μm)	Pulse energy (mJ)	Model			Measured		
		M^2	$2\omega_f$ (mm)	z_r (mm)	M^2	$2\omega_f$ (mm)	z_r (mm)
100	3.5	61	0.40	3.9	76	0.53	7.1
200	14.1	123	0.81	7.9	102	0.68	8.8
600	≥ 30	368	2.4	23	214	1.4	16

The measured values for beam waist and quality are conducted with an optical measurement technique using an acrylic plate in water at an angle of 45 degrees with respect to a camera. The same collimator is used for all these tests, and its design was optimized to not introduce additional aberrations. An image is taken of both the reflection entering and exiting the acrylic plate, the first reflection is then averaged in the vertical direction and the diameter is taken as the two locations on the Gaussian curve where the peak intensity is 50%, Fisaletti et al [16]. The measured M^2 value is estimated as the actual $\omega_{f,\text{measured}}$ divided by $\omega_{f,\text{theoretical}}$ based on an ideal beam with an $M^2 = 1$ and results obtained in Table 4.1. Multiple measurements are taken of the beam waist along its axis and the measured value for z_r is approximated with when ω_f has expanded to $\sqrt{2}\omega_f$. M^2 is underestimated with eq. 2.3 for 600 μm fiber, while it is over-predicted for the larger fibers. Due to the high order of the laser beams, there are discrepancies between observed and computed behavior of the beams (ω_f and z_r), but overall Eq. 2.1 to 2.3 give acceptable results to design the optical system.

The 100 μm diameter fiber satisfies the target criteria set forth for the current experimental campaign for the vertical light sheet seen in Fig. 2.2. The horizontal light sheet required a higher power output due to a need to close the f-stop of the camera to accommodate for the angle of the camera thus limiting the amount of light that can reach the sensor. Hence 600 μm fibers are used for the horizontal plane measurements.

Special precautions are necessary to optimally launch the laser beam into the fiber. Several coupling schemes have been tested to create a focused beam with no hot spots. The hot spots set the safety factor on LDT and hence on core diameter. To sharply focus the laser beam at the fiber entrance, it is possible to use simple plano-convex lenses; however, these lenses introduce aberrations in the beam profile if more than 30\% of the lens diameter is used to focus the beam. This creates undesirable local irregularities in the beam intensity profile and thus limits the spot size that can be attained with a single lens. Instead, aspherical, multiple lens elements [17],

GRADIUM lenses [18], grin lenses, and diffractive optical elements (DOE) [15]; [19] have all been tried to provide a beam spot of high quality at the fiber entrance. For the selected fibers here, an achromatic doublet with 30 mm focal length lens meets requirements on beam waist and NA highlighted above. Here a free launch system with 5 DOF is selected to couple each laser beam into the optical fiber, Fig. 2.3. With this system a coupling efficiency of up to 87% is achieved. The large fiber core diameter allows for providing a soft focus that is less demanding on coupling optics and can tolerate some beam wandering while preserving a good coupling efficiency.

Collimating higher order Gaussian beams from an optical fiber and constraining in a vibrating environment

Light from multimode fibers is difficult to collimate well, additionally, the resulting beam minimum divergence angle typically increases with fiber diameter.

As a result, the groups that have delivered high power laser light through optical fibers for advanced diagnostics have focused primarily on the coupling optics to minimize the fiber core diameter to obtain an output beam of reasonable quality and power. Their test section is typically adjacent to the laser collimator, which simplifies requirements on collimation. However, for this project the region of interest is located at a significant distance from the test section wall. Therefore, we also focused on the collimator at the output of the fiber to recover a beam of acceptable quality.

To collimate the beam after the fiber and create a laser sheet, a total of six lens elements (LE) are employed. All lenses are achromatic doublets to minimize aberrations. Such lenses reduce lateral and transversal aberrations compared to single element plano-convex or bi-convex lenses typically used for PIV. The collimated beam diameter here is up to 80% of the lens diameter and thus these aberrations would be significant and detrimental to focusing the beam to a small spot size. However, achromatic lens doublets have lower damage threshold than single elements lenses. Due to long pulse and large beam, this damage threshold is not exceeded.

When selecting the collimator, one must ensure that its NA corresponds to that of the fiber. The collimator selected for the 100 μm fiber consists of a first surface parabolic mirror (Thorlabs RC12SMA) that nearly matches the numerical aperture of the fiber (0.216) followed by a total of five lenses, Fig. 2.4. After the reflective collimator, the beam still diverges slightly and a long focal length spherical lens element, (LE1 = 500 mm), is used to improve collimation. Its location is found by optimization. Next LE2 = 50 mm and LE3 = 150 mm form a Keplerian 1/3 beam expander to increase ω_o before the last spherical lens (LE4 = 200 mm). This combination generates adequate ω_f and z_r (Tab. 2.1) in the test section, midway between the inner channel wall and the nearest rod in the fuel bundle, Fig. 2.2. LE5 = 50 mm is a plano-convex cylindrical lens used to create the light sheet. LE4 focal length is longer than the distance to the investigation plane, because the beam is focused through a medium with refractive index

larger than air. This last lens is also adjustable within the cage system to set the focal point of the lens at the desired location.

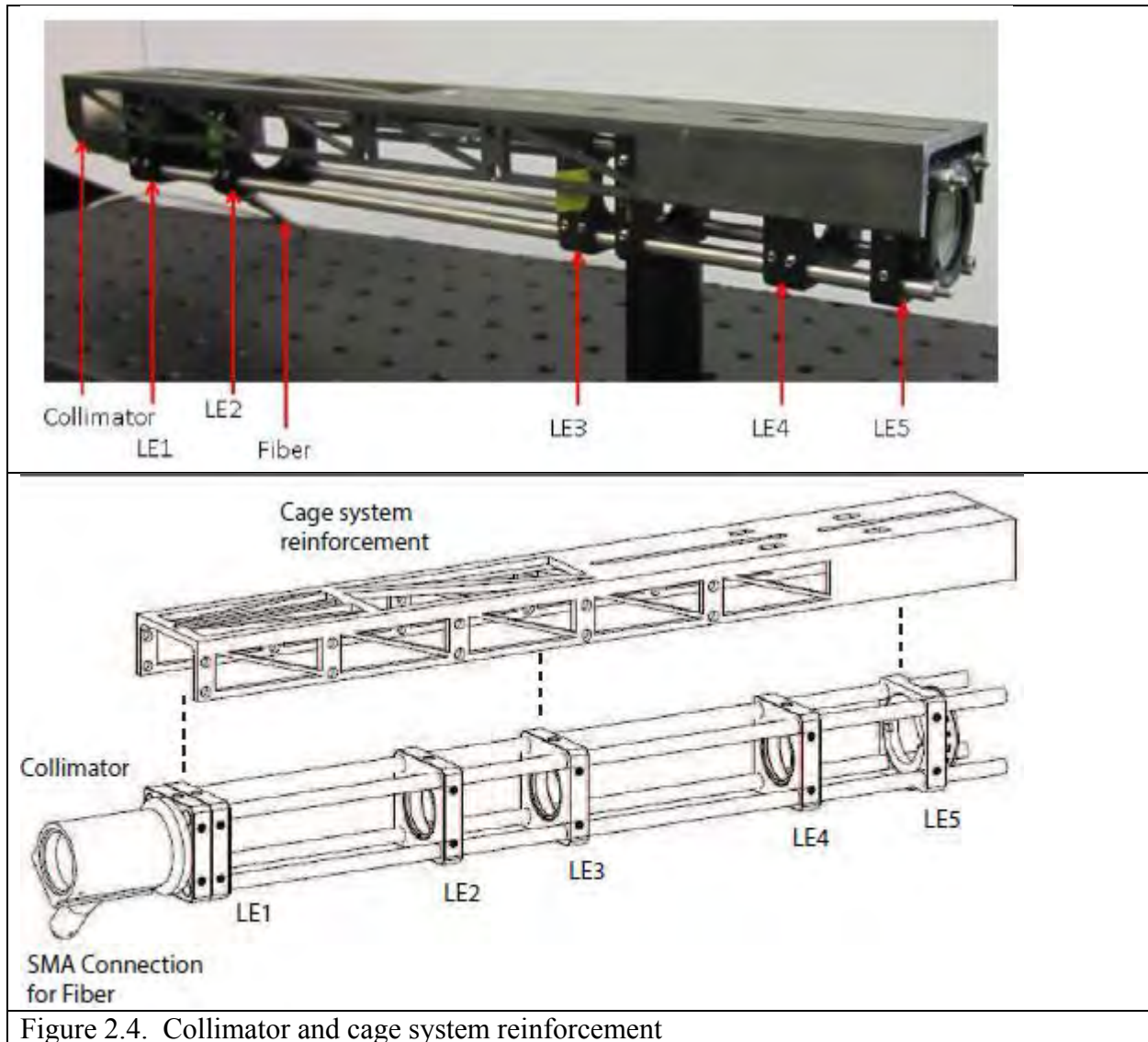


Figure 2.4. Collimator and cage system reinforcement

A cage system holds the collimator and sheet forming optics together. The cage system is also mounted on a structural beam to reinforce it and prevent its vibrations, Fig. 2.2. This offers a rigid, light, and compact assembly that is mounted to the test section at desired locations with X95 structural rails. Alternatively, a tube system could have been used to provide a rigid support, but would have been less practical to align the lenses with respect to each others. Special care is also taken to rigidly hold the last section of the fiber before the collimator as movement there generates modes that can affect the beam uniformity. With this system, RMS deviation of beam wandering is measured, thanks to two planes PIV configuration, as 16% of the PIV sheet

thickness for a shake table forcing of 20 mm and 1.6 Hz which is one of the larger forcing amplitudes utilized.

Camera selection and fixture

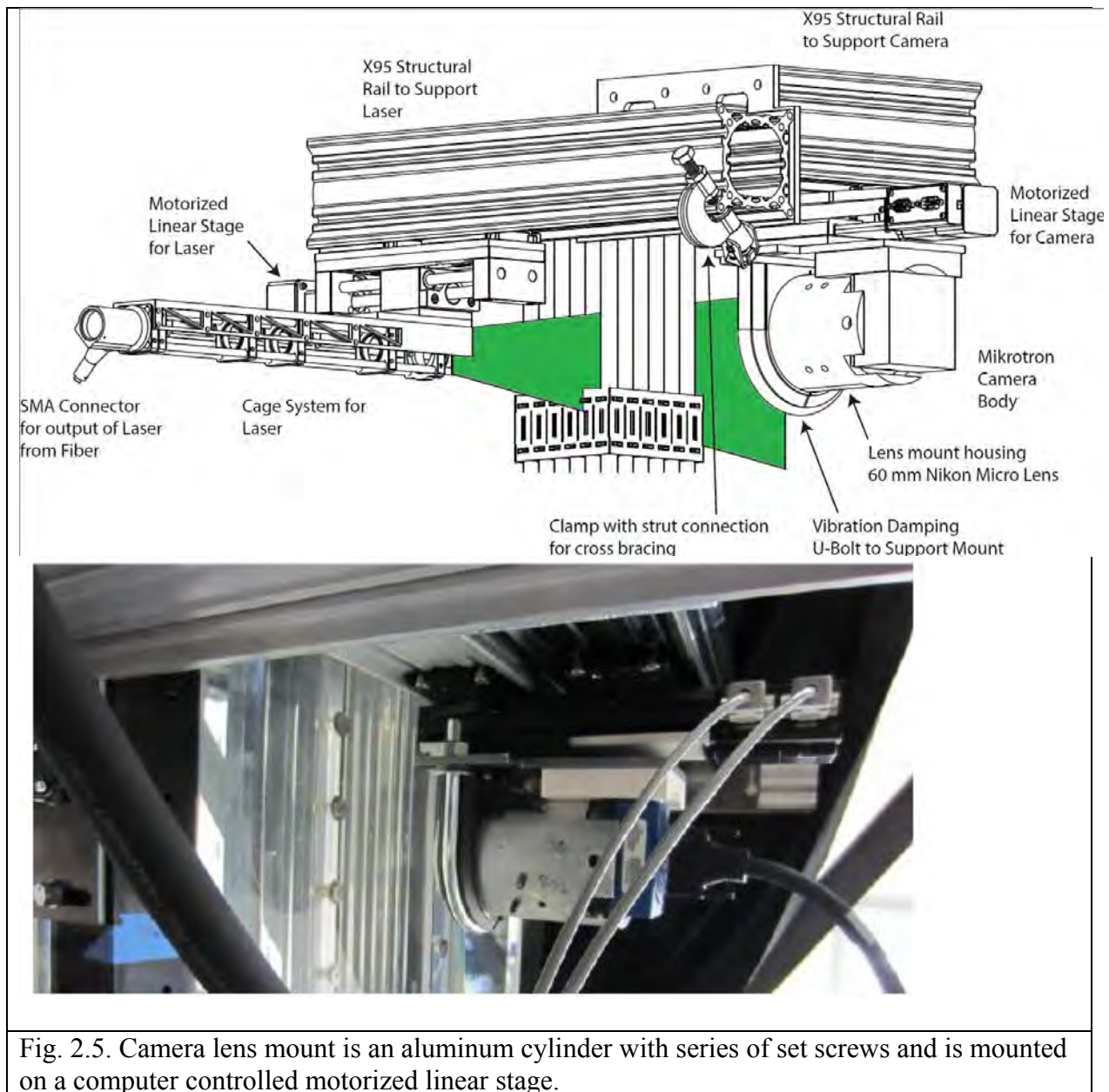
While not specifically tested for conditions expected here, cameras (and lasers) are designed to resist to transportation when not operated, which follows the standard: MIL-STD-8100.

Transportation conditions are not too dissimilar to the forcing encountered during runs of the experiment and selected cameras have no moving parts, so it is likely they can withstand shaking. To record data in the moving frame, cameras have to be rigidly fixed to the test section. Hence to simplify the connection there, the camera should be as light as possible to minimize its inertia. However, if a long recording time is desired, while maintaining time resolution to capture complex transients, one is typically forced to use expensive, rather large and heavy cameras with built-in memory. An alternative, that has only recently become available, are machine vision CMOS cameras with CoaXpress transfer protocol that allow recording straight to computer hard drives at speeds up to 25~Gbit/s. This transfer protocol is faster than Camera Link and was developed to replace it. Additionally, the data transfer cables are coaxial cable, which can be made up to 100 m, hence preventing the need to use expensive fiber optics repeaters for Camera Link cables if the latter need to be longer than 6-7 m.

Currently, available CoaxPress cameras have only 8-10 bits sensors, lower light sensitivity and higher noise than scientific cameras. However, signal quality is acceptable, they can be precisely triggered externally with TTL signal (4 ns jitter for camera employed here), and are also more affordable and lighter than most scientific cameras. For example, the selected camera here (Mikrotron EoSens 4CXP) weighs 450 gram, compared to 5.5 kilogram for a Vision Research Phantom camera, which would require a very stiff connection to the test section. The Mikrotron camera can record directly to hard drive at a nominal 560 fps at 4 Mpixels ($2,336 \times 1,728$ pixels) and 2,048 fps at 1 Mpixels ($2,336 \times 450$ pixels) as employed here. Pixels are 7 μm on their side, which relaxes magnification requirements for resolving small spatial scales as compared to most scientific high-speed CMOS cameras. The frame grabber is BitFlow Cyton CX and the data acquisition software is StreamPix 6 from Norpix. The computer has eight 256 GB SSD drives in RAID 0 configuration to accept the bandwidth coming from the frame grabber. A total of 15 minutes can be acquired with this camera system at its nominal recording parameters. The computer, frame grabber, camera, and software are integrated by MicroDisc, Inc.

A 60 mm Micro-Nikkor lens from Nikon produces the required magnification and working distance. In initial validation test, it is found that the lens moved with respect to the camera body. A special lens mount is designed and built to firmly fix the lens to the camera, Fig. 2.5. With this mount, images are stable up to 0.15 g of lateral acceleration. Above this value, small vibrations are noticeable and are attributed to the lens elements moving inside the lens body. To minimize these vibrations, shims are inserted between the lens groups and additional cross bracings are added to the camera support, shown on Fig. 2.6. With these additions, vibrations of imaging

system are reduced to the micron level for accelerations up to the upper limit of the facility operation, 0.4 g. Therefore, the method for mounting the camera is adequate for high spatial resolution measurements. However, camera lens focus cannot be adjusted once it is set. Instead motorized linear translation stages are used for very fine focus or conveniently changing the depth of the investigation plane. This is presented in greater details in the next subsection.



PIV planes configuration

A total of six cage systems with collimator and light sheet optics are utilized in the current configuration. Three sets of one cage system for a vertical light plane, and one for a horizontal one that intersects the vertical light sheet, Fig. 2.2, 2.6, and 2.7. This intersection of PIV planes has a number of benefits for this in-situ deployment. Images from the horizontal view include one corner of the flow channel, Fig. 2.7, and allow for checking three characteristics of the vertical PIV plane: 1- Ability to monitor that the laser delivery is stable, i.e. it does not vibrate from the external forcing from the shake table. By also having access to one corner of the flow channel, we can define the absolute position of the laser beam if the latter fluctuates. This is also convenient for other practical PIV applications as beam wandering has been found to be an issue on some projects. 2- Confirms calculations on beam waist thickness and location. Finally, 3- provides a close up view of the laser sheet alignment with the bundle and within the flow channel. The latter is valuable to adjust investigation plane location at the start of each run and to monitor whether the bundle moves out of the PIV vertical plane during forcing. To do so, camera and laser delivery optics are each mounted on motorized translation stages. The latter were carefully selected; they have no play in their mechanisms and are not sources of vibrations.

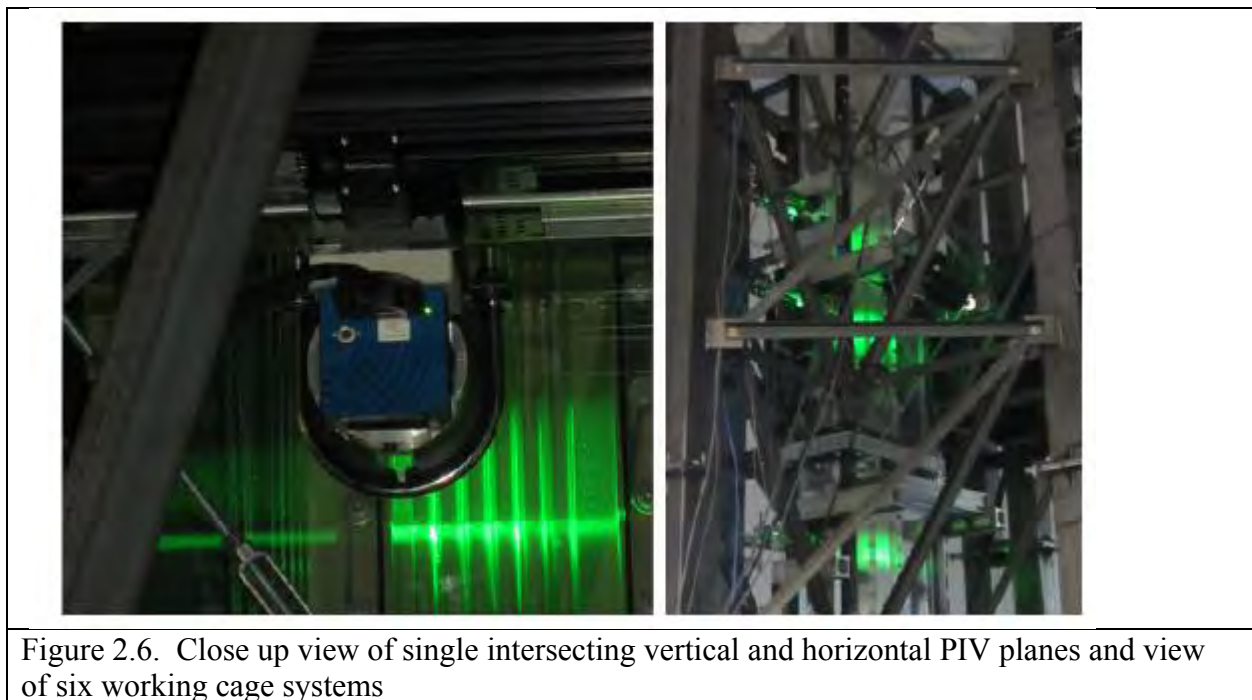


Figure 2.6. Close up view of single intersecting vertical and horizontal PIV planes and view of six working cage systems

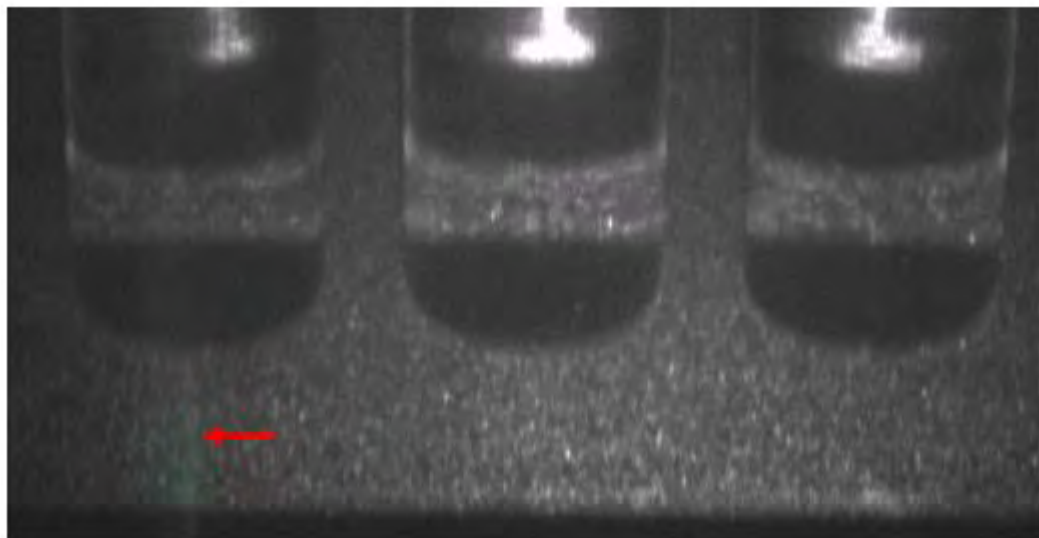


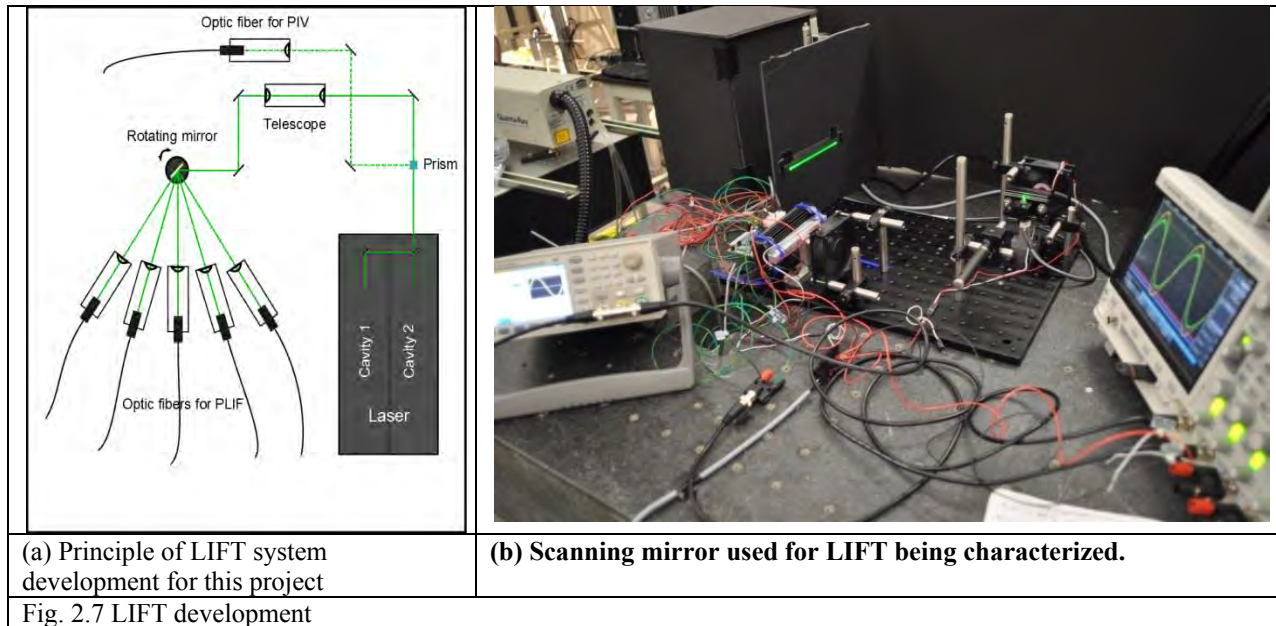
Figure 2.7. Raw image from horizontal PIV plane with vertical laser sheet location marked with red arrow

X95 structural beams that support the cameras and laser delivery optics fasten directly into the bolt holes along the aluminum rails that reinforce the secondary tanks. This enables to conveniently set the PIV planes at any desired elevations.

Task 2-2: Laser induced fluorescence tomography - LIFT

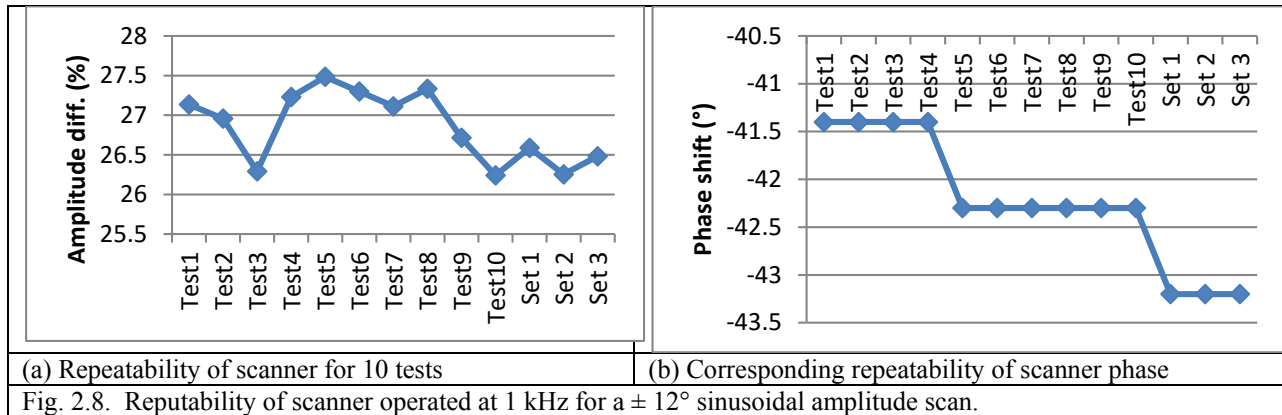
Laser induced fluorescence tomography (LIFT) enables to reconstruct in 3D and as a function of time the vibration of the rods between two consecutive spacer grids. As mentioned in task 1-4, we are adding solvents to p-cymene to increase the level of dissolved fluorescent dye in the liquid to increase signal to noise ratio and improve index matching.

LIFT technique selected here relies on scanning PLIF and each laser pulse is sent to an individual optical fiber, Fig. 2.7 (a). This configuration allows positioning the fibers at unequal distance from each other, particularly at optimum elevation to record displacement of modes center. This system relies on recent improvement in repeatability and accuracy of galvanometer scanning mirrors. The mirror received last quarter is now operational, Fig. 2.7 (b), and has been extensively tested for accuracy, warm up time, and repeatability. Main results are reported below.



The galvanometer scanning mirror we selected was the fastest available and had been “burnt” at the factory to deliver a very high linearity. Its resonant frequency is 1.4 kHz and it has maximum amplitude of 20° or 40° for the laser beam. For LIFT we aim to drive the scanner at 1 kHz, i.e. we would like to acquire 5 independent PLIF planes at 1 kHz, which means that the laser will be operated at 5 kHz. However, 500 Hz is still acceptable to resolve the rod vibration temporally. We found that at our target frequency of 1 kHz, the maximum amplitude was $\pm 12^\circ$ or 24° peak to peak. This corresponds to an input sine wave of 7 Vpp. The maximum amplitude of the scanner could be reached at amplitude up to 540 Hz.

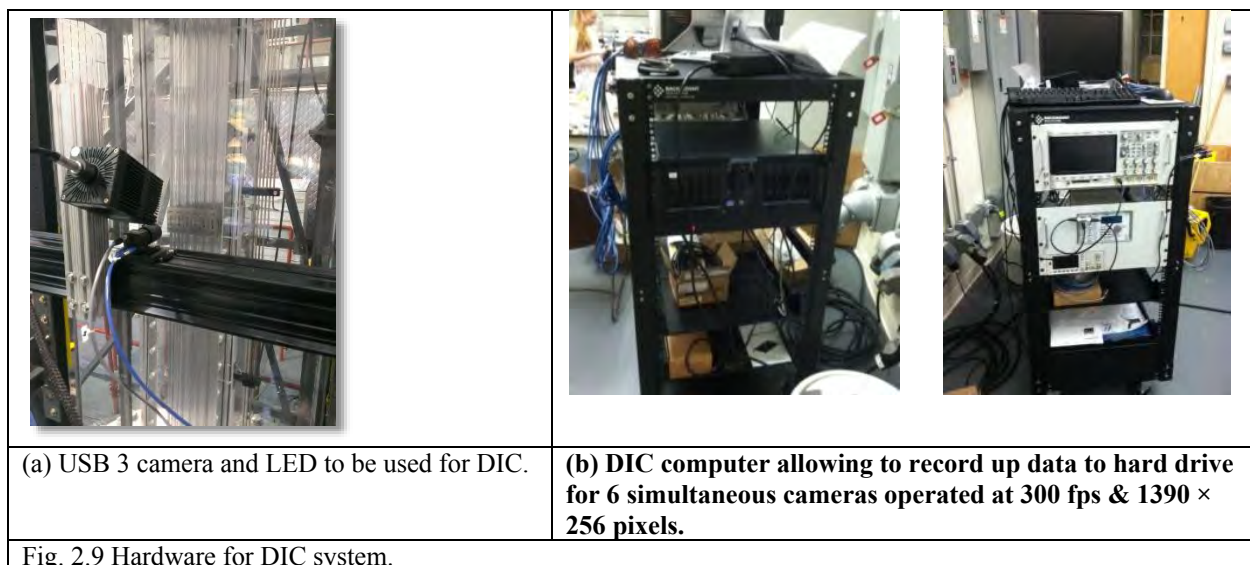
Results for repeatability of scanning angle and phase difference between input signal and actual scan position is given in Fig. 2.8. Fluctuations in amplitude have been attributed mainly to the waveform generator we used to send the control sine to the scanner. We measured that the amplitude of the signal varied by about 0.5%, which is closely consistent with our instrument which has an 8 bit resolution. We are planning on using a National Instrument data acquisition board with 16 bit resolution in the future to output the analog signal and improve the repeatability on scanning amplitude. Phase appears to suddenly increase after a run. This is likely due to accumulation of charges in the system. However, with the advanced oscilloscope we invested in for this project, phase between the signals will be measured on the fly and will be corrected once the system has been started. The phase, of course, will have to be carefully adjusted at every run to guarantee that the laser is in phase with the scanner. In addition to the phase between the input and the scan angle, time delay of the laser will have to be accounted for. Fortunately, this last parameter is stable and only a function of the laser power.



Since the beam steering accuracy of the scanning mirror is known, we calculated that (with 50% safety factor) the optical fibers should be 900 μm in diameter. We therefore ordered fibers of 1000 μm diameter. For 12° scanning amplitude, the fibers need to be located about 53 cm from the scanning mirror to enable enough space between the optical fiber couplers. High-power optical fibers and coupling mounts have been ordered. They should be delivered in mid to late October. Unfortunately time ran out to deploy this instrument on the shake table.

Task 2-3: Digital image correlation - DIC

This task is completed. The DIC has been used and demonstrated on the shake table, see section below for results. The components of the Digital Image Correlation system are: 5xUSB3 cameras with lenses, 5xLED strobe lights, Fig. 2.9 (a), and custom computer with StreamPix 5 software made by NorPIX, Fig. 2.9 (b). We controlled and synchronized the cameras and LED with one time delay generator. We also designed mounts for the cameras and LEDs on the test section that were first tested on the small test section on the shake table that was part of Task 2-4. We also integrated an IRIG timing board (PCI board from SpectraCom) to all of the camera computers to add a common time stamp on all of our data enabling reconstruction of data in post-processing phase.



We utilize a recording time of 256 Hz, which is a common multiplier for the other instruments (LVDT from shake table operate at 512 Hz, accelerometers at 2048 Hz, and PIV in increment of 256 Hz). This allowed us adding a sixth camera to the DIC computer. Hence 4 cameras are used for the in plane displacement of the 4 moving spacer grids, 1 for the out of plane displacement of grid #2, and one for a horizontal PIV plane..

Figure 2.10 shows a sample of DIC data with all the camera views combined. Out of plane motion can also be detected thanks to shadow of scratches on the spacer grids. The scratches were due to uncontrolled acceleration of the shake table in initial shake down trials. However, the extent of the scratches is small enough that they do not interfere with DIC measurements.

We have been able to record continuously with DIC for up to 20 min. The data are then processed with our very efficient processing algorithm in less than 1 hour.

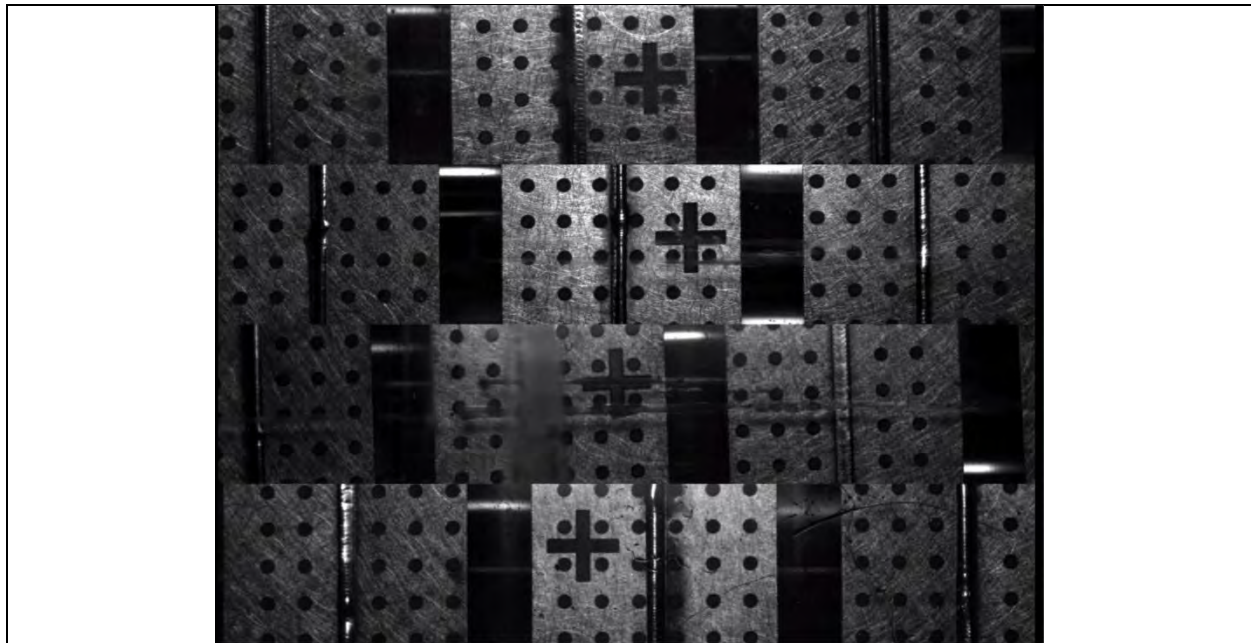


Fig. 2.10. Sample DIC raw data. The top view corresponds to the top spacer grids that moves freely.

Task 2-3-2: Stereoscopic Digital image correlation - SDIC

This was an additional task. In data acquired in water, we found that out of plane motion of the bundle was significant and think the bundle might be twisting as well. As a result, we decided to modify the DIC scheme to capture 3D displacement and rotation, by using a stereoscopic DIC system. The design of this new instrument was initiated with investment in an additional DIC system as 8 cameras were needed to monitor the 4 moving spacer grids (2 per grid) with an additional 3 needed for recording the horizontal PIV plane discussed in Task 2-2. We designed a

custom Scheimpflug mount, Fig. 2.11, to perform stereo DIC on the shake table that was validated in a static environment.



Fig. 2.11. Custom Scheimpflug mount for USB 3.0 cameras.

Task 2-4: Sample test section design to validate instrumentation and optical configuration

The sample test section that was fabricated previously for testing index matching of p-cymene in a rod array was retrofitted to accommodate a small flow loop to demonstrate coupled PIV-PLIF from a single laser and their use on the shake table during the 4th quarter of FY 2013. It can be seen installed on the shake table, Fig 2.12 (a). The system was tested for sinusoidal base motions of up to 0.35 g, which was adequate since our expected runs on the full scale test section would not exceed 0.25 g.

From these tests, the camera and laser mounts were validated. However, as mentioned in Task 2-2, we identified that for PIV the lens was moving with respect to the camera body. This was addressed prior to integration of the cameras on the full scale test section. The USB 3 camera and LEDs for DIC performed flawlessly. These experiments allowed testing the use of fiber optics to deliver laser light and test laser safety procedures. PIV data were acquired in the small experiment when the table was shaken and velocity fields are reported in Fig. 2.13.



(a) Small test section and support structure for instruments on shake table

(b) Loop with flowing p-cymene with 0.25g horizontal vibration.

Fig. 2.12. Small test section to develop instrumentation for shake table

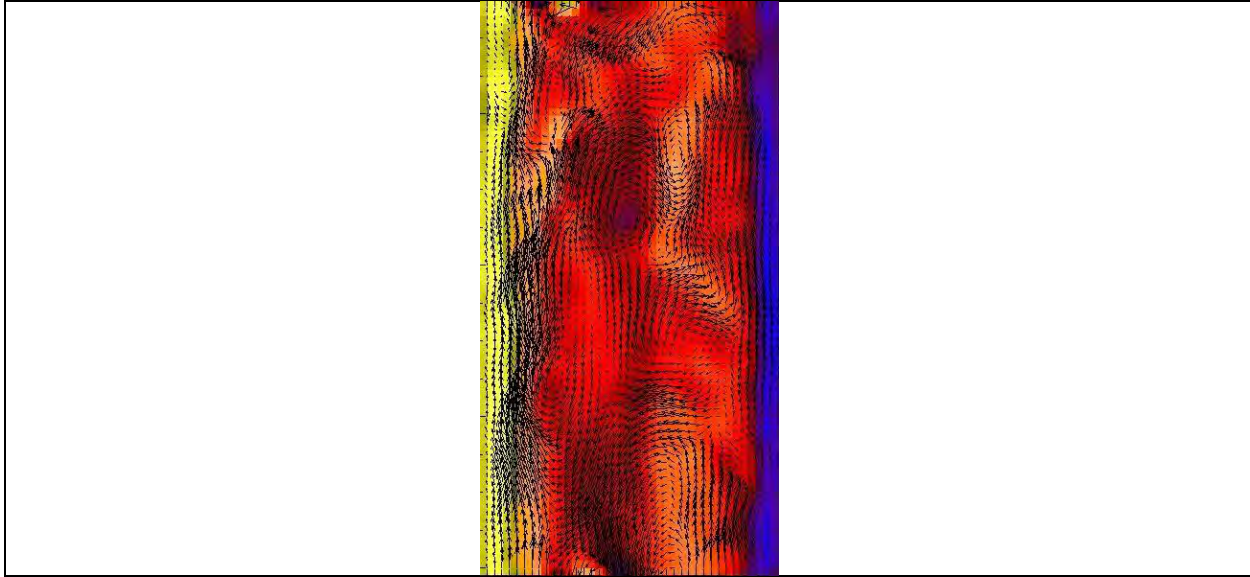


Fig. 2.13. Time-resolved PIV velocity field obtained in the small experiment during static run, i.e. without external forcing.

Task 2-5: Pressure Measurement

This task is completed. We realized the timestamp was not consistent between runs as we were integrating the data from the various instruments. We developed a new data acquisition code in labview that takes better advantage of the data acquisition hardware. This fixed this issue and now all the transducers and National Instrument data acquisition system work together with the rest of the instruments and the IRIG timestamps.

Task 2-6: Integration of instruments

This task has been extensively tested by taking redundant measurements with all the instruments. For example the table displacement (and acceleration) was measured with cameras and checked against accelerometer data to confirm that timestamp worked consistently across all instruments. We also resolved the timestamp issue with the camera (Norpix) software.

To synchronize the various instruments for the fluid and structure measurements, and facilitate the process of data reconstruction, a comprehensive timing and synchronization system has been implemented, Fig. 2.14. At the core of the setup is a Model 575 pulse generator from Berkley Nucleonics. Containing an oscillator with an accuracy of 25ppm and able to produce delays with a high resolution of 250 ps and a low RMS jitter of 50 ps, this device is used to trigger the various instruments involved using TTL pulses.

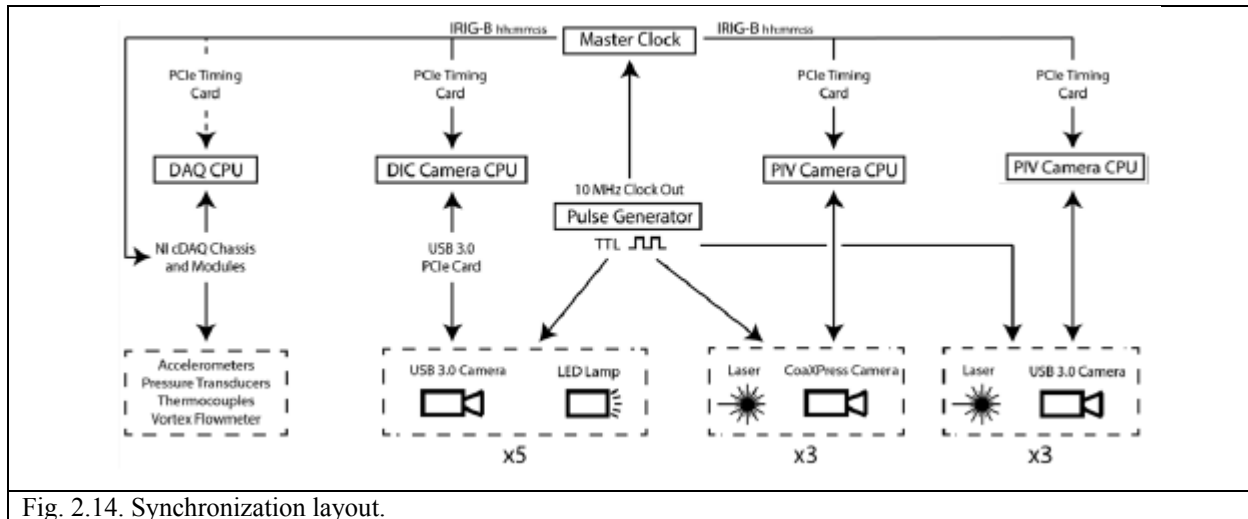


Fig. 2.14. Synchronization layout.

The clock rate of the unit is set to the equivalent of 2048 fps, which is the acquisition rate at which the PIV cameras and lasers operate. For the data reported here the PIV setup is utilized to acquire data in a time series mode, for larger Reynolds number flows the data acquisition can be changed to a frame straddled manner by changing the laser to a twin pulse mode at an acquisition rate of 512 fps. A lower frame rate of 256 fps for the DIC cameras is obtained by operating the associated channels on the pulse generator in a duty cycle mode.

In addition the facility is instrumented with 5 Model 356A17 accelerometers from PCB electronics and 4 pressure transducers from GE. The data acquisition system for the sensors consists of an 8 slot CompactDAQ chassis from National Instruments coupled with 4 NI 9234 modules for the accelerometers and 1 NI 9215 module for the pressure transducers. The system is operated at an acquisition rate of 2048 Hz.

The pulse generator is also used to discipline the master clock using a 10 MHz clock out signal. The master timing unit is a highly customizable SecureSync system from Spectracom. The system has the ability to synchronize its clock with GPS satellite and can output time and frequency information in various forms based on the options selected. In the setup shown, the time is sent to the various computers via military standard IRIG B protocol. Each computer has a dedicated PCIe based TSync card, also from Spectracom, to accept the time signal. This ensures that all the computers are referenced to the same time generated by the SecureSync unit master clock. Since the data acquisition system from National Instruments and associated Labview program are not directly compatible with an IRIG signal for time stamping, the raw IRIG B signal is directly recorded using one of the data acquisition modules. This signal is later post-processed to obtain the time information encoded in the raw signal.

With all computers referenced to the same master clock, the data recorded by each is time stamped to microsecond resolution using the IRIG B time signal obtained from the SecureSync unit via the TSync PCIe card. The StreamPix software used for recording is compatible with the SecureSync components and allows the time stamp to be embedded in the data file easily. Data from each instrument can then be compiled to reconstruct the time history of the entire experiment. Additionally, the accurate time stamp enables identification of skipped frames or data points, given that the acquisition or frame rate for the various instruments is known. A sample of what can be acquired with this setup is portrayed in Fig. 2.15.

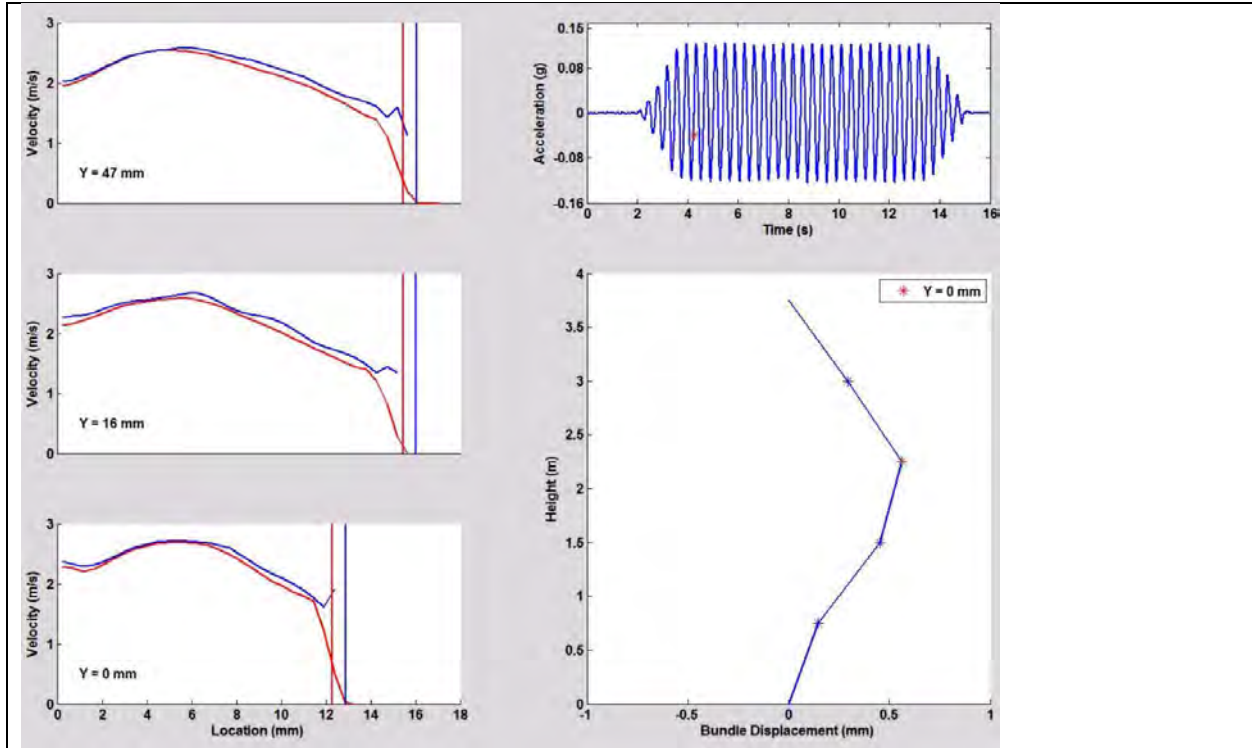


Figure 2.14. Integrated multi-physics data. Left hand side, velocity profile at three different elevations near the spacer grid #2, the channel wall is on the left, the rod is on the right. The red lines indicate the mean velocity, the blue the instantaneous. The vertical lines indicate the rod location, with red being the mean and blue the instantaneous. The time history of the acceleration is displayed on the upper right, while the bundle oscillations are on the lower right.

For tests in still fluid or with axial flow rates of 1 m/s or less, time resolved PIV images are acquired with this system. For still fluid the full resolution is utilized for the PIV cameras at 4 Mpixel with a frequency of 256 Hz. For 1 m/s flow rates a frequency of 2048 Hz is utilized for both the Mikrottron cameras and laser, Fig. 2.16, PIV data are acquired as a time series. What can be observed in Fig. 2.16 are that there are no overlaps between measurement techniques except when done intentionally. Starting with the DIC system it can be seen that the pulse from the LED lamp is offset by almost $100 \mu\text{s}$ from the first pulse from laser cavity 2 (C2) which

is for the vertical laser sheet. Additionally the exposure for the DIC camera ends before the first pulse from the laser. These measures are needed to prevent cross talk between optical based techniques. For the camera exposure for PIV camera 2 it is intentionally overlapped with the pulse from the vertical light sheet to provide the horizontal plane view seen in Fig. where it is desired to be able to monitor both the location of the vertical light sheet and beam wandering during shaking. A sample PIV image acquired from the vertical light sheet is show in Fig. 2.17.

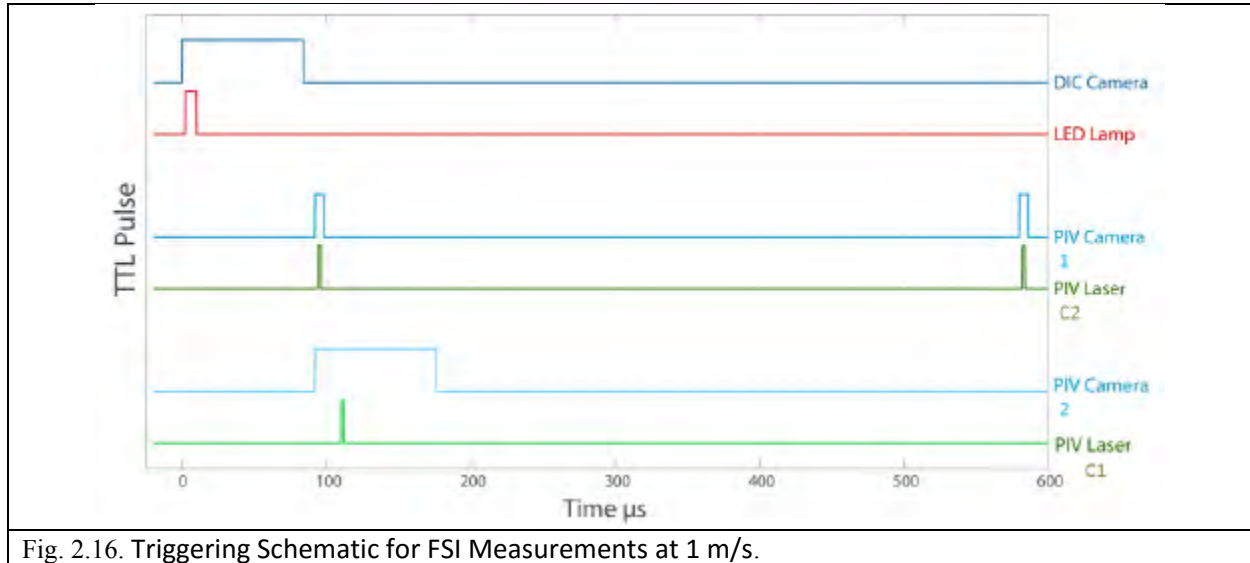


Fig. 2.16. Triggering Schematic for FSI Measurements at 1 m/s.

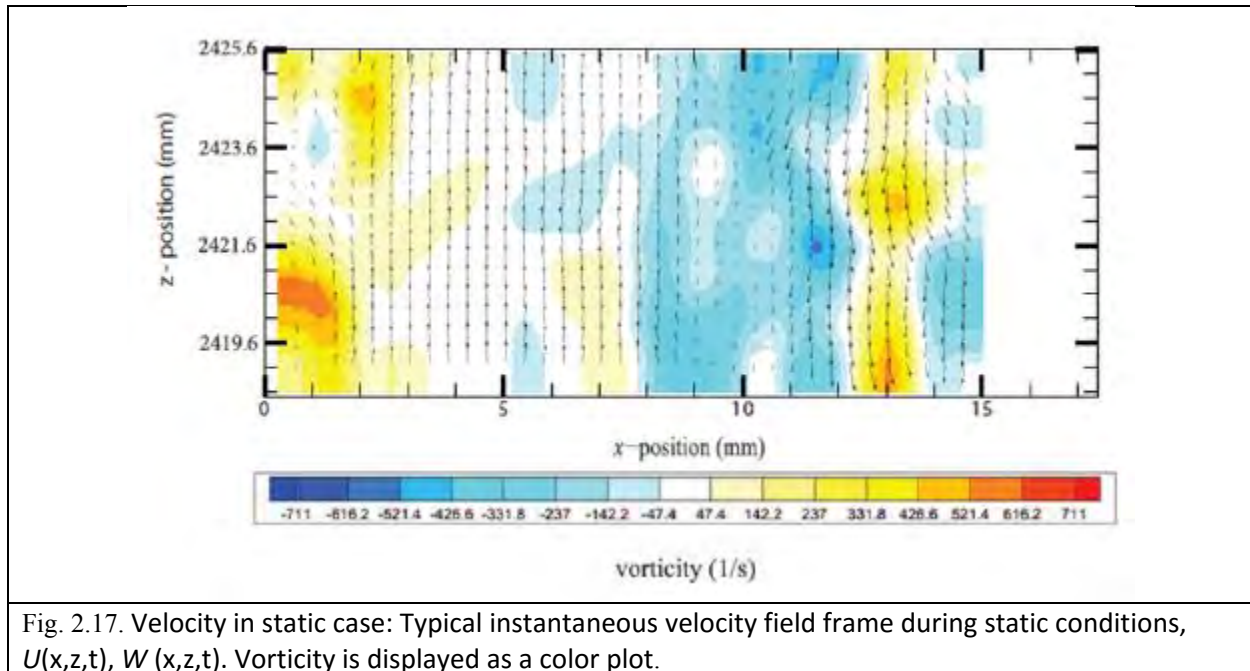


Fig. 2.17. Velocity in static case: Typical instantaneous velocity field frame during static conditions, $U(x,z,t)$, $W(x,z,t)$. Vorticity is displayed as a color plot.

For tests with 2 m/s and 3 m/s axial flow rates, the flow is too fast to be acquired in a time series mode and thus a frame straddled mode is utilized. This has the benefit of recording data with a larger FOV since the acquisition rate of the camera is not limited by frame rate, instead the pulse separation of the laser is the needed parameter to limit particle displacement between frames, Fig. 2.18. The pulse separation used for 2 m/s flow is 55 μs while for 3 m/s the separation is 37.5 μs . In Fig. 2.18 it can be observed that the first exposure captures the first of the dual pulses from the laser at the end of frame 1, and then capture the second of the dual pulses at the beginning of frame 2. A sample processed PIV image is shown in Fig. 2.18 where the increased FOV is evident when compared with Fig. 2.19.

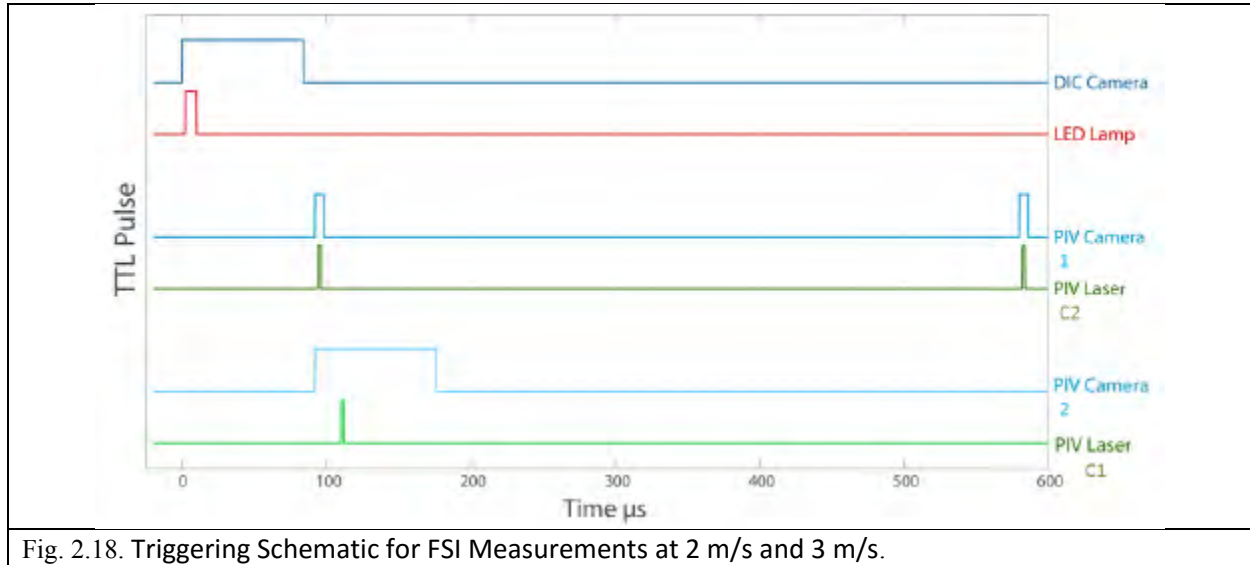


Fig. 2.18. Triggering Schematic for FSI Measurements at 2 m/s and 3 m/s.

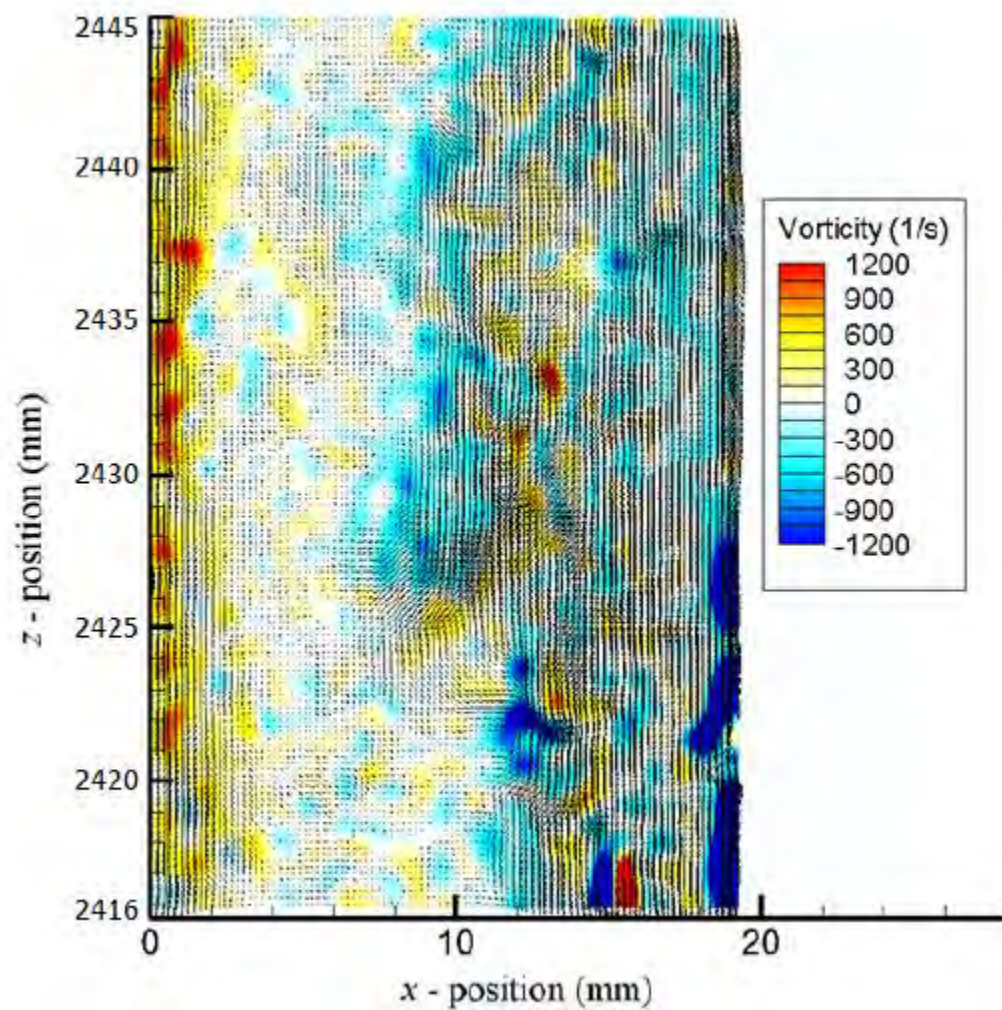


Fig. 2.19. Velocity Vectors with Vorticity contour in Background for 3 m/s Axial Flow.

3. Structural analysis

A large number of numerical and physical simulations were conducted in relation to the design and seismic behavior assessment of the nuclear fuel assembly specimen built at the George Washington University. A summary of the analytical and experimental studies that the laboratory researcher have done on the fuel assembly and its bracing system in collaboration with Professor Bardet's group is presented in this report.

Numerical (Finite Element) Simulations for Design of the Assembly

A large number of finite element analyses were conducted to aid the decisions regarding the geometry and material properties of the fuel assembly. These analyses were performed with different levels of sophistication as discussed below.

Finite element analysis of one single bundle under seismic loads

In this analysis, a full length bundle including the attached springs and dimples were analyzed. All the springs and dimples were modeled and dynamic characteristics of the rod such as natural frequencies and mode shapes were calculated. The rod was also subjected to several base excitations including sinusoidal motions and earthquake records. Maximum lateral displacements of the rod was calculated and noted in each case. Different cross sections and materials such as hollow and solid acrylic and Schott N-Pk52A Glass rods as well as zircaloy rods containing uranium were tested. Acrylic was selected as a surrogate for the fuel rod material for experimental works. Tables 3.1 and 3.2 show the properties of acrylic rods and the real fuel rods (Zircaloy tubes containing Uranium), respectively.

Table 3.1. Material properties of Acrylic

Acrylic Rods			
Material Properties	Modulus of Elasticity	3.30E+09	Pa
	Density	1190	kg/m3
Geometry	Diameter	0.01425	m
	Length	4	m
	Distance between Rod Centers	0.019	m

Table 3.2. Material properties of Zircaloy and Uranium dioxide

Zircaloy and Uranium Dioxide				
Material Properties	Zircaloy	Modulus of Elasticity	9.72E+09	Pa
		Density	6570	kg/m3
	UO2	Density	10970	kg/m3
Geometry	Zircaloy	Tube OD	0.0095	m
		Tube ID	0.0082	m
		Distance between tube Centers	0.0126	m

All the calculations were performed by using 5% and 15% damping ratio. Four different ground motions were used for dynamic analysis. Two sinusoidal motions with acceleration amplitudes of 0.15g and 0.30g and two real ground motions from El Centro and Santa Monica earthquakes. Acceleration time history and spectral acceleration of earthquake records are shown in Figure 3.1.

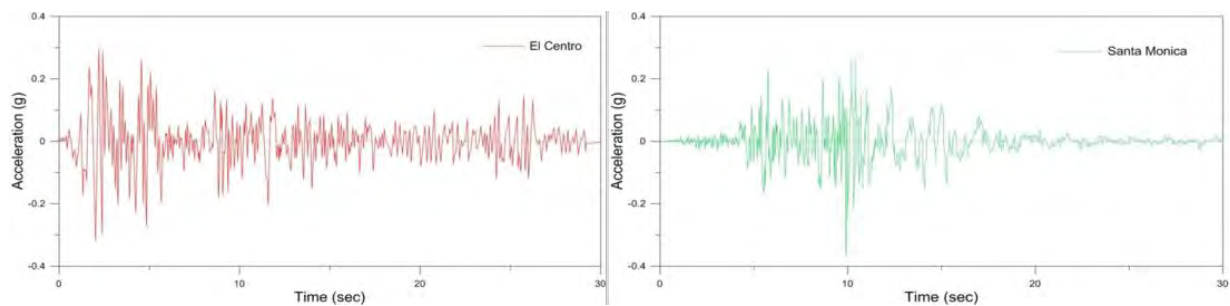


Figure 3.1. Ground motion records of real earthquakes

Finite element analysis of the simplified full length model under seismic loads

In this case a bundle of fuel assembly containing 36 rods (in 6×6 arrangement) was analyzed. All the above mentioned variables such as material properties, cross sectional section type, base excitations and values of damping ratio were considered to obtain the most extreme seismic response of the assembly. The main objective of this part was to calculate the relative lateral displacements of the adjacent rods. All the springs and dimples were considered by imposing proper displacement constraints at the level of springs and dimples.

Finite element analysis of the full model and designing the bracing structure.

The fuel assembly unit and the bracing structure were modeled and analyzed together. In this model all key details were modeled to predict the seismic response of the whole system. The bracing structure which included steel structural members with bolted connections was carefully designed to ensure that the maximum lateral displacement of the bracing system is less than one millimeter under all considered seismic loads. The weight of the bracing system was minimized based on the maximum capacity of the shake table. Figure 3.2 shows the full fuel assembly and the bracing system.

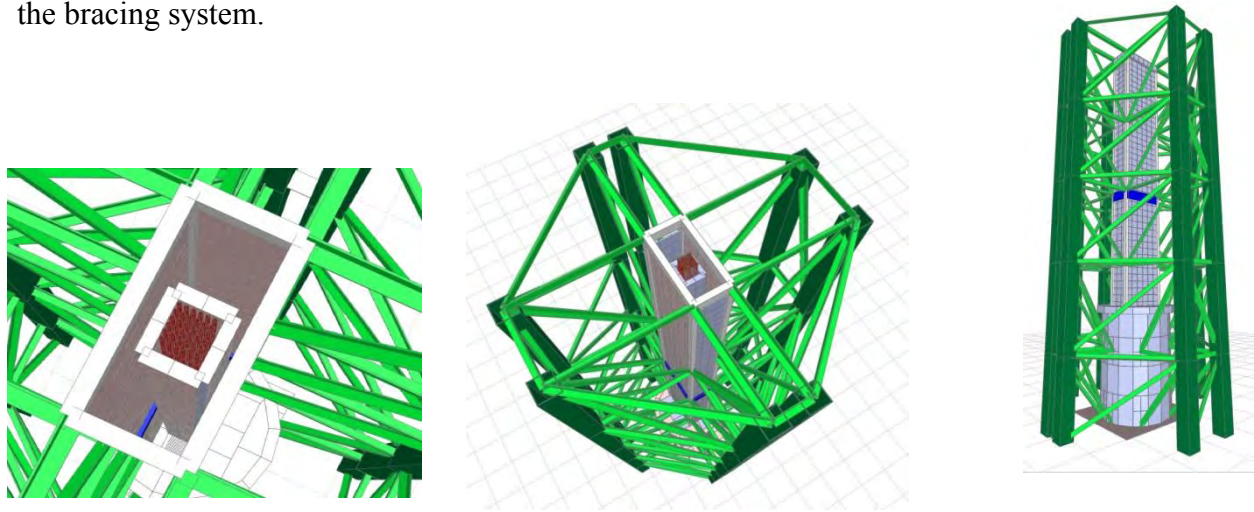


Figure 3.2. Finite element of the fuel assembly and its supporting structure.

Four cases were considered to assess the effects of the fuel rod material and the geometry and arrangement of spacer grids. Details of these cases are presented in Table 3.3.

Table 3.3. Geometric specification of each test

Case 1	Number of Spacer Grids	6
	Spacer Grid Height	0.0571 m
	Distance between spacer grids center to center	0.75 m
	Distance from end of rod to center of first spacer grid	0.125
Case 2	Number of Spacer Grids	8
	Spacer Grid Height	0.0571 m

Distance between spacer grids centers	0.495 m
Distance from end of rod to center of first spacer grid	0.2675 m

Case 3	Number of Spacer Grids	8
	Spacer Grid Height	0.038 m
	Distance between spacer grids centers	0.508 m
	Distance from end of rod to center of first spacer grid	0.222 m

Case 4	Number of Spacer Grids	7
	Spacer Grid Height	0.0571 m
	Distance between spacer grids centers	0.6225 m
	Distance from end of rod to center of first spacer grid	0.1325 m

Modal analyses of the four cases resulted in the predominant periods and frequencies presented in Table 3.4.

Table 3.4. Results of modal analysis

	Case1	Case 2	Case 3	Case 4
Period (Sec)	0.354	0.216	0.276	0.288
Frequency (Hz)	2.826	4.630	3.618	3.472

Figures 3.3.a and 3.3.b show the first three mode shapes of the structure for cases 3 and 4 in which the simplified model was used. Figure 3.3.c shows a sample mode shape of fuel rods from analysis of the sophisticated finite element model.

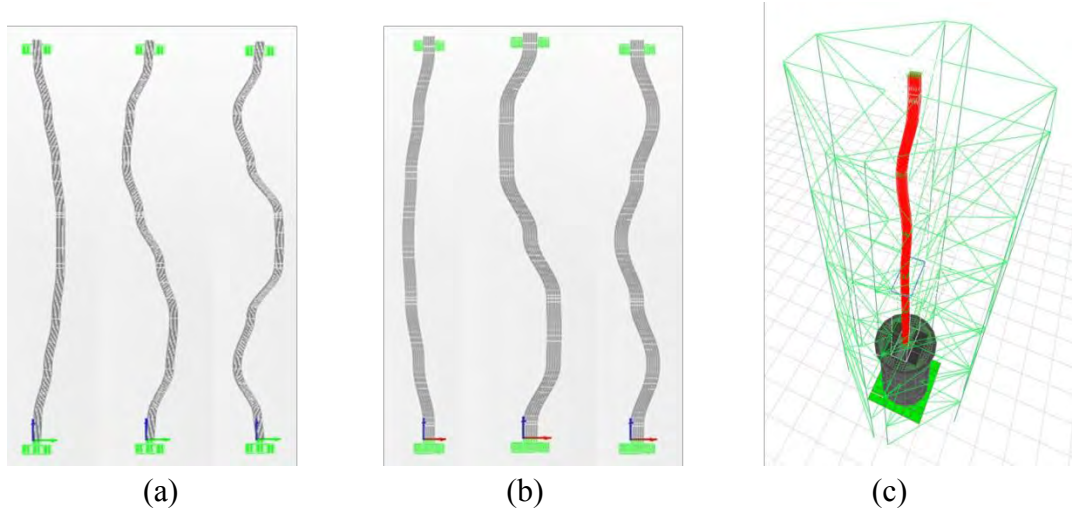


Figure 3.3. Calculated mode shapes of the entire structural system.

The structural response is presented in terms of the maximum displacement of the structure under each seismic loading with 5 and 15 percent of damping ratios, respectively. The results are shown in Tables 3.5 and 3.6.

Table 3.5. Maximum displacements (mm) with 5% of damping

Base Motion	Case1	Case 2	Case 3	Case 4
Sinusoidal ($a=0.15g$)	42.85	14.25	25.43	29.46
Sinusoidal ($a=0.30g$)	85.75	28.49	50.85	58.91
El Centro Record	27.04	9.25	17.22	17.28
Santa Monica Record	18.41	9.89	15.74	17.81

Table 3.6. Maximum displacements (mm) with 15% of damping

Base Motion	Case1	Case 2	Case 3	Case 4
Sinusoidal ($a=0.15g$)	18.63	6.05	11.52	12.80
Sinusoidal ($a=0.30g$)	37.27	12.11	23.03	25.60
El Centro Record	17.82	7.24	12.02	13.11
Santa Monica Record	136.63	6.16	8.81	9.09

Figure 3.6 shows the effect of damping ratio on the lateral displacement of fuel rods at their mid-height under sinusoidal motion for case 3. Figure 3.7 compares the response of the structure under El Centro earthquake for cases 3 and 4 with 5% damping.

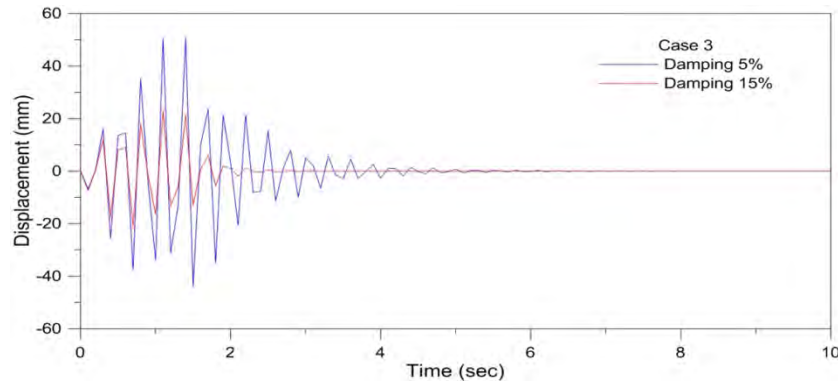


Figure 3.6. Displacement of the structure under sinusoidal motion ($a=0.30g$)

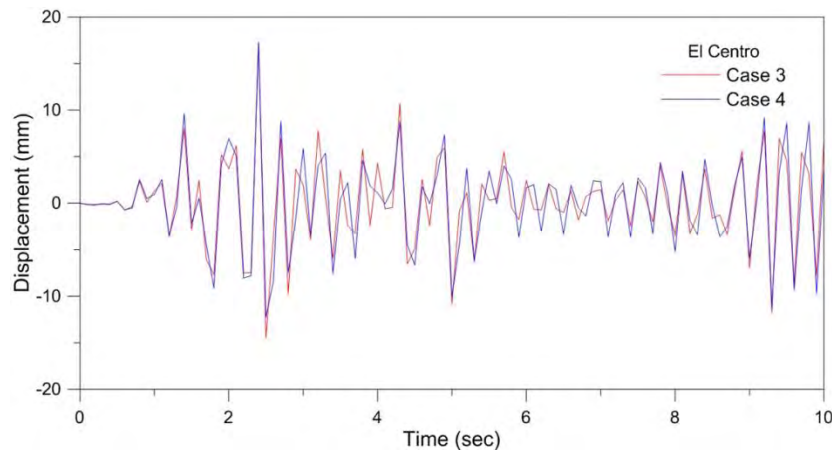


Figure 3.7. Displacement of the structure for the El-Centro record for cases 3 and 4 with 5% of damping

Results of the modal and seismic analyses show that there is a good correspondence between responses of cases 3 and 4. Therefore, Acrylic rods with proper arrangement of spacer grids (case 4) were considered good replacements for Zircaloy tubes with Uranium Dioxide inserts (case 3).

Finalizing the design of bracing structure, preparing the final drawings and ordering the steel structure.

The bracing structure consisted of steel tubes as columns and steel angles as the lateral bracing members with bolted connections. After finalizing the structural design of each member and completing detailed drawings of the members and their connections, the structural system was ordered to be built. The bracing system members were delivered on September 26th 2013 and the whole structural elements were stored in a proper place to be assembled later. The following pictures show samples of structural drawings and delivered steel members of the bracing system.

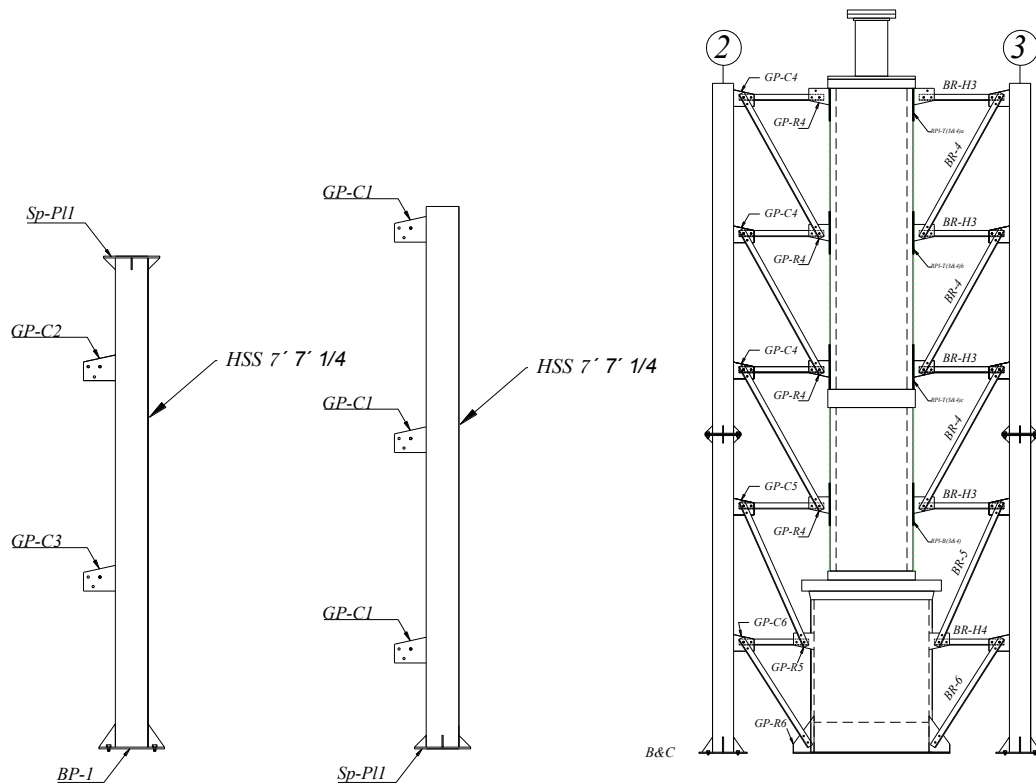


Figure 3.8. A sample of structural drawing



Figure 3.9. Delivered steel columns.

Change in boundary condition of the fuel rods and new finite element analysis.

In order to further refine the design of the fuel assembly, several variants of the boundary conditions for the fuel rods were considered. Based on the changes in the boundary condition and internal supports of the fuel bundle, a new series of finite element analysis were performed. The new supports were placed at the level of the first and last spacer grids instead of bottom and top of the fuel rods. Figure 3.10 shows the location of the new support.

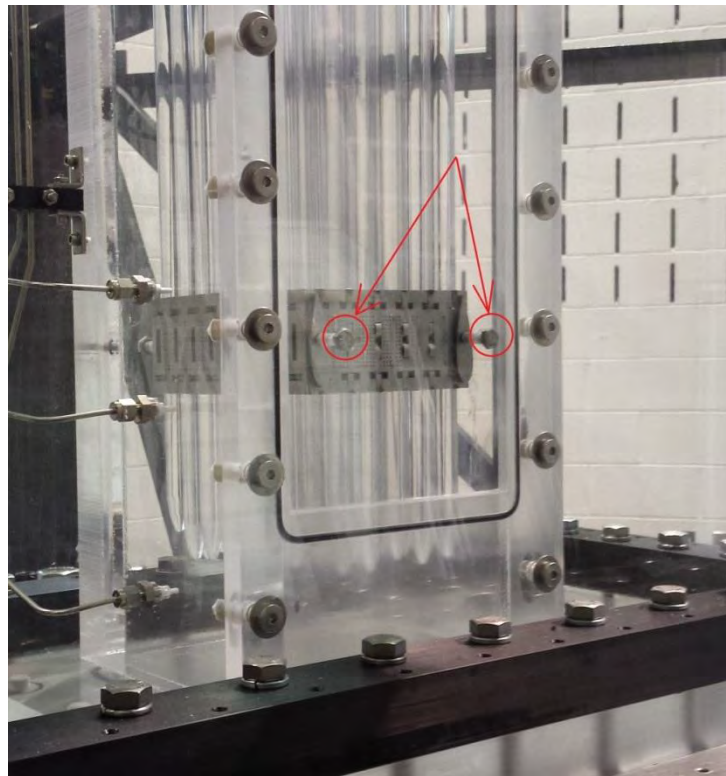


Figure 3.10. Location of the fuel rods support.

Preliminary experiments on the shake table.

As a preliminary test and in order to finalize and test the various aspects of instrumentation of the fuel assembly on the shake table, a small test section containing a single fuel rod in dry and submerged conditions was tested on the shake table using sinusoidal motion. The specimen was subjected to horizontal base accelerations ranging from 0.1g to 0.35g and the responses were recorded to be analyzed, figure 3.11.



Figure 3.11. Small test section on the shake table.

Estimation of damping ratios

The damping ratios of the bundle are estimated numerically by matching experimental data to numerical model. The time domain equations are solved using modal analysis:

$$\begin{aligned}\mathbf{M}\ddot{\mathbf{X}} + \mathbf{C}\dot{\mathbf{X}} + \mathbf{K}\mathbf{X} &= \mathbf{F}(t) = -\mathbf{M} \cdot \mathbf{a}_g(t) \\ \mathbf{X} &= \mathbf{U}e^{i\omega t} \\ [\mathbf{K} - \omega^2\mathbf{M}] \cdot \mathbf{U} &= 0\end{aligned}$$

Transfer functions are then computed:

$$U(i\omega) = H(i\omega)F(i\omega)$$

$$H_{jk}(i\omega) = \sum_{r=1}^N \frac{(A_{jk})_r}{i\omega - \lambda_r} + \frac{(A_{jk}^*)_r}{i\omega - \lambda_r^*}$$

$$(A_{jk})_r = -\frac{\phi_{jf}\phi_{kf}}{2m_r\omega_{dr}} i$$

$$\lambda_r = \sigma_r + j\omega_{dr} = -\xi\omega_{ur} + j\omega_{ur}\sqrt{1 - \xi_r^2}$$

To optimize the damping ratios, error functions are computed and minimized for the selected damping ratios:

$$E_{jk} = \sum_{F=F_i}^{F_f} e_{jk}(w_F) e_{jk}^*(w_F)$$

$$e_{jk}(w) = W(w) \cdot [H_{jk}^{\text{exp}}(w) - H_{jk}^{\text{Comp}}(w)]$$

$$e_{jk}^*(w) = W(w) \cdot [H_{jk}^{\text{exp}*}(w) - H_{jk}^{\text{Comp}*}(w)]$$

$$E^{\text{total}} = \sum_{j=1}^N \sum_{k=1}^N E_{jk} E_{jk}$$

Finally, the damping ratios can be compared to experimental data:

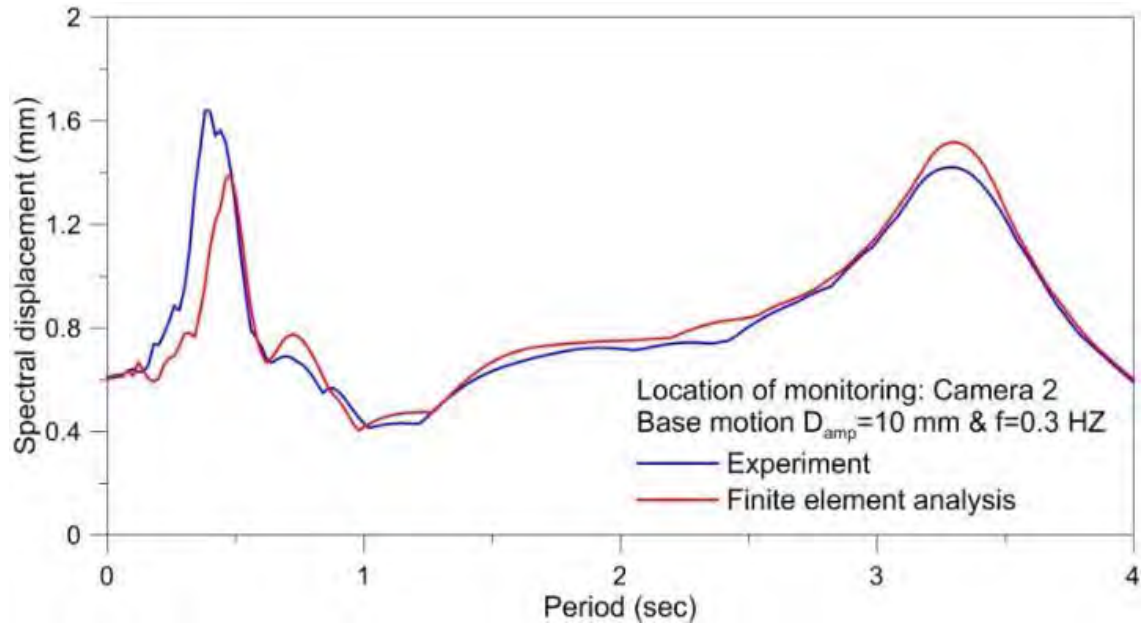


Figure 3.12. experiment vs finite element analysis power spectral densities.

4. CFD validation

After efforts in validating FSI solver for a single flexible rod in axial flow for most of the FY 2013, we switched our efforts to showing the scalability of our solver in this configuration. This is necessary to obtain CPU time through discretionary award and later INCITE award. We also switch HPC platform (we are now using MIRA at ANL). The architecture of the machine has required adapting our code to this machine.

Task 4.1: FSI solver validation

During the past quarter we continued the computations of a single flexible cylinder. Specifically, both laminar ($Re = 1,000$) and turbulent ($Re = 40,000$) flows were explored. Below we present details on the set of non-dimensional governing equations, strongly-coupled approach to modeling fluid-structure interaction problems, and initial results for laminar flow simulations. As we discussed in the second quarter progress report (see Figure 4.1 below), the single cylinder geometry contains both rigid and flexible sections with a prescribed inflow profile and convective outflow boundary condition. The inflow rigid section allows flow to develop before reaching the flexible portion and the outflow rigid section allows flow to exit the domain without reflecting back into the domain and affecting the upstream solution.

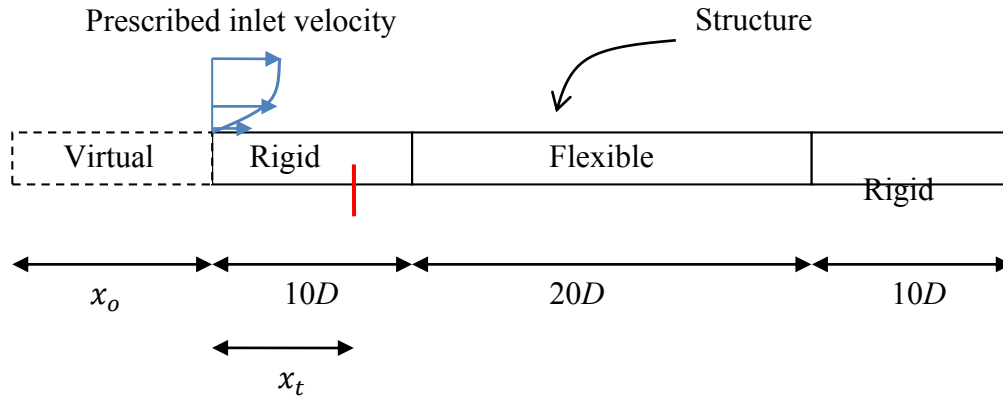


Figure 4.1: Schematic of problem setup; D is the diameter of the cylinder

The three dimensional, unsteady, Navier-Stokes equations governing dynamics of the flow are solved together with the Euler-Bernoulli beam model governing the dynamics of the structure as a coupled system. The non-dimensional form of the equations are as follows: flow equations for velocity \mathbf{u} and pressure p ,

$$\frac{\partial \mathbf{u}}{\partial t} + \nabla \cdot (\mathbf{u}\mathbf{u}) = -\nabla p + \frac{1}{Re} \nabla^2 \mathbf{u} + \mathbf{f},$$

$$\nabla \cdot \mathbf{u} = 0, \tag{1}$$

where \mathbf{u} is the velocity vector, p is the pressure and Re is the Reynolds number. The normalized form of the Euler-Bernoulli beam model governing the dynamics of the structure is:

$$\underbrace{\frac{\partial^2 y}{\partial t^2}}_{\text{mass}} + \underbrace{\left(\frac{\beta}{1-\beta}\right)\left(\frac{1}{\varepsilon^2}\right)\left(\frac{1}{U^2}\right)\frac{\partial^4 y}{\partial x^4}}_{\text{elasticity}} = \underbrace{\left(\frac{4}{\pi}\right)\left(\frac{\beta}{1-\beta}\right)\left(\frac{1}{\varepsilon}\right)F_s}_{\text{force}}, \quad (2)$$

where ε is the length to diameter ratio, U the dimensionless velocity ratio, β mass ratio, F_s is the hydrodynamic force and y is the displacement of the beam as a function of axis position x . The Galerkin finite element method is applied to (2) in order to obtain the corresponding discrete problem for displacement vector \mathbf{y} . With the state space vector, \mathbf{z} , defined as the vector of generalized displacements, $\mathbf{z} = \begin{bmatrix} \mathbf{y} \\ \frac{\partial \mathbf{y}}{\partial t} \end{bmatrix}$, the Crank-Nicholson scheme is used to integrate in time:

$$\left(M + \frac{\Delta t}{2}K\right)\mathbf{z}^{n+1} = \left(M - \frac{\Delta t}{2}K\right)\mathbf{z}^n + \frac{\Delta t}{2}(\mathbf{q}^n + \mathbf{q}^{n+1}), \quad (3)$$

where M is the mass matrix, K is the stiffness matrix, and \mathbf{q} is the force vector from respective finite element approximations of the mass, elasticity, and force terms in (2).

The above set of equations comprise the fluid-structure interaction problem, with the hydrodynamic forcing, \mathbf{q} , evaluated from the fluid solution and the near-body velocity boundary conditions, applied via direct forcing function \mathbf{f} , obtained from the structural solution. We initially used a weak-coupling approach to solve (1) and (2) at each time step. This entails exactly one fluid solution and one structural solution per time step. After systematic testing, this method proved inadequate as fluid-structure interaction problems containing structural and fluid densities of approximately equal magnitude often require additional sub-iterations to avoid instability. An alternative approach is the strongly-coupled, prediction-correction method; Figure 4.2 illustrates the iterative loop for time iteration n using this approach.

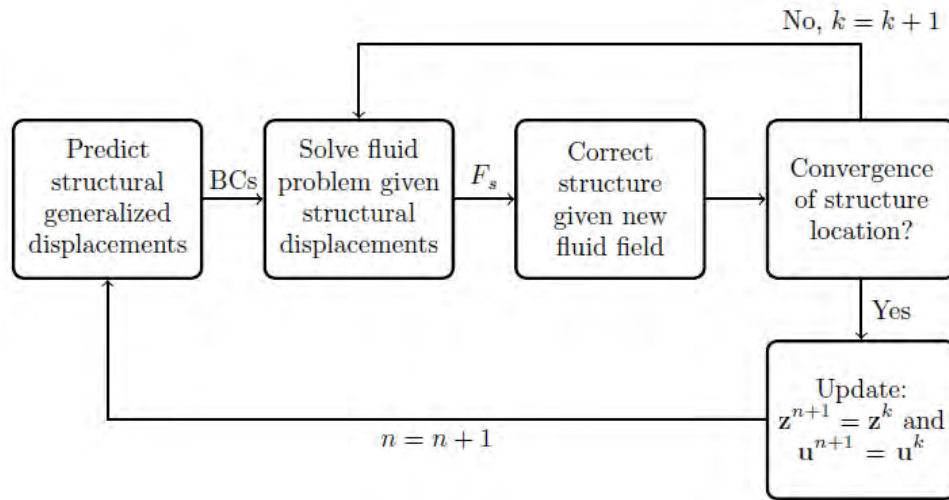


Figure 4.2: Iterative loop for strongly coupled approach; n is the overall time iteration counter and k is the subiteration loop counter

For the given approach, fluid forcing function \mathbf{f}^{n+1} in (2) and hydrodynamic force \mathbf{q}^{n+1} in (4) are updated over each sub-iteration k until the structural displacements converge and the simulation proceeds to the next time step. Solving the discrete set of fluid and structural equations interactively appears to avoid instability issues for this problem. However, the prediction-correction approach is obviously more computationally expensive, primarily due to additional solutions of the pressure Poisson equation.

Using the strongly-coupled method, we have completed two preliminary simulation runs of fluid-structure interaction in laminar flow. The governing parameters are as follows:

Table 4.1: Parameters for fluid-structure interaction problem

Re	Flow Condition	\bar{U}
10,000	Laminar	0.15
		1.5
		3.5
		6
		9
40,000	Turbulent	0.15
		1.5
		3.5
		6
		9

As we now have a successful fluid-structure solver, we plan to continue running simulations in which the Reynolds numbers and non-dimensional parameters are varied. Of primary importance is obtaining turbulent flow by increasing the Reynolds number and implementing a numerical tripwire. At a relatively higher Reynolds number and $\bar{U} \approx 6$, buckling of the cylinder should occur, per published laboratory experiments.

Figure 4.3 shows the displacement of the central node of the finite element model at $\text{Re} = 10,000$ and $\bar{U} = 1.5$.

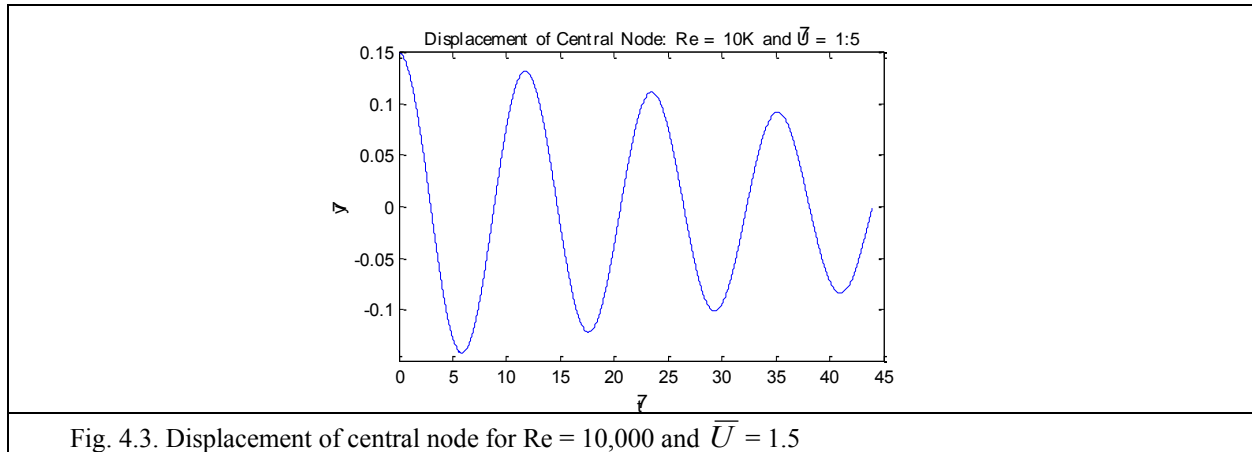


Fig. 4.3. Displacement of central node for $\text{Re} = 10,000$ and $\bar{U} = 1.5$

We show preliminary results of fluid contour plots at $Re = 10,000$. Figure 4.4 shows the initial flow condition for streamwise velocity component along the axis of the cylinder; note the development of boundary layers along the cylinder. Figure 4.5 shows the asymmetry of the boundary layers brought forth by motion of the cylinder, with an adverse pressure gradient on the right and a positive pressure gradient on the left.

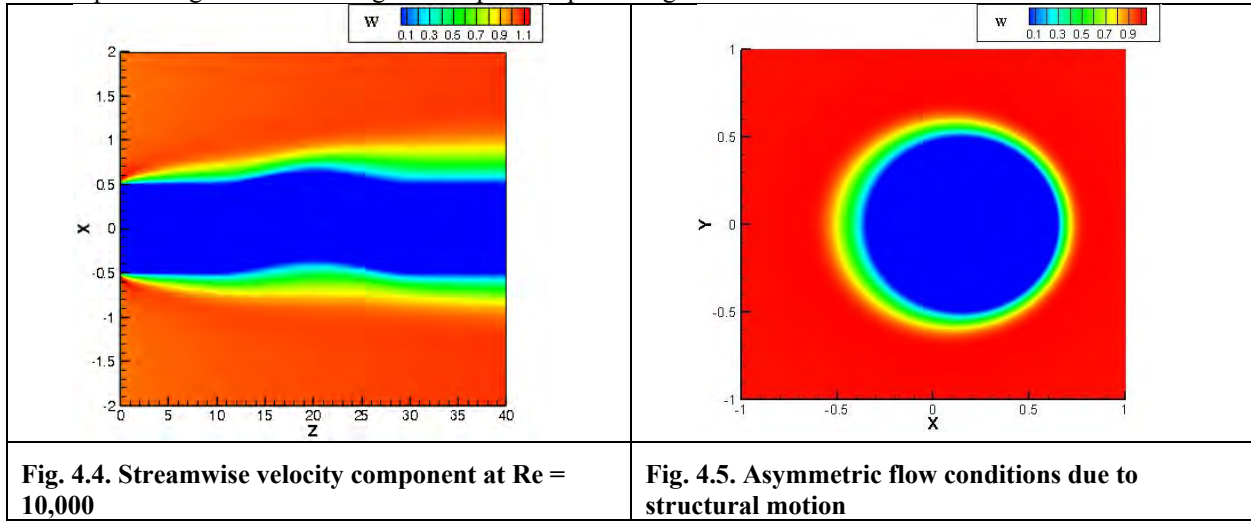


Fig. 4.4. Streamwise velocity component at $Re = 10,000$

Fig. 4.5. Asymmetric flow conditions due to structural motion

Task 4.2: FSI solver testing on MIRA (BG/Q):

The development and testing of the massively parallel fluid-structure interaction flow solver (FLASH-FSI¹) was further advanced and ported and tested on the VESTAS/CETUS/MIRA supercomputing system of the Argonne Leadership Computing Facility, Argonne National Laboratory². As the first series of computations will be done on 2×2 periodic arrays, which are densely packed and are supported by spacer grids with very complex geometry, the use of an immersed boundary³ approach and structured uniform grids (UG) was preferred for reasons of computational efficiency. The primary objective of the preliminary set of computations we conducted was to get an accurate estimate of the computational cost of the different components of the code, for realistic configurations. In this process we also focused on fine tuning and optimizing the solver. Data post-processing and flow visualizations strategies have also been implemented and tested. Below we will summarize all related results.

Navier-Stokes UG scaling test:

First, scaling tests on the uniform grid incompressible Navier-Stokes solver were performed. Then, the infrastructure to compute first and second order turbulent statistics was implemented. The flow solver and statistics module was tested on a channel flow configuration as shown in Figure 4.5. The streamwise, spanwise and wall-normal directions are z , x , and y respectively. The grid that was utilized has $2048 \times 2048 \times 10240$ cells (about 43 billion)⁷. This massive mesh was decomposed and distributed on a processor grid in the y - z directions. The different cases we consider to conduct strong scaling tests are shown in Table 4.2. The HPCToolkit was used to sample times, with almost identical time results.

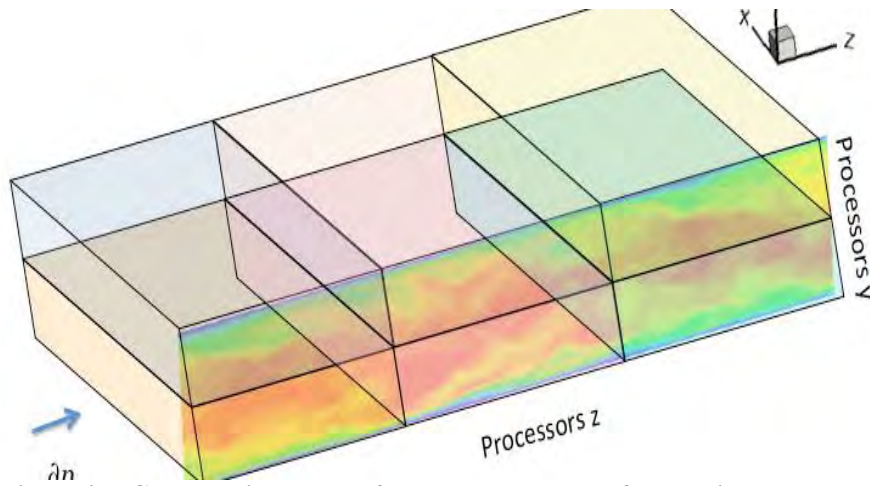


Figure 4.5: Computational setup for turbulent channel flow scaling tests. The uniform Eulerian grid (fluid grid) is split on a processor grid distributed on the y - z axes (rectangular blocks). A pressure gradient is prescribed along the streamwise z direction.

Case	Procs Y	Procs Z	Pencil Grid	Total Procs
(a)	64	128	2048x32x80	8192
(b)	64	256	2048x32x40	16384
(c)	64	512	2048x32x20	32768
(d)	128	512	2048x32x20	65536

Table 4.2: Processor grids for parallel scaling test of UG incompressible solver. The pencil grids for each case correspond to the number of cells owned by each processor.

Processors involved on these runs ranged from 8K up to 65K as shown on the last column of Table 4.2. In figure 4.3, the strong scaling results for the main components of the explicit integration method are shown. The inclusive time is taken as the average of 20 integration time steps, although it was found that wall times on MIRA are repeatable up to a small fraction of a second ($\sim 10^{-2}$ s). Both the computation of the momentum equations, predictor and corrector steps exhibit good scaling behavior up to 65K processors. In similar fashion the trigonometric transform Poisson solver shows good strong scaling over the range of processors employed. It was seen that the overall time step maintains this trend, and the low times required for guardcell filling operation remain flat. This is due to the known fact that guardcell filling is not optimized in Flash for machines like MIRA in either UG or adaptive refinement AMR mode. The statistics from the computation were in excellent agreement experiments in the literature.

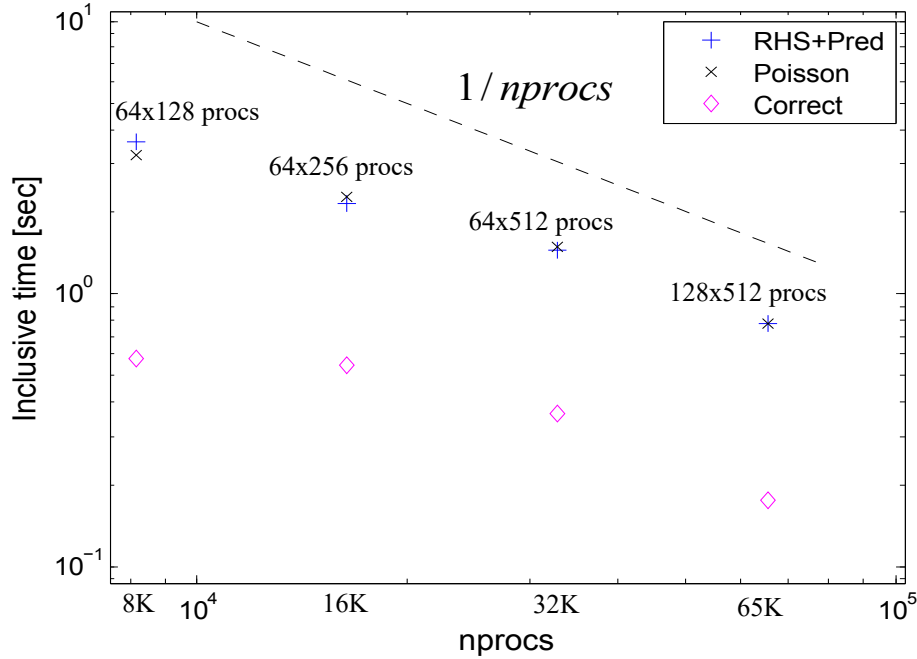


Figure 4.3: Inclusive times for scaling test on channel flow problem. The main time integration scheme components are shown, namely computation of right hand side of momentum equation (RHS) + Adams Bashforth 2 predictor step (Pred), Poisson equation solution (Poisson) and pressure and velocity correction (Correct). Good strong scaling is found up to 65K processors for this problem.

Navier-Stokes + Immersed Boundaries Scaling Test:

A test case was setup, to evaluate the parallel scaling behavior of the explicit Navier-Stokes Solver together with the immersed boundary method that will be used on all FSI problems. Our objective was to evaluate bottlenecks on this architecture (Mira). An assembly with arbitrary number of rods can be defined. In Figure 4.4, the setup of a 2×2 rod assembly can be seen. As in the previous study, the Eulerian fluid grid is domain decomposed among computing processors in both y - z directions⁴. This approach has the advantages of local communication on data transposition operations and the use of fast trigonometric solvers for the elliptic equation resulting from the time integration of incompressible flow. The IB method requires a Lagrangian grid description of the fuel rods. Each cylinder surface is represented by a triangulation and a set of surface marker particles. Interaction between both grids is of the Dirichlet-Neumann type (no-slip condition for the fluid on the rods surfaces, and distributed forces from the fluid to compute loads on rods) using an immersed boundary (IB) technique^{5,6}. Parallelization of the immersed cylinder grids is done by sectioning each rod in an arbitrary number of components and distributing among processors on the computation.

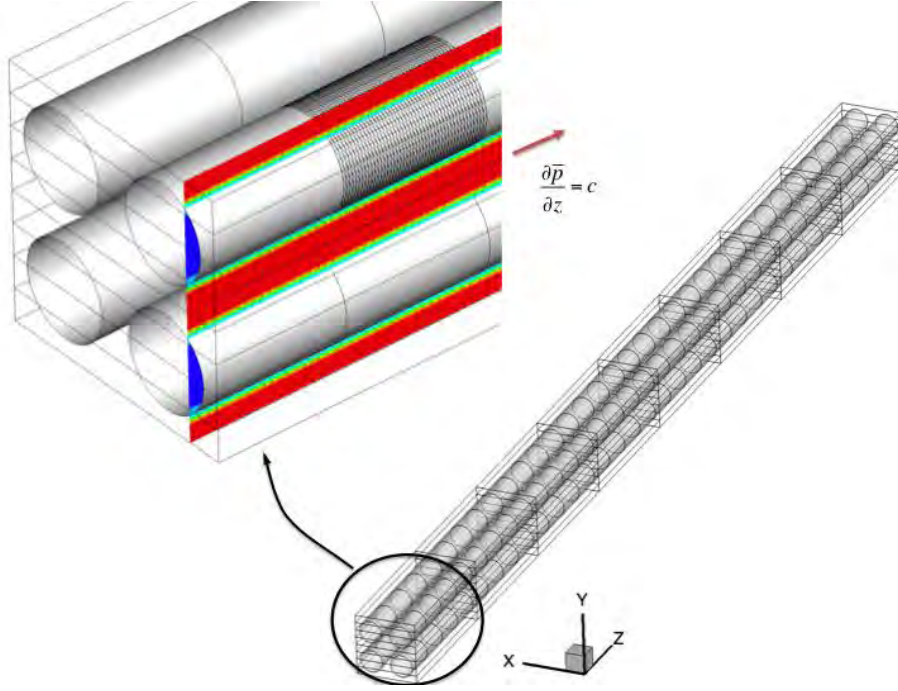


Figure 4.4: Computational setup for 2×2 fuel rod assembly. The uniform Eulerian grid (fluid grid) is split on a processor grid distributed on the y-z axes (rectangular blocks). The rods are split on an arbitrary number of segments and distributed among processors. The cylinder surfaces are triangulated, and their boundary condition treated using an immersed boundary method.

The methodology proposed for these intensive computations is to use a uniform Eulerian fluid grid with domain decomposition among computing processors in both y-z directions. This approach has the advantages of local communication on data transposition operations and the use of fast trigonometric solvers for the elliptic equation resulting from the time integration of incompressible flow.

This grid is combined with a Lagrangian grid description of the fuel rods. Each cylinder surface is represented by a triangulation and a set of surface marker particles. Interaction between both grids is of the Dirichlet-Neumann type (no-slip condition for the fluid on the rods surfaces, and distributed forces from the fluid to compute loads on rods) using an immersed boundary (IB) technique^{3,6}. Parallelization of the immersed cylinder grids is done by sectioning each rod in an arbitrary number of components and distributing among processors on the computation. Both IB optimizations, namely Bitmap communication⁶ and inverse guardcell filling for the resulting IB forcing field⁷, were employed on this study.

The four fuel rods of length $50D$, where D is the rod diameter were placed on a 2×2 array with uniform distance $1.36D$ between rod centers. The boundary conditions for the $2.72D \times 2.72D \times 50D$ domain were periodic in all dimensions, and a driving pressure gradient along the coaxial z-axis was prescribed. Same timing strategy as in the previous case was used, and the 4 cylinders were split in 126, 256, 1048 and 4096 bodies, maintaining the total number of surface triangles

constant. Two grids of different orders of magnitude were used, namely $256 \times 256 \times 2304$ cells (151 million) and $1024 \times 1024 \times 9216$ cells (9.7 Billion).

The times per simulation time step for different number of processors and surface bodies on grids 1 and 2 are shown on Tables 4.3 and 4.4 respectively.

Case	Procs Y	Procs Z	Nodes	Procs per Node	Pencil	Tot Bodies	Tot Procs	Time (s)
(a1)	8	16	16	8	256x32x144	128	128	16.3
			32	4	256x32x144	128	128	14.1
(b1)	8	32	32	8	256x32x72	256	256	7.87
(c1)	16	64	128	8	256x16x36	1024	1024	3.28

Table 4.3: Inclusive times per time step for different processor and body numbers on 2×2 cylinder computation and Grid 1 (151 million cells).

Case	Proc Y	Procs Z	Nodes	Procs per Node	Pencil	Tot Bodies	Particles per Proc	Tot Procs	Time (s)
(a2)	32	128	512	8	1024x32x72	4096	151K	4096	50.11
(b2)	32	256	512	16	1024x32x36	4096	76K	8192	31.00
			1024	8	1024x32x36	4096	76K	8192	25.78
(c2)	64	256	1024	16	1024x16x36	4096	49K	16384	19.35
			2048	8	1024x16x36	4096	49K	16384	15.09
(d2)	64	512	2048	16	1024x16x18	4096	25K	32768	10.48
			4096	8	1024x16x18	4096	25K	32768	8.6

Table 4.4: Inclusive times per time step for different processor and body numbers on 2×2 cylinder computation and Grid 2 (9.7 Billion cells).

It was found from both tables that the main driver of the registered times per timestep was the computational work necessary for the immersed boundary forcing. This work is tied to the maximum number of surface marker particles per processor, which is directly correlated to the

surface area enclosed on the processors Eulerian grid pencil. In Table 4.4, this correlation can be seen by comparing the maximum particles per block column with the inclusive time per timestep (last column). It was also found that sub utilizing the amount of cores per node, the time per step would decrease about 15%, suggesting that memory bandwidth in the node is reducing the computational speed. Several components of the IB algorithm have been revisited since then and the computations optimized: location of closest Eulerian point to marker particle, computation of interpolation functions, single computation of parameters that remain constant for uniform grids.

The speedup of the code with these changes is of the order of 20%. Currently modifications are being made to save on the operations required to obtain the IB interpolation functions, in cases where the stack of cylinders is fixed.

LES of 2×2 Spacer Grid – fuel rod system:

A CAD model of the Spacer Grid designed for the experimental facility was used to define a realistic computation of a 2×2 Spacer Grid and fuel rod system. All dimensions were referred to the rods diameter, and the technology to run constant mass coaxial flow was implemented. The Reynolds number is defined for this problem based on the bulk velocity W_{Bulk} of the axial flow and the rod diameter D . In figure 4.5 the setup for the immersed bodies is shown, where the geometrical complexity of the spacer grid model is closely represented. The distance between spacer grids is taken a periodicity length and corresponds on the experiment to $43.69D$ in the z -axis. The distance between spacer plates is $1.343D$ on the x and y directions.

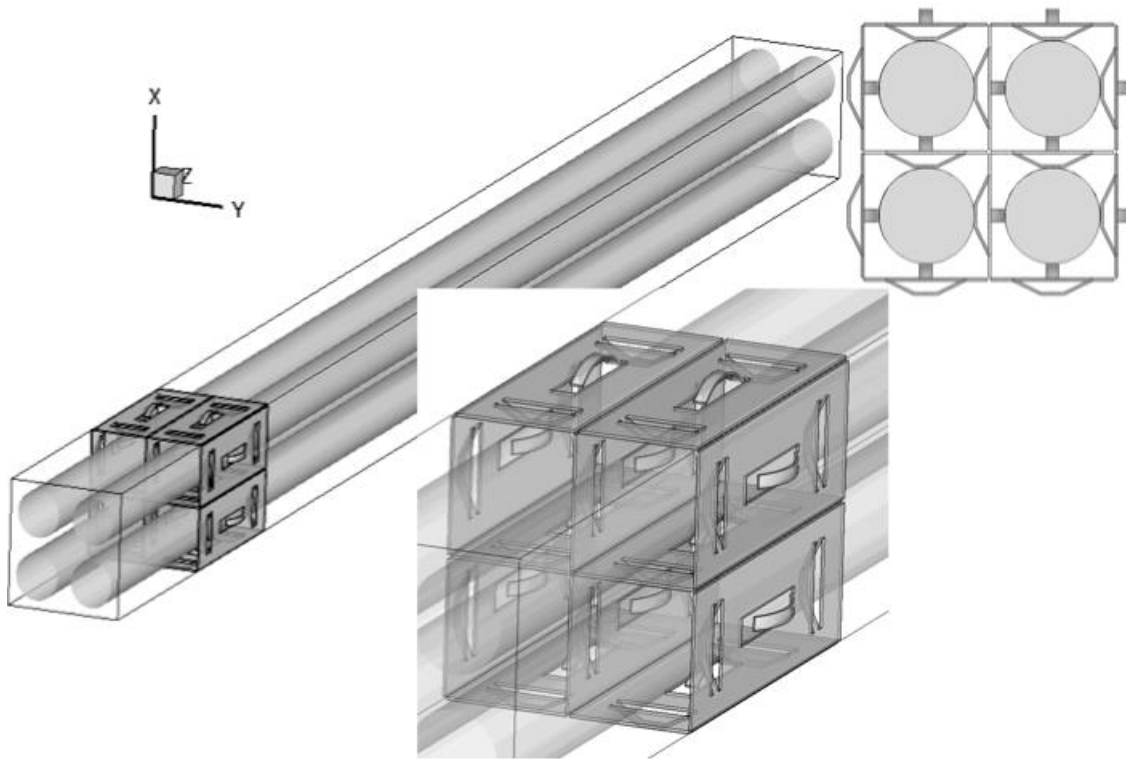


Figure 4.5: Computational setup for 2×2 Spacer Grid + fuel rod assembly. Both Spacer grid and fuel rods surfaces are triangulated, split in a specified amount of bodies and their boundary condition treated using immersed boundaries.

The technology to interpolate flow fields among grids of different cell size has been implemented and a case with $512 \times 512 \times 4060$ (1.1 billion) cells is being run for this problem to advance through the initial transient. The Reynolds number selected for the first set of runs is $Re = 10,000$, and grid a grid convergence test will be performed comparing turbulent statistics to a case with twice the number of cells in each direction. The number of processors being used range from 32K to 130K on MIRA.

For the first set of simulations, the first Eulerian grid is used. The four cylinders and spacer grid were distributed in 14.7K bodies and assigned one per processor on a 32K cores simulation. Two 12 hr runs of this problem were required to advance the solution 27 letots, approximately one flow through time. After, a computation was done for 12 hrs (13 Letots) to obtain resultant flow fields and statistics. In figure 4.6 instantaneous flow-field is shown for the vorticity component along the y direction.

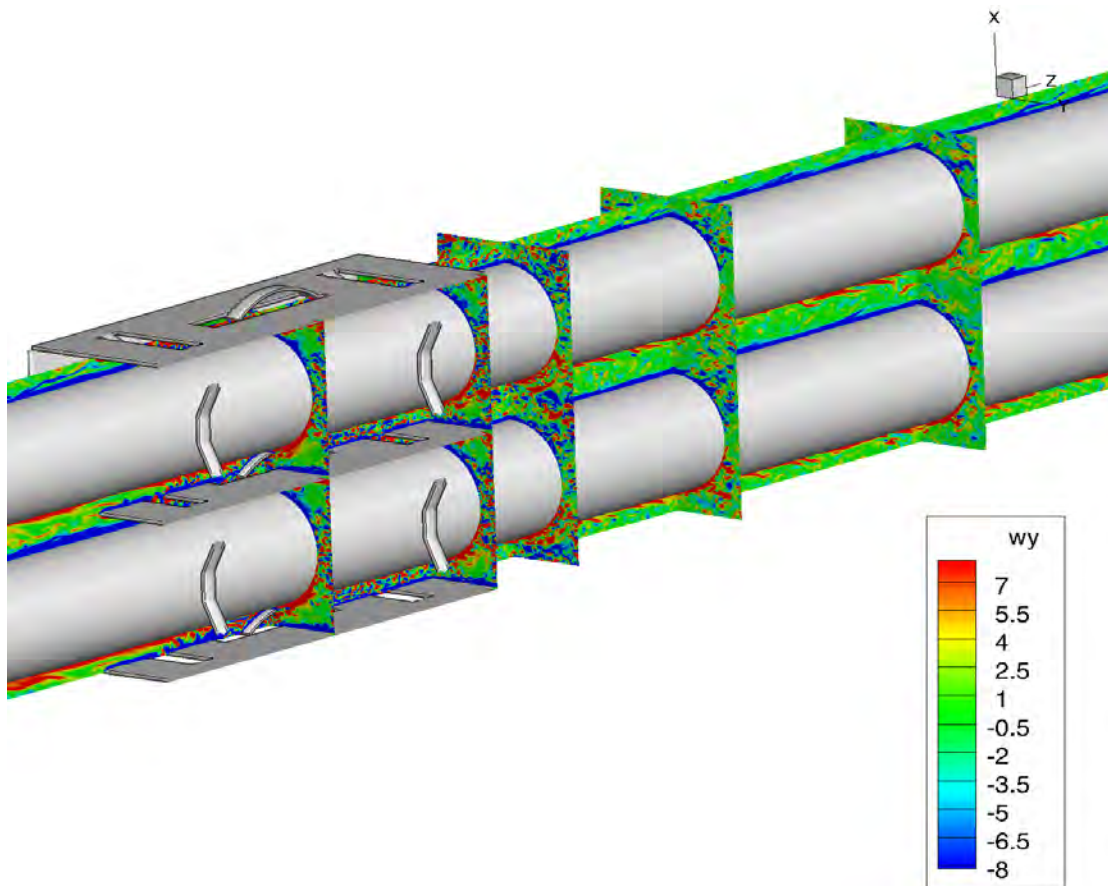


Figure 4.6: 2×2 Spacer Grid + fuel rod assembly: Instantaneous flow field for non-dimensional time $t = 39.0$. Vorticity in span wise y direction is shown on different slices around two rods and the spacer grid assembly.

5. Experimental and Numerical Results

After assembling the test section alongside the bracing structure, several series of tests have been performed. They include sinusoidal motions with different frequencies and displacement amplitudes, as well as frequency sweeps. In the latter, the amplitude of displacement is kept constant and the frequency is increased in small increments. Analysis of the first series of data led to more advanced and refined simulations to reproduce the experimental data.

Background: bundle behavior

The dynamics of prototypical bundles is well known to be significantly affected by the presence of stagnant and moving water.

5.1.1 1 D model of bundle

The fuel bundle in air can be modeled as a one dimensional, dampened, harmonic oscillator with an external force imposed by the shake table, Equation 1.

$$m\ddot{x} + 2c\dot{x} + kx = A\sin\omega t \quad (1)$$

Where m is the mass of the bundle, c the damping coefficient, k the bundle stiffness, x the bundle displacement, and A and ω are the amplitude and frequency inputs to the shake table

respectively. Normalizing the equations and incorporating $\gamma = \frac{c}{m}$, $\omega_o = \sqrt{\frac{k}{m}}$, and $A_o = \frac{A}{m}$

$$\ddot{x} + 2\gamma\dot{x} + \omega_o^2 x = A_o \sin\omega t$$

Solving for displacement $x(t)$

$$x(t) = c_1 e^{-\gamma t} \sin(\beta t + \theta) + \frac{A_o}{\sqrt{(\omega_o^2 - \omega^2)^2 + 4\gamma^2 \omega^2}} \sin(\omega t - \varphi)$$

Where c_1 and θ are arbitrary constants, $\beta = \sqrt{\omega_o^2 - \gamma^2}$, and φ is the phase. The first term on the right hand side is a transient response, while the second term is the steady behavior.

With initial conditions, $x(t = 0) = 0$, $\dot{x}(t = 0) = 0$, and assumption that the system is underdamped $\gamma < \omega_o$, the above equation can be rewritten as

$$x(t) = \frac{A_o}{\sqrt{(\omega_o^2 - \omega^2)^2 + 4\gamma^2 \omega^2}} \frac{\sin\varphi}{\sin\theta} e^{-\gamma t} \sin(\beta t + \theta) + \frac{A_o}{\sqrt{(\omega_o^2 - \omega^2)^2 + 4\gamma^2 \omega^2}} \sin(\omega t - \varphi)$$

Where $\theta = \frac{2\gamma\beta}{\omega_o^2 - \omega^2 + 2\gamma^2}$

Simple model of fluid forces

The fluid forces on the bundle can take the form of an inertial term, the added mass effect ($m_f \ddot{x}$), added damping due to viscous and form drag forces ($c_f \dot{x}$), and a flow stiffening effect, ($k_f x$). Equation (1) is therefore modified to take the form:

$$(m_s + m_f)\ddot{x} + 2(c_s + c_f)\dot{x} + (k_s + k_f)x = A \sin \omega t$$

Where subscript s is the structure and f the fluid. The added mass is an inertial force that is proportional to the amount of displaced fluid where ρ is the density of the fluid, V the volume, and C_m the added mass coefficient.

$$m_f = \rho V C_m$$

For the simple model in stagnant fluid, it is commonly assumed that there is no fluid induced stiffening, $k_f = 0$, and the natural frequency is therefore lower than in dry conditions due to added mass effect:

$$\omega_{o,stagnant} = \sqrt{\frac{k_s}{m_s + m_f}}$$

In presence of axial flow, the added mass is now likely to be different. Additionally, there is flow induced stiffening of the bundle and the natural frequency becomes:

$$\omega_{o,axial} = \sqrt{\frac{k_s + k_f}{m_s + m_f}}$$

The exact values of coefficients (m_f , c_f , k_f) are unknown and need to be determined through a combination of experiment and simulation.

Oscillating bundle in stagnant fluid

The fuel assembly can be assumed to behave similar to an array of cylinders oscillating in stagnant fluid. The dimensionless numbers that determine this type of flow characteristics are the Keulegan-Carpenter number that is the ratio of drag to inertia forces acting on the cylinder, where U_m is the fuel assembly velocity, T the period of oscillation, and D the fuel rod diameter.

$$KC = \frac{U_m T}{D}$$

Two other dimensionless numbers are needed: the Reynolds number, where ν is the kinematic viscosity, and a frequency parameter β .

$$Re = \frac{U_m D}{\nu}$$

$$\beta = \frac{Re}{KC}$$

All tests conducted around the first mode oscillations are at a low β parameter value. Regardless of forcing amplitude, at 1.2 Hz $\beta \sim 240$. KC values are in the range of $0 < KC < 2$, and in this range three flow regions are typically found. In the first region for KC less than a critical value of approximately 1.2, the flow around the fuel rods are attached with no separation, stable and two dimensional. Just above this critical KC value the flow becomes unstable due to vortices being shed from equally spaced axial positions on the fuel rod. There is a steady separation of the boundary layer around the fuel rods in this region. For tests that move to higher KC values it is assumed that the third region will be reached where unsteady vortex shedding from the fuel rods results in the flow becoming fully turbulent.

Experiment: bundle behavior

The model bundle we built exhibits behavior characteristics of published data of prototypical bundles. Specifically, the damping increases in presence of water and flow, the bundle becomes stiffer in presence of flow, and its mode shapes are modified.

Figure 5.1 is an illustration of the effect of water and flow on damping. Once the shaking stops, the number of cycles necessary for the bundle to go back to equilibrium is significantly shorter in stagnant water and in moving flow than in air. By analyzing the reduction of the decrease of the amplitudes between cycles, the damping in air is estimated at 7.5% and 12 % in stagnant water. These values are consistent with published data from Westinghouse for their AP 1000 bundle (Lu and Reed, 2006). In moving water, the damping is too strong and we cannot estimate it from the DIC measurements.

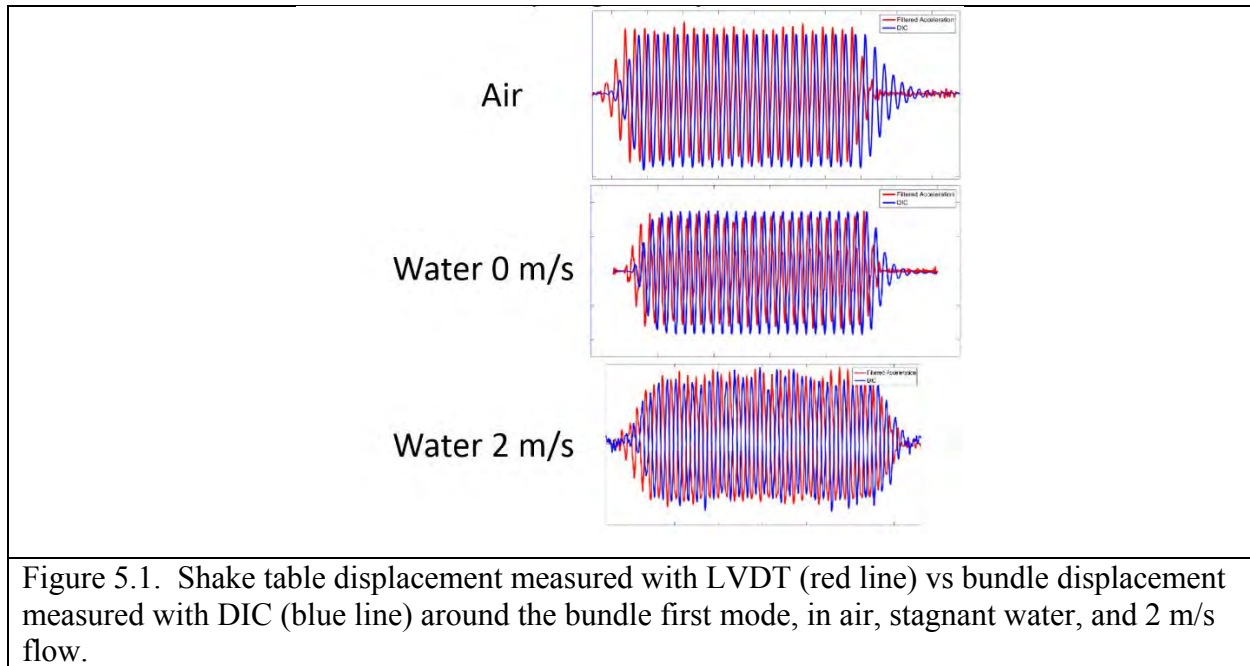


Figure 5.2 shows the frequency of the first mode for cases in air, stagnant water and 2 m/s. In air the natural frequency is near 2 Hz, which is typical of a prototypical bundles as intended. In stagnant water, the natural frequency of our bundle drops to 1.2 Hz, which is mainly due to an added mass effect. This decrease is larger than for prototypes, due to lower mass of acrylic rods compared to zircaloy rods filled with UO_2 pellets. In presence of flow, the natural frequency increases to 2.6 Hz. This increase can be attributed to a stiffening of the bundle in the presence of flow and a modification of the added mass by the axial flow. This increase appears also larger than for prototypical conditions. This is further confirmed by the use of P-cymene which has a lower density than water. For P-cymene it is found that the first mode frequency is at 1.35 Hz and in the presence of axial flow it is around 2.4 Hz, Fig. 5.3.

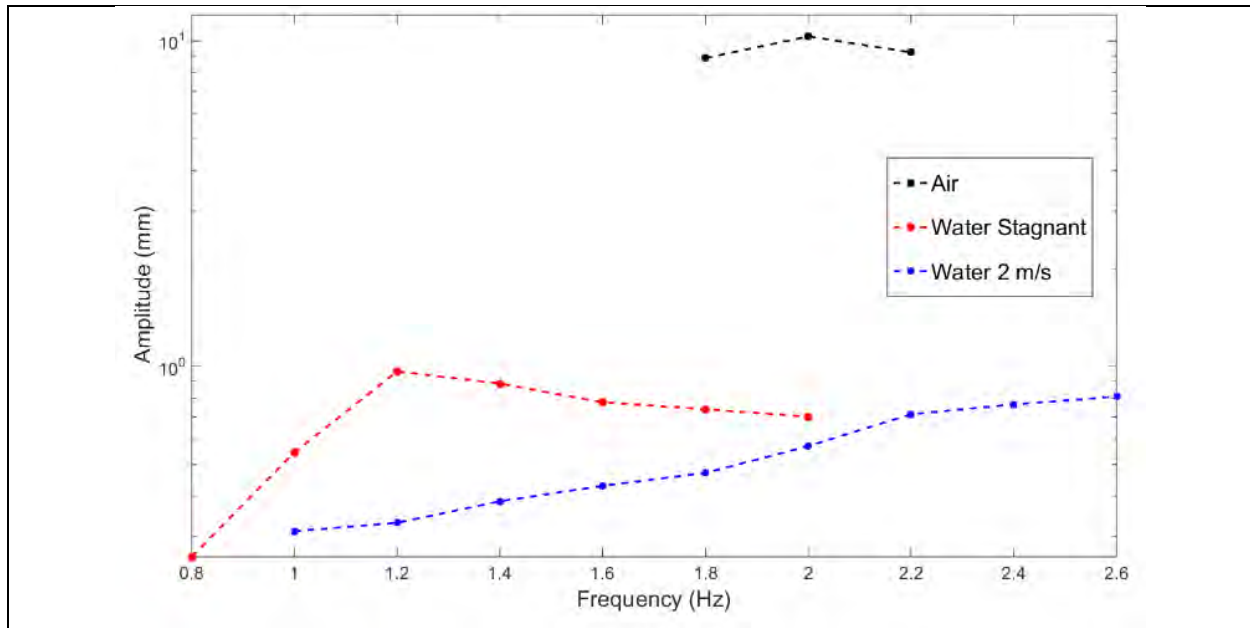


Figure 5.2. Frequency of first more in air (black), stagnant water (red), and 2 m/s water (blue).

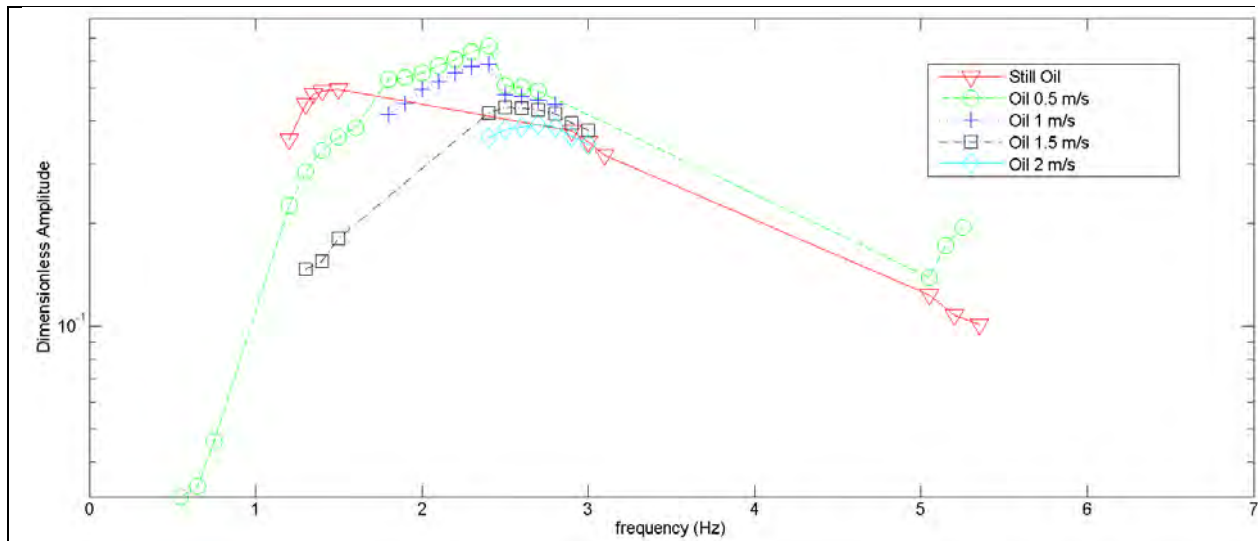


Figure 5.3. Frequency of first more in still oil (red), oil at 0.5 m/s (green), oil at 1 m/s (blue), oil at 1.5 m/s (black), and oil at 2 m/s (cyan).

The first modes are fairly symmetric for air and stagnant water, however, in the presence of axial flow, the displacement peak is shifted towards the top, Figure 5.4.

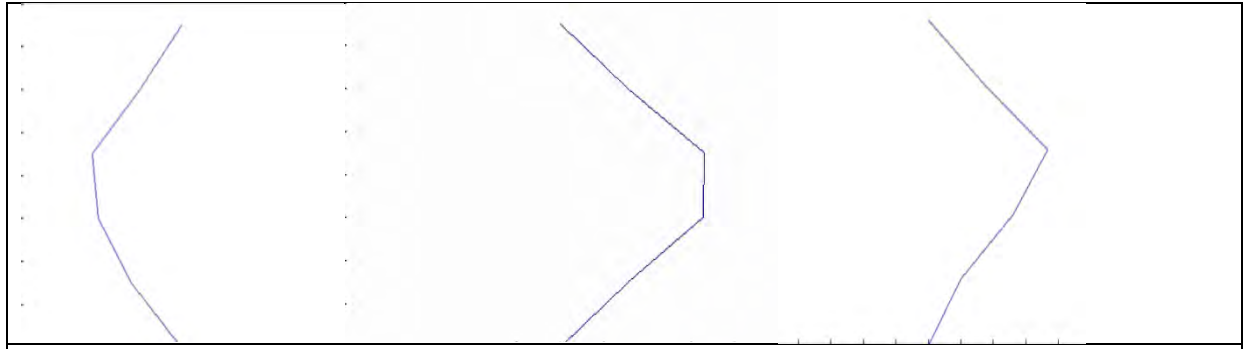


Figure 5.4. First mode shape in air, stagnant water, and in 2 m/s water

Experiment: frequency sweeps

To determine the fuel bundle natural frequencies a series of frequency sweeps are performed. During a frequency sweep, the sinusoidal motion is increased by a small increment (0.01 or 0.02 Hz) for each cycle. If necessary several cycles can be performed at each frequency. The bundle displacement is acquired with DIC, while in presence of water the associated velocity field in the bypass is also acquired with PIV. Sweep can last up to 10 min each and it is remarkable that our cameras can record all the data at frequencies up to several kilohertz for PIV for 10 min.

The second spacer grid displacement acquired with DIC is presented in figure 5.5 for cases in air, stagnant water and 1 m/s flow. In the presence of axial flow, the effect of bundle vibration is clearly seen.

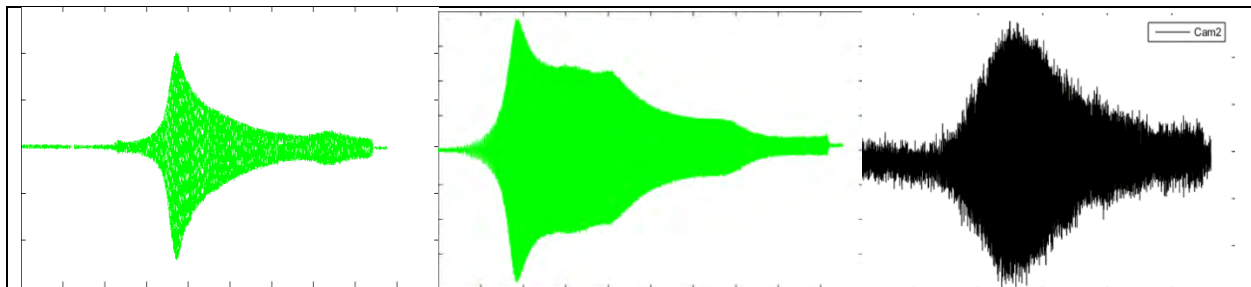


Figure 5.5. response of third spacer captured with DIC to frequency sweep. Left: air 0-5 Hz, middle stagnant water: 0-7 Hz, right, 1 m/s water 0-7 Hz.

Experiment: Test Cases in Air and Modification of Boundary Conditions

Shake Table Tests, Series 1 (Prior to BC modification)

For the first series of tests in air, it was important to capture the various modes of the structure and confirm its behavior and produce any necessary adjustments. Tests were conducted in small frequency increments between 0.1 and 0.5 Hz for a range between 0.1 and 9.0 Hz. For each frequency a total of 20 cycles were conducted to obtain steady state response of the structure.

Forcing amplitude input was varied between 0.8 and 3.0 mm. In practice, the actual displacement of the table is recorded with LVDT and real forcing amplitude and acceleration is computed from these values. Figure 5.6 shows typical LVDT and DIC outputs; the twenty steady cycles are clearly identifiable. In the DIC data for this case, a slight asymmetry is noticeable in the oscillation. This can be explained by the geometry of the spacer grids. When the bundle displaces against the springs, the latter are loaded (compressed), which results in a structural damping. On the other this damping is different (not present) when rods are pushed against the dimples, which can be modeled as hard stops. This effect is more preponderant as the oscillation amplitudes increases.

From the DIC data, it is possible to reconstruct the spectral behavior of the bundle. Figure 5.7 shows the spectrum for the 33 test cases performed. The results obtained from the high speed DIC cameras show that the natural frequency and period of the structure is about 1.8 Hz and 0.556 s respectively. The reason for the difference between experimental results and analytical results obtained from finite element modeling was the change in the boundary condition, slight change in weight of spacer grids and also initial curvature of the fuel rods at the mid height which cause the whole system being more flexible.

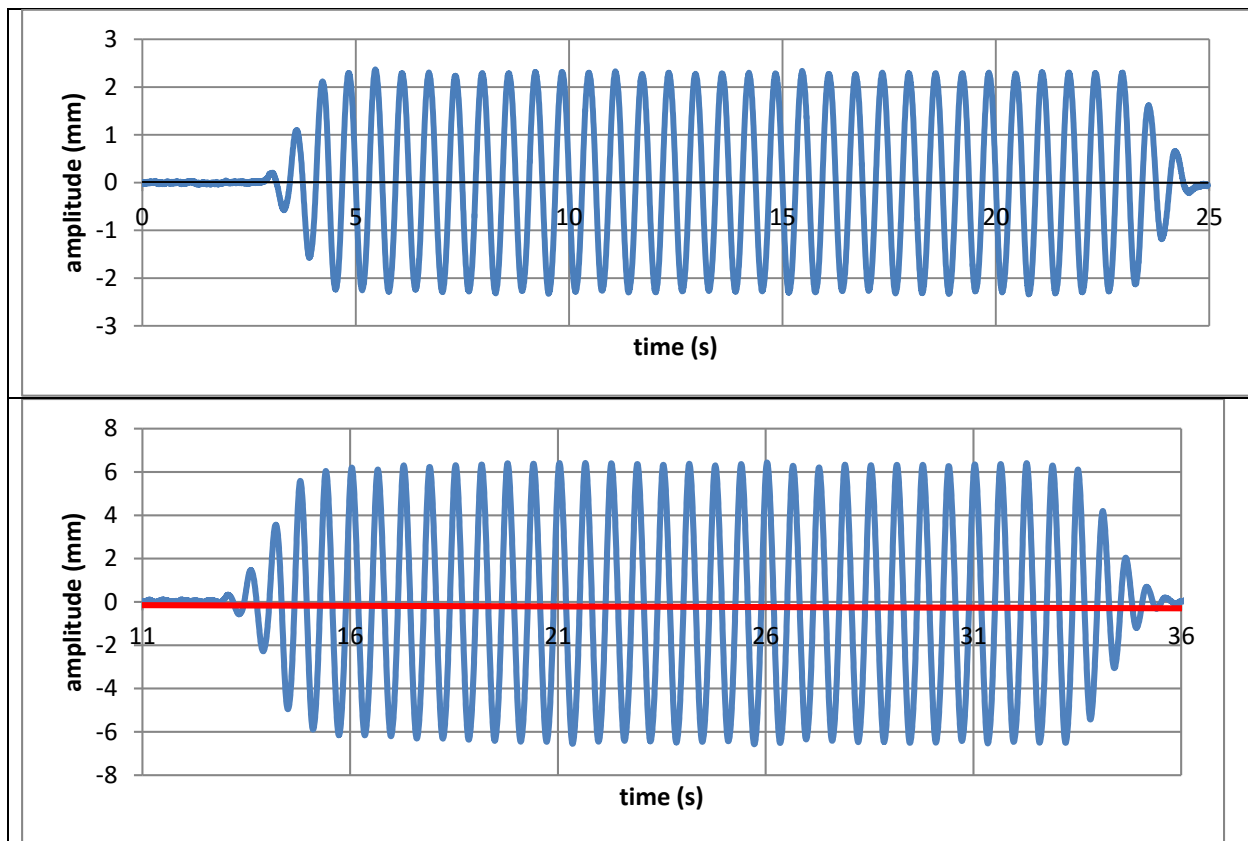


Figure 5.6. LVDT (top) vs DIC (bottom, 2nd spacer grid) data of shake table horizontal displacement for 1.5 mm, 1.8 Hz of excitation. DIC data look “pixelated” due to plotting software. Red line in DIC data indicate mean value of oscillation, ie since it is not null, the bundle oscillation is not symmetrical.

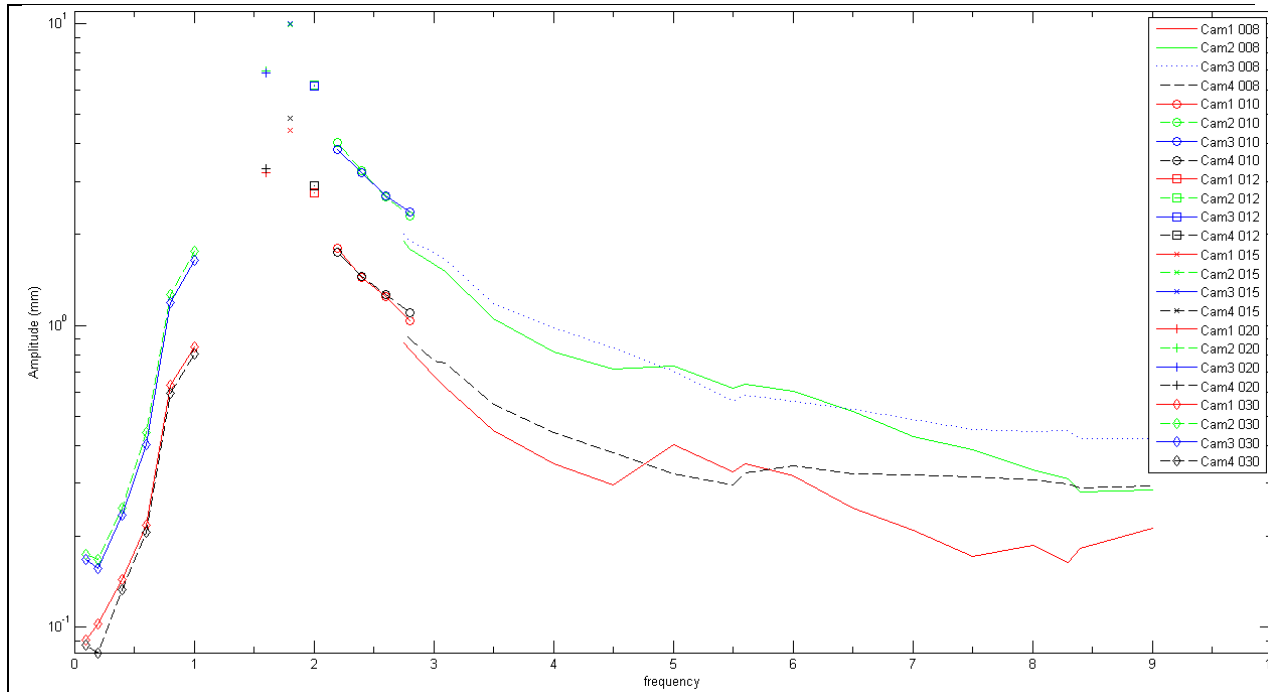


Figure 5.7. Spectral response of fuel bundle maximum displacement obtained with DIC for the first series of test. The maximum displacement for each spacer grid is reported.

Figure 5.8 shows displacement response spectra for two sample motions. These response spectra confirm that the fundamental frequency of the system was around 1.8 Hz. Additional analysis of the results is currently underway to further investigate the reason for differences in experimentally obtained results with those computed in finite element simulations. It is believed the initial geometry of the fuel assembly had a profound effect in this regard.

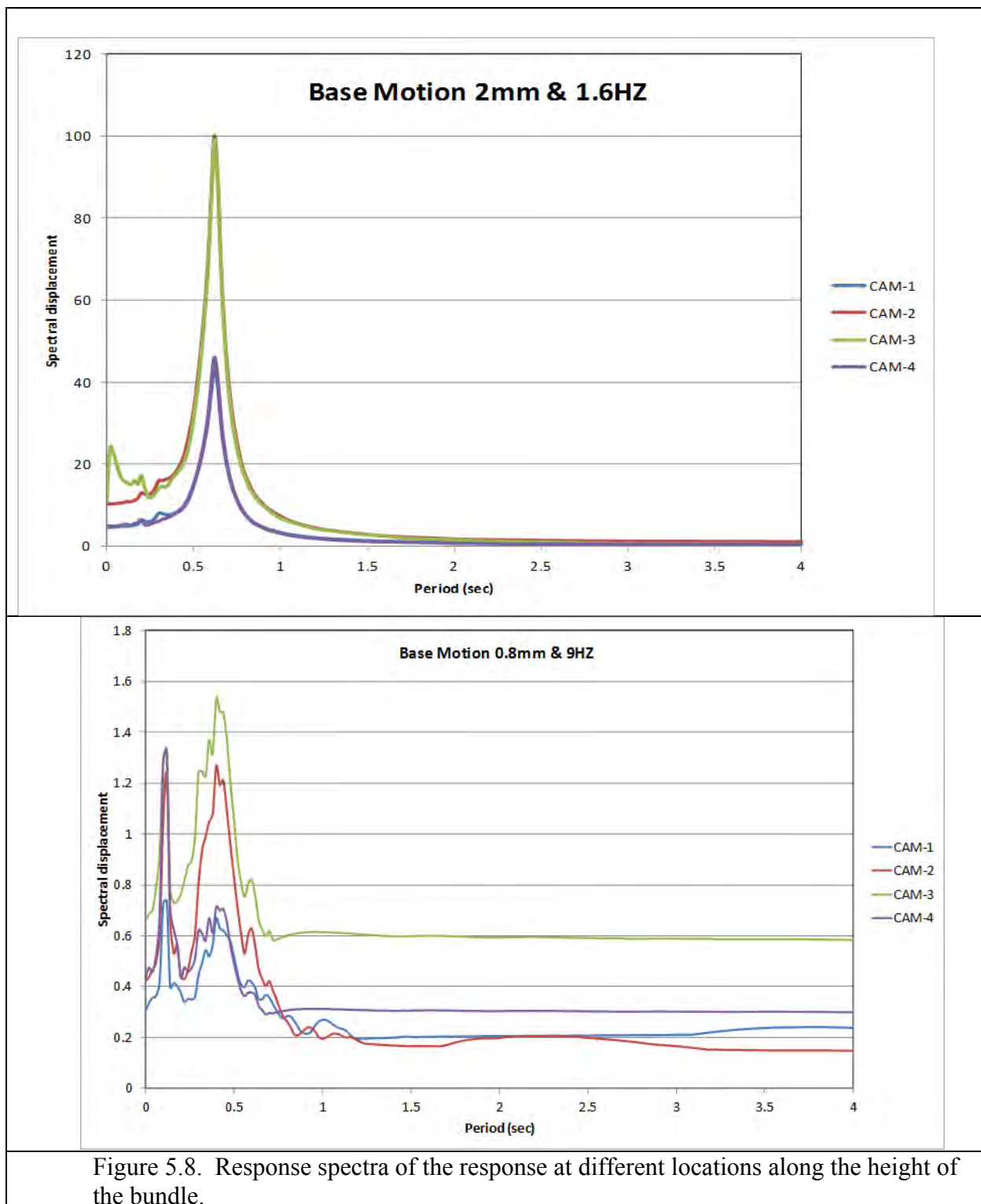


Figure 5.8. Response spectra of the response at different locations along the height of the bundle.

Shake Table Tests, series 2 (After BC modification)

The second series of tests were done after the fuel rods were subjected to tension and stretched from the top of the assembly to correct the bundle shape. Measurements were conducted in

average increments of 0.5 Hz between 0.1 and 6.0 Hz. Similar to first series of tests, the forcing amplitudes varies between 0.8 and 3.0 mm. The experimental results show that the natural frequency of the structure went up to around 2 Hz, figure 5.9. Figure 5.10 shows the response spectra of displacements for one of the base motions.

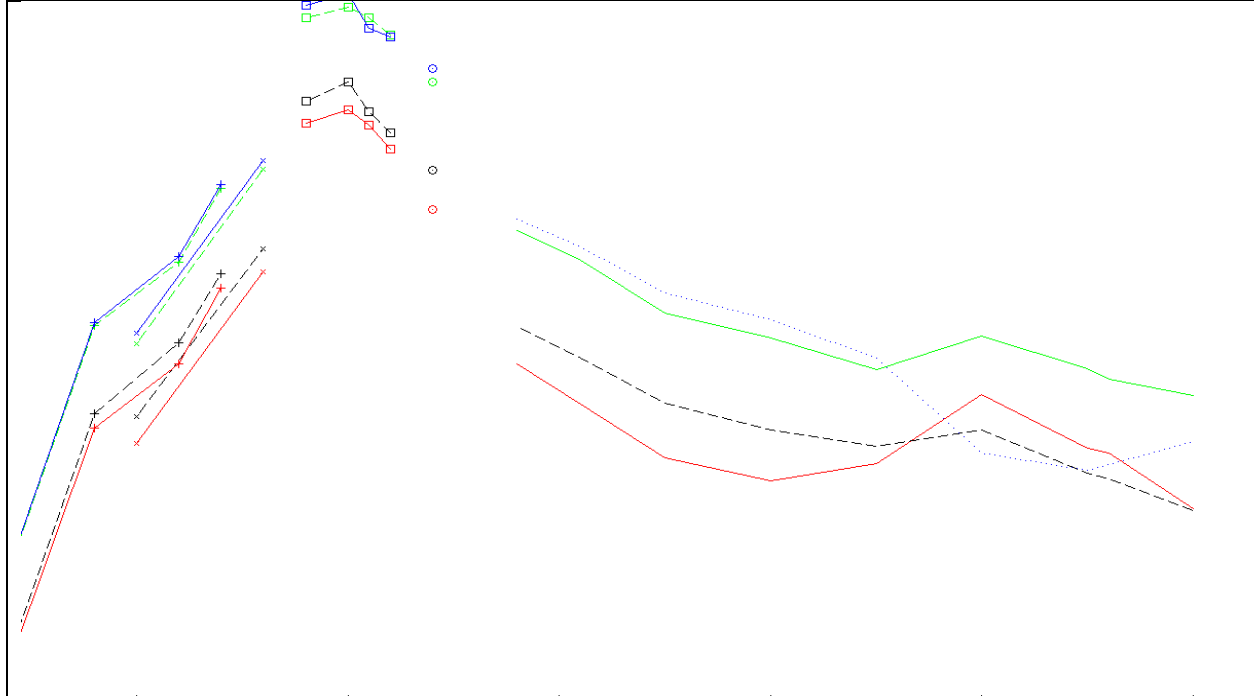


Figure 5.9. Spectral response of fuel bundle maximum displacement obtained with DIC for the second series of tests.

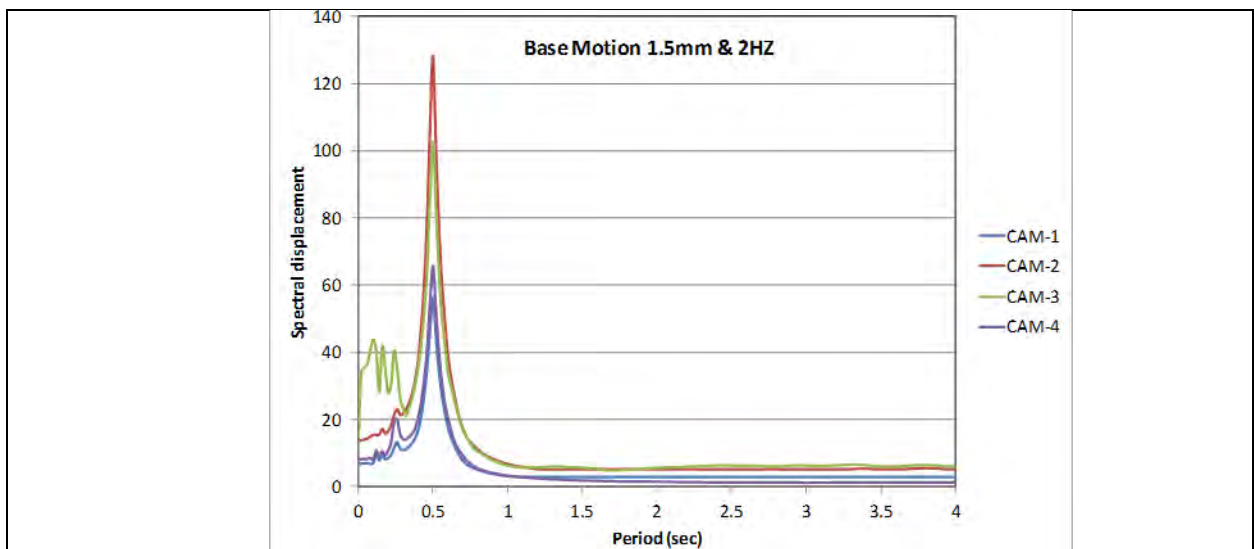


Figure 5.10 Response spectra of displacements measured at different locations along the height of the bundle in the second test series. High frequency signal on camera 3 is an artifact due to scratches on the shroud inner wall. This will be corrected for in the future.

Revised analytical model based on new boundary conditions

The finite element model was modified to be consistent with the real boundary condition of the fuel bundle. In the new model, the top and bottom supports were moved to the level of first and last spacer grids. For more consistency, at the level of supports, some translational and rotational springs with proper stiffness were used. The results of modal analysis are presented in table 5.1.

Table 5.1. Comparison of the fundamental frequencies obtained from finite element analysis and shake table experiments

	Model1	Mode 2	Mode 3	Mode 4
Analytical Model	2.17	4.44	6.82	9.1
Experiment	2.00	4.90	5.6	8.0

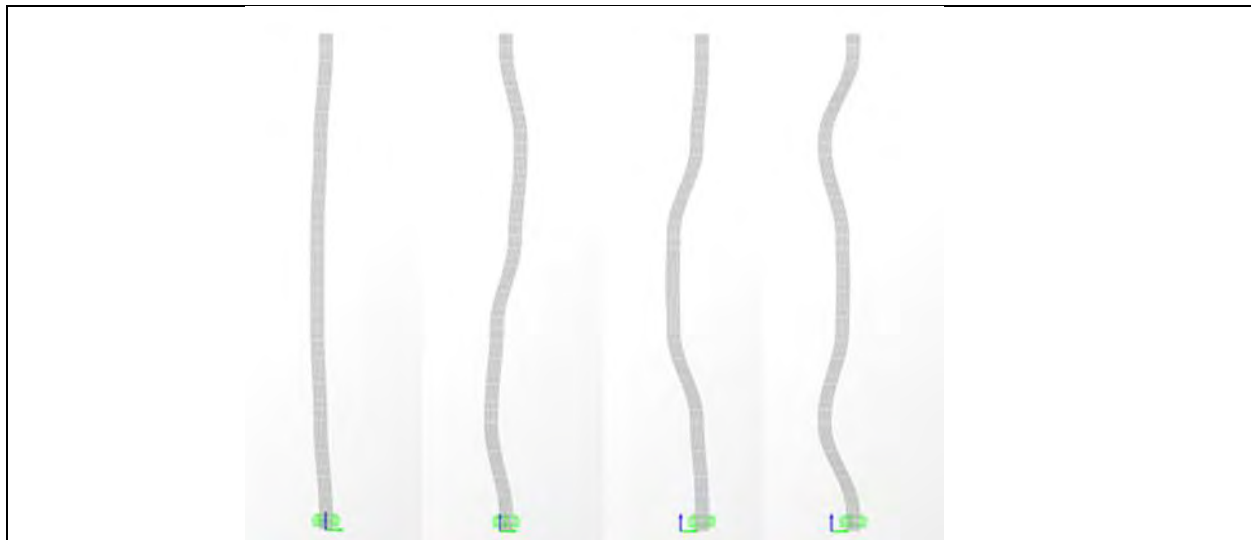


Figure 5.11. Calculated mode shapes 1 to 4 from left to right for bundle with refined boundary conditions.

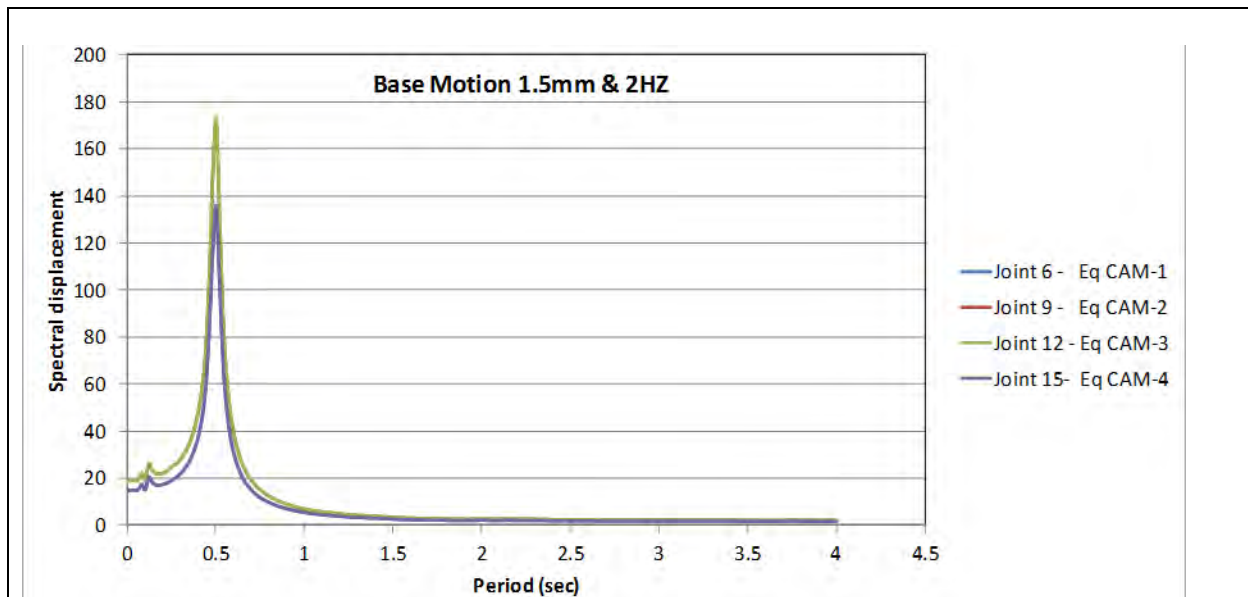


Figure 5.12. Response spectra of displacements simulated at different locations along the height of the bundle. Each curve has similar location that DIC data.

Modal shapes are shown in Figure 5.11, while spectral displacements of analytical results in Figure 5.12. They show almost the same natural period and frequencies, but have higher amplitude of displacements at the locations of cameras 1 and 4 for five percent of damping, see table 5.2. The results presented in Table 5.2 are preliminary and more refined simulations are currently being conducted to see if the asymmetric response observed in the experiments can be simulated by a more detailed model of spacer grids.

Table 5.2. Comparison between analytical and experimental results for displacements (mm)

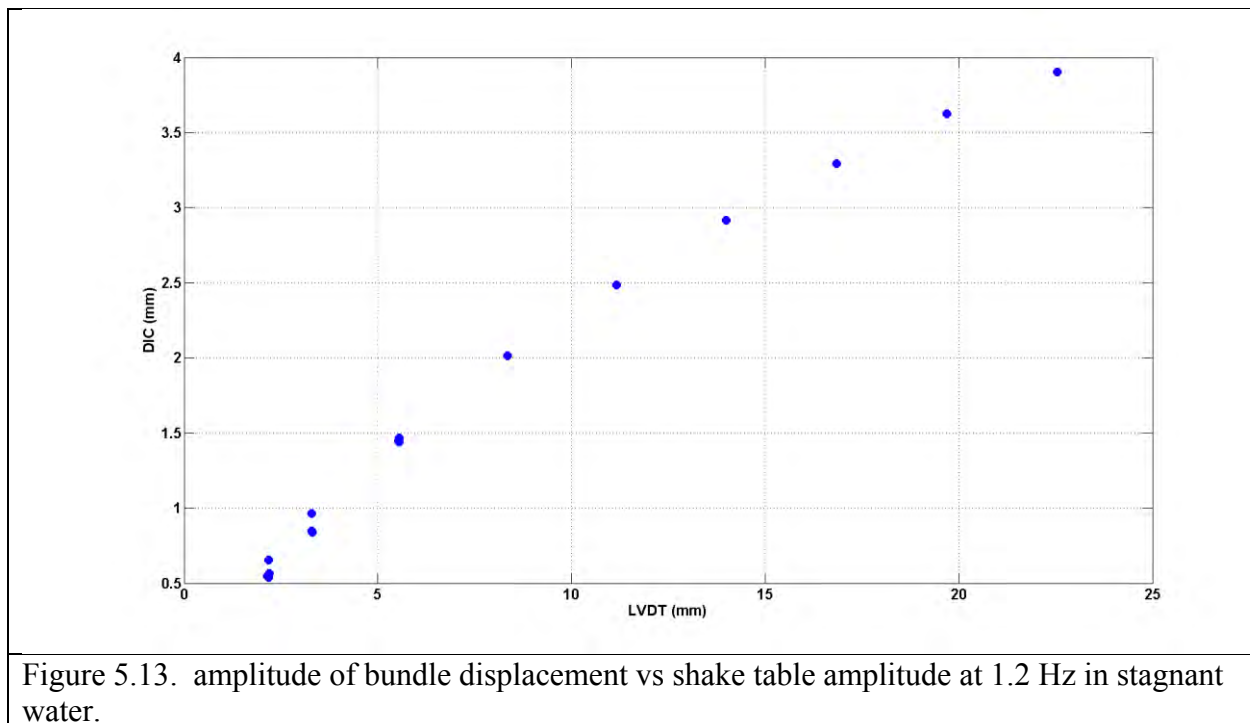
	Cam-1	Cam-2	Cam-3	Cam-4
Analytical Model	9.68	13.03	13.03	9.68
Experiment	6.83	13.69	16.52	7.85

Experiment: Initially stagnant water: flow induced by bundle oscillation

A series of tests are conducted in stagnant fluid for a range of frequencies and amplitudes. The fuel bundle has a complex geometry, and there are little to no data on what to expect from the response of the fluid. Figure 5.13 shows amplitude response of bundle measured with DIC as the frequency is kept fixed at 1.2 Hz and the amplitude of the forcing (shake table displacement measured with LVDT) is increased. More detailed analysis is necessary (looking also at cases

for other frequencies); however, the following conclusions can be drawn. The bundle amplitude increases linearly with the external forcing, for table displacement inferior to 10 mm, and then follows a different trend. This observation will be further discussed in the following sections.

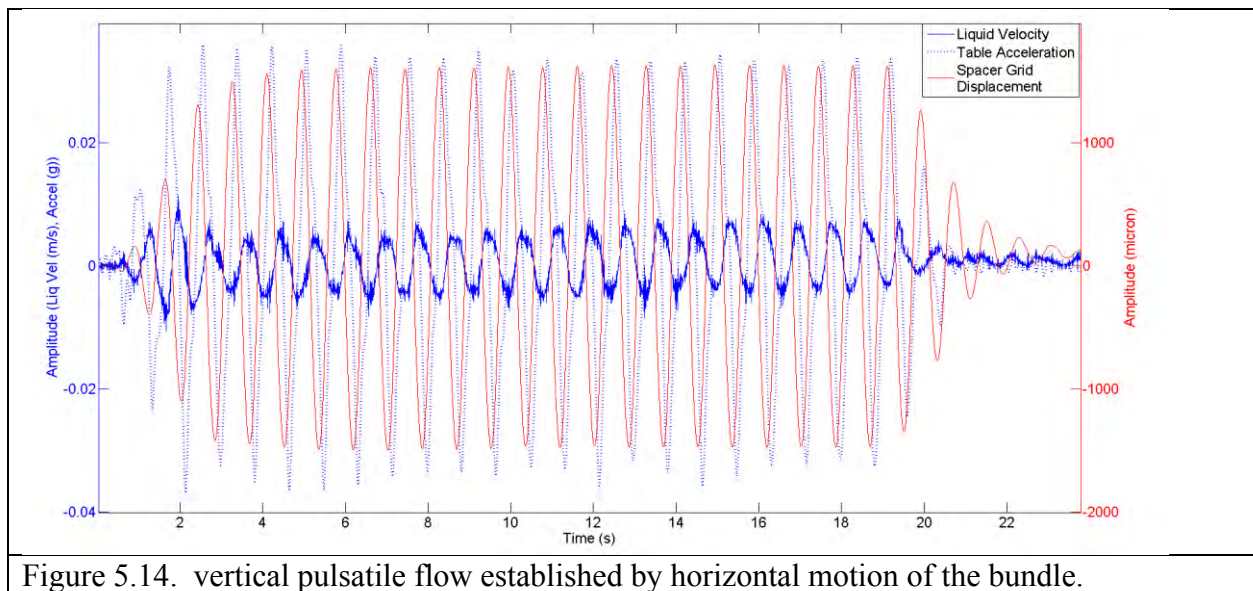
For the lower amplitude cases, the data have been reproduced three times on three different weeks to assess randomness of the process, which is why several points appear. Of this group of point it appears that for a forcing inferior to 5 mm two points are fairly close, while a third stands significantly. This is attributed to the laboratory environment. With the outside temperature increasing in March, the laboratory is now warmer and a significant stratification establishes in it. For the stagnant cases, we have been observing large convection in the test section, which we attribute to natural convection. The latter is driven by the cube of the height, and with the facility standing at 7 m tall overall, this effect is non negligible. For bundle amplitude larger than 5 mm, this effect becomes negligible and the three points collapse. Thermal stratification in the laboratory was addressed in the second phase of the experimental campaign with the oil as the working fluid by turning the stand alone HVAC system in the earthquake lab to hand. This allowed for the ducts at the top of the room to continuously output cool air and not be controlled by the thermostat at ground level where the air temperature was lower.



One unexpected behavior that we found was the establishment of a vertical pulsatile flow as the bundle oscillates horizontally. Figure 5.14 shows a time history of the velocity in the center of the bypass and the middle of the bundle and illustrate this behavior. The data were acquired at 256 Hz and the camera resolution was set at 4 MPixels. It is remarkable that we are able to record these data for more than 30 seconds and that we can start the recording again a few

second later. This would not have been possible without the new cameras we invested in for this project. On figure 5.14, the first two cycles of the flow oscillations have larger amplitudes than the rest. This behavior is observed consistently across all other data.

We are still analyzing this in greater details, but it appears the amplitude of the induced water velocity scales with the acceleration of the bundle, Fig. 5.15. It is also independent of frequency, as long as the bundle is still oscillating mainly in a first mode. We are also further analyzing the phase between the liquid and bundle motion away from the bundle. Preliminary data indicate that for small oscillations, the phase depends only on the forcing frequency. For high oscillation amplitude, the phase difference now depends also on the amplitude. This analysis will be further refined as more data are analyzed and the processing techniques refined.



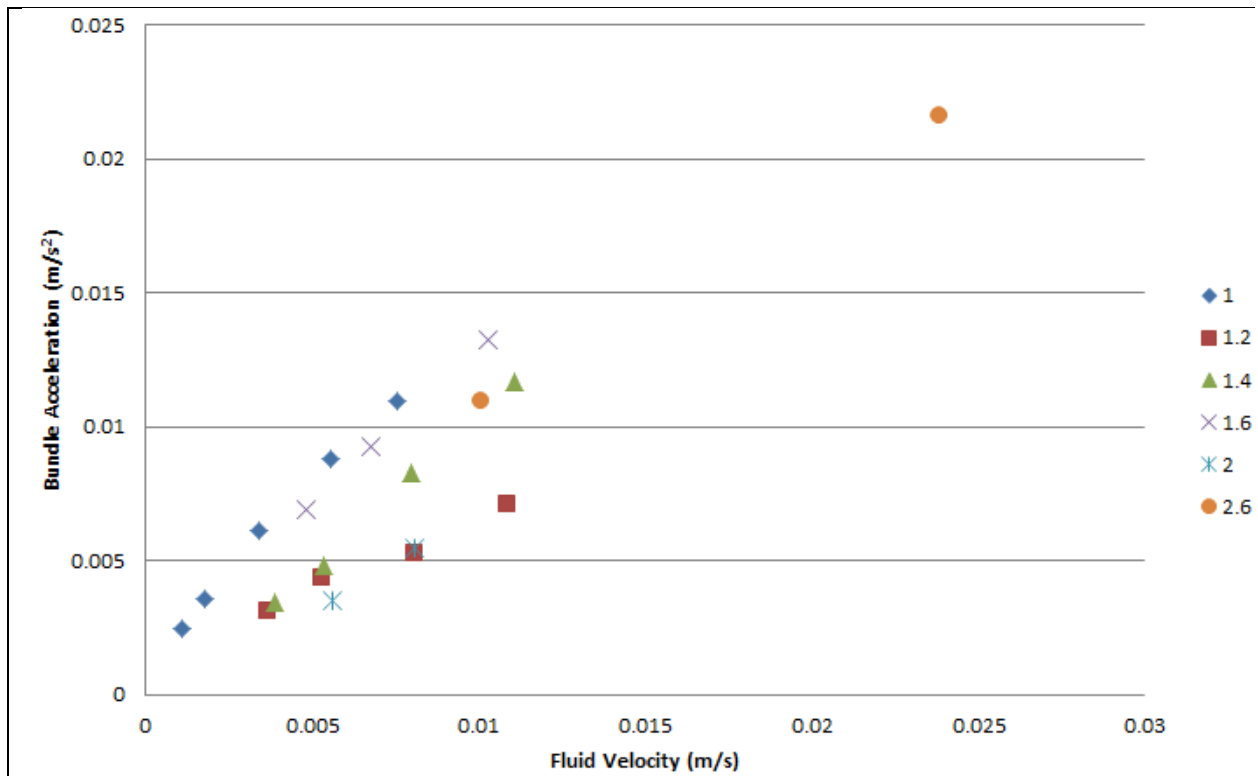


Figure 5.15. Acceleration of bundle vs. Velocity of vertical pulsatile flow.

Figure 5.16.a) shows phase averaged vertical and horizontal velocities as a function of phase angle. The latter is defined with respect to the fuel bundle oscillations, Fig. 5.16.b).

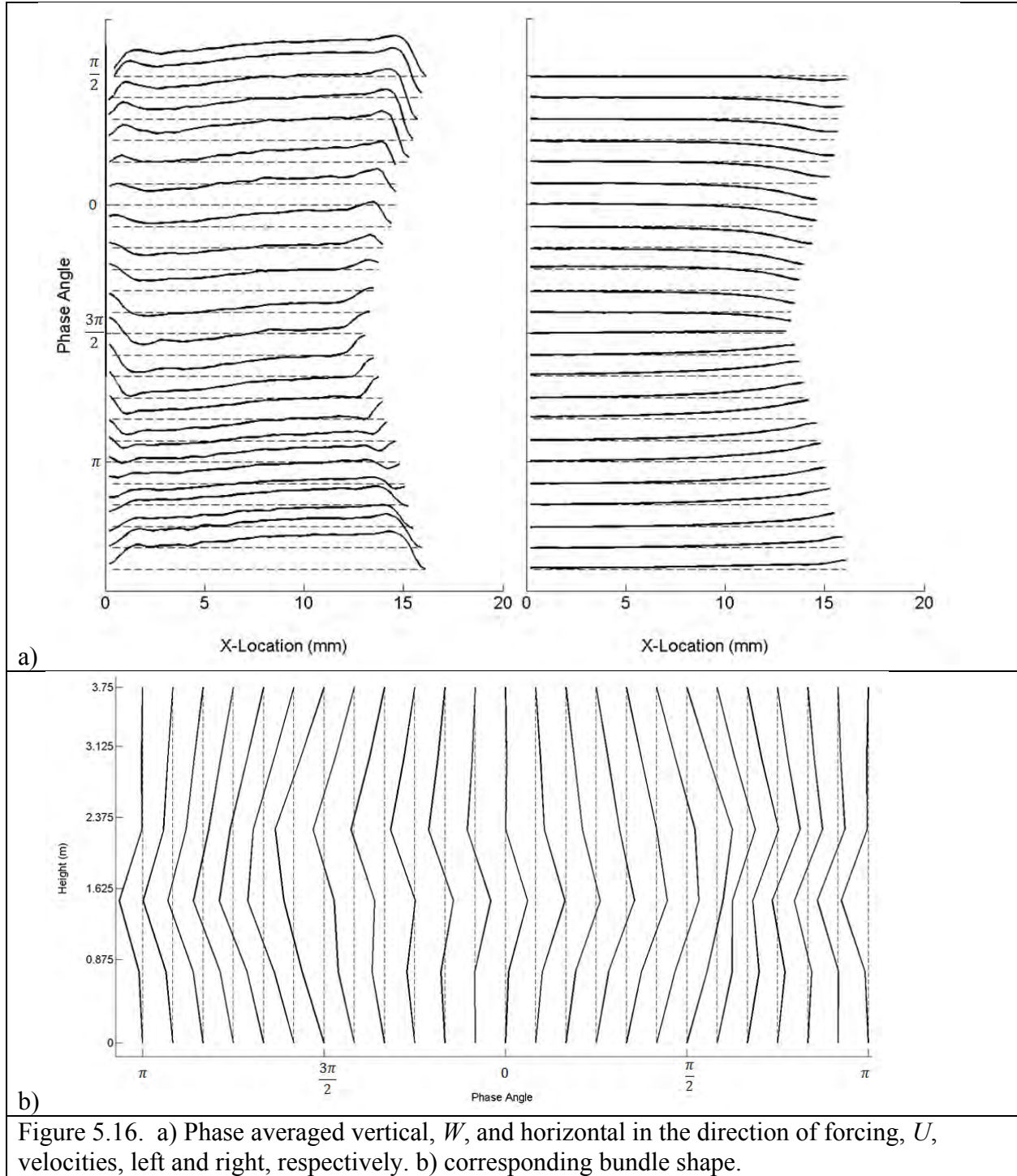


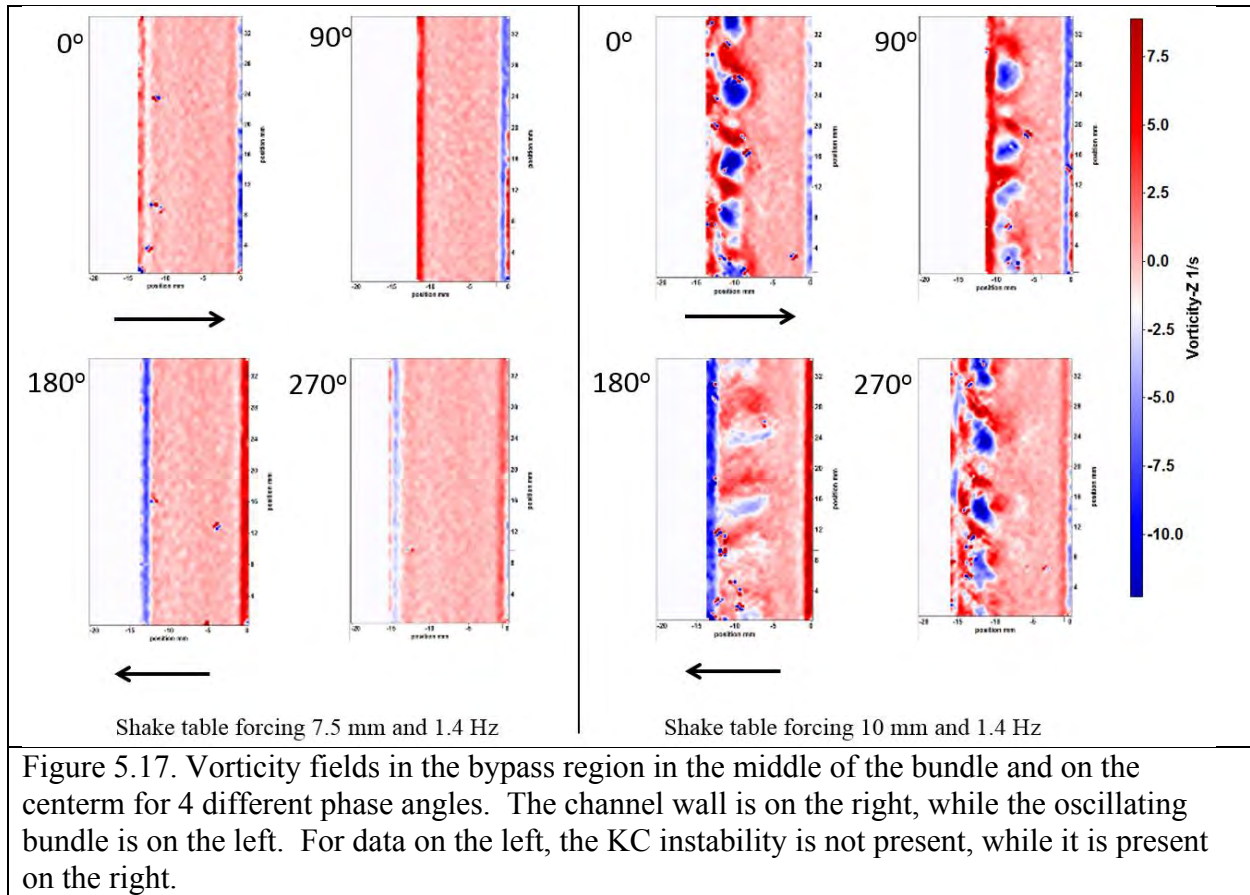
Figure 5.16. a) Phase averaged vertical, W , and horizontal in the direction of forcing, U , velocities, left and right, respectively. b) corresponding bundle shape.

Figure 5.17 shows vorticity fields in the bypass and at the center of the bundle. The laser plan is centered on the second row of rods. The vorticity is plotted as a contour plot over the velocity vector fields. The wall of the flow channel is on the left, while the bundle is on the right. No special treatment is applied near the walls, so the resolution there is limited in the (preliminary) processed data. This will be improved in the future.

For oscillations with small acceleration, the flow in the bypass is very uniform axially and away from the boundaries, Figure 5.17 left. The vorticity near the channel wall and the bundle is significantly stronger than in the rest of the flow and changes sign. This is the signature of an oscillatory viscous boundary layer there. One can therefore speculate that the bulk of the flow in the bypass is inertia driven, in contrast to the viscosity dominated flow near the walls. We are conducting a phase analysis to better determine this assumption. However, in light of this assumption, one can associate the oscillation of the bundle with a pressure wave across the flow channel. Physically, this can be interpreted in the following manner. As the bundle moves forward, a (high-pressure) stagnant point establishes itself on the “front” of the bundle, while in the back of the bundle, viscosity forces a lower pressure point. Hence one can speculate that as the bypass region is closing, above the bundle mid-height the flow will be driven upwards and downwards below the mid-height. With the supplemental funds received we are working on verifying this assumption with the data acquired with our 3 flying PIV systems with locations in the middle of the bundle, above spacer grid #2, and above spacer grid #4 as defined in Task 2-1. This pressure wave also indicate that a cross flow establishes through the bundle as it oscillates that is better observed in Section 5.7.

For low acceleration one can therefore conclude that drag coefficient on the bundle will take a complex shape that has not anticipated before. Their development will be reserved for future work. As the oscillation acceleration increases, flow instabilities appear behind the last row of rods. The observed instability is consistent with reported flows for super-critical Keulegan-Carpenter number introduced in section 5.1. Figure 5.17 right shows signature of these instabilities. There are regularly spaced regions of positive and negative vorticity.

Horizontal PIV planes, such as Figure 2.5, are also beneficial to understand 1- viscous boundary layer behavior in this oscillatory flow and 2- the onset of this instability due to rod oscillations.



We analyzed other cases where the KC is present, they are presented in figure 5.18. They show a decrease of the vortices spacing with increasing β parameter.

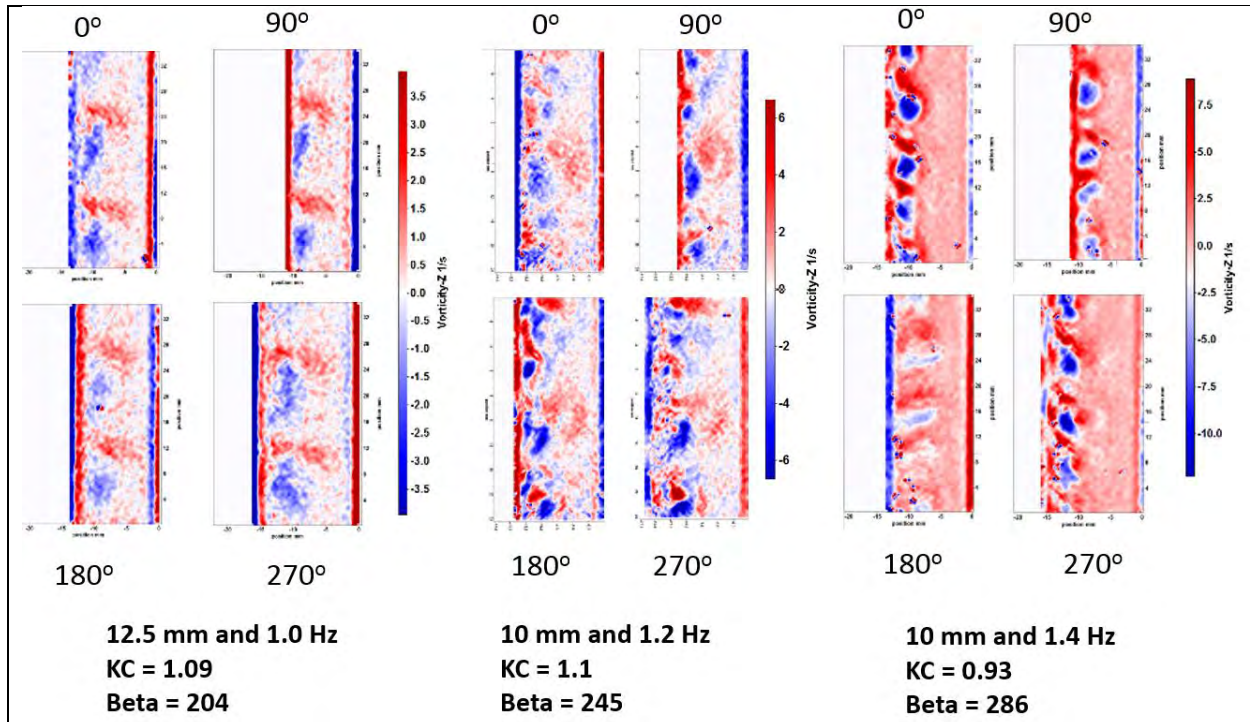


Figure 5.18. secondary instability as a function of KC and β . The orientation is the same than on figure 5.17.

From these data, one can start to establish a criteria for occurrence of the instability. This analysis is still preliminary, but is presented in figure 5.19. Here the bundle displacement follows a linear trend with shake table forcing up the critical KC value that is the colored data point for each respective shake table forcing frequency. After the critical KC value it is apparent that the bundle dynamics diverge from this linear trend.

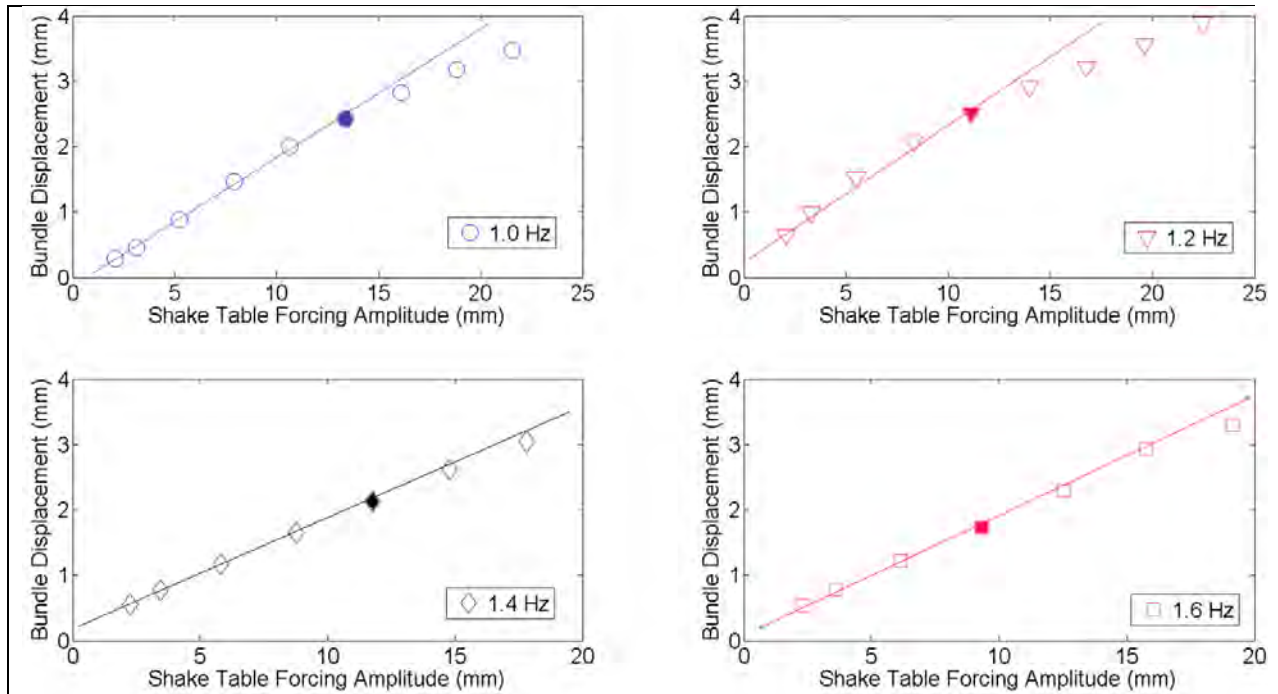


Figure 5.19. Bundle displacement vs. Shake Table Forcing Amplitude at Fixed Frequencies in water. The colored point shows the occurrence of the instability.

Experiment: Initially stagnant binary mixture: flow induced by bundle oscillation

As discussed in Task 1-3 in the 4th quarter of FY 2015 the working fluid was changed to a binary mixture of P-cymene and cinnamic aldehyde that is index matched with acrylic to allow for measurements both in the bypass around the fuel bundle and within the fuel bundle itself. Fig. 5.20 shows a sample of these measurements in still fluid near the first mode frequency at 1.3 Hz with a 5 mm forcing amplitude which is at the critical KC value in this fluid. Again the critical KC value is found to define the occurrence of this instability, however, the amplitude of forcing is much lower here due to differences in the density ($\rho_{water} = 1000 \text{ kg/m}^3$, $\rho_{P-cym} = 854 \text{ kg/m}^3$) and kinematic viscosity ($\nu_{water} = 10^{-6} \text{ m}^2/\text{s}$, $\nu_{P-cym} = 9.4 \times 10^{-7} \text{ m}^2/\text{s}$) of water and P-cymene.

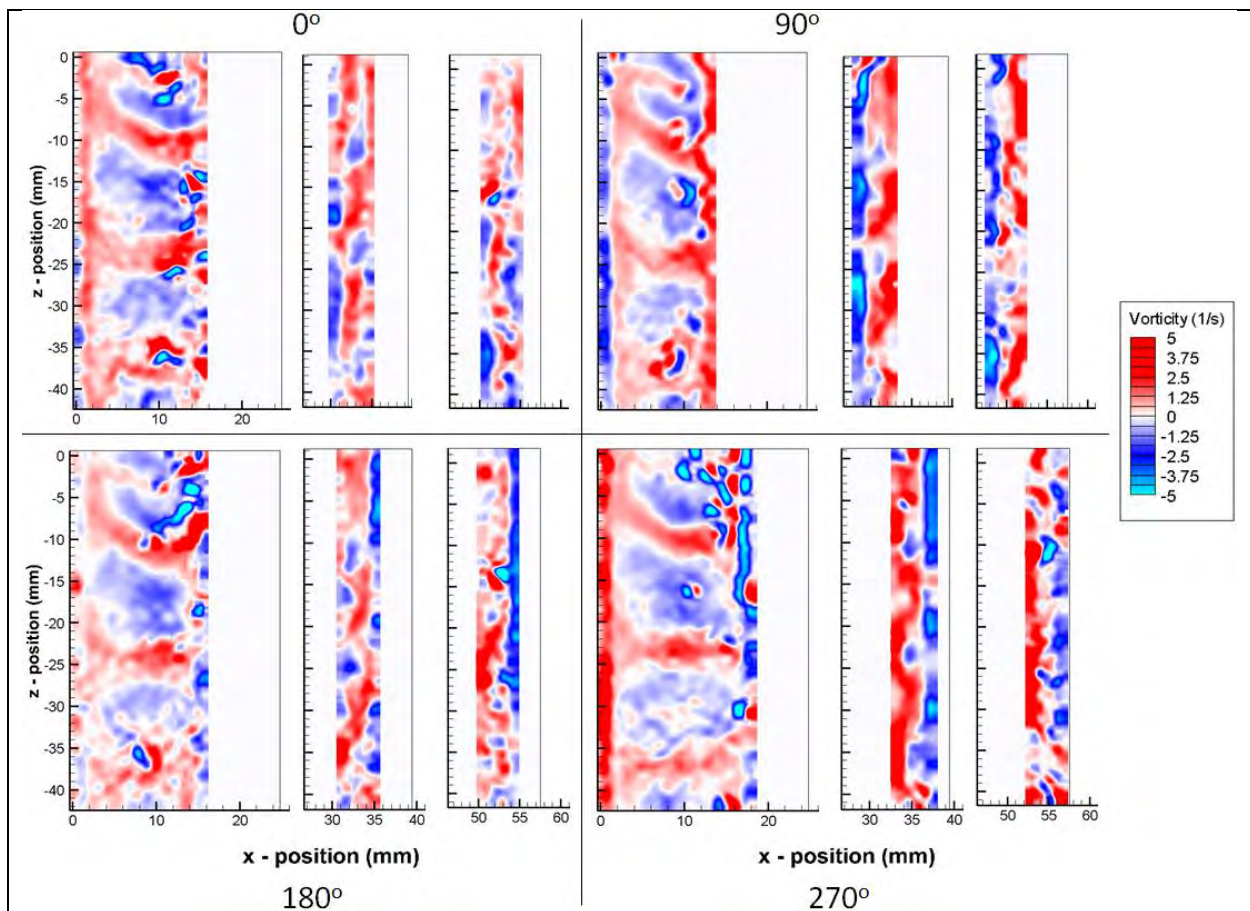


Figure 5.20. Stagnant Fluid Pulsatile Flow Velocity vs. Shake Table Forcing Amplitude at Fixed Frequencies. The last point shows the occurrence of the instability.

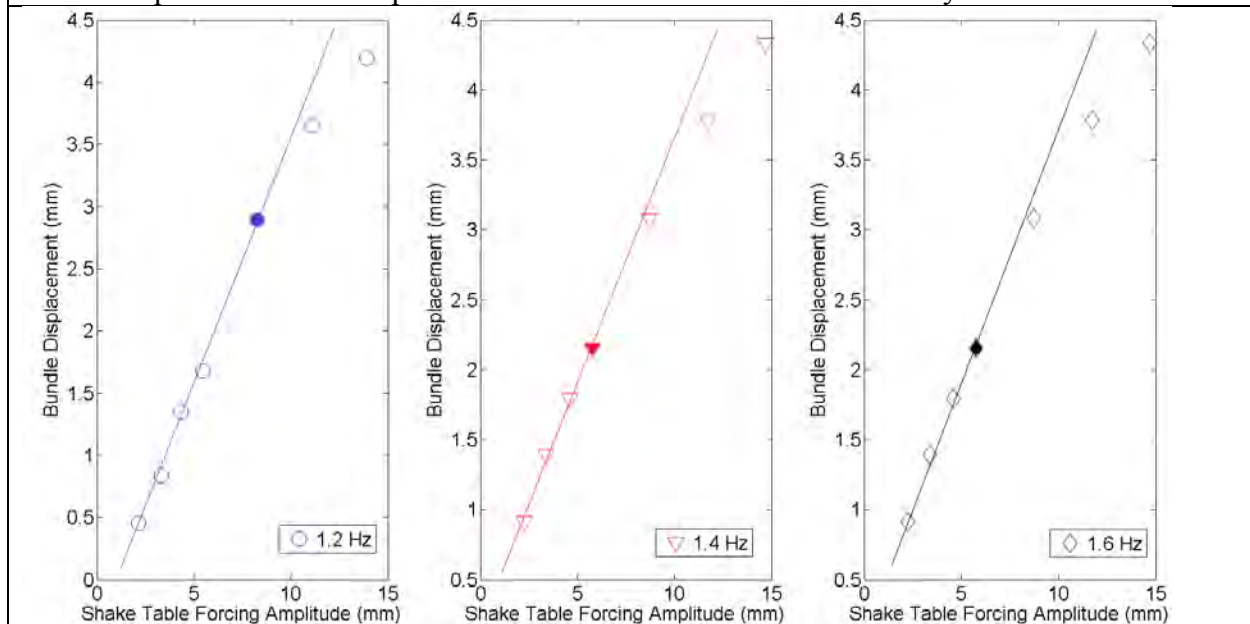


Figure 5.21. Bundle displacement vs. Shake Table Forcing Amplitude at Fixed Frequencies in binary mixture. The colored point shows the occurrence of the instability.

Experiment: 3D data of velocity in the bypass

We took advantage of the scanning system implemented with the two planes PIV system to acquire 3D data of the velocity in the bundle. Figure 5.22 shows the vertical, W , and horizontal in the direction of forcing, U , velocities in a horizontal plane. Figure 5.23 shows where the data of Figure 5.22 were acquired with respect to the bundle oscillation cycle. An extended abstract was submitted to the ANS conference on the topic.

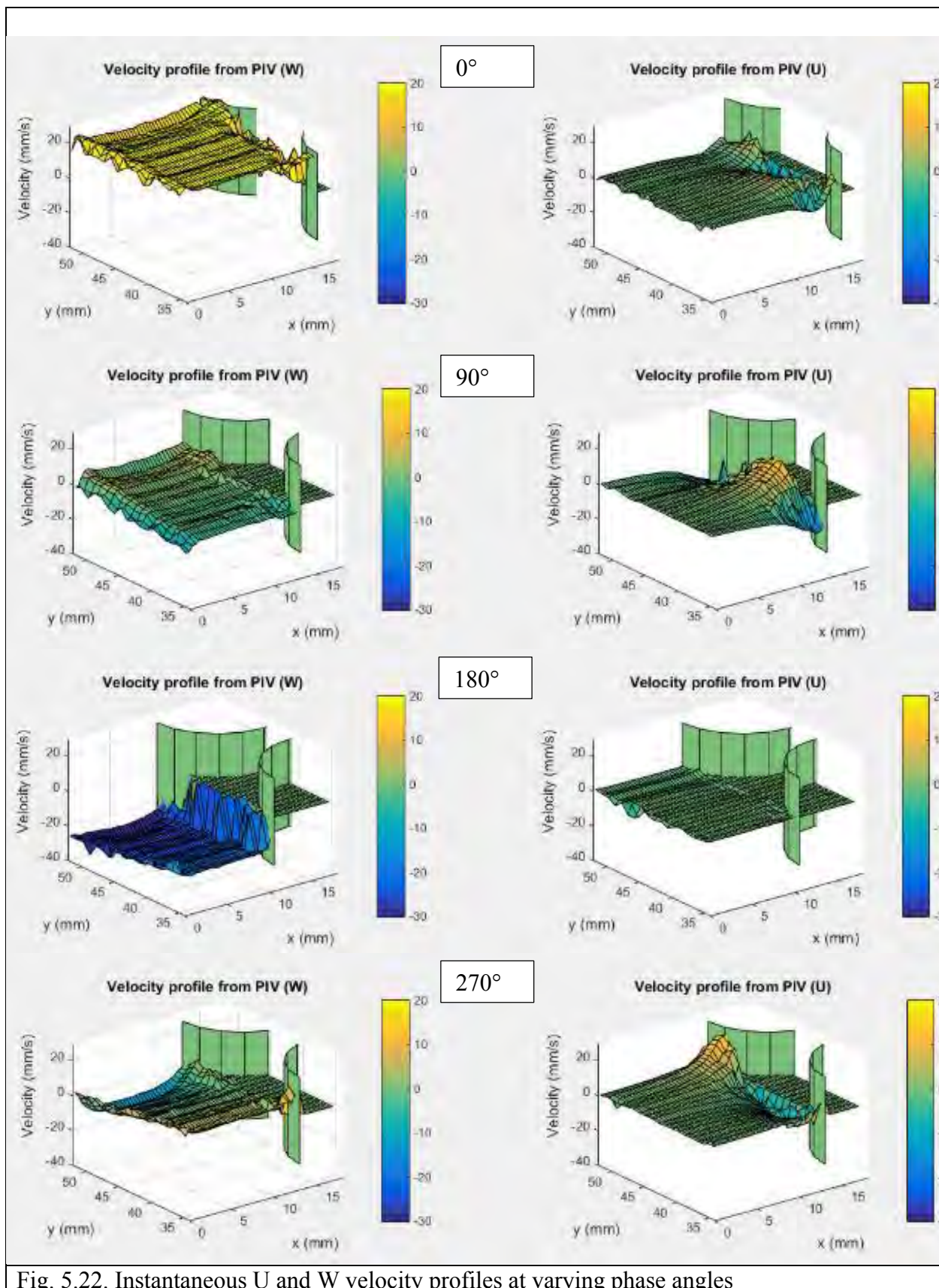


Fig. 5.22. Instantaneous U and W velocity profiles at varying phase angles

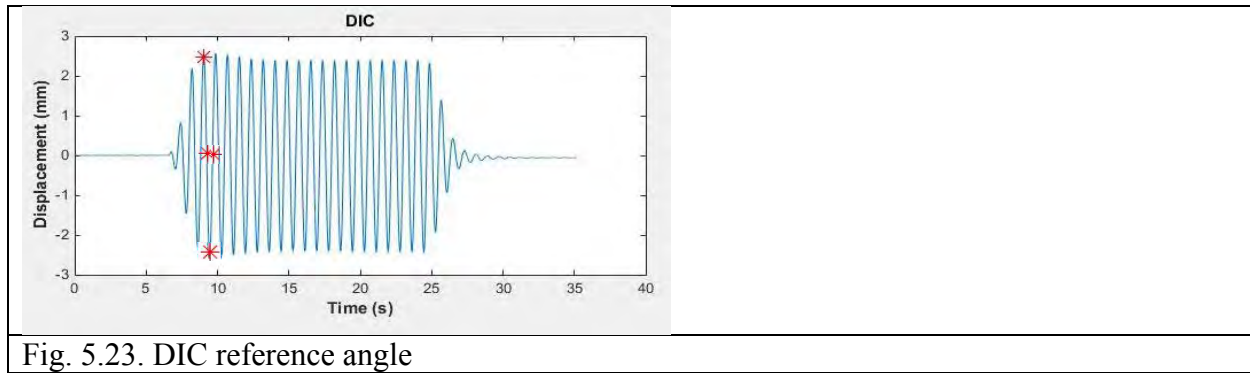


Fig. 5.23. DIC reference angle

Experiment: 1m/s axial water flow: secondary flow induced by bundle oscillation

With the PIV scheme defined in Task 2-1, we analyzed data at 1 m/s extensively and have been accepted for publication in Experiments in Fluids. We confirmed the behavior reported by the CEA that a pulsatile flow developed as the bundle oscillates, fig. 5.25. This might be related to the same mechanism than observed in stagnant flow. However, our velocity field data enabled us to remark that turbulent kinetic energy (TKE) was produced as the bundle oscillates, a value that could not be captured with the CEA pointwise measurements. The TKE production is best seen in the last graph of fig. 5.25 that shows the rms of the fluctuating velocity. The data are summarized below.

To obtain data and statistics in static versus shaking environments, the PIV frames are acquired in the following fashion for the data with axial flow. The flow loop is started prior to activating the shake table to establish a steady flow. The table is then activated at which point the table is supported solely by hydraulic actuators. Data acquisition then starts and stays active for the next phase of the experimental run where for the sample data reported here the shake table is forced with sinusoidal oscillations at 17.5 mm and 1.6 Hz.

Each run consists of sinusoidal forcing of about 30 cycles of fixed frequency and amplitude. Time resolved PIV data are recorded at 2,048 fps at 1 Mpixel. At this speed, data are treated as time series when processing them. Nearly 9,000 images are recorded prior to beginning the table oscillations. While the table oscillates another 29,000 images are acquired; the shake table is then stopped and an additional 2,000 images are recorded to compare to the initial flow. This corresponds to a run length of 19.5 s and 39,921 images, which result in 39,920 vector fields. The magnification attained with the current setup is 0.28, to illuminate the PIV particles within this FOV (21.2 mm \times 7.19 mm) without saturating the camera sensor, 0.47 mJ per pulse are launched into the fiber. This is well below the determined laser damage threshold for 100 μ m fibers of 3.5 mJ per pulse.

The measurements presented here are from the vertical PIV plane, Fig. 5.24, which is approximately 2.4 m above the entrance and is approximately 15 mm above the fourth spacer grid from the bottom. This plane captures the $(U(x,z,t), W(x,z,t))$ velocity components. The field of view here is between the inner acrylic channel wall ($x = 0$) and the surface of one of the rods that comprises the fuel bundle which is a moving boundary. The waists of each laser sheet are centered in the middle of the region between the wall and first rod. The Rayleigh range, Tab., is about half of the horizontal field of view which for static conditions is 14.6 mm; this guarantees that the investigation plane is sufficiently thin and uniform. The magnification is also selected such that one full rod is in the PIV view, which enables to calibrate PIV by giving correspondence from pixel to millimeters. Here it is $25 \mu\text{m}/\text{pixel}$.

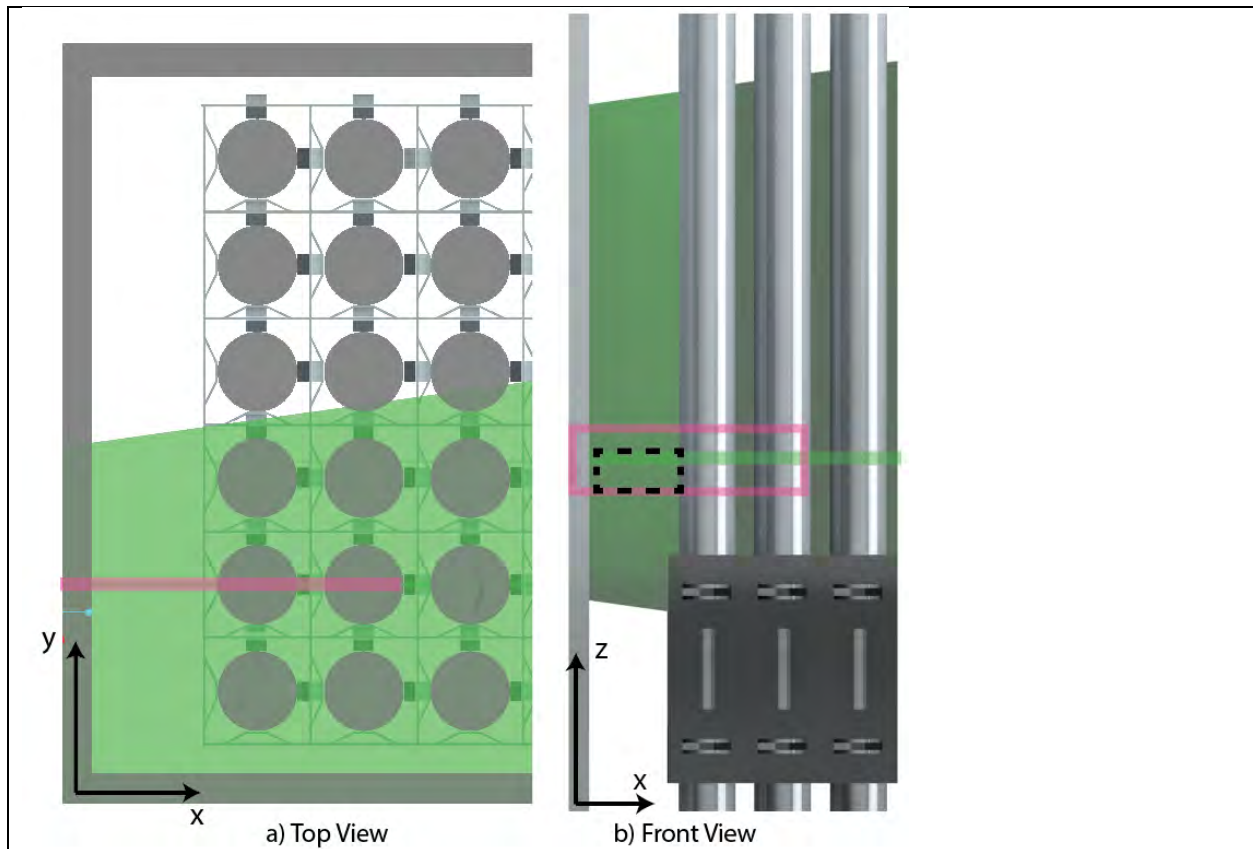


Fig. 5.24. Definition of measurement region- (a) top view portraying vertical plane alignment with center of rod 2, measurement region shown in solid red line (b) front view, vertical PIV plane measurement region shown in red outline, processed PIV FOV shown in black dashed line prior to shaking, lower boundary 15 mm above spacer grid 2

Mean axial flow goes from the bottom to the top of the frame. The Reynolds number at the entrance is defined in the section on the scaling analysis and is found to be $Re = 1.9 \times 10^4$ for a mean velocity before the bundle of 0.74 m/s. A second Reynolds number is defined that is based

on the hydraulic diameter of the bypass region where this measurement is taken, here c_x is the channel width and c_y is the channel depth.

$$Re_b = \frac{2W c_x c_y}{(c_x + c_y)\nu}$$

Eq. 5.1

The local mean flow velocity in the bypass is 1.62 m/s that corresponds to $Re_b = 59.2 \times 10^3$. The higher velocity at this elevation is a well-known effect in fuel bundle testing. The lower pressure losses in the bypass region compared to inside the bundle leads to the mean flow rate through the bundle to decrease with axial development whereas the flow rate increases in the bypass region.

To accommodate for a moving boundary in the field of view for the PIV processing the following steps are taken. In these PIV images on the right side of the domain is the rod wall which oscillates from the shake table forcing. Thus prior to cross correlation processing, an algorithmic mask is utilized to automatically define the moving boundary and the PIV interrogation domain. In present PIV processing, no special treatment is applied near the walls. The edge of the first interrogation window corresponds to the fixed wall location. On the moving side, windows that are at least 60% in the flow domain are processed. At near first mode resonance the rod wall in the PIV field of view oscillates about the neutral axis +2.70 mm and -2.47 mm, or between +19% and -17% of the rod diameter D . PIV processing consists of four-passes scheme, with interrogation window starting at 96×96 pixels and the final deformable window 32×32 pixels in size with 50% overlap. This satisfies criteria specified by Adrian [1] for the ratio of the displacement of particle image pairs, $|\Delta X|$, to interrogation size, d_I , $|\Delta X|/d_I \leq 0.25$ for the current magnification and data acquisition rate. The final pass results in 56×18 vectors per frame with a spatial spacing of 0.39 mm between vectors for velocity fields when the bundle is in the neutral position. This is of the order the laser sheet thickness.

To display and interpret the data, the velocity is decomposed into a mean and fluctuating components. The averaging procedure is different for data acquired for static (prior to shaking) or forced cases. For static case, the instantaneous velocity, \mathcal{W} , is decomposed into a time averaged velocity, \bar{W} , and fluctuating, w , components following a Reynolds decomposition. Here the derivation is given for \mathcal{W} , but the same applies to \mathcal{U} .

$$\mathcal{W}(x, z, t) = \bar{W}(x, z) + w(x, z, t)$$

Eq. 5.2

Once the shaking starts a secondary oscillatory flow develops and becomes stable. As a result, a phase averaged mean velocity, \hat{W} , is determined for each point along the mean cycle (as a

function of the phase angle, θ), and averaged over N cycles. It is then subtracted from the instantaneous velocity and leads to fluctuating velocity, \hat{w} .

$$\mathcal{W}(x, z, t) = \widehat{W}(x, z, \theta) + \hat{w}(x, z, t) \quad \text{Eq. 5.3}$$

with

$$\widehat{W}(x, z, \theta) = \frac{1}{N} \sum_{i=1}^N \mathcal{W}(x, z, t = t_o + (\theta + 2\pi i)T) \quad \text{Eq. 5.4}$$

where t_o is the time at which phase averaging begins, T is the fundamental period of the oscillating flow.

Of greater interest than the fluctuating velocity here, its root mean square (RMS) for the axial velocity is computed, w' and \hat{w}' for static and forced cases, respectively. This statistics shows the variability of the fluctuating velocity and \hat{w}' is a particularly practical statistics to give a first indication of turbulent kinetic energy levels over a forcing cycle.

To provide a baseline to analyze the data during forcing, static velocity data are presented first.

Fig. 5.24.a) shows the time history of the oscillations of the rod wall extracted from the PIV images. For three points within the bypass, time histories for \mathcal{W} are presented, Fig. 5.24.b) as well as for rms, Fig. 5.24.c). All the time-scales are identical in Fig. 5.24. The three points traverse the width of the bypass channel at the mid-height of the PIV field of view with the first point at 3 mm from the inner channel wall displayed in red, and the second and third points at 7 mm and 10 mm from the wall shown in green and blue respectively. In all of these images the colored lines are filtered data where a low-pass filter with a cutoff frequency of 6 Hz has been applied, while gray or black lines are the raw data. In Fig. 5.24.c), for each case the RMS of fluctuating velocities have their respective mean velocity prior to shaking added so that they appear on the same height as that of the filtered instantaneous velocity.

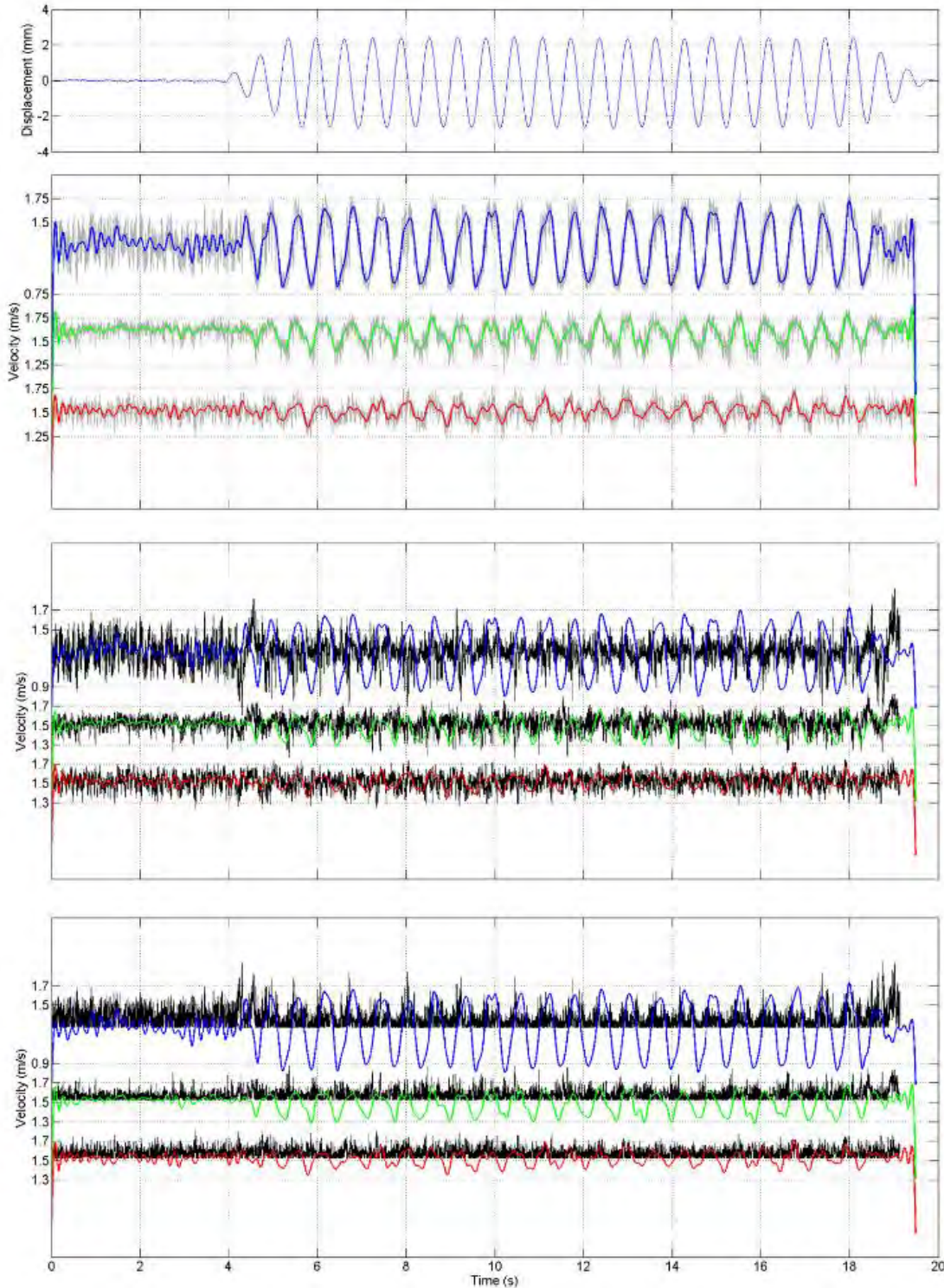


Fig. 5.24. Time series for 39,920 PIV fields, from top (a) displacement of rod wall extracted from PIV images, (b) instantaneous axial velocity \mathcal{W} in grey with 6 Hz low pass filtered data in colored lines over-imposed at 3 points in channel; red = 3 mm, green = 7 mm, blue = 10 mm from the channel wall, and (c) filtered data for 3 points with RMS velocities in black for each respective point.

From Fig. 5.24, two distinct regions in these time series are noticeable. The first from $t = 0$ to $t = 4.3$ s is the static case prior to the shake table starting, after which sinusoidal oscillations in bundle and \mathcal{W} are apparent. This latter behavior will be the focus of the next section.

In static case, small oscillations of the bundle are noticeable on Fig. 5.24.a). They are of amplitude less than $100\text{ }\mu\text{m}$ and due to turbulence. These vibrations most likely find their source at the spacer grids that are the biggest contributors to pressure drop and turbulent kinetic energy production in a bundle.

The mean velocity and RMS of fluctuations are similar for both points nearest to the wall. The third point, closest to the bundle, has a lower mean velocity; the RMS of velocity fluctuations, w' , are also significantly larger there. This is likely the signature of the spacer grid wake.

The mean axial velocity profile, $W(x)$, clearly shows the spacer grid wake, Fig. 5.25. In this profile, from left to right, the boundary layer at the channel wall is first visible, followed by a region of nearly uniform velocity, which is the bulk of the flow. Starting around $x \sim 8$ mm, the mean velocity decreases to reach a minimum at $x \sim 12$ mm. It reaches a local maxima before decreasing again near the rod wall. The local velocity deficit and excess near the spacer grid has a significant influence compared to solid channel wall. Its origin lays in the geometry of the spacer grids. The straps of the latter are 2.88 mm from the rod wall at the rod center, which corresponds to $x = 11.92$ mm, and create a shear layer in the spacer grids wake, Fig. 5.26. The openings in the vertical direction along the strap are likely to contribute to the large velocity gradient observed on the bulk side of the wake.

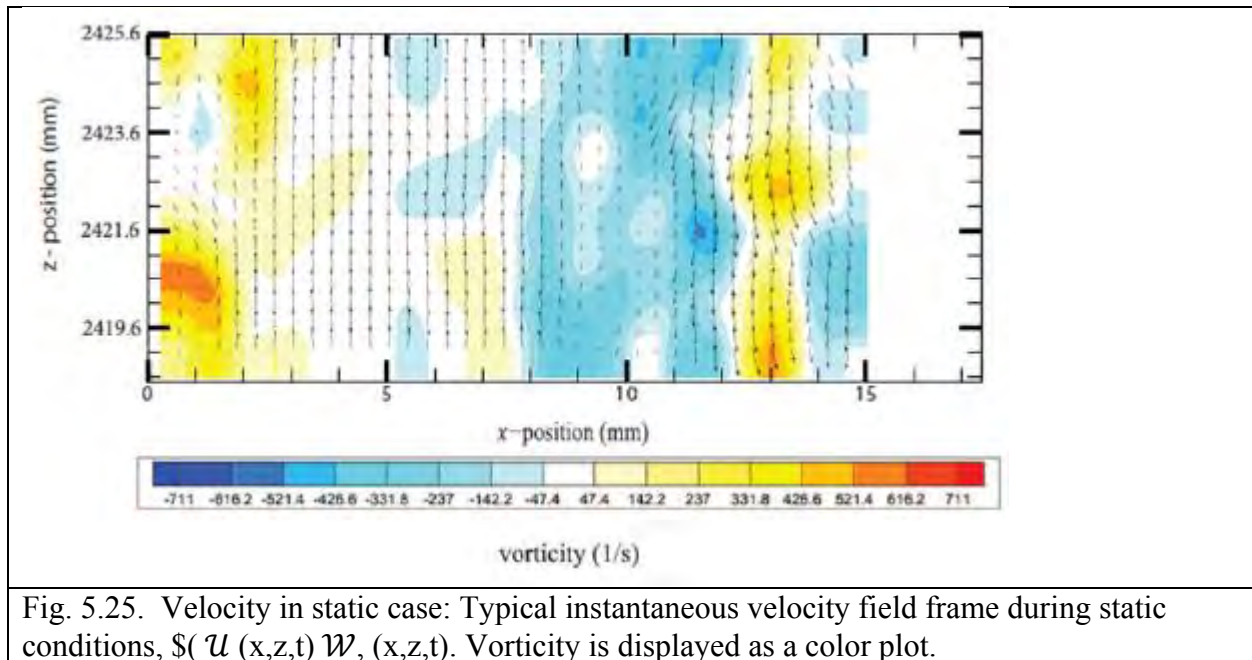


Fig. 5.25. Velocity in static case: Typical instantaneous velocity field frame during static conditions, $(U(x,z,t), W(x,z,t))$. Vorticity is displayed as a color plot.

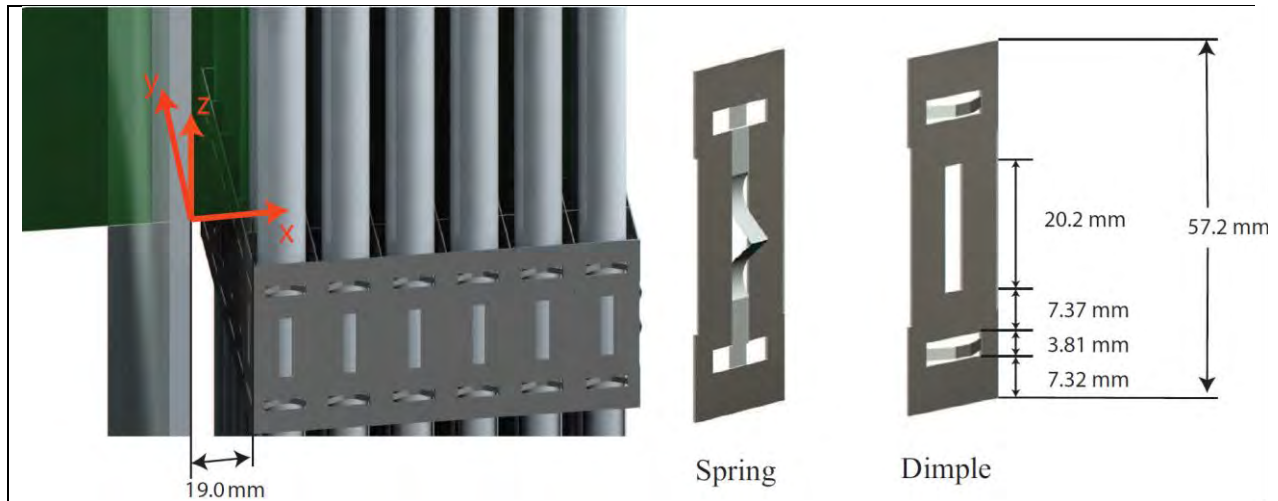


Fig. 5.26. Vertical plane measurement region and details of spacer grid design.

This shear layer is best visualized with velocity and vorticity fields, Fig. 5.25. On this figure, a Lagrangian averaging is performed (a constant velocity is subtracted to the whole frame) to assist in identifying flow structures. In fact, two columns of regularly spaced vortices are noticeable on the frame, at location $x \sim 11$ and 14 mm, which are boundary layers that develop along the wall of the straps that rolled up into discrete vortices in a Karman-like vortex street. They are consistent with the wake identified in Fig. 5.25. Such vortices are at the limit of spatial resolution of PIV here; however, time resolved velocity fields confirm that vorticity patches travel downstream coherently. These velocity field data confirm the conclusion of the uncertainty analysis that higher magnification is necessary in this domain of the flow.

From Fig. 5.24.b) and c) it can be observed that sinusoidal oscillations in \mathcal{W} appear when the bundle is shaken after $t=4.3$ s. The prominent harmonic in the axial velocity is the same as the forcing frequency applied by the shake table: 1.6 Hz. This behavior was first reported from pointwise (LDV) measurements by Ricciardi and Boccaccio [2].

The secondary pulsating flow starts with the bundle motion. Likewise, it ends abruptly with bundle oscillation pointing to an inertial forcing as identified in stagnant fluid, Weichselbaum et al. [3]. The three filtered time histories in Fig. 5.24.b) show that amplitude of oscillations is smaller when going away from the bundle. This will be further explored next when looking at phase averaged velocity profiles. Similarly, the phase lag between the velocity and the bundle oscillations appears to depend on the horizontal location. Finally, the axial velocity seems to accelerate as the bypass region opens.

To better observe this phenomenon phase averaged velocity profiles are presented in Fig. 5.27. Here the origin of the phase is the zero crossing of the rod wall for a positive rod velocity, Fig. 5.27.a), this is the same as in Section 5.5. In Fig. 5.27.b), the lines are color coded with respect to phase angle. For each respective phase angle, the dashed line is the zero velocity, the solid line

the phase averaged velocity profile, and the dotted line the mean static velocity profile averaged from the 9,000 images prior to shaking, $W(x)$, initially displayed on Fig. 5.25.

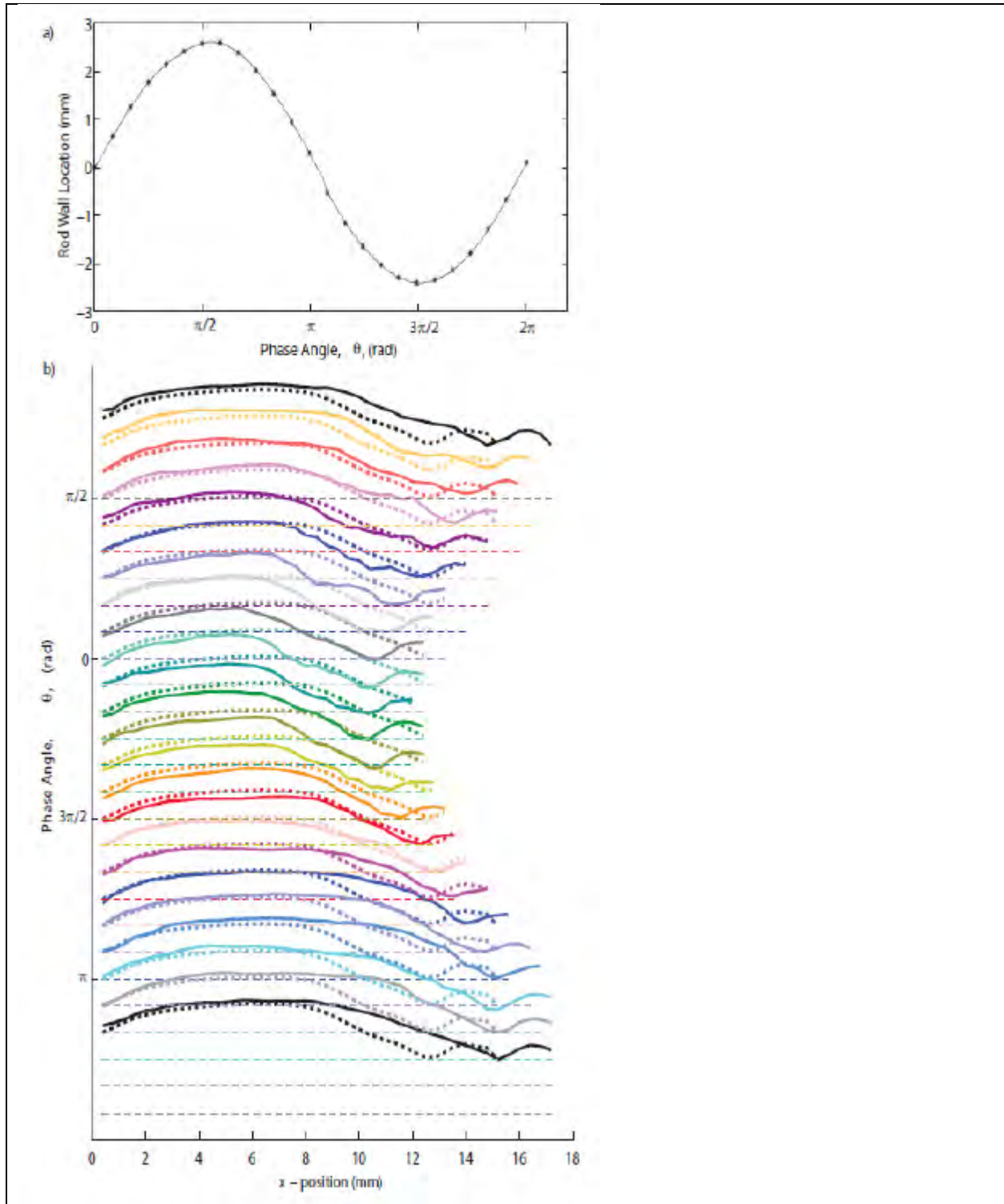


Fig. 5.27. (a) Rod wall location vs. phase angle and (b) Phase average velocity profile of vertical velocity where lines are color coded per phase angle; dashed line is zero velocity,

solid line is fluctuating velocity, and dotted line is mean velocity prior to shaking colored lines over-imposed at 3 points in channel; red = 3 mm, green = 7 mm, blue = 10 mm from the channel wall, and (c) filtered data for 3 points with RMS velocities in black for each respective point.

It is found that the velocity profiles reach a pseudo-steady state after nine cycles of bundle displacement. Hence on the rising edge of the tenth cycle (t_0 of eq. 5.4), the velocity profile is phase averaged for the ensuing ten cycles and presented with a separation of $\pi/12$ between phase angles.

In Fig. 5.27.b), the jetting effect (velocity excess between strap and rod) that was described for the static case, has distinct and repeatable variations as the bundle oscillates. This could be the signature of a larger wake being shed from the spacer grid as the bundle moves in the positive x -direction due to presence of a cross-flow in the bundle or compression of the springs (resulting opening of the flow area locally).

The latter may be the result of the spacer grid geometry, Fig. 5.26, where in the positive direction (moving away from the channel wall) the acceleration of the rod leads the spacer grid and compresses the spring, similar to the results presented in air for the frequency sweeps in Section 5.3. This could create a gap between the rod wall, where these measurements are being taken and the dimple that it was in contact with prior to this direction of movement. The observed oscillations in the jetting is likely to find its origin in the establishment of a cross flow in the bundle.

In Fig. 5.27.b), as the phase angle increases from 0 to $\pi/2$, it can be observed that the jet moves closer to the left of the domain. This shift in the jet appears to continue up to a phase angle of $9\pi/12$, after which the jet appears again closer to the rod wall. Compared to the static case, the jetting is this time markedly more pronounced and is phase dependent.

The other observation from these velocity profiles is the effect of the secondary pulsating flow. The secondary flow results in velocity increases in the bulk flow that are out of phase with the bundle oscillations. The peak axial velocity across the bypass occurs at $10\pi/12$ as the bundle is moving towards the inner channel wall from its maximal displacement. This behavior contradicts mass conservation where the velocity should increase as the bypass decreases. Instead variation in velocity is attributable to a cross flow that develops across the bundle as it oscillates. This cross flow is driven by a difference in pressure losses in the bypass region as it opens on one side and closes on the other as noted by Ricciardi and Boccaccio [2].

The phase averaged velocity profiles show much stronger velocity fluctuations in the wake region than in the bulk. This confirms the presence of a strong cross flow that must develop across the bundle.

Fig. 5.24.c) also shows that the rms of fluctuations appear to be modulated periodically. \hat{w}' is larger when the bundle moves away from the wall, i.e. when the bypass under investigation opens. This indicates that as the bundle moves away from the wall, it injects flow structures and turbulent kinetic energy in the bypass region. The nature of these structures is explored next.

Instantaneous velocity fields are presented in Fig. 5.28 with vorticity shown as contour plot. A single cycle from Fig. 5.24.c), that portrays \hat{w}' in black aligned with the filtered instantaneous velocity in dashed green (7 mm location) on Fig. 5.28.a), shows where each respective velocity field on Fig. 5.28.b) correlates to on a segment of the full time series. Also shown on Fig. 5.28.a) are the rod wall location for in-plane and out-of-plane displacements in blue and red, respectively. The magnitude of the out of plane motion has been increased by a factor of 10 for clarity. The out-of-plane motion is on the order of 0.17 mm that is approximately 6.5% of the in-plane motion. The phase angle for the in-plane displacements that correlate to Fig. 5.27 are shown along the top axis of Fig. 5.28.a).

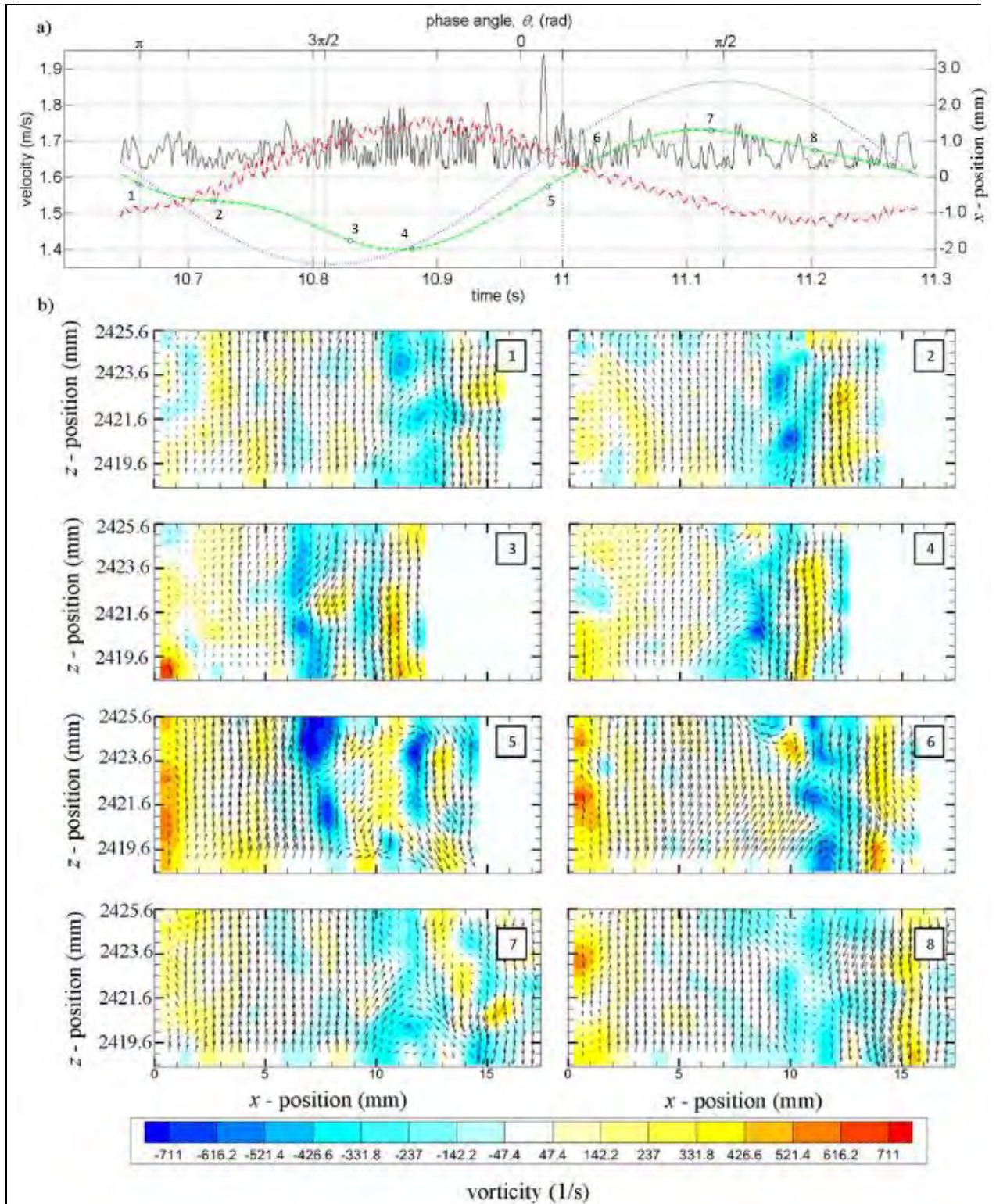


Fig. 5.28. a) time history of filtered \mathcal{W} (green dashed line), \widehat{w} (solid black line), rod wall oscillations (blue dotted line), and out of plane motion scaled by factor of 10 (red dashed-dotted line) at 7 mm for one cycle,. b) Fluctuating velocity field with

vorticity in background for 8 points along the cycle. Lagrangian averaging has been performed on these figures to assist in identifying flow structures.

The pattern in \hat{w}' mentioned above can now be inspected more closely over a single cycle, Fig.5.28.a). In conjunction with the increase in \hat{w}' when the bundle moves away from the bypass wall, the time history of \hat{w}' indicates that the frequency of disturbances increase at 7 mm from the wall (from 10.8 to 11.05 s). This could be the signature that flow structures are injected from spacer grid or the bundle in the bypass region.

The velocity and vorticity fields show that the shear layer identified in the static case on Fig. 5.25 is still present for all the frames. However, its extent in the bypass changes as a function of the bundle displacement. At its smallest, the shear layer is 5 mm wide on frame 2 where the bundle moves towards closing the bypass; it grows up to 8 mm in width on frame 5 when the bundle is moving away from the channel wall. On this last frame, the intensity of vortices in the shear layer issuing from the strap is also the strongest and it appears that there are now two shear layers. The second shear layer is clearly visible on frame 5 and the following one (frame 6, taken 50 ms later). In fact, the secondary vortex street is seen to be angled towards the wall as the bundle moves away from it. Additionally, on frame 5, nearly half of the bypass is occupied by large vortices issuing from the spacer grid. These vortices seem to interact with the boundary layer near the bypass wall, which now grows significantly.

Finally, the last two frames show the weakest vortices in the shear layer; in fact, they appear to be almost suppressed at the current PIV resolution.

All of the analysis thus far has focused on the vertical PIV plane above spacer grid 2. As these tests were conducted at first mode resonance it was also of interest to look at a vertical PIV plane in the middle of the bundle. PIV measurements at the middle of the bundle are in fact taken at the same time as the measurements above spacer grid 2 with the same acquisition rate parameters, however a slightly longer recording time is done for this view. For this plane 60,236 images are acquired at 2,048 fps at 1 Mpixel, which results in 60,235 time resolved vector fields. 25,000 images are captured prior to forcing, while the shake table oscillates another 29,000 images are recorded, and finally after shaking 6,000 are acquired. To compare the effect on the spacer grid on the axial flow, results from both vertical PIV planes are plotted on the same figure in Fig. 5.29.

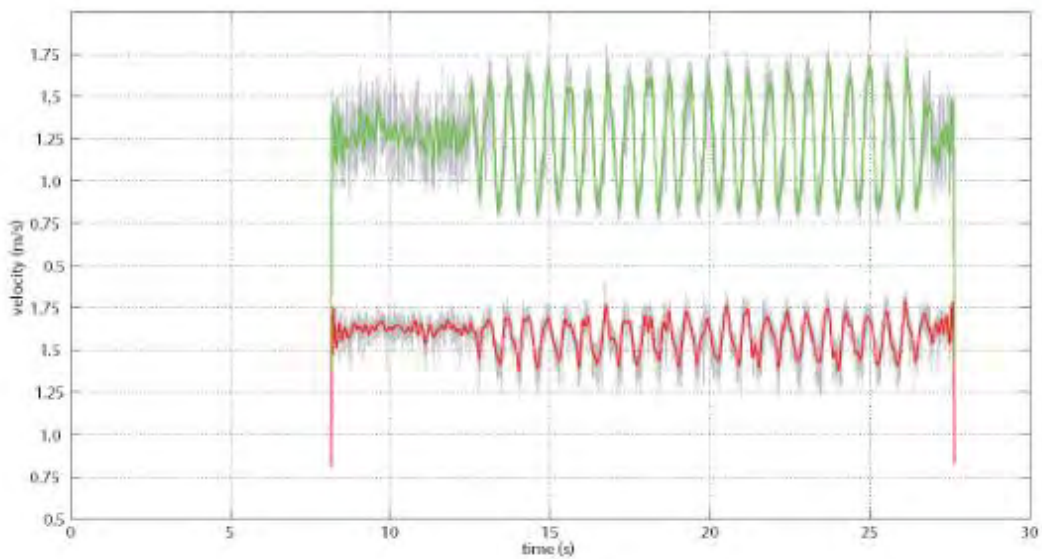
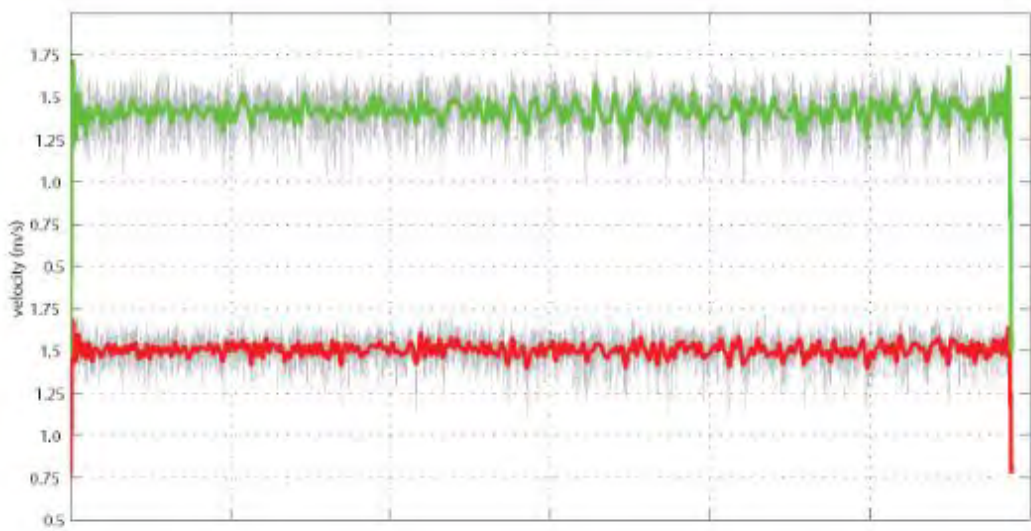
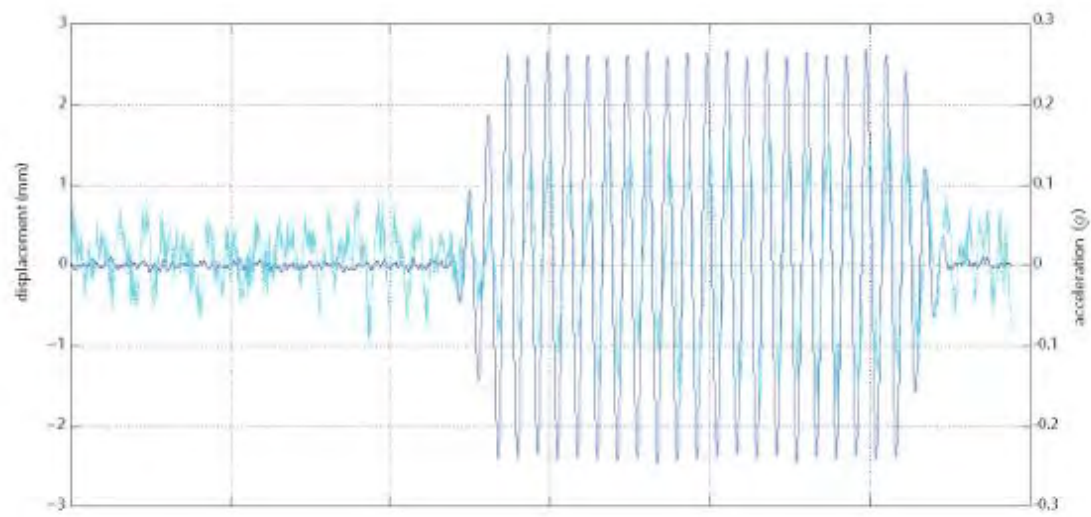
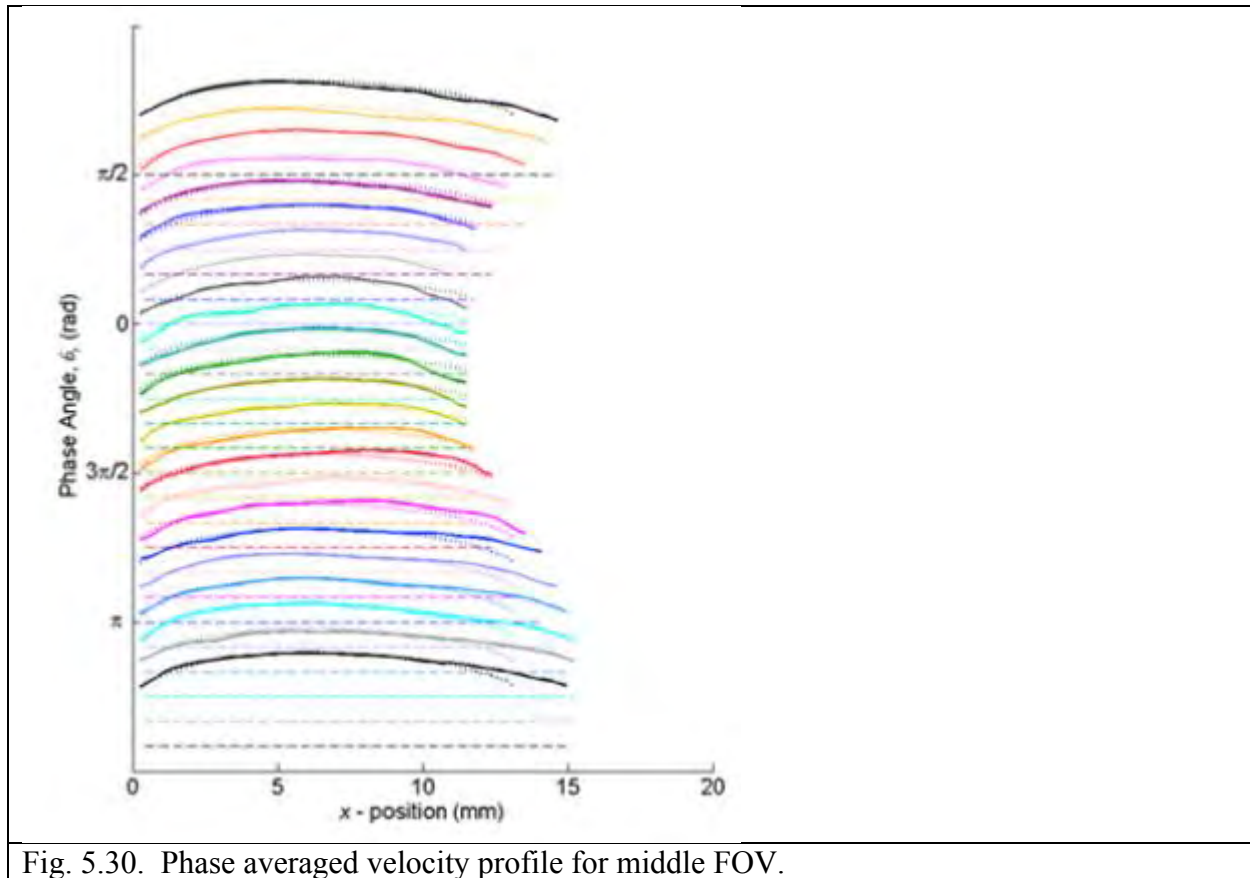


Fig. 5.29. Time series (a) DIC measurements of spacer grid 2 (solid blue = in plane displacement and dashed cyan = out of plane displacement scale by factor of 10), (b) time series for \mathcal{W} from middle of fuel bundle at two points ($x = 7$ mm (red) and $x = 10$ mm (green)) with unfiltered data in gray and filtered ($f_c = 6$ Hz) in colored lines, and (c) time series for \mathcal{W} from above spacer grid 2 with same definition for line coloring as (b)

The complex spacer grid geometry, Fig. 5.26, clearly has an effect on the axial velocity profile both in static conditions and with external forcing from the shake table. In static conditions for \mathcal{W} closer to the rod wall at $x = 10$ mm, it is evident in comparing Fig. 5.29.b and Fig. 5.29.c that the velocity fluctuations are greater for the measurement region just above spacer grid 2. The mean of \mathcal{W} in static conditions is also greater for the middle plane with a mean velocity of 1.41 m/s compared to a mean velocity of 1.27 m/s above spacer grid 2. Once the shaking starts at $t = 12.4$ s, sinusoidal oscillations in the fuel bundle and \mathcal{W} are clearly present. The secondary oscillatory flow, that is easier to observe in Fig. 5.29.c, appears to both begin and end with the bundle oscillations. The effect of the proximity of the spacer grid on the axial flow profile is of greater prevalence, with fluctuations above spacer grid 2 on the order of five times greater than those observed in the middle of the fuel bundle. The fluctuations are still evident in the middle plane measurement region, however do not appear to extend into the middle of the bypass at $x = 7$ mm. Closer to the rod wall they appear more distinct and to better observe this, phase averaged velocity profiles for both cases are plotted in Fig. 5.30.



The velocity profiles in Fig. 5.30 are presented the same as in Fig. 5.27. For the measurement region in the middle of the bundle a secondary oscillation in the flow is still evident but harder to discern than in Fig. 5.27. Also this middle plane is clearly far enough downstream from spacer grid 3 that the turbulent effects of the spacer grid have fully decayed at this elevation. It is noticeable in Fig. 5.30 that near the rod wall it appears the inflection point changes for varying phase angles that correspond to the bundle oscillations, Fig. 5.31.

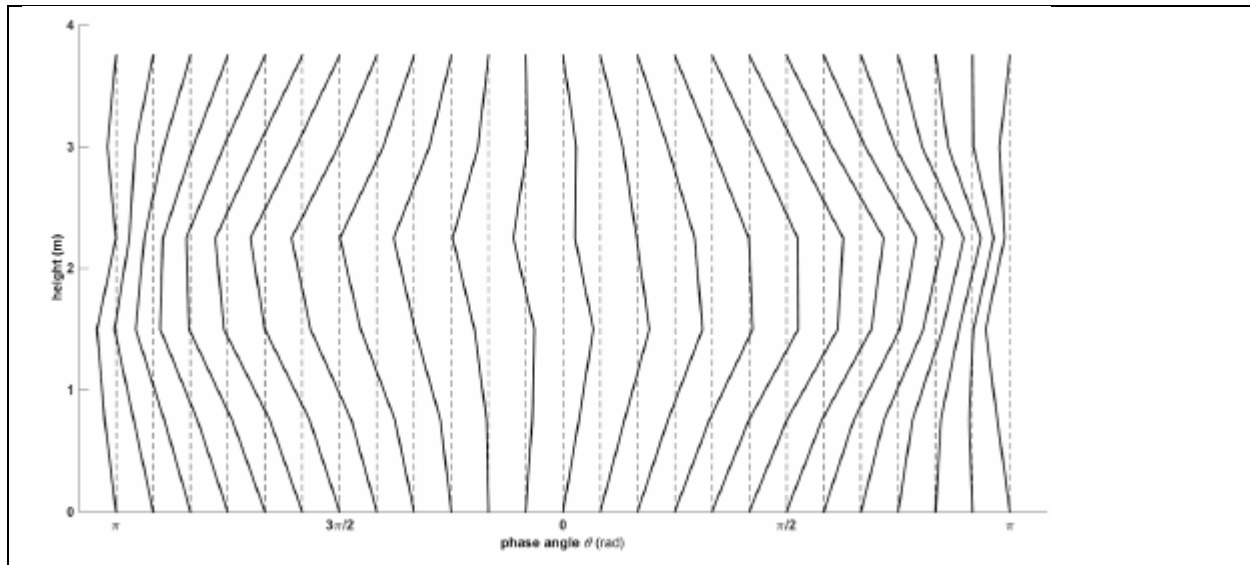


Fig. 5.31. Phase averaged bundle shape. Dashed lines represent the zero position of the bundle for each phase and are spaced by the equivalent of 1 mm of displacement. Spacing between each mode shape is 15° , which represents 1 every 4 frames.

What is clearly portrayed from the results presented thus far, are that in the presence of axial flow with external forcing, the domain just downstream of the spacer grid has a larger impact on the FSI coupling. Hence further PIV analysis is focused on the region above spacer grid 2.

First cases with an axial flow of 1 m/s but varying forcing frequencies and amplitudes are investigated, Table 5.3. At varying forcing frequencies it is found that two things are consistent; 1- the presence of two shear layers at data points 6-7 (depending on case) which for all cases is when the bypass is the widest and the bundle is at the maximum positive x-displacement, 2- just prior to this maximum bundle displacement a vorticity is shed into the bypass. For the second observation it is found that the angle with which the vorticity is shed varies depending on frequency, where the angle is found to decrease with increasing frequency, Table 5.3

Table 5.3 FSI Coupling for Shake Table Forcing with Axial Flow - 1 m/s

Axial Velocity in Bundle (m/s)	Forcing Frequency (Hz)	Forcing Amplitude (mm)	Phase Shift	Shedding Angle (θ)
1	1.6	20		40
1	2.0	7.5	109.9	
1	2.0	10	103.4	37.5
1	2.4	5	114.7	32.5
1	2.8	5	119.4	30

Conducting the same analysis with 3 m/s axial flow, it is found that again the angle of shedding follows the same trend, Table 5.4. However, it can be observed that the angle has now increased for the same forcing frequency and amplitude.

Table 5.4 FSI Coupling for Shake Table Forcing with Axial Flow - 3 m/s

Axial Velocity in Bundle (m/s)	Forcing Frequency (Hz)	Forcing Amplitude (mm)	Shedding Angle (θ)
3	1.6	20	47.5
3	2	10	40
3	3	5	35
3	5	3	

In Table 5.3 the phase lag between the vertical pulsations in the axial flow with the horizontal movement of the bundle can also be seen. This phase lag is found to increase with increasing frequency.

Experiment: 2m/s axial water flow: secondary flow induced by bundle oscillation

In presence of axial flow, the velocity in the bypass also presents an oscillatory behavior. However, compared with the stagnant water case, this oscillatory flow now appears out of phase with the bundle oscillation. In other words, the velocity decreases as the bypass area decreases. This contradicts expected behavior from a mass conservation point of view. However, if similarly to stagnant case, the bundle oscillation is seen as a pressure wave, there is a high-pressure region in front of the advancing bundle, ie receding flow domain. This high pressure region entrains a decrease in the axial pressure gradient that drives the flow, hence resulting in a velocity deficit. This is illustrated with Figure 5.27. In this figure, it can be seen that the instantaneous velocity is higher than the bypass region opens. There is also a strong viscous effect near the rod wall that will influence the pressure drop there.

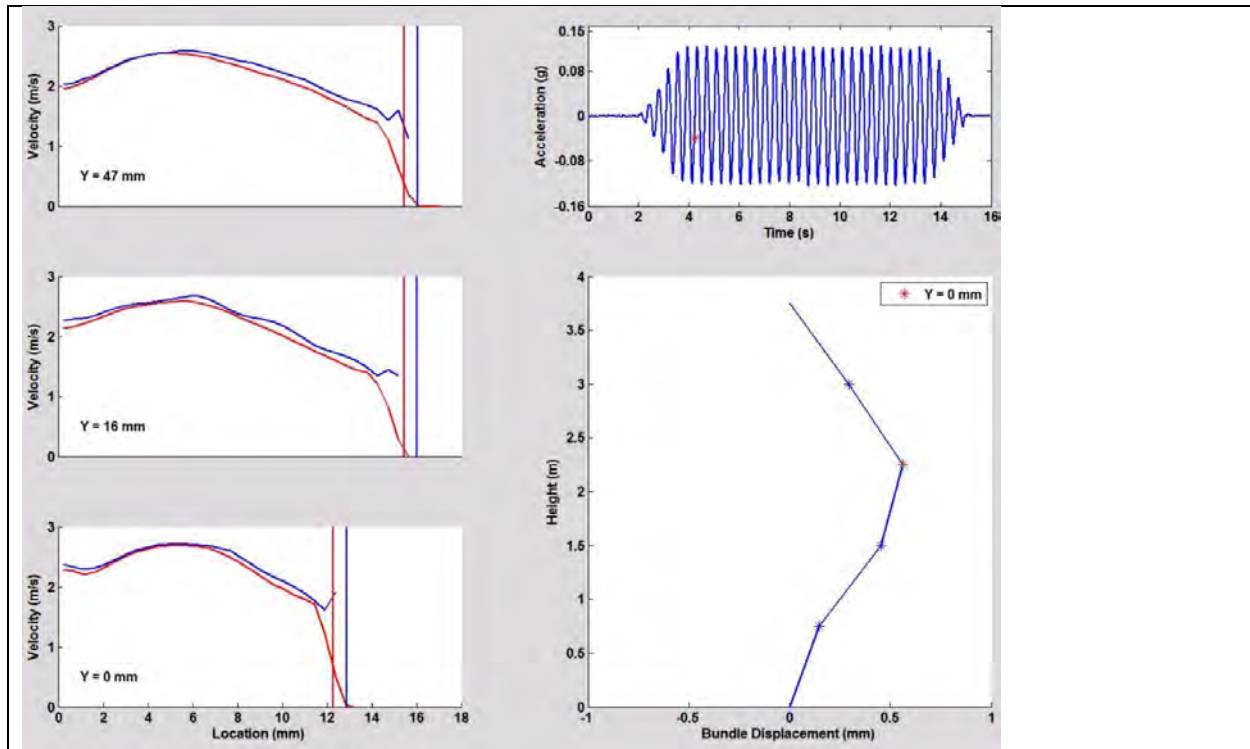


Figure 5.27. Integrated multi-physics data. Left hand side, velocity profile at three different elevations near the spacer grid #2, the channel wall is on the left, the rod is on the right. The red lines indicate the mean velocity, the blue the instantaneous. The vertical lines indicate the rod location, with red being the mean and blue the instantaneous. The time history of the acceleration is displayed on the upper right, while the bundle oscillations are on the lower right.

Experiment: Initial conditions characterization

The initial conditions have been extensively characterized, as well as the flow inside the bundle when it is not excited by external forcing. Figure 5.28 displays a sample averaged velocity profile prior to the fuel bundle with vorticity in the background showing the stable and uniform flow entering the test section at 2 m/s. Figure 5.29 is a sample of the measurements taken inside of the bundle directly after the spacer grid. Here averaged velocity fields in the middle show the effect of the spacer grid on the axial flow. While the velocity profiles at the bottom show how the turbulent effect of the spacer grid decays as the axial flow moves further downstream, here the lower velocity profile is 1 mm downstream and the upper velocity profile is 8 mm.

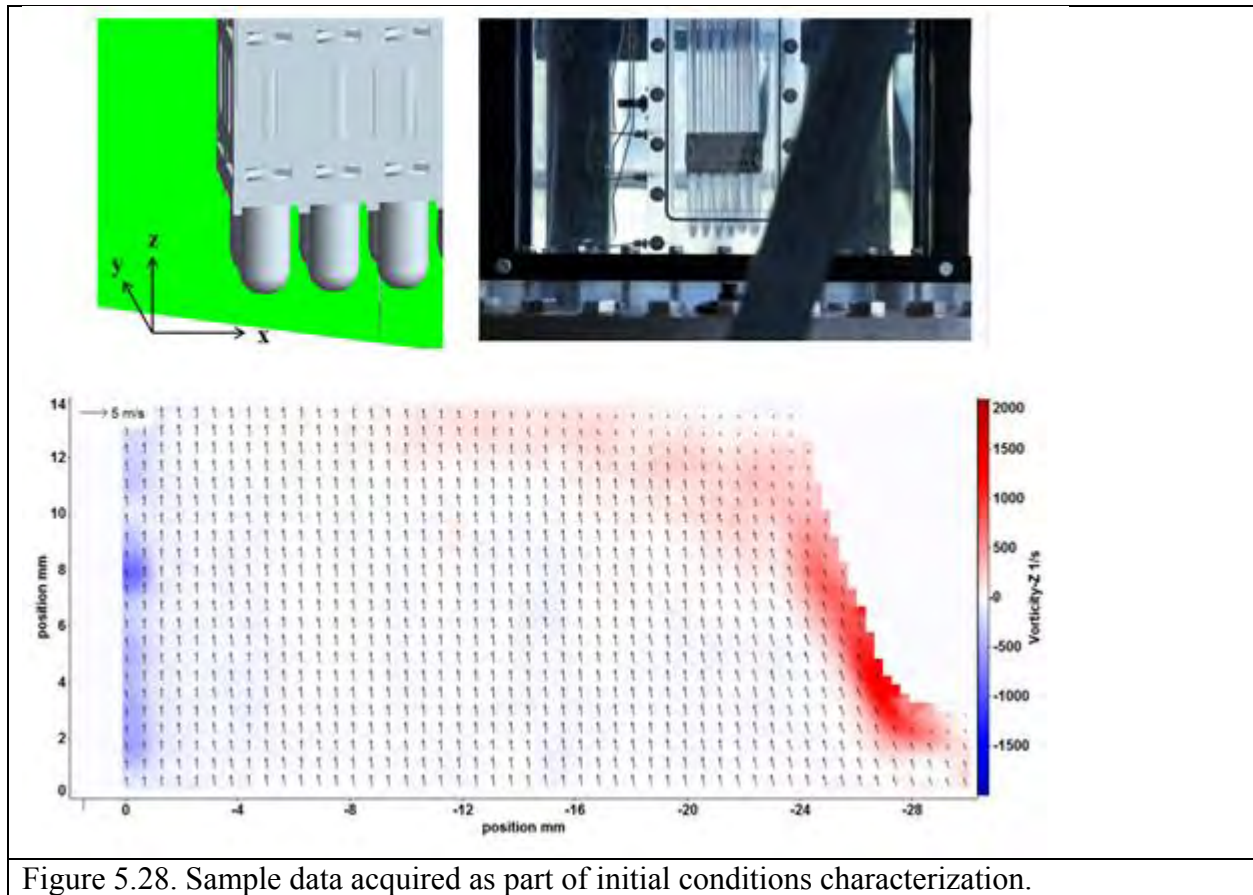


Figure 5.28. Sample data acquired as part of initial conditions characterization.

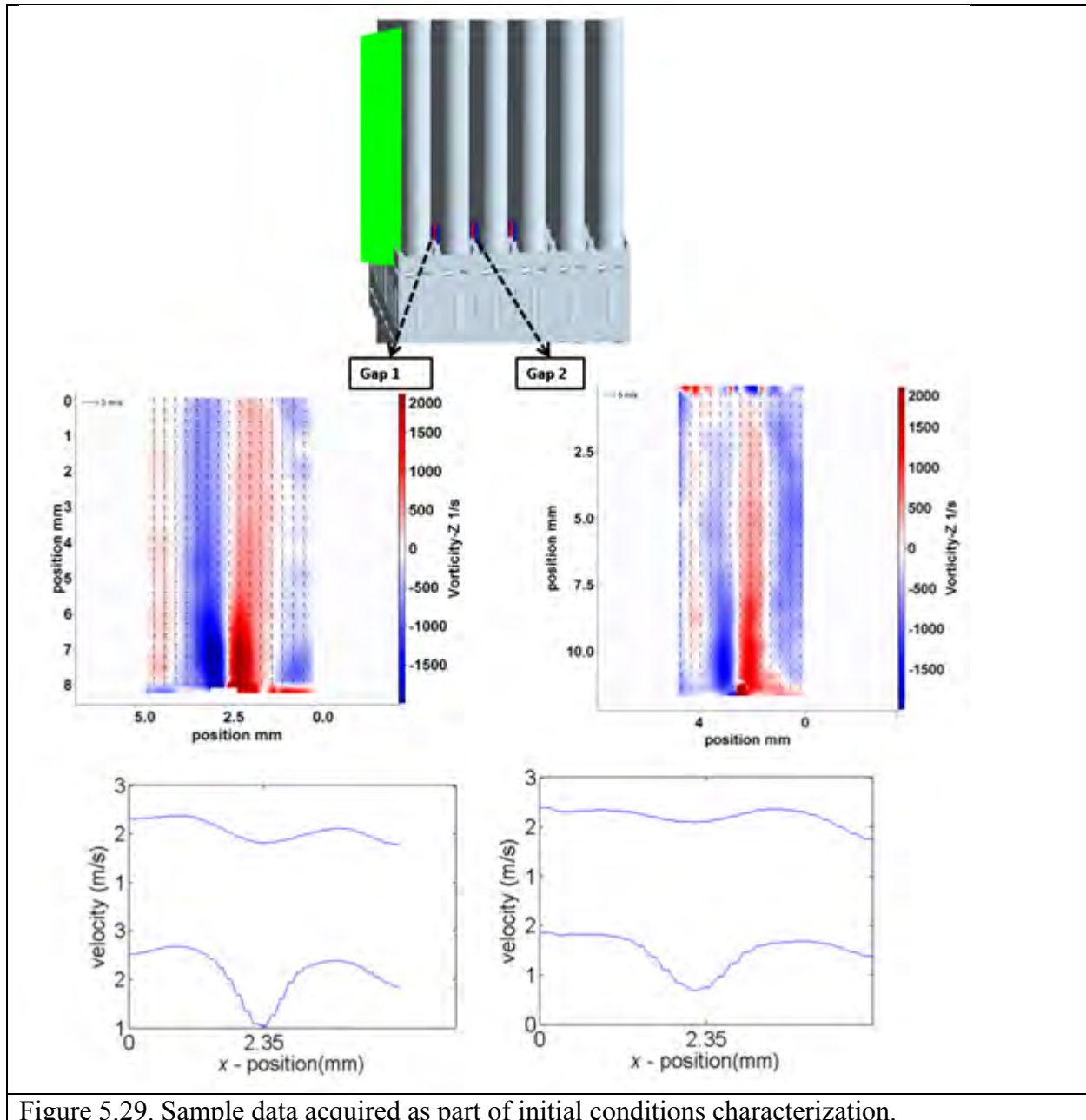


Figure 5.29. Sample data acquired as part of initial conditions characterization.

Experiment: Characterization of Uncertainty

The uncertainty on the DIC system was quantified by replicating the experimental setup with a benchtop experiment where displacements of the spacer grid were controlled with a micrometer linear stage. Measurements were taken in air, water, and P-cymene. For P-cymene the average error is found to be on the order of $4\text{ }\mu\text{m}$, Fig. 5.30.

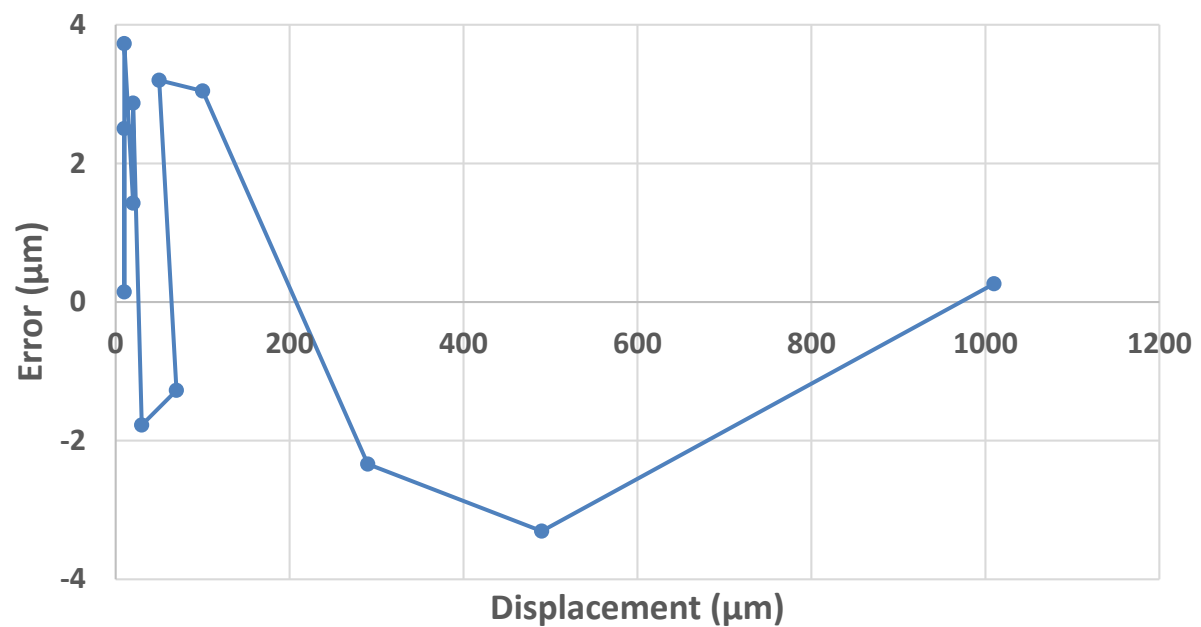


Figure 5.30. Measurement error vs. Applied displacement in P-cymene

Quantification of the uncertainty on the PIV measurements were also conducted and is based on three factors; 1- camera calibration, 2- PIV processing, and 3- precision in determining the velocity. This data will be published in the journal article that has been accepted by Experiments in Fluids for measurements with a 1 m/s axial flow. Here it was found that the overall uncertainty in the bulk of the velocity profile, Fig. 5.31, is 1.2% and 4.1% in the wake of the spacer grid which is on the right side of the velocity field.

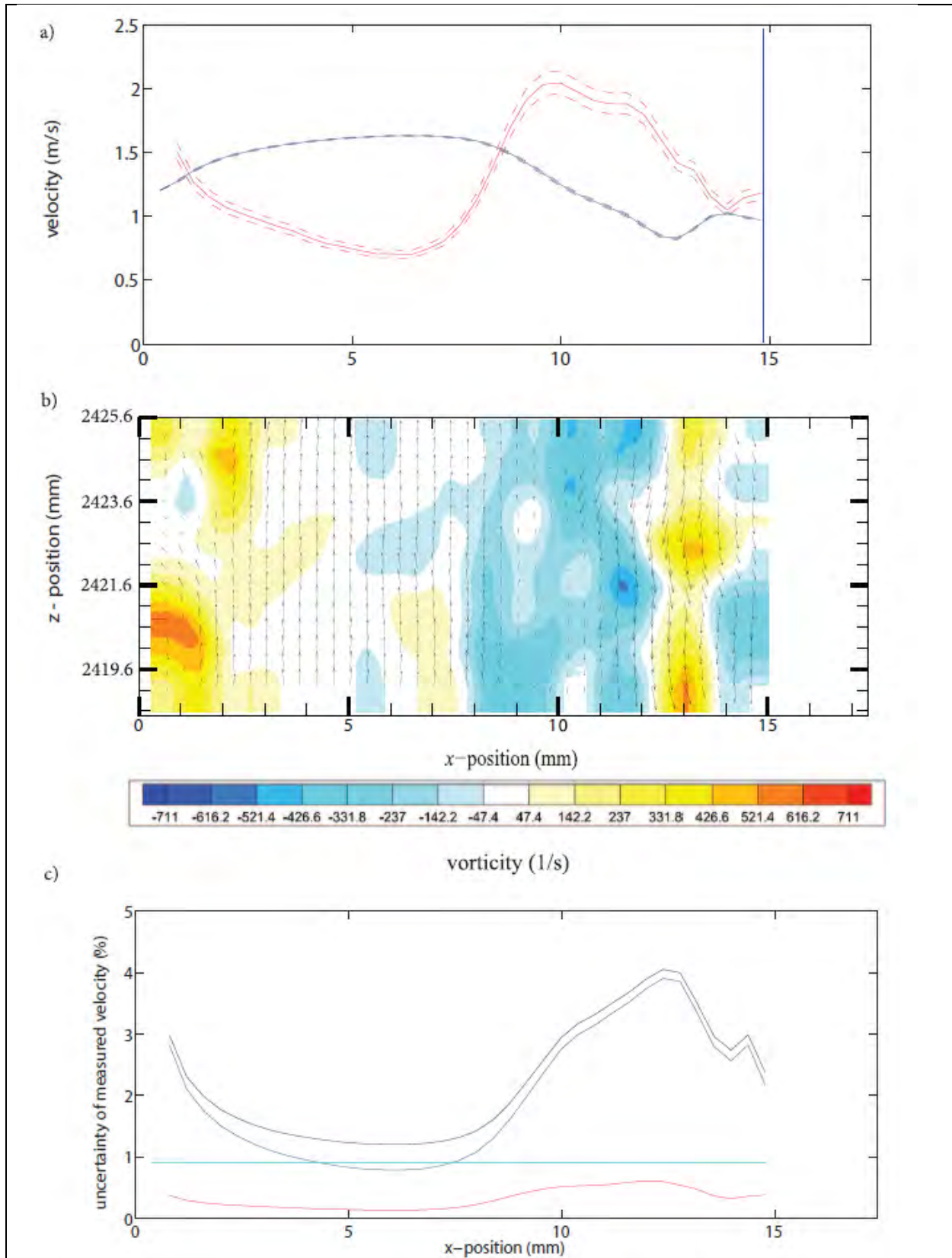


Figure 5.31. Velocity in static case: a) Mean axial velocity profile, $W(x, z)$, in blue with 95% confidence interval in blue dashed and standard deviation in red scaled by a factor of 10 with

95% confidence interval in red dashed. b) Uncertainty on PIV processing error in blue, precision error in red, calibration error in cyan, and overall error in black

CFD results

Due to the ALCC award being received late in this project, the results below are still preliminary. We expect to have more complete results in the coming months.

The simulation of flows over 6 x 6 cylinder bundle. The cylinder bundle with spacer grids is set up according to the experiments in Prof. Bardet's group. The Reynolds number of the flow is set as $Re = 10,000$, defined on W , the bulk velocity and D is the diameter of the cylinder. The grid number is $512 \times 512 \times 4096$ (about 1.1 billion cells). The simulation is conducted on Mira by using 8,192 cores. The preliminary results are provided, where the spacer grid significantly disturbs the vorticity near the cylinder. The strong scalability and weak scalability of the code in simulating flows over cylinder bundle are reported. The estimated cost for the simulation with a grid $1024 \times 1024 \times 8192$ is 20 million core hour.

The fluid motion is modeled by the Navier-Stokes equations for incompressible flows,

$$\frac{\partial \mathbf{u}}{\partial t} + \mathbf{u} \cdot \nabla \mathbf{u} = -\nabla p + \frac{1}{Re} \nabla^2 \mathbf{u} + \mathbf{f}, \quad (1a)$$

$$\nabla \cdot \mathbf{u} = 0, \quad (1b)$$

where \mathbf{u} is the non-dimensional velocity, p is the non-dimensional pressure, t is non-dimensional time. The characteristic length, velocity magnitude, density, time, and force to get the non-dimensional variables are L , W , ρ_f , L/W , and $\rho_f(WL)^2$, respectively, where ρ_f is the density of fluid. The Reynolds number Re is defined by $Re = WL/\nu$, where ν is the kinematic viscosity of fluid. \mathbf{f} is the IB forcing term, which is a body force density reflecting the effect of solid boundary on fluids in the IB method.

The cylinder bundle is stationary in the current simulation. The geometry of the cylinder bundle with spacer grids is shown in figure 1.

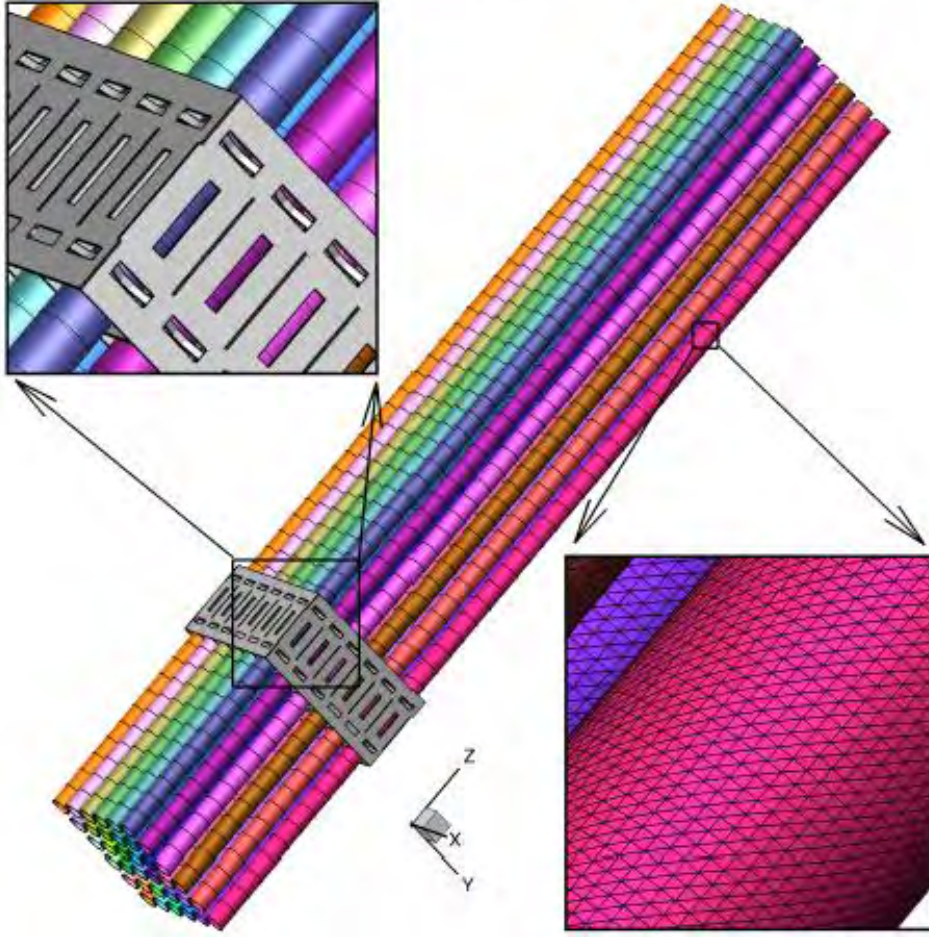


Figure 1: The computational model of the cylinder bundle with spacer grid and details of the triangular panels on the model surface.

3. Numerical method and setups

The flow equation is solved by using the in-house FLASH-INS, where the immersed boundary method is used to deal with the boundary with complex geometry.

The non-dimensional computational domain is $[0, 10.8] \times [0, 8.7] \times [-15, 35]$ in the x , y , and z direction, respectively. The characteristic length is the diameter of the cylinder D . The center distance between neighbor cylinders is 1.333.

The height of spacer grid is 4.01. The distance between the spacer center and bottom of the computational domain is 15, i.e. the center of the spacer grid is at $z = 0$. The Reynolds number is $Re = WD/\nu = 10000$.

The periodic boundary condition is used along the cylinder axis. The non-slip boundary condition is applied at other boundaries.

The grid number is $512 \times 512 \times 4096 \approx 1.1b$. The time step is dynamically computed to keep the CFL number at 0.25.

4. Preliminary results

The results show that the spacer grid significantly affects the evolution of the vorticity near the spacer grid, as shown in figures 2. The details of the instantaneous flow near the spacer grid in a slice is shown in figure 4. The position of the slice is shown in figure 3, where the slice crosses the center of the second cylinder from the dimple side. Notice that the vorticity in figures 4 and figure 3 are defined by

$$\omega = -\nabla \times \mathbf{u}, \quad (2)$$

which has a reversed direction as the traditional definition, aiming at keeping consistent with the plot in Noah's EiF manuscript.

The averaged vorticity and axial velocity field are shown in figure 5 and figure 6, respectively. The average is computed as follows,

$$\phi_{avg}(x, y, z) = \frac{1}{N} \sum_{i=1}^N \phi_i(x, y, z, t), \quad (3)$$

where ϕ can be any component of velocity or vorticity. The results shown in figures 5 and 6 are computed from 60 files saved at every 0.25 non-dimensional time.

The average velocity increases between the cylinder and outer wall, and decreases between the cylinders, as shown in figure 7. The peak average velocity between the cylinder and outer wall is around 1.65, and the peak of the average velocity between the cylinders is around 0.5. The peaks of the average axial velocity depend on the vertical positions. The velocity peak decrease along the

downstream from the spacer grid. The increase of the average velocity between the cylinder and outer wall is consistent with the experimental result.

The axial velocity deficit is found near the boundary of spacer grid ($x=1.4$), as shown in figure 8, which results from the shear layers of the spacer grid. The velocity deficit decreases along the downstream. The deficit of velocity is generally consistent with the experiment. The deficit still exist at $1D$ downstream of the spacer grid in the experiments, while it disappears after about $0.7D$ downstream of spacer grid in the numerical simulation, as shown in figure 9.

The difference between the experiment and the simulation might be caused by: (1) the relatively low Reynolds number in the simulation, (2) the low spacial resolution, (3) the position to take the slices (try the slices offset the center, because the spanwise wave might affect the results). As will be reported in Section 5, the differences might not be caused by the Reynolds number and the spacial resolution. Another possible reason is difference of the upstream flow profiles. The periodic boundary condition is used in the numerical simulation, while the different inlet and outlet are used in the experiment.

The deficit of the velocity can also be found between the cylinders, and has the similar behaviors as that between the cylinder and outer wall, as shown in figure 10. This means that we can investigate the effects of Reynolds number and spacial resolution by the flow over one single cylinder with periodic boundary conditions.

The time dependent velocity at 12 points are recorded in the simulation. The positions of the marker points are shown in figure 11. The filtered velocity decreases and the difference of the velocity increases, when the points moves closes to the wall or cylinder, as shown in figure 12. The behaviors of the time-dependent velocity are similar to these in the experiment. The velocities in the far wake ($z = 5.0$ and $z = 7.0$) are shown in figure 13 and figure 14. The variation of velocity in $z = 5.0$ or $z = 7.0$ is similar to that in $z = 3.0$.

The filtered velocity at the n time step $< w >$ is computed by a moving

average filter as follows,

$$\langle w \rangle = \frac{1}{N_{win}} \sum_{i=0}^{N_{win}-1} w(n+i), \quad (4)$$

where, N_{win} is the width of the filter window. The current simulation use a step of $\delta t \approx 1.0 \times 10^{-3}$. $N_{win} = 1000$ is used in the computation.

The difference between the instantaneous velocity and the filtered velocity is computed by

$$dw = w - \langle w \rangle. \quad (5)$$

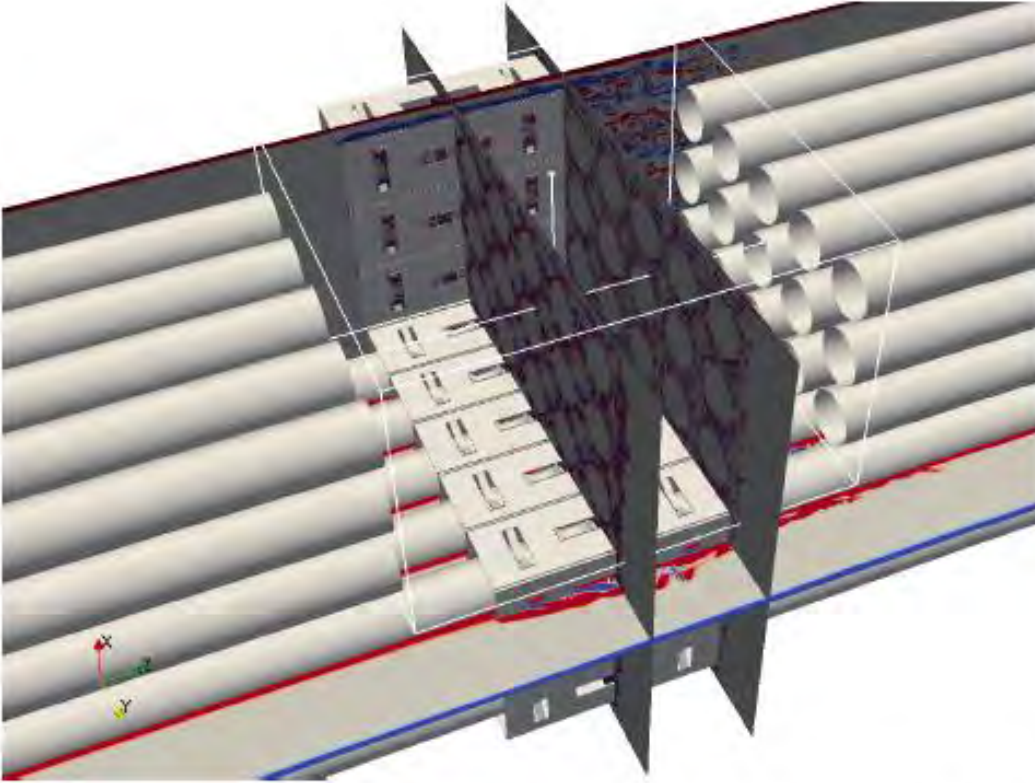


Figure 2: The vorticity near the spacer grid. The spacer grid is clipped to show the disturbed vorticity.

5. Effects of Reynolds number

This section investigates the effects of Reynolds number on the flow by using the flow over one single cylinder with a fine mesh. The results show that the difference between the numerical simulation and the experiment reported in

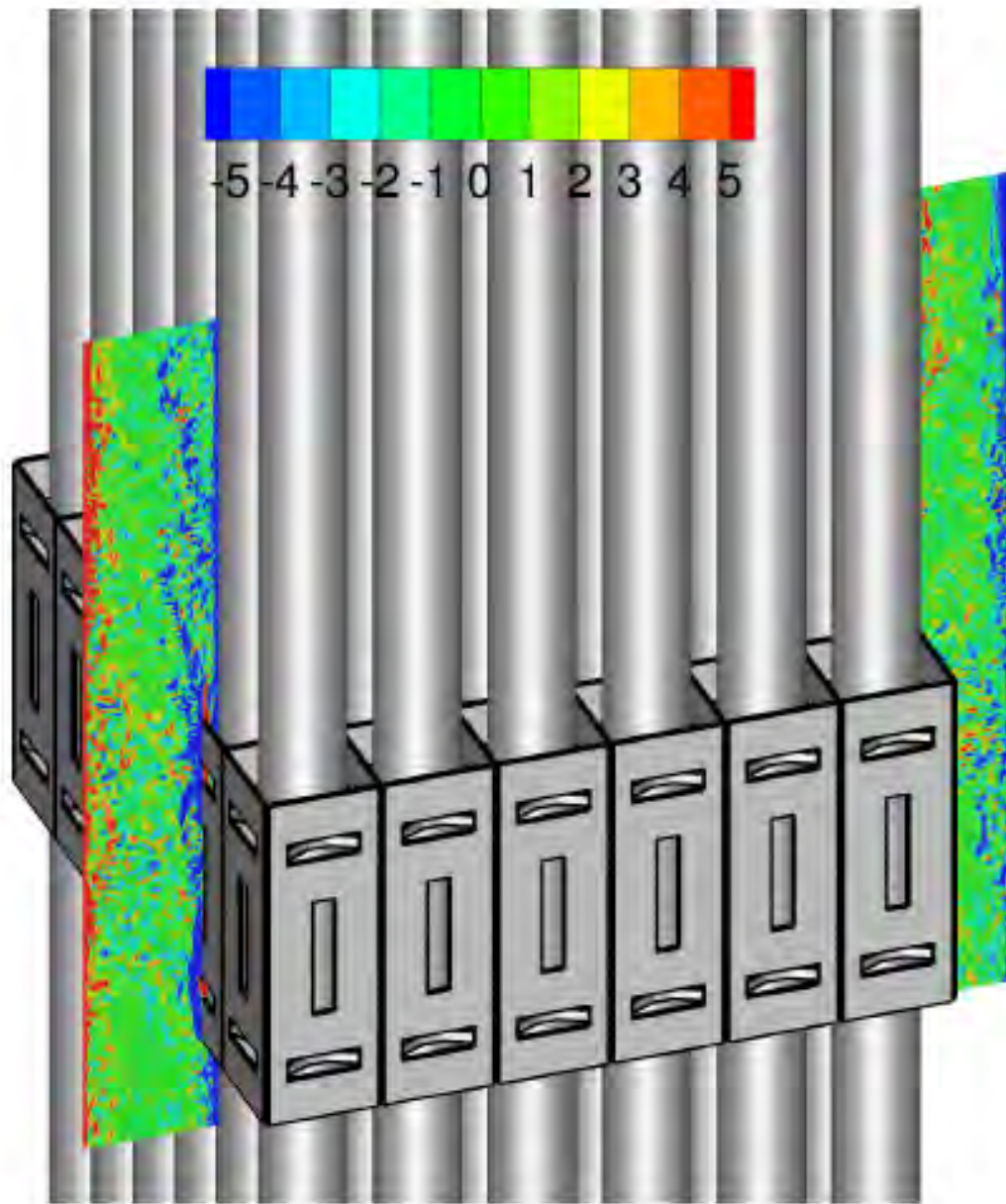
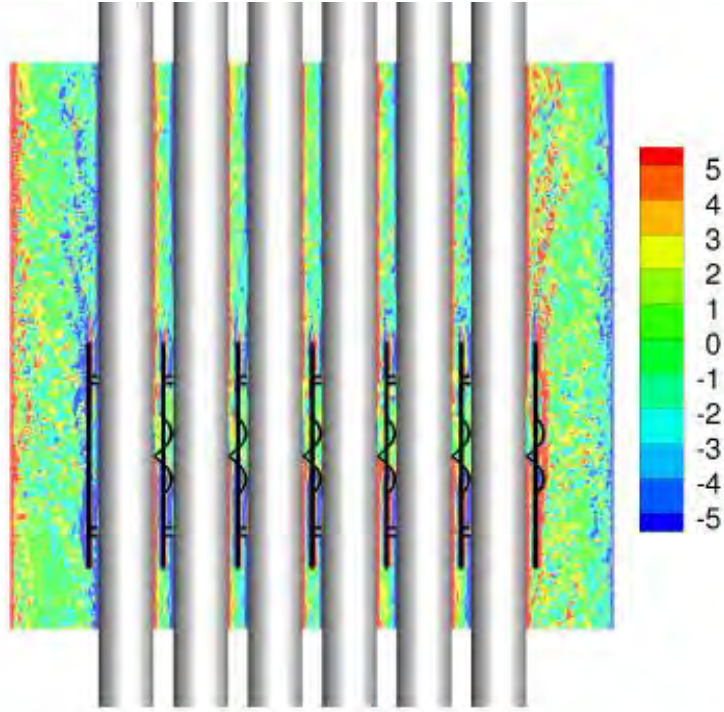
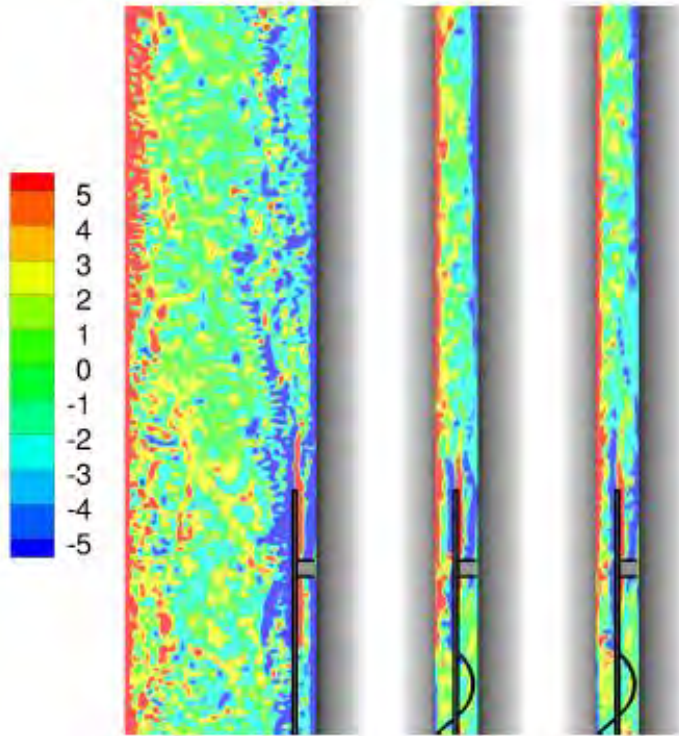


Figure 3: The slices across the spacer grid.

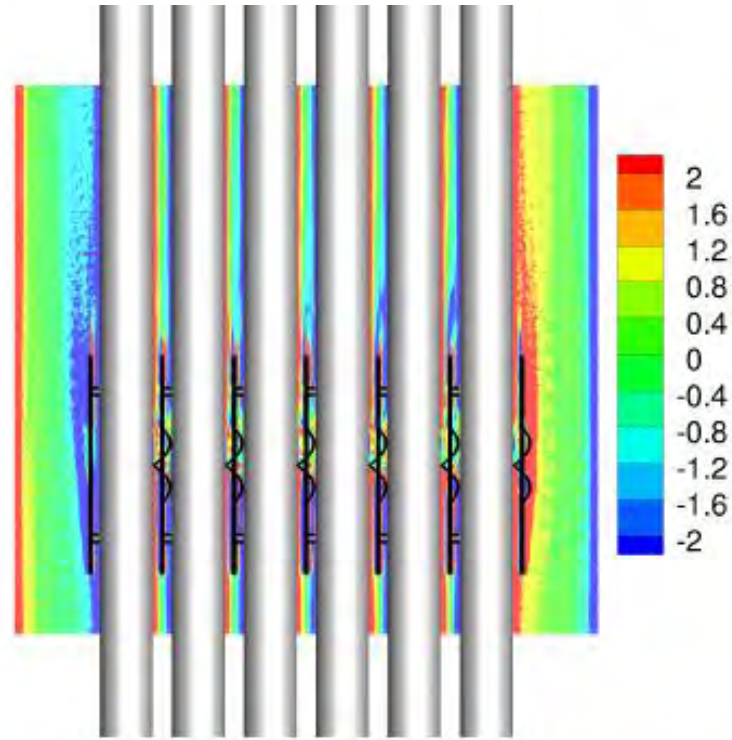


(a)

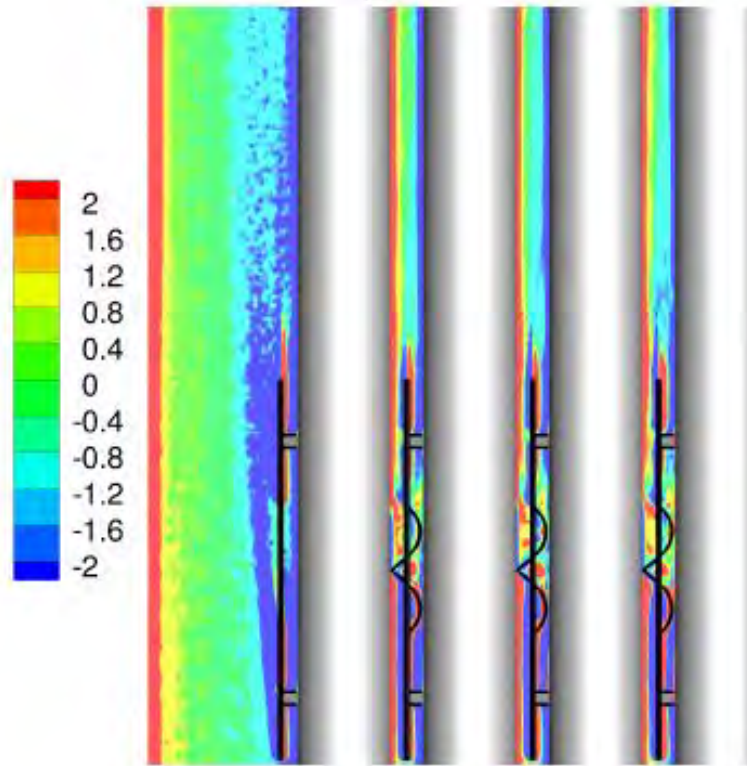


(b)

Figure 4: The instantaneous vorticity ω_x near the spacer grid. The slice at $x = 2.0$ is shown. The spacer is within the region $-2.005 < z < 2.005$, (a) global view, (b) local view.

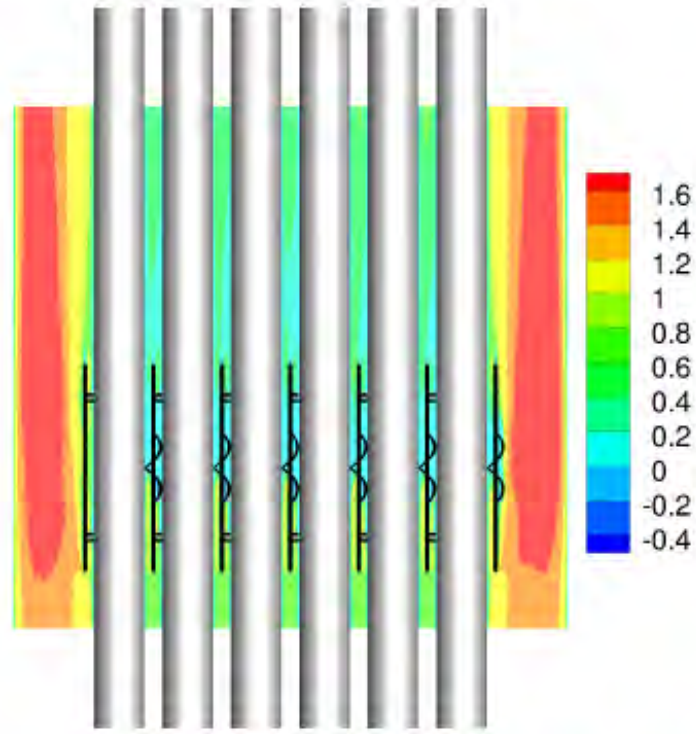


(a)

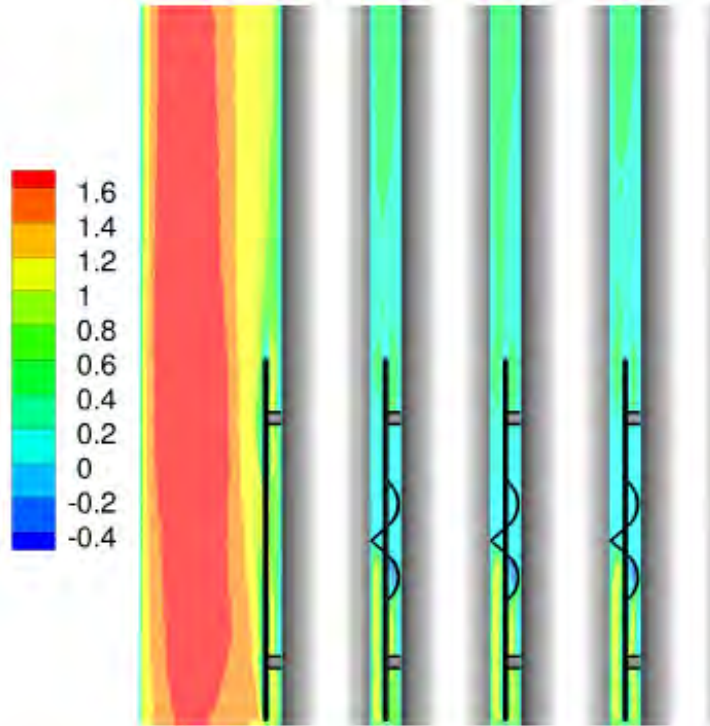


(b)

Figure 5: The average vorticity ω_x near the spacer grid. The slice at $x = 2.0$ is shown. The spacer is within the region $-2.005 < z < 2.005$, (a) global view, (b) local view.



(a)



(b)

Figure 6: The average axial velocity w near the spacer grid. The slice at $x = 2.0$ is shown. The spacer is within the region $-2.005 < z < 2.005$, (a) global view, (b) local view.

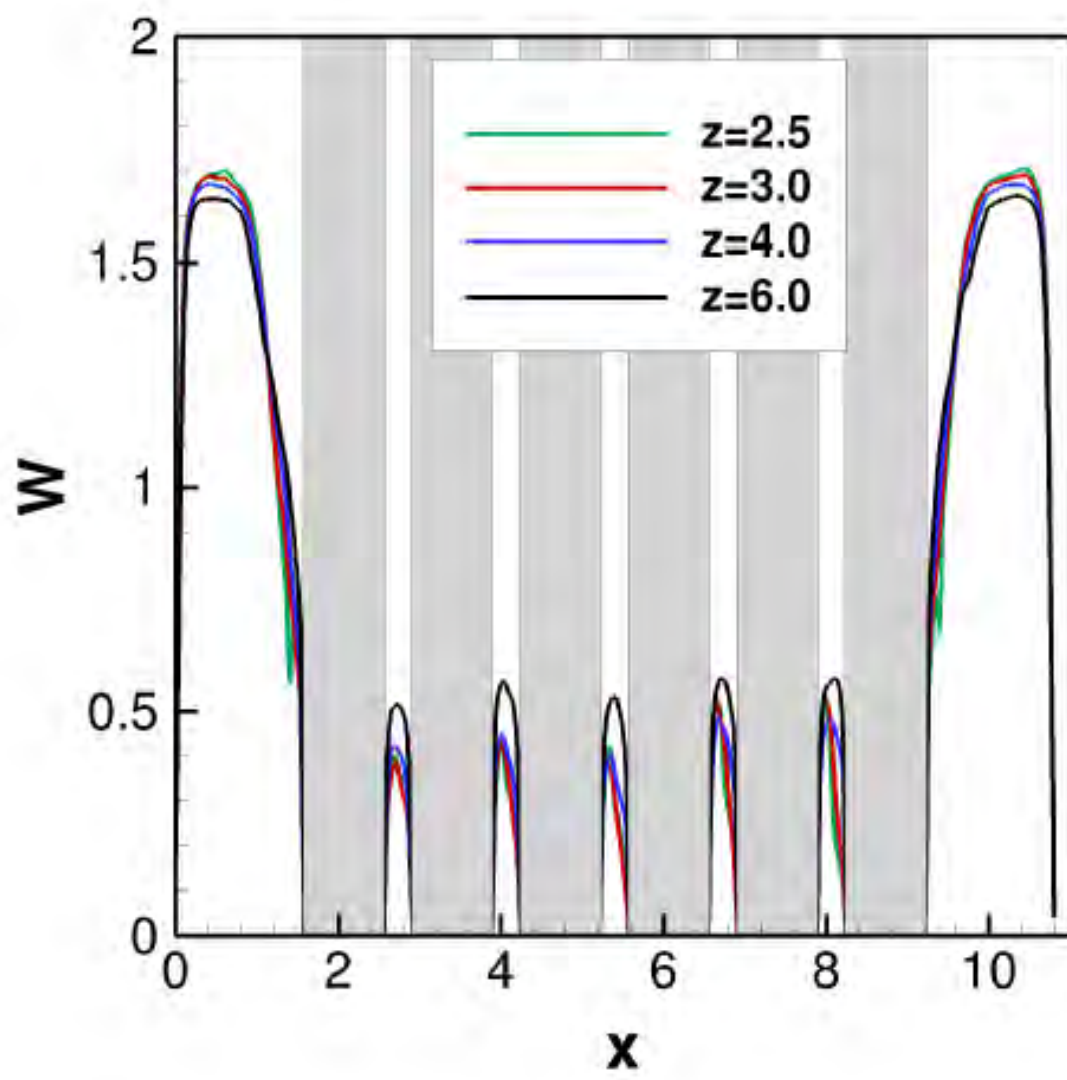


Figure 7: The distribution of the average axial velocity at different axial positions.

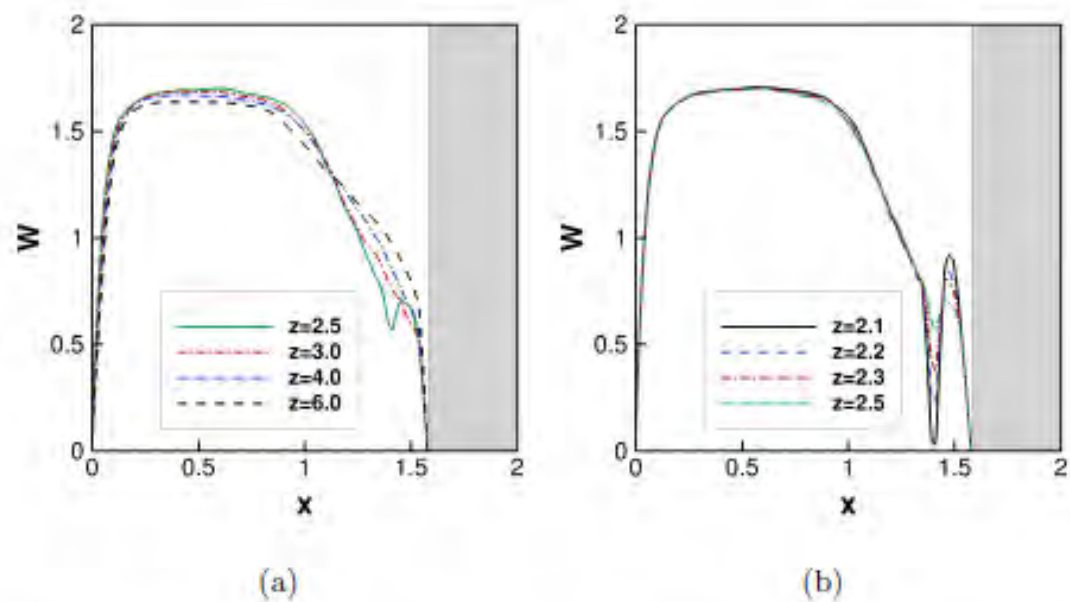


Figure 8: The distribution of average axial velocity between the cylinder and outer wall, (a) far wake, (b) near wake. The spacer is within the region $-2.005 < z < 2.005$.

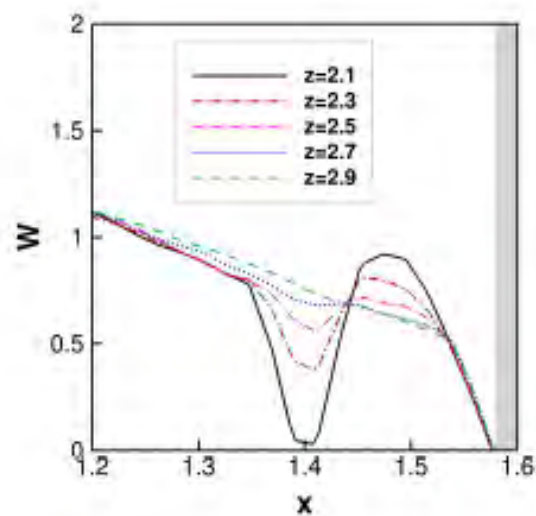


Figure 9: The distribution of average axial velocity near the spacer grid. The spacer is within the region $-2.005 < z < 2.005$.

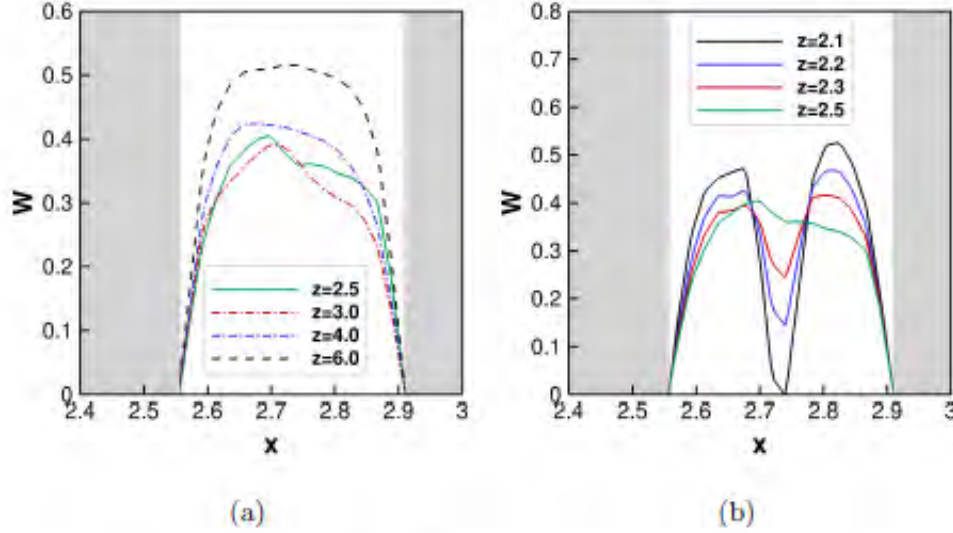


Figure 10: The distribution of average axial velocity between cylinders , (a) far wake, (b) near wake. The spacer is within the region $-2.005 < z < 2.005$.

Section 4 might not be caused by the mesh size and difference in Reynolds number.

The computational model of the single cylinder with spacer grid is shown in figure 15. The single cylinder is stationary in the simulation. The computational domain is $[-0.667, 0.667] \times [-0.667, 0.667] \times [-5, 15]$ in the x , y , and z directions, respectively. The grid size is $256 \times 256 \times 3280$. The grid length is about $1/7$ of that in the simulation of 6×6 cylinder bundle. The non-slip boundary condition is used on the cylinder surface and the spacer grid. The periodic boundary condition is applied at the external computational domain.

The simulations are conducted at 4 different Reynolds numbers, $Re = WD/\nu = 1000$, 5000, 10000, and 15000. The simulations at $Re = 1000$, 5000, and 10000 are finished and reported in this section. The simulations of the flow at $Re = 15000$ has not been finished, thus will be reported later.

The instantaneous vorticity field at the first 3 Reynolds number is shown in figure 16. The small scale vortex structures increase as the Reynolds number increases.

The average vorticity filed at different Reynolds numbers is shown in fig-

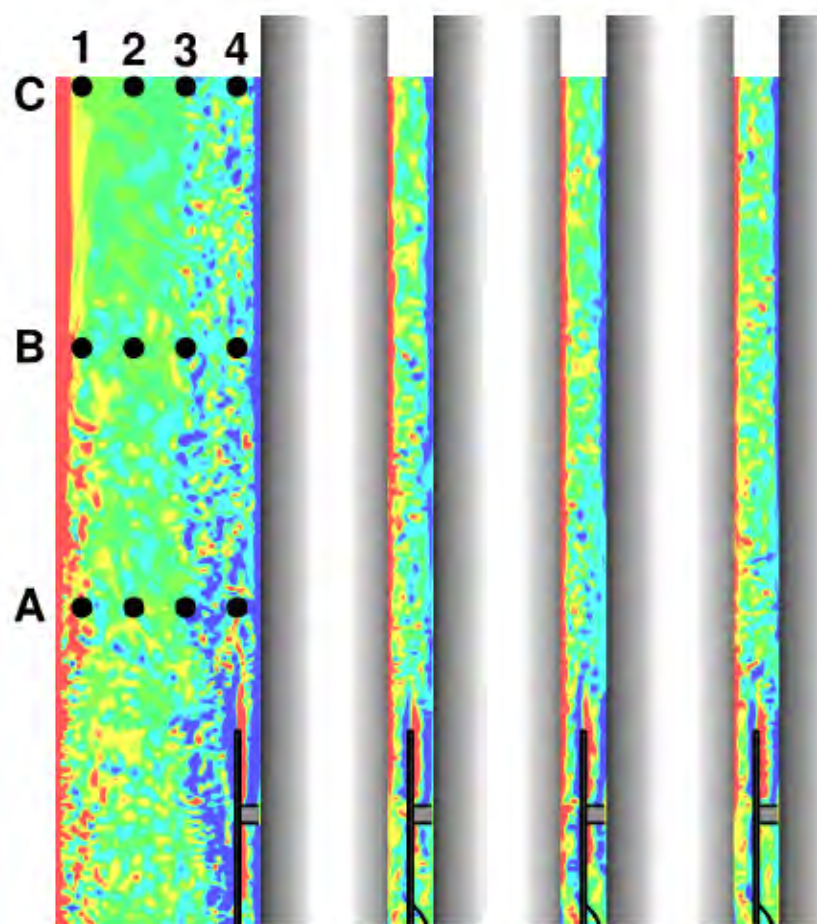
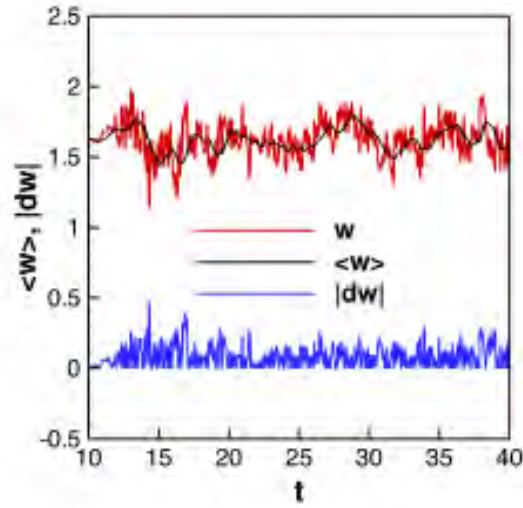
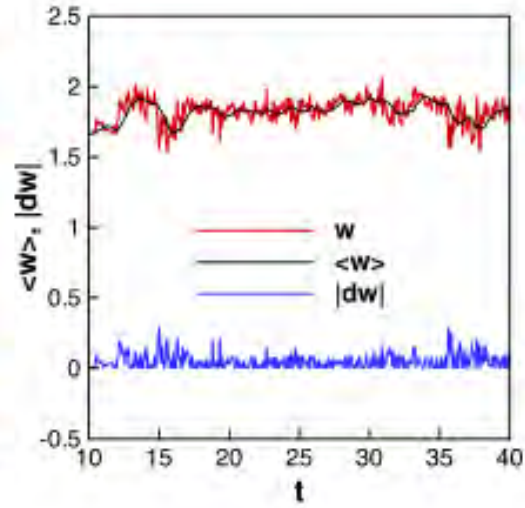


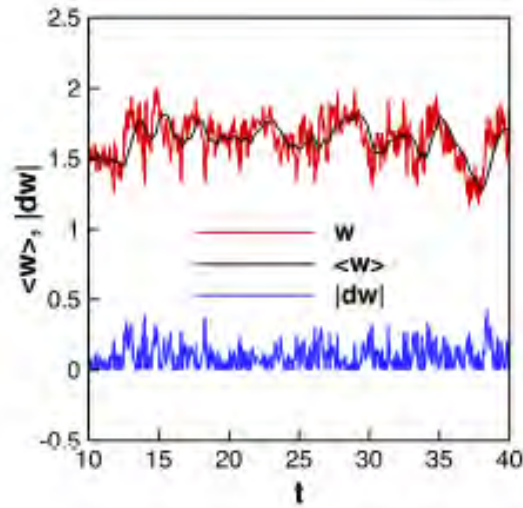
Figure 11: Markers to record the velocity.



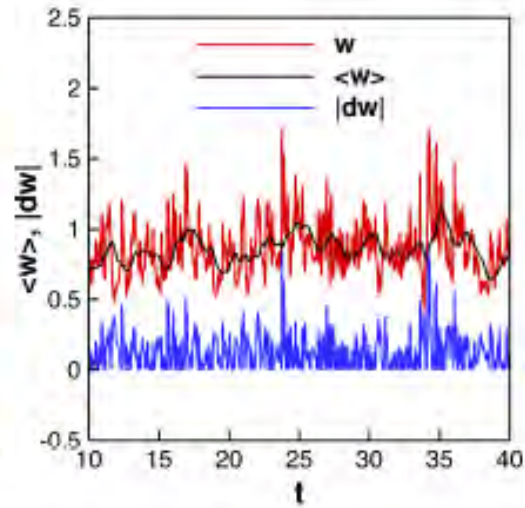
(a)



(b)

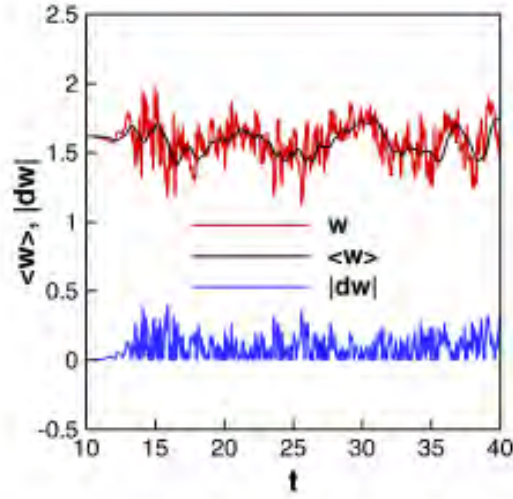


(c)

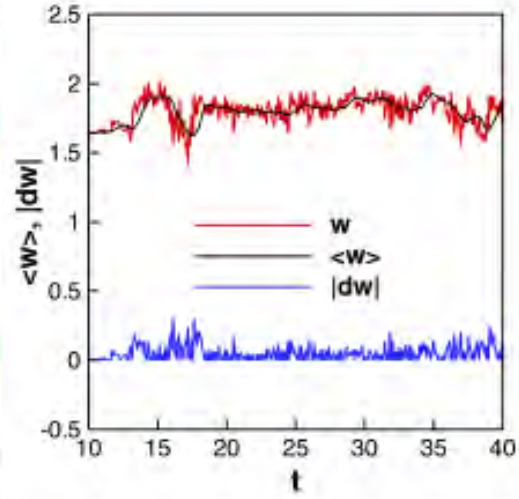


(d)

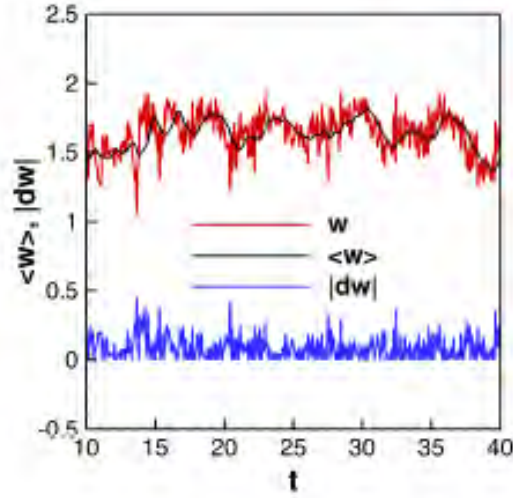
Figure 12: Time dependent velocity in the slice $z = 3.0$ at different points, (a) A1, 0.2D from the wall, (b) A2, 0.6D from the wall, (c) A3, 1.0D from the wall, (d) A4, 1.4D from the wall. The spacer is within the region $-2.005 < z < 2.005$.



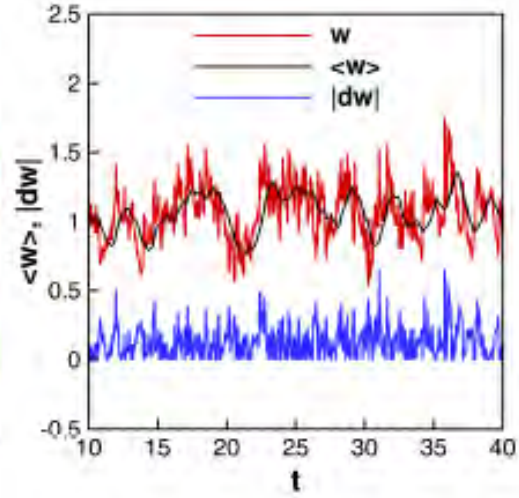
(a)



(b)

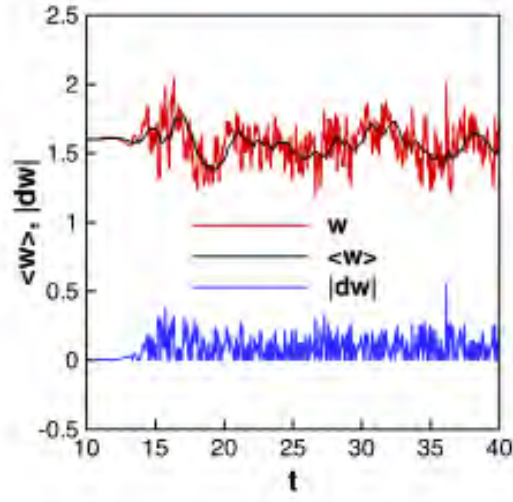


(c)

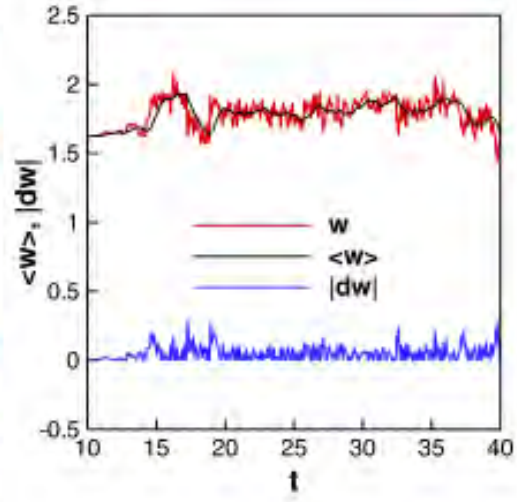


(d)

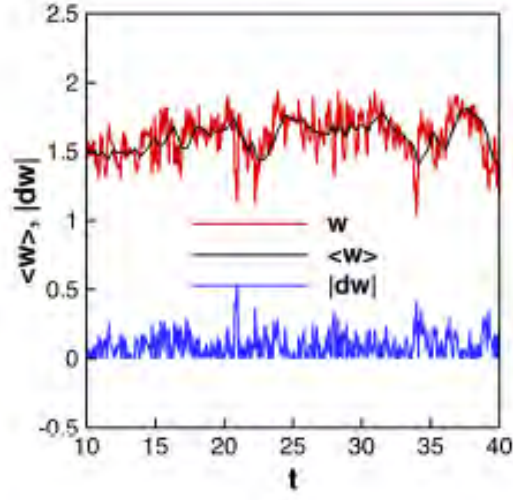
Figure 13: Time dependent velocity in the slice $z = 5.0$ at different points, (a) B1, 0.2D from the wall, (b) B2, 0.6D from the wall, (c) B3, 1.0D from the wall, (d) B4, 1.4D from the wall. The spacer is within the region $-2.005 < z < 2.005$.



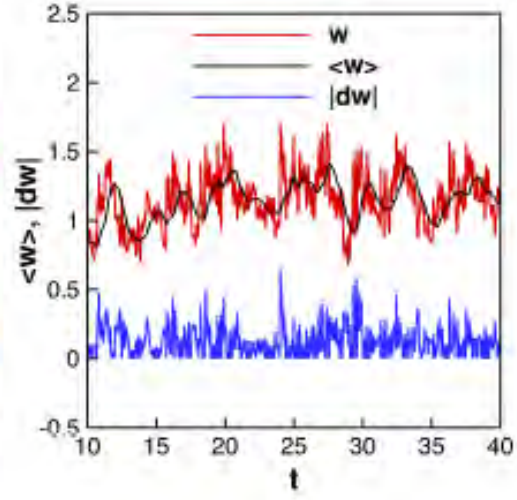
(a)



(b)



(c)



(d)

Figure 14: Time dependent velocity in the slice $z = 7.0$ at different points, (a) C1, 0.2D from the wall, (b) C2, 0.6D from the wall, (c) C3, 1.0D from the wall, (d) C4, 1.4D from the wall. The spacer is within the region $-2.005 < z < 2.005$.

ure 17. The length of the wake has not significant difference at the different Reynolds numbers.

The average axial velocity filed at different Reynolds numbers is shown in figure 18. The average velocity in the slice $x = 0$ increases as the Reynolds number increases.

The average axial velocity profiles at different axial positions are shown in figures 19 and 20. The deficit of velocity seems decreased as the Reynolds number increases. For example, the minimum velocity near the spacer grid is around 0.1 at $Re=5000$, while it is around 0.2 at $Re=10000$. The deficit of the velocity disappears at $z=3.0$ in all the cases.

The distribution of the axial velocity in the slice $z = -3$ is shown in figure 21. The axial velocity varies at different x positions, but might not response to the difference between the simulation and experiment.

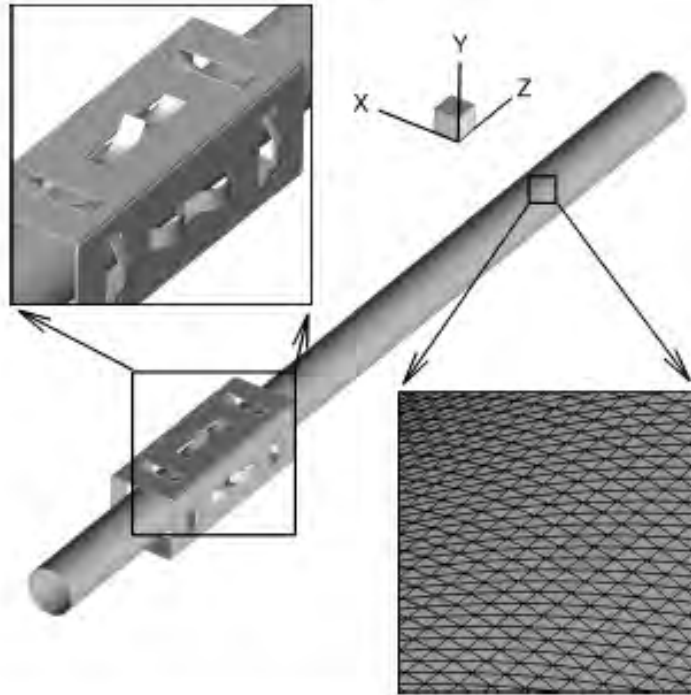


Figure 15: The computational model of the single cylinder with spacer grid.

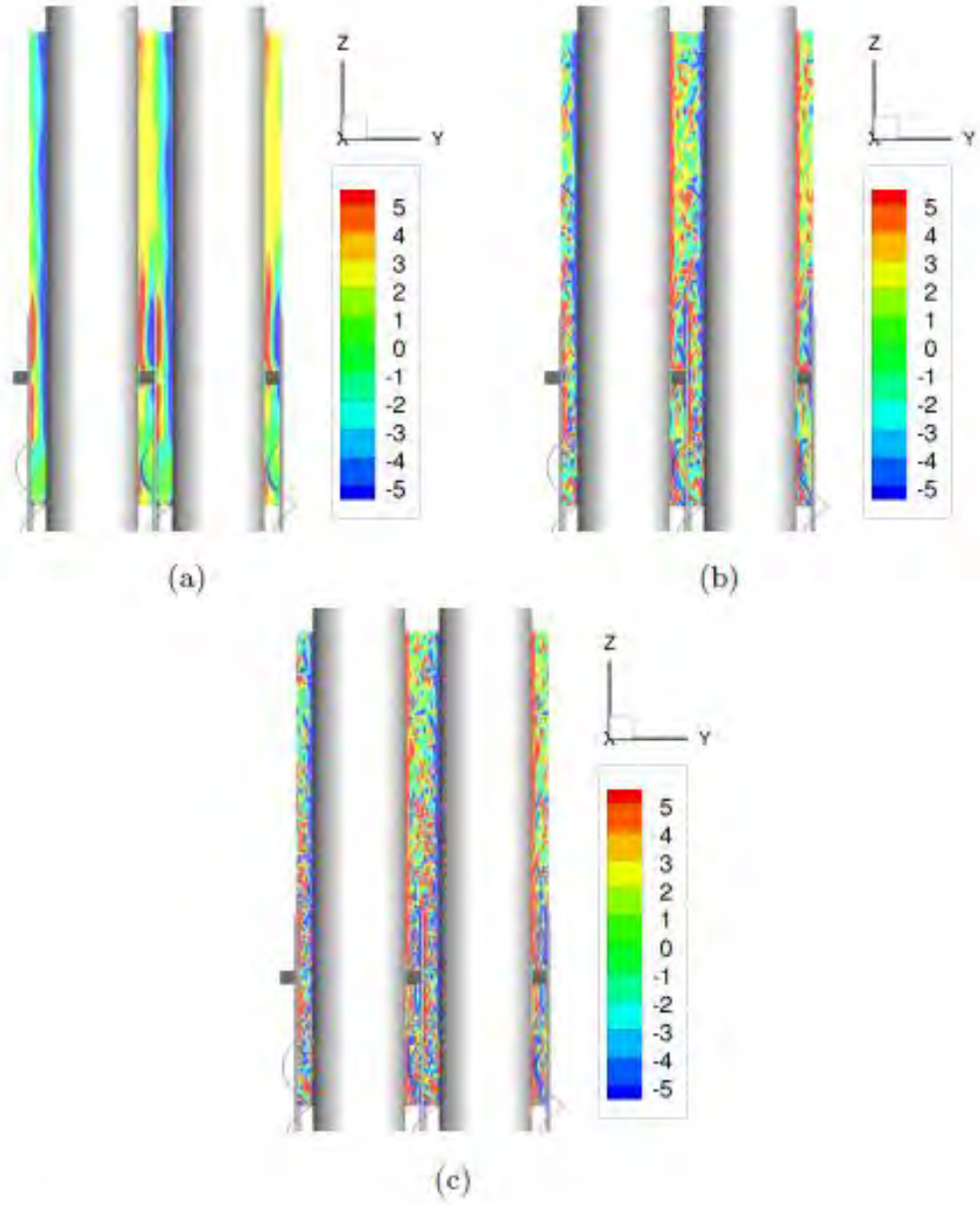


Figure 16: Instantaneous vorticity (ω_x) field at different Reynolds numbers, (a) $Re=1000$, (b) $Re=5000$, (c) $Re = 10000$. The flow field is copied and translated with $d = 1.333D$ along the y direction to visualize the flow over spacer grid. The spacer grid is within the region $-2.005 < z < 2.005$.

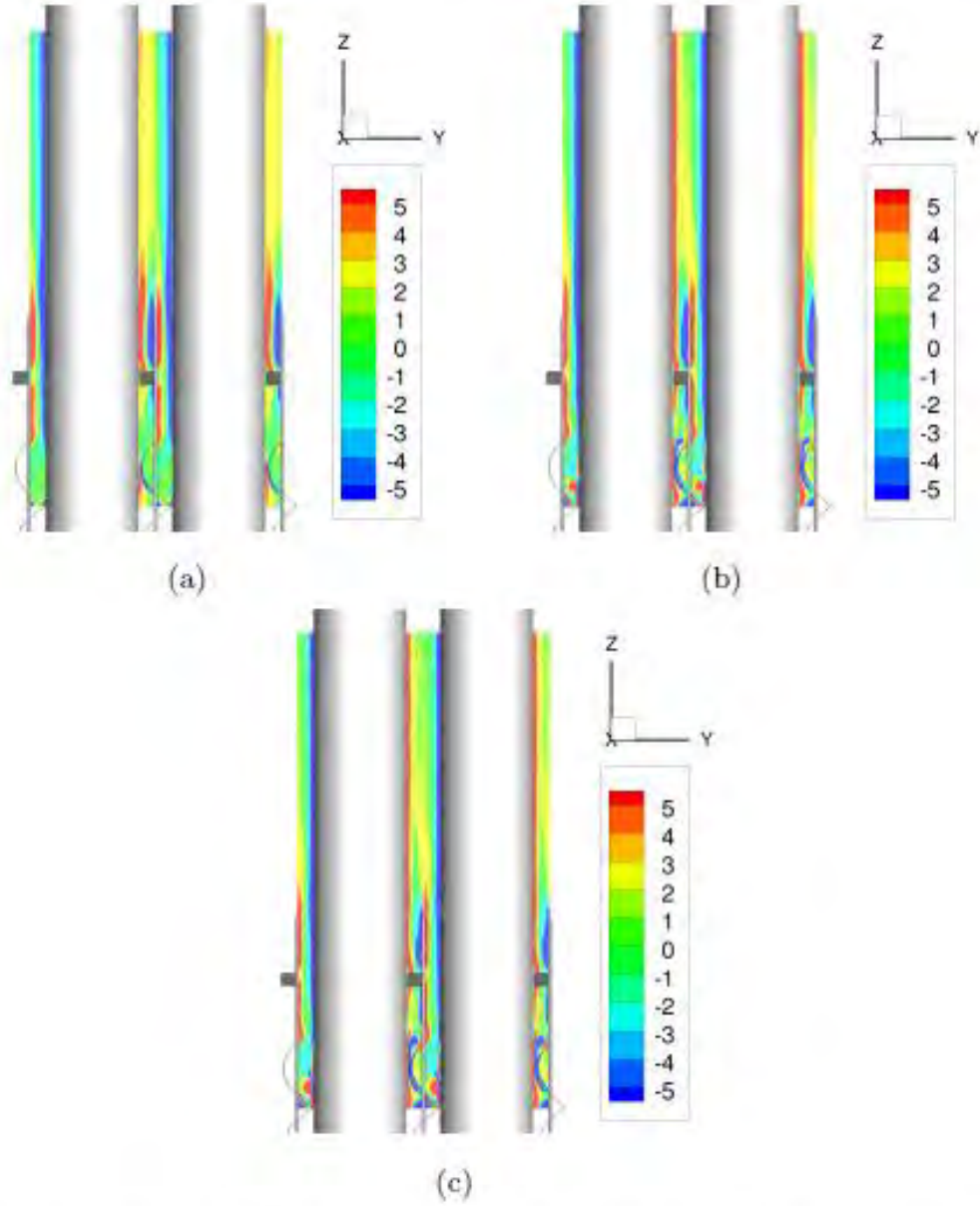


Figure 17: Average vorticity (ω_x) field at different Reynolds numbers, (a) $Re=1000$, (b) $Re=5000$, (c) $Re = 10000$. The flow field is copied and translated with $d = 1.333D$ along the y direction to visualize the flow over spacer grid. The spacer grid is within the region $-2.005 < z < 2.005$.

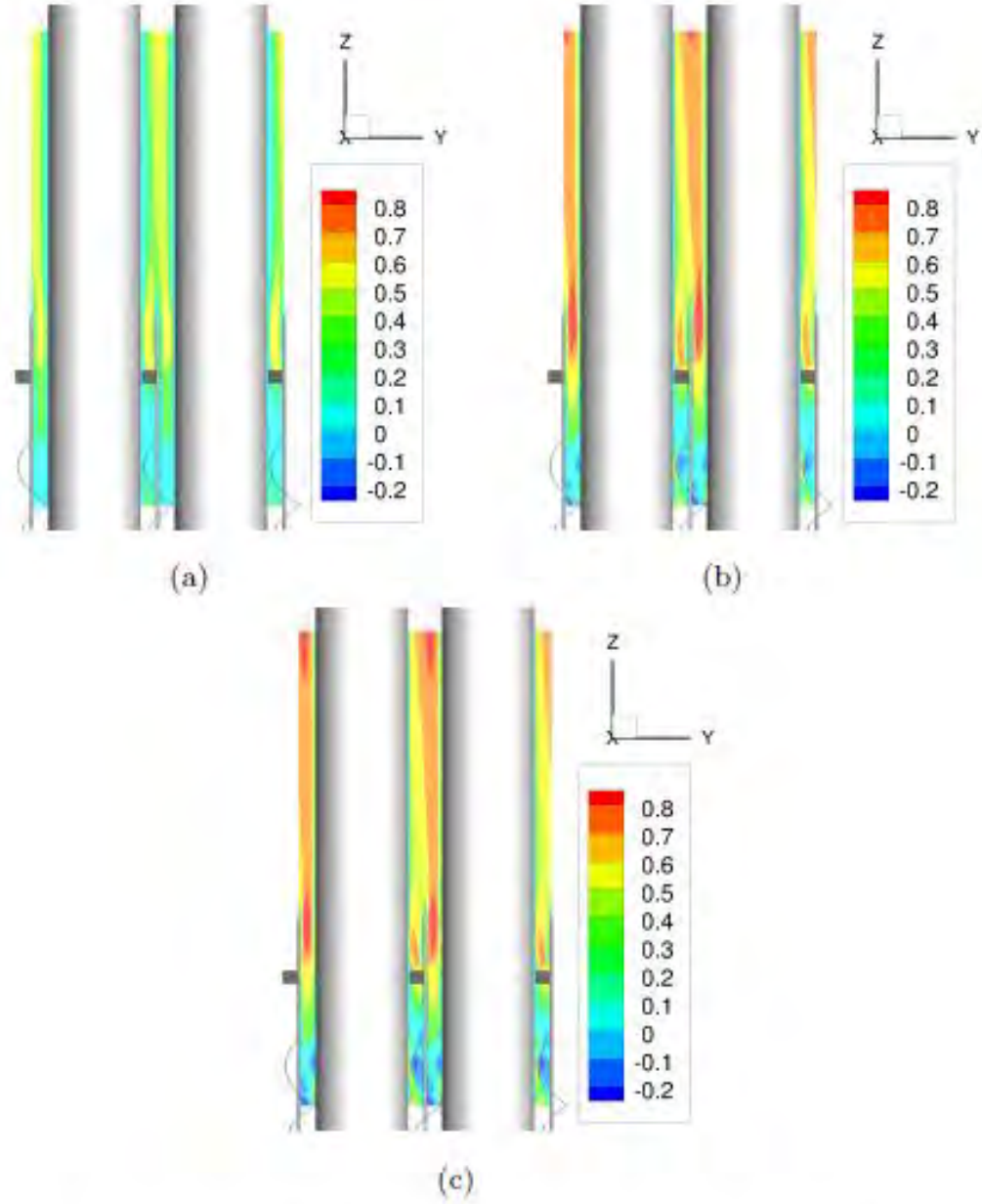


Figure 18: Average velocity (W) field at different Reynolds numbers, (a) $Re=1000$, (b) $Re=5000$, (c) $Re = 10000$. The flow field is copied and translated with $d = 1.333D$ along the y direction to visualize the flow over spacer grid. The spacer grid is within the region $-2.005 < z < 2.005$.

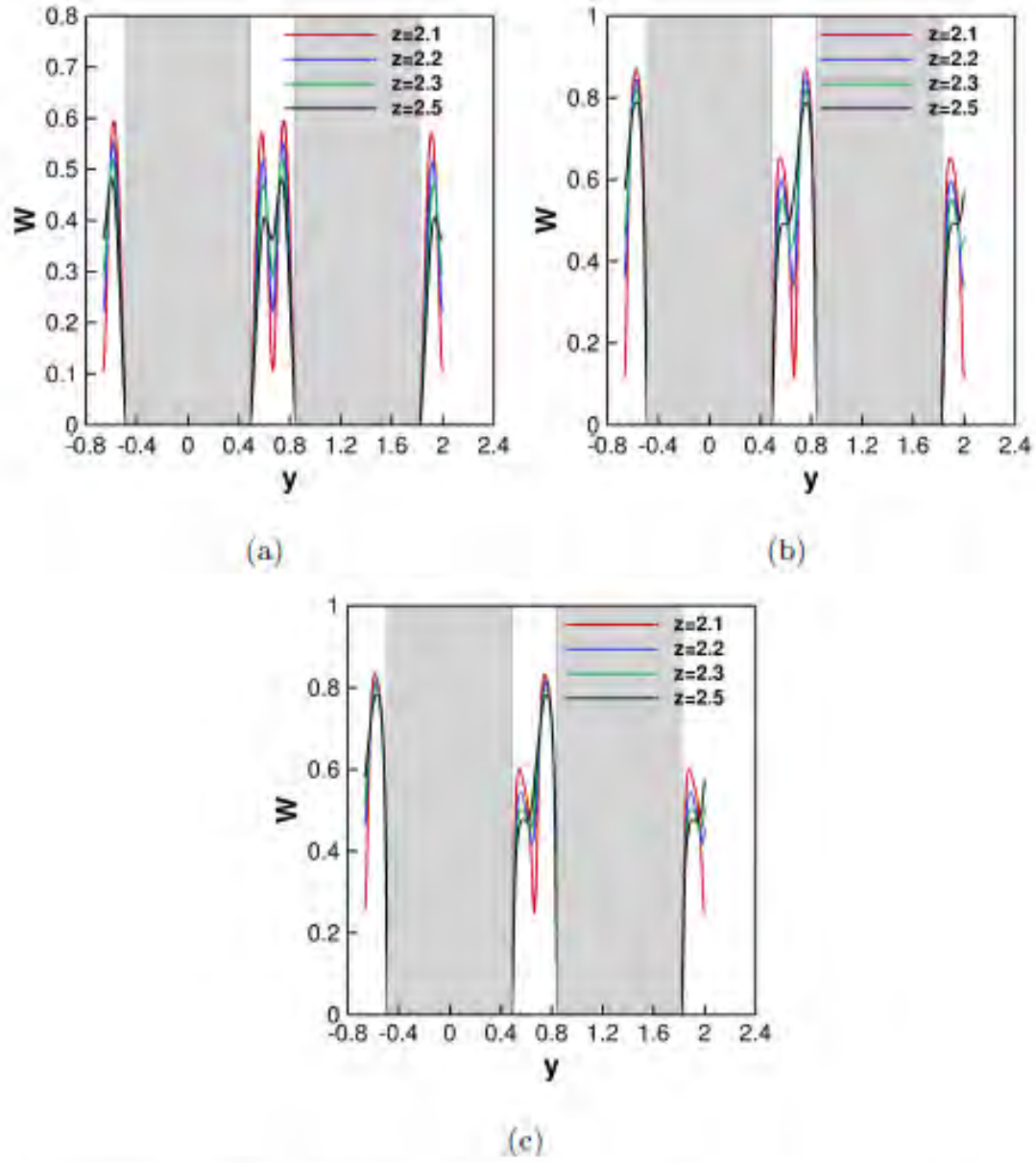


Figure 19: Average axial velocity (W) profile at different Reynolds numbers, (a) $Re=1000$, (b) $Re=5000$, (c) $Re = 10000$. The spacer grid is within the region $-2.005 < z < 2.005$.

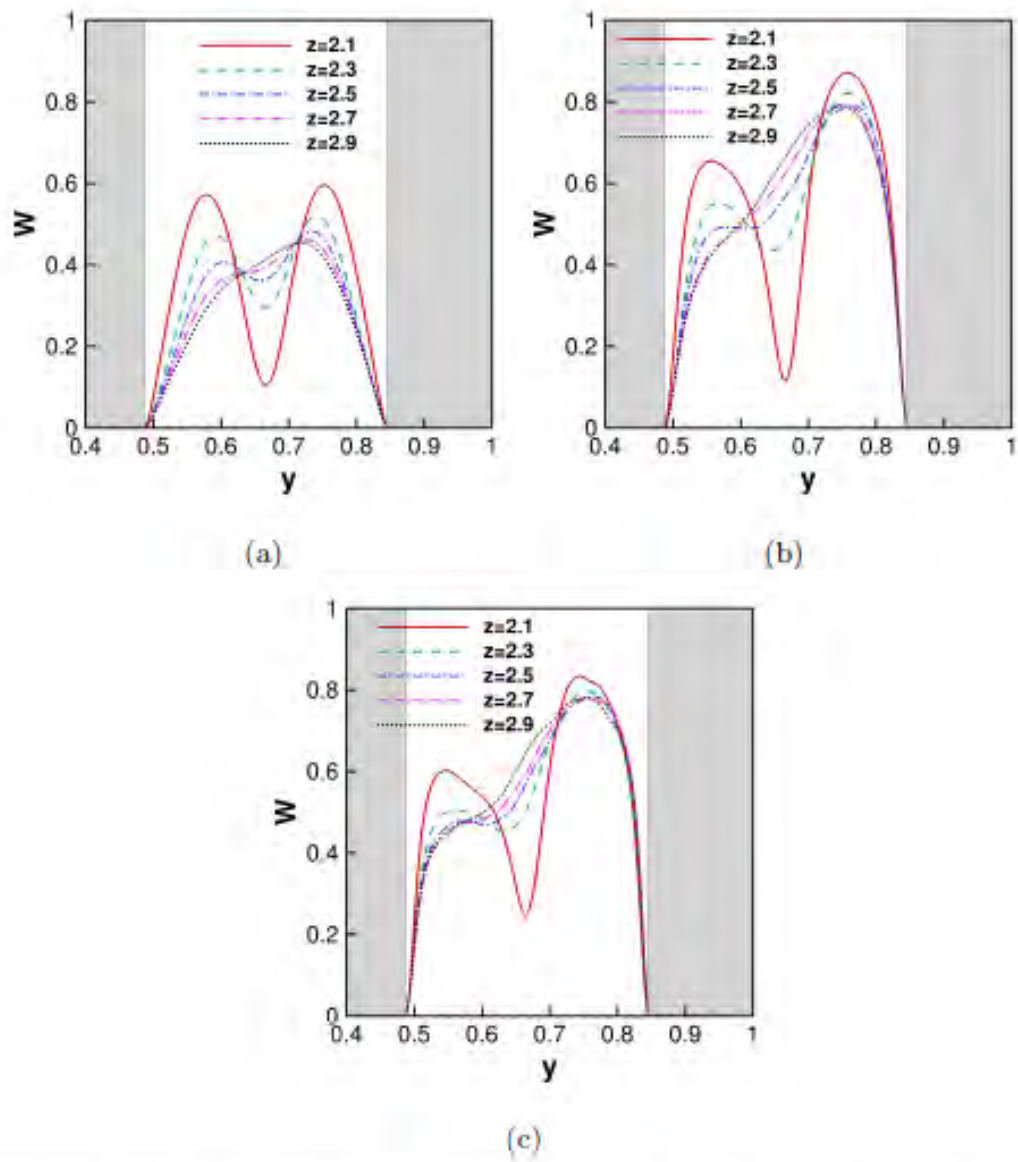


Figure 20: Average axial velocity (W) profile near the spacer grid at different Reynolds numbers, (a) $Re=1000$, (b) $Re=5000$, (c) $Re = 10000$. The spacer grid is within the region $-2.005 < z < 2.005$.

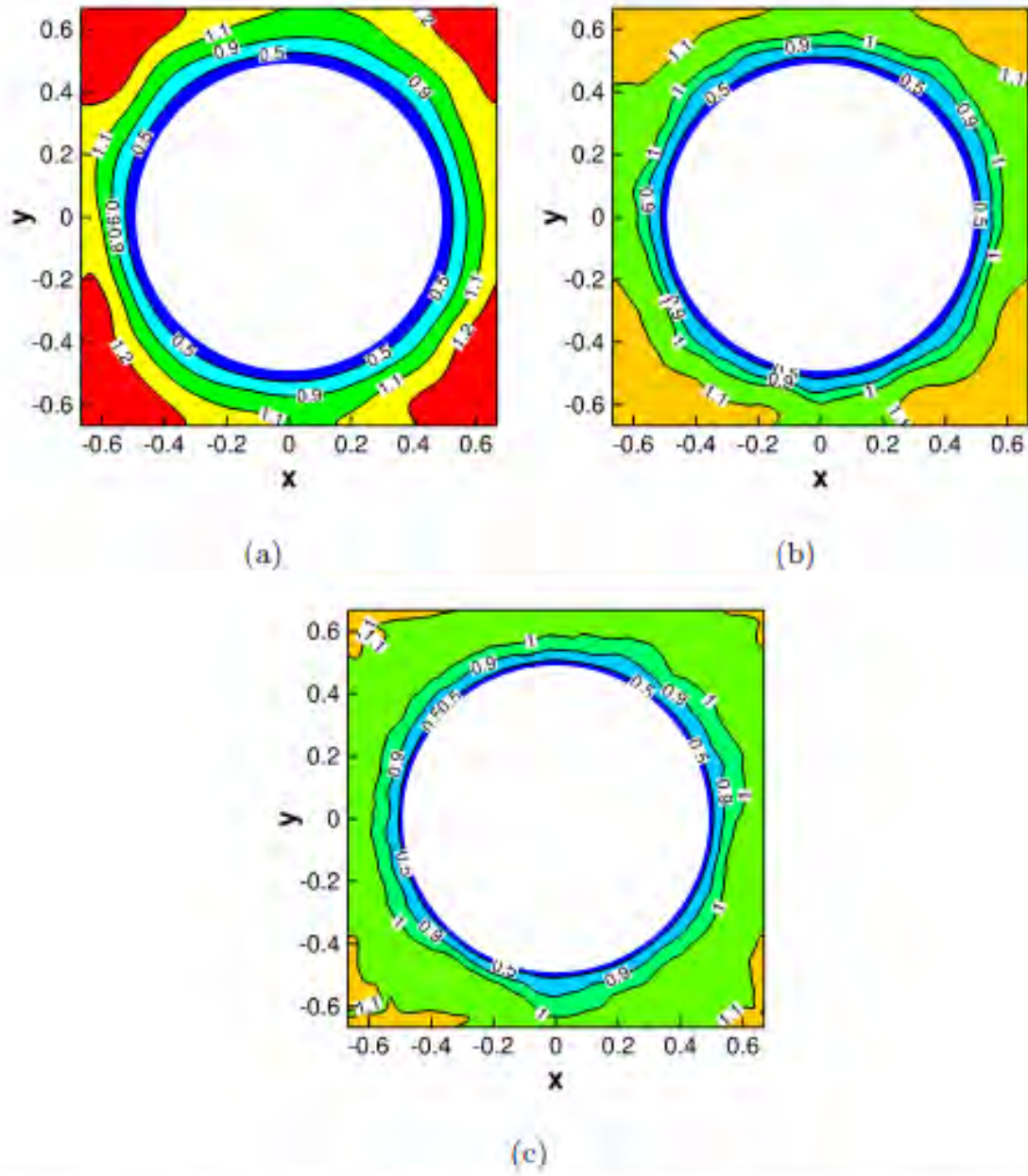


Figure 21: Average axial velocity (W) profile near the spacer grid at different Reynolds numbers in the slice $z = -3$, (a) $Re=1000$, (b) $Re=5000$, (c) $Re = 10000$. The spacer grid is within the region $-2.005 < z < 2.005$.

6. Scalability in parallel computing

The code has both nearly linear strong and weak scalabilities in the simulation of flows over 6×6 cylinder bundle, as shown in table 1 and table 2.

The estimated cost for the simulation with a grid of $1024 \times 1024 \times 8192$ is about 20 million core · hour, as shown in table 3.

7. Summary

This is a brief note on the simulation of 6x6 cylinder bundle. The preliminary simulation is conducted on a grid of $512 \times 512 \times 4096$ at $Re = UD/\nu = 10000$. The results show that the spacer grid significantly affects the evolution of vorticity near the cylinder surface. The code shows both nearly linear strong and weak scalability in the simulations. The estimated cost on a a grid of $1024 \times 1024 \times 8192$ is about 20 million core · hour.

8. Appendix

Some parameters in the experiment are listed in table 4

Table 1: Strong scalability of the simulation of flows over 6×6 cylinder bundle on a mesh of $512 \times 512 \times 4096$ (about 1.1 billion) at $Re = 10000$. The number of grid cells on each boundary is 4.

Total Proc.	No. nodes	Proc. per node	Marker per proc.	Pencil	time per step (s)
4096	256	16	4.7×10^4	$512 \times 16 \times 16$	13.6
8192	512	16	3.6×10^4	$512 \times 16 \times 16$	9.5
16384	1024	16	2×10^4	$512 \times 16 \times 8$	5.5
32768	2048	16	1.5×10^4	$512 \times 8 \times 8$	4.3

Table 2: Weak scalability of the simulation of flows over 6×6 cylinder bundle. The number of grid cells on each boundary is 4.

Total Proc.	No. nodes	Proc. per node	Marker per proc.	Pencil	time per step (s)
1024	64	16	5.1×10^4	$256 \times 32 \times 16$	10.1
8192	512	16	3.6×10^4	$512 \times 16 \times 16$	9.5
65536	4096	16	3.4×10^4	$1024 \times 16 \times 8$	11.7

Table 3: Estimations of computational cost

Item	Case A (current)	Case B
Cylinder	6×6	6×6
Grid	$512 \times 512 \times 4096 \approx 1.1b$	$1024 \times 1024 \times 8192 \approx 8.6b$
Pencil	$512 \times 16 \times 16$	$1024 \times 16 \times 16$
No. Lag. points per proc.	3.6×10^4	6.4×10^4
No. cores	8,192	32768
Time step	8×10^{-4}	4×10^{-4}
Total time	50	50
Total No. step	62,500	125,000
cost per step (sec.)	9.5	17.2
Total cost (core · hour)	1.4×10^6	19.5×10^6
Wall clock cost (hours)	165 (about a week)	597 (about 25 days)

Table 4: Parameters in the experiment

Item	dimensional value	Non-dimensional value
Diameter of the cylinder	14.25 mm	1
Pitch to diameter ratio		1.33
Cross section	$154 \times 124 \text{ mm}^2$	10.8×8.7
Width of the spacer grid	113.7^a mm	7.98
Gap 1 between the wall and spacer grid	20.2^b mm	1.42
Gap 2 between the wall and spacer grid	5.2^c mm	0.36
Gap between the rod wall and spacer grid	2.35^d mm	0.165
Height of the rod array	4000 mm	280.7
Position of the vertical PIV plane	$15 \text{ mm} + 4\text{th SG}^e$	1.05
Bulk velocity	1.01 m/s	-
Reynolds number $Re_D = WD/\nu$		14335^f
Sampling time	4 s	283.5^g
Sample point 1 (from the wall)	3 mm	0.21
Sample point 2 (from the wall)	7 mm	0.49
Sample point 3 (from the wall)	10 mm	0.70
Filter frequency	6 Hz	0.085^h

^a $1.33 \times 6 \times 14.25$ ^b $(154 - 113.7)/2$ ^c $(124 - 113.7)/2$ ^d $(1.33 - 1.0) \times 14.25/2$, at the center of rod^e Is it measured from the lower edge ?^f $1.01 \times 0.01425 / (1.004 \times 10^{-6})$ ^g $4 / (0.01425 / 1.01)$ ^h $6 / (1.01 / 0.01425)$

6. List of Experimental Runs

Tests in air (dry conditions):

Tests in Air Sorted by Shake Table Frequency and Amplitude			
Frequency (Hz)	Displacement (mm)	Testing Date	Notes
0-6 Hz	1	14-Nov-14	Sweeping frequency test with 0.01 Hz increment
0-6 Hz	1.2	14-Nov-14	
0-6 Hz	1.5	14-Nov-14	
0.01	10	14-Nov-14	
0.02	10	14-Nov-14	
0.03	10	14-Nov-14	
0.05	10	5-Nov-14	
0.1	3	6-Oct-14	
0.1	90	5-Nov-14	
0.2	50	5-Nov-14	
0.3	50	5-Nov-14	
0.4	3	6-Oct-14	
0.5	50	5-Nov-14	
0.8	3	6-Oct-14	
1	2	6-Oct-14	
1	10	5-Nov-14	
1	15	5-Nov-14	
1	20	5-Nov-14	
1.2	3	6-Oct-14	
1.2	10	5-Nov-14	
1.4	3	6-Oct-14	
1.5	2	5-Nov-14	
1.5	3	5-Nov-14	
1.5	4	5-Nov-14	
1.5	5	5-Nov-14	
1.6	2	6-Oct-14	
1.6	2	5-Nov-14	
1.6	3	5-Nov-14	
1.6	4	5-Nov-14	
1.8	1	5-Nov-14	
1.8	1	14-Nov-14	
1.8	1.5	6-Oct-14	
1.8	1.5	5-Nov-14	
1.8	1.5	14-Nov-14	
1.8	2	5-Nov-14	
1.8	2	14-Nov-14	
2	1	5-Nov-14	
2	1	14-Nov-14	
2	1.2	5-Nov-14	
2	1.2	14-Nov-14	
2	1.5	6-Oct-14	

Tests in Air Sorted by Shake Table Frequency and Amplitude

Frequency (Hz)	Displacement (mm)	Testing Date	Notes
2	1.5	5-Nov-14	
2	1.5	14-Nov-14	
2.1	1.5	6-Oct-14	
2.2	1	5-Nov-14	
2.2	1.2	5-Nov-14	
2.2	1.5	6-Oct-14	
2.2	1.5	5-Nov-14	
2.2	2	5-Nov-14	
2.4	1.2	6-Oct-14	
2.8	0.8	6-Oct-14	
3.1	0.8	6-Oct-14	
3.5	0.8	6-Oct-14	
4	0.8	6-Oct-14	
4.5	0.8	6-Oct-14	
5	0.8	6-Oct-14	
5	0.8	5-Nov-14	
5	1.5	5-Nov-14	
5	3	5-Nov-14	
5	6	5-Nov-14	
5.5	0.8	6-Oct-14	
5.5	0.8	5-Nov-14	
5.5	1.5	5-Nov-14	
5.5	3	5-Nov-14	
5.5	6	5-Nov-14	
5.6	0.8	6-Oct-14	
6	0.8	6-Oct-14	
6.8	0.8	5-Nov-14	
6.8	1.5	5-Nov-14	
6.8	3	5-Nov-14	
8.5	0.8	5-Nov-14	
8.5	1.5	5-Nov-14	
8.5	3	5-Nov-14	
8.5	4.5	5-Nov-14	

Tests in Water:

Tests in Still Water Sorted by Shake Table Frequency and Amplitude			
Frequency (Hz)	Displacement (mm)	Testing Date	Notes
0-5 Hz	2	1-Apr-15	Sweeping frequency test with 0.02 Hz increment
0-7 Hz	2	7-Apr-15	
5-7 Hz	2	1-Apr-15	
0.2	5	13-Jan-15	
0.2	5	29-Jan-15	
0.2	5	12-Feb-15	
0.2	10	13-Jan-15	
0.2	10	29-Jan-15	
0.2	20	13-Jan-15	
0.2	20	29-Jan-15	
0.2	20	12-Feb-15	
0.2	40	13-Jan-15	
0.2	40	29-Jan-15	
0.2	60	29-Jan-15	
0.2	80	13-Jan-15	
0.2	80	12-Feb-15	
0.4	60	24-Mar-15	
0.4	80	24-Mar-15	
0.6	2	12-Feb-15	
0.6	5	12-Feb-15	
0.6	5	1-Apr-15	
0.6	7.5	1-Apr-15	
0.6	10	1-Apr-15	
0.6	12.5	1-Apr-15	
0.6	15	1-Apr-15	
0.6	17.5	1-Apr-15	
0.6	20	1-Apr-15	
0.6	25	1-Apr-15	
0.6	30	1-Apr-15	
0.6	35	1-Apr-15	
0.8	2	12-Feb-15	
0.8	3	4-Feb-15	
0.8	5	4-Feb-15	
0.8	5	12-Feb-15	
1	2	29-Jan-15	
1	2	12-Feb-15	
1	2	22-Apr-15	
1	2	23-Apr-15	3 planes, between rod 2 (P3) and rod 3 (P1)
1	3	4-Feb-15	
1	3	22-Apr-15	
1	3	23-Apr-15	3 planes, between rod 2 (P3) and rod 3 (P1)
1	5	4-Feb-15	

Tests in Still Water Sorted by Shake Table Frequency and Amplitude

Frequency (Hz)	Displacement (mm)	Testing Date	Notes
1	5	12-Feb-15	
1	5	22-Apr-15	
1	5	23-Apr-15	3 planes, between rod 2 (P3) and rod 3 (P1)
1	7.5	22-Apr-15	
1	7.5	23-Apr-15	3 planes, between rod 2 (P3) and rod 3 (P1)
1	10	22-Apr-15	
1	10	23-Apr-15	3 planes, between rod 2 (P3) and rod 3 (P1)
1	12.5	22-Apr-15	
1	15	22-Apr-15	
1	17.5	22-Apr-15	
1	20	22-Apr-15	
1.1	2	29-Jan-15	
1.1	2	12-Feb-15	
1.1	5	12-Feb-15	
1.2	2	29-Jan-15	
1.2	2	4-Feb-15	
1.2	2	12-Feb-15	
1.2	2	24-Mar-15	
1.2	2	1-Apr-15	
1.2	2	7-Apr-15	
1.2	3	29-Jan-15	
1.2	3	4-Feb-15	
1.2	3	24-Mar-15	
1.2	3	1-Apr-15	
1.2	3	7-Apr-15	
1.2	3	9-Apr-15	19 plane scan, between rod 2 (P1) and rod 3 (P19), only 16 planes completed before shake table had to be shut down
1.2	5	4-Feb-15	
1.2	5	12-Feb-15	
1.2	5	24-Mar-15	
1.2	5	1-Apr-15	
1.2	5	7-Apr-15	
1.2	7.5	24-Mar-15	
1.2	7.5	1-Apr-15	
1.2	7.5	7-Apr-15	
1.2	7.5	15-Apr-15	19 plane scan, between rod 2 (P1) and rod 3 (P19)
1.2	7.5	30-Apr-15	19 plane scan, between rod 2 (P1) and rod 3 (P19)
1.2	7.5	1-May-15	19 plane scan, between rod 2 (P1) and rod 3 (P19)
1.2	9	7-Apr-15	
1.2	10	24-Mar-15	
1.2	10	1-Apr-15	

Tests in Still Water Sorted by Shake Table Frequency and Amplitude			
Frequency (Hz)	Displacement (mm)	Testing Date	Notes
1.2	10	7-Apr-15	
1.2	10	21-Apr-15	19 plane scan, between rod 2 (P1) and rod 3 (P19)
1.2	11	7-Apr-15	
1.2	12.5	24-Mar-15	
1.2	12.5	1-Apr-15	
1.2	12.5	7-Apr-15	
1.2	12.5	22-Apr-15	19 plane scan, between rod 2 (P1) and rod 3 (P19)
1.2	15	24-Mar-15	
1.2	15	1-Apr-15	
1.2	15	21-Apr-15	
1.2	17.5	24-Mar-15	
1.2	17.5	1-Apr-15	
1.2	17.5	21-Apr-15	
1.2	20	24-Mar-15	
1.2	20	1-Apr-15	
1.2	20	21-Apr-15	
1.2	20	5-May-15	6 planes, between rod 3 (P1) and rod 1 (P6)
1.3	2	29-Jan-15	
1.3	2	12-Feb-15	
1.3	5	12-Feb-15	
1.4	2	29-Jan-15	
1.4	2	12-Feb-15	
1.4	2	22-Apr-15	
1.4	2	23-Apr-15	3 planes, between rod 2 (P3) and rod 3 (P1)
1.4	3	29-Jan-15	
1.4	3	4-Feb-15	
1.4	3	22-Apr-15	
1.4	3	23-Apr-15	3 planes, between rod 2 (P3) and rod 3 (P1)
1.4	5	4-Feb-15	
1.4	5	12-Feb-15	
1.4	5	22-Apr-15	
1.4	5	23-Apr-15	3 planes, between rod 2 (P3) and rod 3 (P1)
1.4	7.5	22-Apr-15	
1.4	7.5	23-Apr-15	
1.4	10	22-Apr-15	
1.4	10	23-Apr-15	3 planes, between rod 2 (P3) and rod 3 (P1)
1.4	12.5	22-Apr-15	
1.4	15	22-Apr-15	
1.5	2	29-Jan-15	
1.6	2	13-Jan-15	
1.6	2	29-Jan-15	
1.6	2	12-Feb-15	

Tests in Still Water Sorted by Shake Table Frequency and Amplitude

Frequency (Hz)	Displacement (mm)	Testing Date	Notes
1.6	2	7-Apr-15	
1.6	3	29-Jan-15	
1.6	3	4-Feb-15	
1.6	3	7-Apr-15	
1.6	5	4-Feb-15	
1.6	5	12-Feb-15	
1.6	5	7-Apr-15	
1.6	7.5	7-Apr-15	
1.6	10	7-Apr-15	
1.6	10	15-Apr-15	
1.6	11	15-Apr-15	
1.6	12	15-Apr-15	
1.6	12.5	7-Apr-15	
1.6	13	15-Apr-15	
1.6	14	15-Apr-15	
1.6	15	15-Apr-15	
1.7	2	13-Jan-15	
1.7	2	29-Jan-15	
1.8	1	13-Jan-15	
1.8	1.5	13-Jan-15	
1.8	2	13-Jan-15	
1.8	2	29-Jan-15	
1.8	2	12-Feb-15	
1.8	3	29-Jan-15	
1.8	3	4-Feb-15	
1.8	5	4-Feb-15	
1.9	2	13-Jan-15	
1.9	2	29-Jan-15	
2	0.2	13-Jan-15	
2	0.4	13-Jan-15	
2	0.6	13-Jan-15	
2	0.8	13-Jan-15	
2	1	13-Jan-15	
2	1.2	13-Jan-15	
2	1.5	13-Jan-15	
2	2	13-Jan-15	
2	2	29-Jan-15	
2	2	4-Feb-15	
2	2	12-Feb-15	
2	2	7-Apr-15	
2	3	29-Jan-15	
2	3	4-Feb-15	

Tests in Still Water Sorted by Shake Table Frequency and Amplitude

Frequency (Hz)	Displacement (mm)	Testing Date	Notes
2	3	7-Apr-15	
2	5	4-Feb-15	
2	5	7-Apr-15	
2	7.5	7-Apr-15	
2	10	7-Apr-15	
2.1	2	13-Jan-15	
2.2	2	13-Jan-15	
2.2	2	12-Feb-15	
2.3	2	13-Jan-15	
2.4	2	13-Jan-15	
2.4	2	12-Feb-15	
2.5	2	13-Jan-15	
2.6	2	12-Feb-15	
2.6	2	24-Mar-15	
2.6	2	1-Apr-15	
2.6	3	24-Mar-15	
2.6	3	1-Apr-15	
2.6	5	24-Mar-15	
2.6	5	1-Apr-15	
2.6	6	1-Apr-15	
2.8	3	24-Mar-15	
3	3	24-Mar-15	
3	3	30-Apr-15	
3	4	30-Apr-15	
3	5	30-Apr-15	
3.2	3	24-Mar-15	
3.4	3	24-Mar-15	
3.6	3	24-Mar-15	
3.8	3	24-Mar-15	
4	3	24-Mar-15	
4.2	3	24-Mar-15	
4.4	3	24-Mar-15	
4.6	3	24-Mar-15	
4.8	3	24-Mar-15	
5	3	24-Mar-15	
5.2	2	30-Apr-15	
5.2	3	30-Apr-15	
5.2	4	30-Apr-15	
7	2	15-Apr-15	

Tests with Axial Flow with Water as Working Fluid Sorted by Shake Table Frequency and Amplitude per Flow Rate						
Frequency (Hz)	Displacement (mm)	Velocity in Bundle (m/s)	Flow Rate (GPM)	VFD Frequency	Date	Notes
0.7	3	2	30	437	23-Apr-15	Sweeping frequency test with 0.02 Hz increment
0.7	3	3	45	670	28-Apr-15	Sweeping frequency test with 0.02 Hz increment
0.7 Hz	2	1	15	220	15-Apr-15	Sweeping frequency test with 0.02 Hz increment
0.7 Hz	3	1	15	220	21-Apr-15	Sweeping frequency test with 0.02 Hz increment
1.6	2	1	15	220	21-Apr-15	
1.6	3	1	15	220	21-Apr-15	
1.6	5	1	15	220	21-Apr-15	
1.6	7.5	1	15	220	21-Apr-15	
1.6	10	1	15	220	21-Apr-15	
1.6	10	1	15	220	1-May-15	19 plane scan, between rod 2 (P1) and rod 3 (P19)
1.6	15	1	15	220	30-Apr-15	
1.6	15	1	15	220	5-May-15	6 planes, between rod 3 (P1) and rod 1 (P6)
1.6	17.5	1	15	220	30-Apr-15	
1.6	17.5	1	15	220	5-May-15	
1.6	20	1	15	220	5-May-15	
2	2	1	15	220	28-Apr-15	
2	3	1	15	220	28-Apr-15	
2	5	1	15	220	28-Apr-15	
2	7.5	1	15	220	28-Apr-15	
2	10	1	15	220	5-May-15	6 planes, between rod 3 (P1) and rod 1 (P6)
2	12.5	1	15	220	5-May-15	
2.4	2	1	15	220	28-Apr-15	3 planes, between rod 2 (P3) and rod 3 (P1)
2.4	3	1	15	220	28-Apr-15	3 planes, between rod 2 (P3) and rod 3 (P1)
2.4	5	1	15	220	28-Apr-15	3 planes, between rod 2 (P3) and rod 3 (P1)
2.8	2	1	15	220	28-Apr-15	
2.8	3	1	15	220	28-Apr-15	
3	3	1	15	220	5-May-15	
3	5	1	15	220	5-May-15	6 planes, between rod 3 (P1) and rod 1 (P6)
1.6	2	2	30	437	6-May-15	
1.6	3	2	30	437	6-May-15	
1.6	5	2	30	437	6-May-15	

Tests with Axial Flow with Water as Working Fluid Sorted by Shake Table Frequency and Amplitude per Flow Rate						
Frequency (Hz)	Displacement (mm)	Velocity in Bundle (m/s)	Flow Rate (GPM)	VFD Frequency	Date	Notes
1.6	7.5	2	30	437	6-May-15	
1.6	10	2	30	437	6-May-15	
1.6	12.5	2	30	437	6-May-15	
1.6	15	2	30	437	6-May-15	
1.6	15	2	30	437	6-May-15	6 planes, between rod 3 (P1) and rod 1 (P6), repeat for rod 2 (P3)
1.6	17.5	2	30	437	6-May-15	
1.6	20	2	30	437	6-May-15	
2	2	2	30	437	6-May-15	
2	3	2	30	437	6-May-15	
2	5	2	30	437	6-May-15	6 planes, between rod 3 (P1) and rod 1 (P6), repeat for rod 2 (P3)
2	5	2	30	437	6-May-15	
2	7.5	2	30	437	6-May-15	
2	10	2	30	437	6-May-15	6 planes, between rod 3 (P1) and rod 1 (P6), repeat for rod 2 (P3)
3	5	2	30	437	6-May-15	
5	3	2	30	437	23-Apr-15	
5	3	2	30	437	6-May-15	
7	3	2	30	437	23-Apr-15	
1.6	2	3	40	593.4	6-May-15	
1.6	3	3	40	593.4	6-May-15	
1.6	5	3	40	593.4	6-May-15	
1.6	7.5	3	40	593.4	6-May-15	
1.6	10	3	40	593.4	6-May-15	
1.6	12.5	3	40	593.4	6-May-15	
1.6	15	3	40	593.4	6-May-15	
1.6	15	3	40	593.4	6-May-15	6 planes, between rod 3 (P1) and rod 1 (P6)
1.6	17.5	3	40	593.4	6-May-15	
1.6	20	3	40	593.4	6-May-15	
2	2	3	40	593.4	6-May-15	
2	3	3	40	593.4	6-May-15	
2	5	3	40	593.4	6-May-15	6 planes, between rod 3 (P1) and rod 1 (P6)
2	5	3	40	593.4	6-May-15	
2	7.5	3	40	593.4	6-May-15	
2	10	3	40	593.4	6-May-15	
3	5	3	40	593.4	6-May-15	

Tests with Axial Flow with Water as Working Fluid Sorted by Shake Table Frequency and Amplitude per Flow Rate

Frequency (Hz)	Displacement (mm)	Velocity in Bundle (m/s)	Flow Rate (GPM)	VFD Frequency	Date	Notes
5	3	3	40	593.4	6-May-15	
5	2	3	45	670	28-Apr-15	
7	2	3	45	670	28-Apr-15	
0.6	3		12.4	189	12-Feb-15	
0.8	3		12.4	189	12-Feb-15	
1	3		12.4	189	12-Feb-15	
1.2	3		12.4	189	12-Feb-15	
1.6	3		12.4	189	12-Feb-15	
1.8	3		12.4	189	12-Feb-15	
2	3		12.4	189	12-Feb-15	
2.2	3		12.4	189	12-Feb-15	
2.4	3		12.4	189	12-Feb-15	
2.6	3		12.4	189	12-Feb-15	
1	3		24	362	12-Feb-15	
1.2	3		24	362	12-Feb-15	
1.4	3		24	362	12-Feb-15	
1.6	3		24	362	12-Feb-15	
1.8	3		24	362	12-Feb-15	
2	3		24	362	12-Feb-15	
2.2	3		24	362	12-Feb-15	
2.4	3		24	362	12-Feb-15	
2.6	3		24	362	12-Feb-15	
0.2	5		85.8	17.5	29-Jan-15	
0.2	10		85.8	17.5	29-Jan-15	
0.2	10		264.5	17.5	4-Feb-15	
0.2	20		264.5	17.5	4-Feb-15	
0.2	40		264.5	17.5	4-Feb-15	
0.2	50		264.5	17.5	4-Feb-15	
0.2	80		264.5	17.5	4-Feb-15	
0.8	5		264.5	17.5	4-Feb-15	
1	5		264.5	17.5	4-Feb-15	
1.2	3		264.5	17.5	4-Feb-15	
1.2	5		264.5	17.5	4-Feb-15	
1.4	3		264.5	17.5	4-Feb-15	
1.4	5		264.5	17.5	4-Feb-15	
1.6	3		264.5	17.5	4-Feb-15	
1.6	5		264.5	17.5	4-Feb-15	
1.8	3		264.5	17.5	4-Feb-15	
1.8	5		264.5	17.5	4-Feb-15	
2	3		264.5	17.5	4-Feb-15	
1.2	2		285	19	29-Jan-15	
1.6	2		285	19	29-Jan-15	
1.8	2		285	19	29-Jan-15	
1.4	2		285	19	29-Jan-15	

Test conducted in dry environment between water and oil testing

Interlude Tests In Air Sorted by Shake Table Frequency and Amplitude			
Frequency (Hz)	Displacement (mm)	Testing Date	Notes
0-7 Hz	1	2-Jul	
0-7 Hz	1.2	10-Jul	
0-7 Hz	1.5	10-Jul	
0-7 Hz	0.8	14-Jul	
0-7 Hz	1.3	14-Jul	
0-7 Hz	1	15-Jul	
0-7 Hz	1.1	15-Jul	
0-7 Hz	1.2	16-Jul	
0-7 Hz	1.5	16-Jul	
1.6-2.4 Hz	1.5	16-Jul	
5-7Hz	3	16-Jul	
0.6	14.9	9-Jul	
0.6	14.94	9-Jul	
0.6	14.98	9-Jul	
0.6	15.02	9-Jul	
0.6	15.06	9-Jul	
1	9.9	9-Jul	
1	9.94	9-Jul	
1	9.98	9-Jul	
1	10.02	9-Jul	
1	10.06	9-Jul	
1	10.1	9-Jul	
1.15	2	2-Jul	
1.16	2	2-Jul	
1.17	2	2-Jul	
1.18	2	2-Jul	
1.19	2	2-Jul	
1.2	2	2-Jul	
1.21	2	2-Jul	
1.22	2	2-Jul	
1.23	2	2-Jul	
1.24	2	2-Jul	
1.25	2	2-Jul	
1.6	1.9	9-Jul	
1.6	1.94	9-Jul	
1.6	1.98	9-Jul	
1.6	2.02	9-Jul	
1.6	2.06	9-Jul	
1.6	2.1	9-Jul	
1.88	1	9-Jul	
1.92	1	9-Jul	
1.94	1	9-Jul	
1.96	1	9-Jul	

Sweeping
frequency test
with 0.02 Hz
increment

Interlude Tests in Air Sorted by Shake Table Frequency and Amplitude			
Frequency (Hz)	Displacement (mm)	Testing Date	Notes
2	0.95	2-Jul	5 tests
2	0.96	2-Jul	
2	0.97	2-Jul	
2	0.98	2-Jul	
2	0.99	2-Jul	
2	1	2-Jul	
2	1	9-Jul	
2	1	9-Jul	
2	1.01	2-Jul	
2	1.02	2-Jul	
2	1.03	2-Jul	
2	1.04	2-Jul	
2	1.05	2-Jul	
2.04	1	9-Jul	
2.08	1	9-Jul	
2.12	1	9-Jul	
4	2.94	9-Jul	
4	2.98	9-Jul	
4	3.02	9-Jul	
4	3.06	9-Jul	
7	2.94	9-Jul	
7	2.98	9-Jul	
7	3.02	9-Jul	
7	3.06	9-Jul	

Tests conducted in index matched fluid

Tests in Still P-cymene Sorted by Shake Table Frequency and Amplitude			
Frequency (Hz)	Displacement (mm)	Date	Notes
0-5 Hz	3	13-Aug-15	Pure p-cymene, Sweeping frequency test with 0.02 Hz increment
0-7 Hz	3	27-Aug-15	
1.1	3	13-Aug-15	Pure p-cymene
1.1	3	13-Aug-15	Middle of rods 2 and 3
1.1	5	13-Aug-15	Pure p-cymene
1.15	3	13-Aug-15	Pure p-cymene
1.2	3	13-Aug-15	Middle of rods 2 and 3
1.25	3	13-Aug-15	Pure p-cymene
1.3	3	13-Aug-15	Pure p-cymene
1.3	3	13-Aug-15	Middle of rods 2 and 3
1.3	5	13-Aug-15	Pure p-cymene
1.3	7.5	13-Aug-15	Pure p-cymene
1.35	3	13-Aug-15	Pure p-cymene
1.4	3	13-Aug-15	Middle of rods 2 and 3
1.4	5	13-Aug-15	Pure p-cymene
1.4	7.5	13-Aug-15	Pure p-cymene
1.45	3	13-Aug-15	Pure p-cymene
1.5	3	13-Aug-15	Pure p-cymene
1.55	3	13-Aug-15	Pure p-cymene
1.5	3	13-Aug-15	Middle of rods 2 and 3
1.55	3	13-Aug-15	Pure p-cymene
1.2	5	27-Aug-15	Pure p-cymene
1.2	7.5	27-Aug-15	Pure p-cymene
1.2	10	27-Aug-15	Pure p-cymene
1.2	12.5	27-Aug-15	Pure p-cymene
1.3	5	27-Aug-15	Pure p-cymene
1.3	7.5	27-Aug-15	Pure p-cymene
1.3	10	27-Aug-15	Pure p-cymene
1.3	12.5	27-Aug-15	Pure p-cymene
1.4	5	27-Aug-15	Pure p-cymene
1.4	7.5	27-Aug-15	Pure p-cymene
1.4	10	27-Aug-15	Pure p-cymene
1.4	12.5	27-Aug-15	Pure p-cymene
1.5	5	27-Aug-15	Pure p-cymene
1.5	7.5	27-Aug-15	Pure p-cymene
1.5	10	27-Aug-15	Pure p-cymene
1.5	12.5	27-Aug-15	Pure p-cymene
0.55	2	9-Sep-15	Binary Mix P-cymene and Cinnamic Aldehyde
0.55	3	9-Sep-15	Binary Mix P-cymene and Cinnamic Aldehyde

Tests in Still P-cymene Sorted by Shake Table Frequency and Amplitude			
Frequency (Hz)	Displacement (mm)	Date	Notes
0.55	4	9-Sep-15	Binary Mix P-cymene and Cinnamic Aldehyde
0.55	5	9-Sep-15	Binary Mix P-cymene and Cinnamic Aldehyde
0.55	6	9-Sep-15	Binary Mix P-cymene and Cinnamic Aldehyde
0.55	7.5	9-Sep-15	Binary Mix P-cymene and Cinnamic Aldehyde
0.65	2	9-Sep-15	Binary Mix P-cymene and Cinnamic Aldehyde
0.75	3	9-Sep-15	Binary Mix P-cymene and Cinnamic Aldehyde
0.85	4	9-Sep-15	Binary Mix P-cymene and Cinnamic Aldehyde
0.95	5	9-Sep-15	Binary Mix P-cymene and Cinnamic Aldehyde
1.05	6	9-Sep-15	Binary Mix P-cymene and Cinnamic Aldehyde
1.2	2	18-Sep-15	Binary Mix P-cymene and Cinnamic Aldehyde
1.2	3	18-Sep-15	Binary Mix P-cymene and Cinnamic Aldehyde
1.2	4	18-Sep-15	Binary Mix P-cymene and Cinnamic Aldehyde
1.2	5	18-Sep-15	Binary Mix P-cymene and Cinnamic Aldehyde
1.2	6	9-Sep-15	Binary Mix P-cymene and Cinnamic Aldehyde
1.2	7.5	9-Sep-15	Binary Mix P-cymene and Cinnamic Aldehyde
1.3	2	18-Sep-15	Binary Mix P-cymene and Cinnamic Aldehyde
1.3	3	18-Sep-15	Binary Mix P-cymene and Cinnamic Aldehyde
1.3	4	18-Sep-15	Binary Mix P-cymene and Cinnamic Aldehyde
1.3	5	18-Sep-15	Binary Mix P-cymene and Cinnamic Aldehyde
1.3	6	9-Sep-15	Binary Mix P-cymene and Cinnamic Aldehyde
1.4	7.5	9-Sep-15	Binary Mix P-cymene and Cinnamic Aldehyde
1.3	7.5	9-Sep-15	Binary Mix P-cymene and Cinnamic Aldehyde
1.35	2	18-Sep-15	Binary Mix P-cymene and Cinnamic Aldehyde
1.35	3	18-Sep-15	Binary Mix P-cymene and Cinnamic Aldehyde
1.35	4	18-Sep-15	Binary Mix P-cymene and Cinnamic Aldehyde
1.35	5	18-Sep-15	Binary Mix P-cymene and Cinnamic Aldehyde
1.35	6	9-Sep-15	Binary Mix P-cymene and Cinnamic Aldehyde
1.35	7.5	9-Sep-15	Binary Mix P-cymene and Cinnamic Aldehyde
1.4	2	18-Sep-15	Binary Mix P-cymene and Cinnamic Aldehyde
1.4	3	18-Sep-15	Binary Mix P-cymene and Cinnamic Aldehyde
1.4	4	18-Sep-15	Binary Mix P-cymene and Cinnamic Aldehyde
1.4	5	18-Sep-15	Binary Mix P-cymene and Cinnamic Aldehyde
1.4	6	9-Sep-15	Binary Mix P-cymene and Cinnamic Aldehyde
1.4	7.5	9-Sep-15	Binary Mix P-cymene and Cinnamic Aldehyde
1.5	2	18-Sep-15	Binary Mix P-cymene and Cinnamic Aldehyde
1.5	3	18-Sep-15	Binary Mix P-cymene and Cinnamic Aldehyde
1.5	4	18-Sep-15	Binary Mix P-cymene and Cinnamic Aldehyde
1.5	5	18-Sep-15	Binary Mix P-cymene and Cinnamic Aldehyde
1.5	6	9-Sep-15	Binary Mix P-cymene and Cinnamic Aldehyde

Tests in Still P-cymene Sorted by Shake Table Frequency and Amplitude			
Frequency (Hz)	Displacement (mm)	Date	Notes
1.5	7.5	9-Sep-15	Binary Mix P-cymene and Cinnamic Aldehyde
1.6	2	9-Sep-15	Binary Mix P-cymene and Cinnamic Aldehyde
1.7	3	9-Sep-15	Binary Mix P-cymene and Cinnamic Aldehyde
1.8	4	9-Sep-15	Binary Mix P-cymene and Cinnamic Aldehyde
1.9	5	9-Sep-15	Binary Mix P-cymene and Cinnamic Aldehyde
2	6	9-Sep-15	Binary Mix P-cymene and Cinnamic Aldehyde
2.1	7.5	9-Sep-15	Binary Mix P-cymene and Cinnamic Aldehyde
2.9	2	9-Sep-15	Binary Mix P-cymene and Cinnamic Aldehyde
2.9	3	9-Sep-15	Binary Mix P-cymene and Cinnamic Aldehyde
3	2	9-Sep-15	Binary Mix P-cymene and Cinnamic Aldehyde
3.1	2	9-Sep-15	Binary Mix P-cymene and Cinnamic Aldehyde
3.1	3	9-Sep-15	Binary Mix P-cymene and Cinnamic Aldehyde
3.2	3	9-Sep-15	Binary Mix P-cymene and Cinnamic Aldehyde
5.05	2	9-Sep-15	Binary Mix P-cymene and Cinnamic Aldehyde
5.05	3	18-Sep-15	Binary Mix P-cymene and Cinnamic Aldehyde
5.05	4	18-Sep-15	Binary Mix P-cymene and Cinnamic Aldehyde
5.15	3	9-Sep-15	Binary Mix P-cymene and Cinnamic Aldehyde
5.25	3	18-Sep-15	Binary Mix P-cymene and Cinnamic Aldehyde
5.15	4	18-Sep-15	Binary Mix P-cymene and Cinnamic Aldehyde
5.2	3	18-Sep-15	Binary Mix P-cymene and Cinnamic Aldehyde
5.2	4	18-Sep-15	Binary Mix P-cymene and Cinnamic Aldehyde
5.25	4	18-Sep-15	Binary Mix P-cymene and Cinnamic Aldehyde
5.3	3	18-Sep-15	Binary Mix P-cymene and Cinnamic Aldehyde
5.35	3	18-Sep-15	Binary Mix P-cymene and Cinnamic Aldehyde
5.35	4	18-Sep-15	Binary Mix P-cymene and Cinnamic Aldehyde

Tests with Axial Flow with Binary Mix of P-cymene and Cinnamic Aldehyde as Working Fluid Sorted by Shake Table
Frequency and Amplitude per Flow Rate

Frequency (Hz)	Displacement (mm)	Velocity in Bundle (m/s)	Flow Rate (GPM)	VFD Frequency	Date	Notes
0.55	5	0.5	113	8.2	21-Sep	
0.55	10	0.5	113	8.2	21-Sep	
0.55	15	0.5	113	8.2	21-Sep	
0.65	5	0.5	113	8.2	21-Sep	
0.65	10	0.5	113	8.2	21-Sep	
0.75	10	0.5	113	8.2	21-Sep	
1.2	2	0.5	113	8.2	21-Sep	
1.2	2	0.5	110	6	25-Sep	2 VFD
1.2	3	0.5	113	8.2	21-Sep	
1.2	3	0.5	110	6	25-Sep	2 VFD
1.2	5	0.5	113	8.2	21-Sep	
1.2	5	0.5	110	6	25-Sep	2 VFD
1.2	10	0.5	113	8.2	21-Sep	
1.3	2	0.5	113	8.2	21-Sep	
1.3	2	0.5	110	6	25-Sep	2 VFD
1.3	3	0.5	113	8.2	21-Sep	
1.3	3	0.5	110	6	25-Sep	2 VFD
1.3	5	0.5	113	8.2	21-Sep	
1.3	5	0.5	110	6	25-Sep	2 VFD
1.3	10	0.5	113	8.2	21-Sep	
1.4	2	0.5	113	8.2	21-Sep	
1.4	2	0.5	110	6	25-Sep	2 VFD
1.4	3	0.5	113	8.2	21-Sep	
1.4	3	0.5	110	6	25-Sep	2 VFD
1.4	5	0.5	113	8.2	21-Sep	
1.4	5	0.5	110	6	25-Sep	2 VFD
1.4	10	0.5	113	8.2	21-Sep	
1.4	10	0.5	113	8.2	21-Sep	
1.5	2	0.5	113	8.2	21-Sep	Test x2 (repeat)
1.5	3	0.5	113	8.2	21-Sep	Test x2 (repeat)
1.5	5	0.5	113	8.2	21-Sep	Test x2 (repeat)
1.5	10	0.5	113	8.2	21-Sep	Test x2 (repeat)
1.5	15	0.5	113	8.2	21-Sep	
1.6	2	0.5	113	8.2	21-Sep	Test x2 (repeat)
1.6	3	0.5	113	8.2	21-Sep	Test x2 (repeat)
1.6	5	0.5	113	8.2	21-Sep	Test x2 (repeat)
1.6	10	0.5	113	8.2	21-Sep	Test x2 (repeat)
1.7	2	0.5	113	8.2	21-Sep	
1.7	3	0.5	113	8.2	21-Sep	
1.7	5	0.5	113	8.2	21-Sep	

Tests with Axial Flow with Binary Mix of p-cymene and Cinnamic Aldehyde as Working Fluid Sorted by Shake Table
Frequency and Amplitude per Flow Rate

Frequency (Hz)	Displacement (mm)	Velocity in Bundle (m/s)	Flow Rate (GPM)	VFD Frequency	Date	Notes
1.7	10	0.5	113	8.2	21-Sep	
1.8	2	0.5	113	8.2	21-Sep	
1.8	3	0.5	113	8.2	21-Sep	
1.8	5	0.5	113	8.2	21-Sep	
1.8	10	0.5	113	8.2	21-Sep	
1.9	2	0.5	113	8.2	21-Sep	
1.9	3	0.5	113	8.2	21-Sep	
1.9	5	0.5	113	8.2	21-Sep	
1.9	10	0.5	113	8.2	21-Sep	
2.9	2	0.5	113	8.2	21-Sep	
2.9	3	0.5	113	8.2	21-Sep	
2.9	15	0.5	113	8.2	21-Sep	
3	2	0.5	113	8.2	21-Sep	
3	3	0.5	113	8.2	21-Sep	
3.1	2	0.5	113	8.2	21-Sep	
3.1	3	0.5	113	8.2	21-Sep	
5.05	2	0.5	113	8.2	21-Sep	
5.15	2	0.5	113	8.2	21-Sep	
5.25	2	0.5	113	8.2	21-Sep	
5.35	2	0.5	113	8.2	21-Sep	
5.45	2	0.5	113	8.2	21-Sep	
1.5	2	1	220	15.2	21-Sep	
1.5	3	1	220	15.2	21-Sep	
1.5	5	1	220	15.2	21-Sep	
1.5	10	1	220	15.2	21-Sep	
1.6	2	1	220	15.2	21-Sep	
1.6	3	1	220	15.2	21-Sep	
1.6	5	1	220	15.2	21-Sep	
1.6	10	1	220	15.2	21-Sep	
1.7	3	1	220	15.2	21-Sep	
1.7	5	1	220	15.2	21-Sep	
1.7	10	1	220	15.2	21-Sep	
1.7	2	1	220	15.2	21-Sep	
1.8	2	1	220	15.2	21-Sep	
1.8	3	1	220	15.2	21-Sep	
1.8	5	1	220	15.2	21-Sep	
1.8	10	1	220	15.2	21-Sep	
1.9	3	1	220	15.2	21-Sep	
1.9	5	1	220	15.2	21-Sep	
1.9	10	1	220	15.2	21-Sep	

Tests with Axial Flow with Binary Mix of P-cymene and Cinnamic Aldehyde as Working Fluid Sorted by Shake Table
Frequency and Amplitude per Flow Rate

Frequency (Hz)	Displacement (mm)	Velocity in Bundle (m/s)	Flow Rate (GPM)	VFD Frequency	Date	Notes
1.9	2	1	220	15.2	21-Sep	
1.3	2	1.5	334	16.1	25-Sep	2 VFD
1.3	3	1.5	334	16.1	25-Sep	2 VFD
1.3	5	1.5	334	16.1	25-Sep	2 VFD
1.3	7.5	1.5	334	16.1	25-Sep	2 VFD
1.4	2	1.5	334	16.1	25-Sep	2 VFD
1.4	3	1.5	334	16.1	25-Sep	2 VFD
1.4	5	1.5	334	16.1	25-Sep	2 VFD
1.4	7.5	1.5	334	16.1	25-Sep	2 VFD
1.5	2	1.5	334	16.1	25-Sep	2 VFD
1.5	3	1.5	334	16.1	25-Sep	2 VFD
1.5	5	1.5	334	16.1	25-Sep	2 VFD
1.5	7.5	1.5	334	16.1	25-Sep	2 VFD
2.4	3	1.5	334	16.1	25-Sep	2 VFD
2.4	4	1.5	334	16.1	25-Sep	2 VFD
2.5	3	1.5	334	16.1	25-Sep	2 VFD
2.5	4	1.5	334	16.1	25-Sep	2 VFD
2.6	3	1.5	334	16.1	25-Sep	2 VFD
2.6	4	1.5	334	16.1	25-Sep	2 VFD
2.7	3	1.5	334	16.1	25-Sep	2 VFD
2.7	4	1.5	334	16.1	25-Sep	2 VFD
2.8	3	1.5	334	16.1	25-Sep	2 VFD
2.8	4	1.5	334	16.1	25-Sep	2 VFD
2.9	3	1.5	334	16.1	25-Sep	2 VFD
2.9	4	1.5	334	16.1	25-Sep	2 VFD
3	3	1.5	334	16.1	25-Sep	2 VFD
3	4	1.5	334	16.1	25-Sep	2 VFD
2.4	2	2	444	21.5	25-Sep	2 VFD
2.5	2	2	444	21.5	25-Sep	2 VFD
2.6	2	2	444	21.5	25-Sep	2 VFD
2.7	2	2	444	21.5	25-Sep	2 VFD
2.8	2	2	444	21.5	25-Sep	2 VFD
2.9	2	2	444	21.5	25-Sep	2 VFD
3	2	2	444	21.5	25-Sep	2 VFD

7. Publications

Journal publications

- Weichselbaum, N.A., Rahimi-Abkenar, M., Vanella, M., Manzari, M.T., Balaras, E., Bardet, P.M., 2015, “Validation Facility and Model Development for Nuclear Fuel Assembly Response to Seismic Loading,” *Journal of Nuclear Engineering and Radiation Science*.
- Fort, C., Fu, C.D., Weichselbaum, N.A., Bardet, P.M., 2015, “Refractive Index and Solubility Control of Para-cymene Solutions,” *Experiments in Fluids*.
- Weichselbaum, N.A., Hussain, S., Rahimi-Abkenar, M., Manzari, M.T., Bardet, P.M., 2015, “Fuel Assembly Oscillation Induced Flow in Initially Stagnant Fluid,” *Journal of Nuclear Technology*. In Print
- Weichselbaum, N.A., Andre, M.A., Rahimi-Abkenar, M., Manzari, M.T., Bardet, P.M., 2016, “High-Resolution Flying-PIV with Optical Fiber Laser Delivery,” *Experiments in Fluids*. In Print

Journal publications in preparation

- We currently working on 4 manuscript drafts for journals such as: Journal of Fluid and Structure, Journal of Fluid Mechanics, Nuclear Technology, etc.

Conference Proceedings

- PIV 2013 conference. June 2013
 1. Systematic timing errors in laser-based transit-time velocimetry.
- American Nuclear Society National Meeting, Washington, DC, November 2013
 1. “Model Development for Nuclear Fuel Assembly Response to Seismic Loads”
 2. “Fuel Rod in Axial Flow on Integral Effects Shake Table”
- 17th International Symposium on Applications of Laser Techniques to Fluid Mechanics, Lisbon, Portugal July 2014
 1. “Single Camera PIV/Shadowgraphy and Laser Delivery on Earthquake Shake Table for Fluid-Structure Interaction Measurements”
 2. “Refractive index and solubility control of para-cymene solutions.”
- ASME International Mechanical Engineering Congress & Exposition, Montreal, Canada November 2014
 1. “Validation Data and Model Development for Nuclear Fuel Assembly Response to Seismic Loading”
- 16th International Topical Meeting on Nuclear Reactor Thermal hydraulics, Chicago, IL, August 2014
 1. “Surrogate Spacer Grid Design for Fluid-structure Interaction Studies in Fuel Bundles”
- 11th International Symposium on Particle Image Velocimetry, Santa Barbara, CA September 2015

1. "Utilization of non-intrusive optical techniques and laser delivery for measuring fluid-structure interaction on an earthquake shake table"
- American Nuclear Society National Meeting, Washington, DC, November 2015
 1. "PWR Fuel Bundle Response to Earthquake Motions in Still Water"
 2. "Three Dimensional Phase Averaged Velocity in PWR Fuel Bundles under External Forcing"
 3. "Fluid Structure Interaction Measurements of a PWR Fuel Bundle with Seismic Forcing"*

Presentations

We had a total of 12 conference presentations over the duration of this project. Including some in the most prestigious conferences such as the Lisbon Laser Symposium, or PIV Symposium.

- ASME Verification and Validation Conference, Las Vegas, NV, May 2013
 1. "Validation Data and Model Development for Nuclear Fuel Assembly Response to Seismic Loads"
- 66th Annual Meeting of the American Physical Society Division of Fluid Dynamics, Pittsburgh, PA November 2013
 1. "Single Rod Vibration in Axial Flow"
- American Nuclear Society National Meeting, Washington, DC, November 2013
 1. "Model Development for Nuclear Fuel Assembly Response to Seismic Loads"
 2. "Fuel Rod in Axial Flow on Integral Effects Shake Table"
- 17th International Symposium on Applications of Laser Techniques to Fluid Mechanics, Lisbon, Portugal July 2014
 1. "Single Camera PIV/Shadowgraphy and Laser Delivery on Earthquake Shake Table for Fluid-Structure Interaction Measurements"
- ASME International Mechanical Engineering Congress & Exposition, Montreal, Canada November 2014
 1. "Validation Data and Model Development for Nuclear Fuel Assembly Response to Seismic Loading"
- Johns Hopkins Univ. CEA FM-Burgers-GWU Research Symposium, Washington, DC, May 2015
 1. "Fluid Structure Interaction Measurements on Seismic Shake Table,"
- 16th International Topical Meeting on Nuclear Reactor Thermal hydraulics, Chicago, IL, August 2014
 1. "Surrogate Spacer Grid Design for Fluid-structure Interaction Studies in Fuel Bundles"
- 11th International Symposium on Particle Image Velocimetry, Santa Barbara, CA September 2015
 1. "Utilization of non-intrusive optical techniques and laser delivery for measuring fluid-structure interaction on an earthquake shake table"

- American Nuclear Society National Meeting, Washington, DC, November 2015
 1. “PWR Fuel Bundle Response to Earthquake Motions in Still Water”
 2. “Three Dimensional Phase Averaged Velocity in PWR Fuel Bundles under External Forcing”
 3. “Fluid Structure Interaction Measurements of a PWR Fuel Bundle with Seismic Forcing”*

Invited Talks

- “Seismic response of nuclear fuel bundles,” University of Wisconsin, Engineering Physics Department, Madison, WI, 03/08/2016.
- “Seismic response of nuclear fuel bundles,” University of Florida, Materials Science and Engineering Department, Gainesville, FL, 02/18/2016.
- “FSI measurements of nuclear fuel bundles during earthquakes,” AIAA SciTech conference, special session on Fluid-Structure Interaction diagnostics, January 2016.
- “Seismic response of nuclear fuel bundles,” Virginia Commonwealth University, Richmond, VA, 2015/08/02.
- “Validation data and model development for nuclear fuel assembly response to seismic loading,” University of Massachusetts, Amherst, MA, 2015/04/13.
- “Validation data and model development for nuclear fuel assembly response to seismic loading,” Idaho National Laboratory, Idaho Falls, ID, 2015/03/10.
- “Validation data and model development for nuclear fuel assembly response to seismic loading,” EDF R&D, Chatou, France, 2014/12/12.
- “Vorticity generation and air entrainment at Free surfaces,” University of Maryland, Aerospace Engineering, 2014/10/22.
- “Seismic response of fuel assemblies,” French Embassy, Washington, DC, 2014/03/24.
- “Validation datasets for high-fidelity simulations of seismic response of fuel assemblies,” Nuclear Science and Engineering, MIT, Cambridge, MA, 2014/02/27.

8. Honors and Awards

1- American Nuclear Society National Meeting, Washington, DC, November 2015, Winner of young professional thermal hydraulics research competition:

Noah A. Weichselbaum: “Fluid Structure Interaction Measurements of a PWR Fuel Bundle with Seismic Forcing”

2- DOE, ASCR Leadership Computing Challenge (ALCC) award for 34 M CPU hours for conducting large scale simulations of this project.

9. Students Involvement

Several students and postdoctoral scholars were involved in this project.

Noah Weichselbaum, PhD in Mechanical Engineering 12/2015, US citizen. He is currently a postdoctoral scholar in Prof. Bardet's laboratory and is looking for permanent employment either in academia or industry.

Morteza Rahimi-Abkenar, PhD in Civil Engineering, expected graduation date of 05/2015.

Shadman Hussain, PhD candidate in Mechanical Engineering.

Matthieu Andre, Postdoctoral scholar Mechanical Engineering.

Pierre Korysko, MS, Nuclear Engineering

Charles Fort, MS, Aerospace Engineering

10. Conclusions

This project required the development of several complex and custom experimental systems and numerical codes. The resulting experimental data have accomplished some “firsts”. It was the first time a flow loop is operated on an earthquake shake table. The data are the first velocity field data acquired on an earthquake shake table (and they were time-resolved). This was the largest number of PIV planes deployed simultaneously in a large facility. This is the first deployment of several non-intrusive diagnostics to study the dynamic response of fuel bundle. In addition to providing benchmark and validation datasets, the data have led to many insights into dynamics of fuel bundles under normal operation and during earthquakes. Furthermore, these insights enabled us to revisit sequence of events at North Anna Power Plant during the VA earthquake of 2011 and provide new explanation for large reactivity excursion observed there.

A large experimental dataset has been obtained from a unique experimental facility for testing a surrogate nuclear fuel bundle exposed to external forcing from seismic forcing. More than 1,000 experimental runs were acquired, many of them were repeat runs sometimes several months apart to gain confidence in repeatability and in the “aging” of the structure. The test section stands 7 m high and has a footprint of 3 m x 3 m. It weights nearly 6 Mtons. It was custom designed by us and is a flexible, modular, refractive index matched facility, Fig. c.1. It can accommodate up to 3 full height fuel bundles at near prototypical Reynolds number. Scaling analysis informed bundle design to guarantee dynamic similarities with vibration dynamics of fuel bundles. Structural dynamics analysis and data confirm that our bundle has the same first, second, and third modes than published data for real bundle. Furthermore, the effect of added mass and bundle stiffening under flow are also consistent with our design. Hence, our scaling analysis is confirmed a posteriori.



**Full height bundle
with custom spacer
grid**



**Test section on
earthquake shake
table**



Complete flow loop

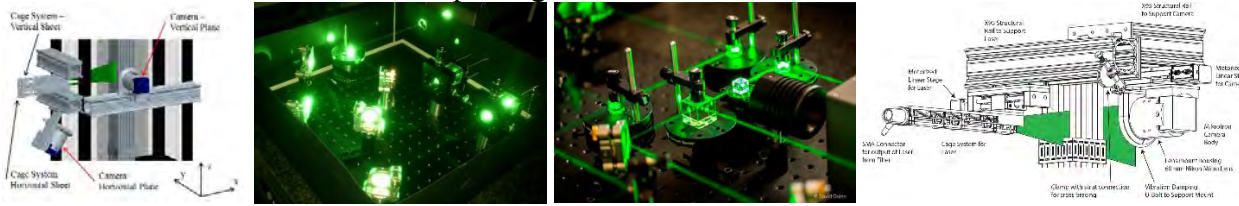


**Test section illuminated by 6
PIV laser planes**

Fig. c.1. Facility design

The data are acquired with both high spatial and temporal resolutions thanks to a custom flying PIV system that is rigidly fixed to the shake table to acquire measurements in the non-inertial reference frame. The development of this PIV system required several experimental “tour de force” such as coupling of laser to optical fibers, selection of new type of cameras, or mounting of custom opto-mechanical system on the test section, Fig. c.2. A small subset of the PIV data has been thoroughly analyzed, ensuring quality of the acquired data by performing uncertainty analysis. From the analysis of still water cases new insights into a pressure gradient driven axial flow are presented for the first time, in addition to a new physical mechanism that can account for the increased damping seen in structural measurements of fuel bundle response to pluck tests above

a certain amplitude (Lu & Steel (2006)). From these cases in still water, insights are applied to cases with axial flow where there is found to be a secondary oscillatory flow present. The secondary flow is driven by pressure gradients in the cross flow that were first observed in still water combined with effects of the spacer grid on the axial flow.



Flying PIV configuration

1st generation optical multiplexer (2 outputs)

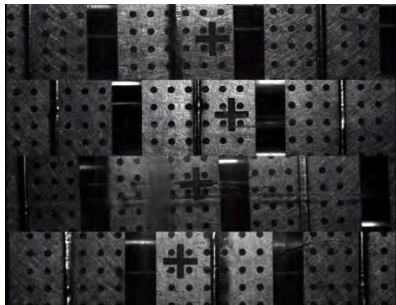
2nd generation optical multiplexer (6 outputs)

Custom opto-mechanical mounts for in-situ PIV.

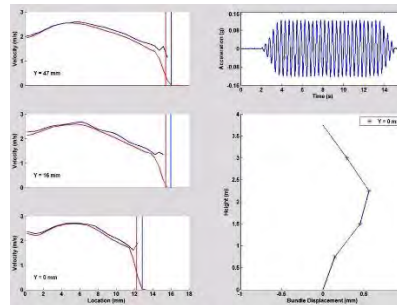
Fig. c.2. Custom optical and opto-mechanical systems developed for new Flying PIV system.

From the tests in air it is apparent that the non-linearity of the structure is captured with the surrogate fuel bundle thanks to the careful design of the scaled spacer grids. The effect of the spacer grids on the fluid coupling is significant, particularly the ability for the fuel rods to slide and rotate with the boundary conditions imposed by the orthogonal set of springs and dimples, and it is important for this to be modeled properly.

From the tests in stagnant fluid a physical mechanism is proposed to describe the source of flow development observed in Fig. c.3. Away from the walls, velocity profiles in the bypass region have a plug flow profile. Flow also starts and stops with bundle oscillation. This indicates that the flow is pressure driven. For the test conditions, pressure gradients in the facility can have two origins; they can be generated by the external forcing and by the assembly oscillation.



DIC cameras composite image



Integrated data, accelerometer, DIC, PIV at three elevations with 1 m/s flow.

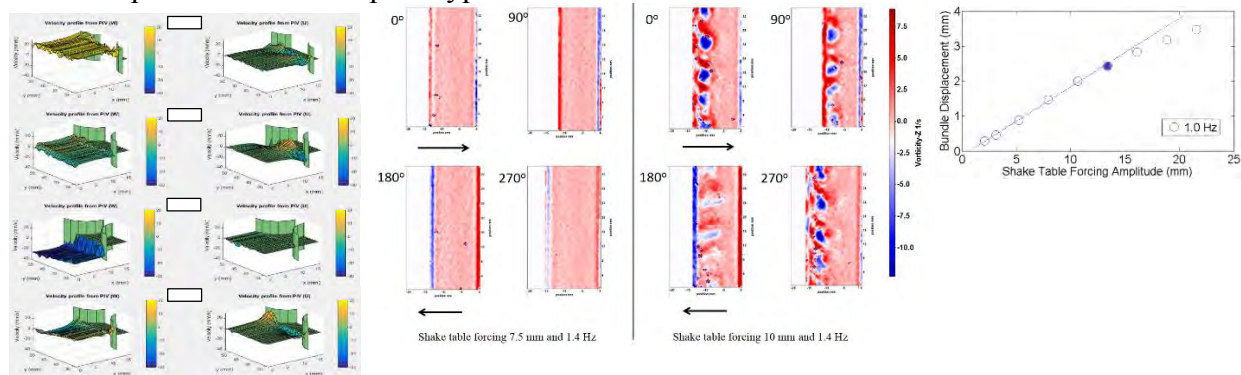
Fig. c.3. Sample PIV and DIC data

In initially stagnant homogeneous fluids, a rigid bundle free to translate in the direction of forcing oscillates under the external forcing; a time varying pressure gradient develops. In a non-inertial frame of reference moving with the bundle, the bundle is stationary and sees an oscillatory flow through it. The rods on the edge of the bundle that face the incoming flow, the “front”, have stagnation lines that develop along their height; due to viscous effects, the “rear” of the bundle will see a lower pressure. Hence a pressure gradient develops across the bundle width; it sustains the cross-flow acceleration through the bundle. The stagnation pressure is the

sum of static pressure with the product of the square of the bundle translation velocity and half of the liquid density. The bundle velocity is the time derivative of the bundle displacement, which scales with the displacement amplitude and frequency. Hence it can be inferred that the transverse pressure fluctuations due to bundle translation scale with the square of the bundle velocity.

In the current facility and in prototypical conditions, the bundles does not translate horizontally, but deflects. In the first mode of vibration considered here, the displacement is maximal near the center and zero at the bundle ends. The vertical deflection of the bundle results in stagnation pressure that varies along the height of the bundle. For an advancing bundle, the stagnation pressure is therefore the greatest at the point of maximum displacement and null at the bundle extremities. Hence, in the closing bypass, two vertical pressure gradients develop between the bundle center and its ends; the gradients are of opposite sign. In the other bypass, two gradients develop between the bundle ends and its center. These gradients are responsible to generate the axial flow observed in the bypass region. Similar to the cross-flow gradient, they might scale with the square of the bundle velocity.

In the flow channel, there are thus several pressure gradients that establish themselves and drive the flow both axially and transversally. The cross flow component through the bundle cannot be observed with the current investigation plane that is centered on a rod. The vertical flow has a phase lag with respect to the bundle oscillation, which might be a signature of the pressure gradients that establish themselves in the flow channel. This is best observed with 3D velocity measurements acquired in the facility, Fig. c.4. Above a certain amplitude of forcing a vortex instability develops between the rods along the axial length. These vortices were first observed in maritime environments due to wave induced oscillatory flows over long cylinder (oil platform support columns) and are referred as Keulegarian-Carpenter (KC) instability. This is the first time this instability is noticed in an enclosed configuration. It has significant effect on bundle response: below the instability limit, the response of the bundle is linear with forcing; above, it is nonlinear, Fig. c.4. This instability might explain noticeable change in damping in bundle in stagnant flow noticed in published data for prototypical bundles.



3D velocity

**Vorticity showing data below and above
KC instability**

**Bundle displacement vs
forcing. Solid point is
onset of KC instability**

Fig. c.4. Velocity data in stagnant flow

These observations from shake testing in still water are found to be applicable to shake testing in axial flow. Particularly the secondary pulsatile flow in the vertical direction is found to be prevalent in the testing in axial flow, which is portrayed in Fig. c.5, where again the fluctuations in vertical velocity, W , can be seen to start and stop with the shake table forcing. Additionally, from this simple observation of the flow and main structures during a forcing cycle of the bundle, it appears that spacer grids markedly affect the local flow. The modulation of the shear layer due to the direct strap wake correlates with the velocity in the wake, as observed in Fig. c.5; the strength of shed vortices increases with wake velocity. Furthermore, from vorticity plots in Fig. c.5, a second shear layer can be observed in frames 5 and 6 that likely is the result of bundle displacement and local flow. In these frames, the bundle moves the fastest away from the bypass wall. This transversal velocity of the bundle is associated with a rapid increase of the axial velocity, hence the cross-flow velocity necessary to satisfy this condition is at its largest and opposes spacer grid motion. These combined effects might lead to separation at the upstream edge of the spacer grid or through the opening through the strap.

This behavior of vortex shedding and the second shear layer are confirmed through analysis of cases with varying shake table forcing frequencies and amplitudes, and with varying axial flow rates. It is found here that the phase lag in the secondary oscillatory flow increases with forcing frequency, which is the same trend found by Ricciardi & Boccaccio (2014). It can also be speculated that the spacer grid redirects the cross-flow; the spacer grid cells act as vanes that constrain transversal flow. As a result, when the bypass opens one expects faster flow near the trailing side of the spacer grid. Reciprocally, when the bypass closes the flow issuing from the spacer grid will be skewed towards the right side of the spacer grid cells. This behavior is consistent with jetting observed in the phase averaged velocities and might explain this observation. This momentum transfer leads to fluctuating pressure losses in the flow and added drag on the spacer grid.

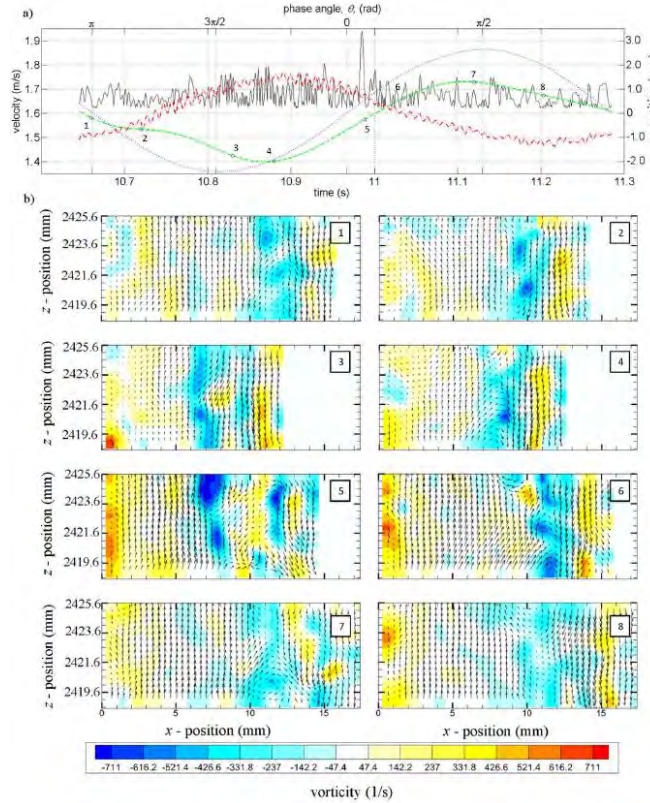


**Fig. c.5. a) time history of filtered W (green dashed line), w (solid black line), rod wall oscillations (blue dotted line), and out of plane motion scaled by factor of 10 (red dashed-dotted line) at 7 mm for one cycle.,
b) Fluctuating velocity field with vorticity in background for 8 points along the cycle. Lagrangian averaging has been performed on these figures to assist in identifying flow structures.**

The modulation of vortex shedding by flow separation and momentum transfer, coupled with growth of the boundary layer along the bypass wall are likely to contribute to flow induced stiffening and damping of the fuel bundle. This contribution might be significant to the overall structure response and requires further analysis to improve understanding of this coupling. This effect is not taken into account in existing analytical models and current simulations for seismic response of fuel bundles.

Our CFD analysis is still ongoing due to getting an ALCC award on MIRA in 2015. Simulation so far have been performed for stationary non-shaking cases at very high-resolution LES (near DNS resolution). Preliminary data indicate that presence of small turbulence induced bundle oscillations ($\sim 200 \mu\text{m}$ amplitude) significantly affect the wake of the spacer grids. We are currently refining our simulations to include this effect, which was well characterized in our facility and has been typically neglected in others.

Finally, the data gathered have enable us to reanalyze the event of the Virginia earthquake in August 2011. The flux sensor signals of the North Anna Power Plant during this event are reproduced in Fig. c.6 and our conclusions differ from the findings from the published official report. Several phases can be identified in the sequence from neutron flux sensor data. In a first phase, the P-waves interact with the core creating a compression and decompression of the core,

as can be seen in the oscillation of the flux. This effect is mostly driven by FSI and our experimental data are representative of it. In a second phase, much stronger S-waves arrive. As a result, an important reactivity excursion is observed that led to SCRAM of the plant. Based on our data, it is likely that these waves are sufficiently energetic to result in bundle-to-bundle or bundle-to-baffle impacts. To dissipate the energy of the impacts, the rods within each assembly will vibrate at high-frequency. Published data on such vibration and the experience gained here on the establishment time for secondary flows indicate that their frequencies are high enough for the creation of a secondary flow around each individual rod. This secondary flow might lead to apparition of thermal boundary layers and local reduction in heat transfer, which could ultimately lead to local boiling and the observed reactivity excursion. These hypothesis could be checked with reasonably simple experiments and resources and could provide very good test cases for conjugate heat transfer validation.

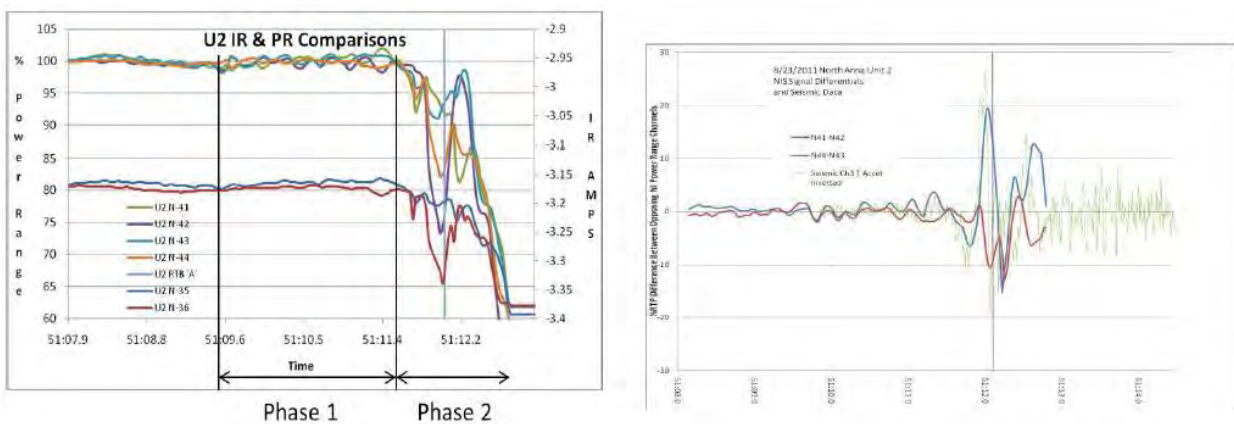


Fig. c.6. Neutron flux of the PRNIs versus time (left). Neutron flux difference between opposite PRNIs and seismic excitation versus time (right).

11. References:

1. Viallet, E.; Bolsee, G.; Ladouceur, B.; Goubin, T. & Rigau, J. Validation of PWR core seismic models with shaking table tests on interacting scale 1 fuel assemblies Transactions of the 17th International Conference on SMiRT, 2003
2. Todreas, N. E. & Kazimi, M. S. Nuclear Systems Volume I: Thermal Hydraulic Fundamentals CRC Press, 2011
3. Paidoussis, M. P. Dynamics of flexible slender cylinders in axial flow J. Fluid Mech., 1966, 26, 737-751
4. Bilello, C.; Bergman, L. A. & Kuchma, D. Experimental Investigation of a Small-Scale Bridge Model Under a Moving Mass J. of Struct. Eng., 2004, 130, 799-804
5. Moncarz, P. D. & Krawinkler, H. Theory and application of experimental model analysis in earthquake engineering Stanford University, 1981, 50
6. Harris, H. G. & Sabnis, G. Structural modeling and experimental techniques CRC press, 1999
7. Peterson, P. Thermal Aspects of Nuclear Reactors Department of Nuclear Engineering, UC Berkley, 2007
8. Ricciardi, G. & Boccaccio, E. Measurements of fluid fluctuations around an oscillating nuclear fuel assembly J. of Fluids and Structures, Springer, 2014, 48
9. Rubin, A.; Schoedel, M.; Avramova, M.; Utsuno, H.; Bajorek, S. & Velazquez-Lozada, A. OECD/NRC Benchmark Based on NUPEC PWR Subchannel and Bundle Tests (PSBT) NRC, 2010
10. Kang, H. S.; Song, K. N.; Kim, H. K.; Yoon, K. H. & Jung, Y. H. Verification Test and Model Updating for a Nuclear Fuel Rod with its Supporting Structure J. of the Korean Nuc. Soc., Springer, 2001, 33, 73
11. Park, K. J.; Kang, B. S.; Song, K. N. & Park, G. J. Design of a Spacer Grid using Axiomatic Design J. of Nuc. Sci. and Tech., Springer, 2003, 40, 989
12. Song, K. & Kim, S. J. Determination of the Optimum Welding Parameters for a Laser Welded Spacer Grid Assembly for PWRs J. of Las. Micro/Nano Eng., Springer, 2007, 2, 95
13. GUM-1995 Evaluation of measurement data - guide to the expression of uncertainty in measurement JCGM 100:2008, 2008
14. Adrian, R. & Westerweel, J. Particle Image Velocimetry Cambridge University Press, 2011
15. Ricciardi, G. & Boccaccio, E. Modelling of the flow induced stiffness of a PWR fuel assembly Nuclear Engineering and Design, Springer, 2015, 282, 8-14
16. Weichselbaum, N. A.; Hussain, S.; Rahimi-Abkenar, M.; Manzari, M. T. & Bardet, P. M. Fuel assembly oscillation induced flow in initially stagnant fluid Nuc. Tech., 2015

17. Jackson, D.; Jones, J. & Chan, R. A high power fiber optic laser doppler velocimeter J. Phys. E: Sci. Instrum., Springer, 1984, 17, 977-980
18. Koga, D. J.; Abrahamson, S. D. & Eaton, J. K. Development of a portable laser sheet Exp. in Fluids, Springer, 1987, 5, 215-216
19. Kriesel, J. M.; Gat, N. & Plemmons, D. Fiber optics for remote delivery of high power pulsed laser beams AIAA Conference, 2010
20. Matsuura, Y.; Takada, G.; Takashi, Y. & Yi-Wei S and Miyagi, M. Hollow fibers for delivery of harmonic pulses of Q-Switched Nd:YAG lasers Applied Optics, Springer, 2002, 41, 442
21. Boechat, A. A. P.; Su, D.; Hall, D. R. & Jones, J. D. C. A submersible particle image velocimetry system for turbulence measurements in the bottom boundary layer Applied Optics, Springer, 1991, 30, 321-327
22. Kovacevic, M. S. & Nikezic, D. Influence of bending on power distribution in step-index plastic optical fibers and the calculation of bending loss Applied Optics, Springer, 2006, 45, 6675-6681
23. Anderson, D. J.; Morgan, R. D.; McCluskey, D. R.; Jones, J. D. C.; Easson, W. J. & Greated, C. A. An optical fiber delivery system for pulsed laser particle image velocimetry illumination Meas. Sci. Tech., Springer, 1995, 6, 809-814
24. Hunter, B.; Leong, K.; Miller, C.; Golden, F.; Glesias, R. & Lavery, P. Understanding High Power Fiber Optic Laser Beam Delivery J. of Laser Applications, Springer, 1996b, 8, 307
25. Hunter, B.; Leong, K.; Miller, C.; Golden, F.; Glesias, R. & Lavery, P. Selecting a High Power Fiber Optic Laser Beam Delivery System Argonne National Laboratory, 1996a
26. Bettis, J.; House II, R. & Guenther, A. Spot size and pulse duration dependence of laser-induced damage Laser induced damage in optical materials 1976, NBS spec. pub. 462, 1976, 338-345
27. Hsu, P. S.; Patnaik, A. N.; Gord, J. R.; Meyer, T. R.; Kulatilaka, W. R. & Roy, S. Investigation of optical fibers for coherent anti-Stokes Raman scattering (CARS) spectroscopy in reacting flows Experiments in Fluids, Springer, 2010, 49, 696-984
28. Allison, S. W.; Cates, M. R.; Gillies, G. T. & Noel, B. W. Fiber Optic Pulsed Laser Delivery for Remote Measurements Optical Engineering, Springer, 1987, 26, 538-546
29. Mann, G.; Vogel, H.; Preub, R.; Vaziri, P.; Zoheidi, M.; Eberstein, M. & Kruger, J. Nanosecond laser damage resistance of differently prepared semi-finished parts of optical multimode fibers Appl Surf Sci, Springer, 2007, 254, 1096-1100
30. Smith, A.; Do, B.; Schuster, R. & Collier, D. Rate Equation model of bulk optical damage of silica, and the influence of polishing in surface optical damage of silica Proc. Of SPIE, 2008
31. Hand, D. P.; Entwistle J D and Maier, R. R. J.; Kuhn, A.; Greated, C. A. & Jones, J. D. C. Fiber optic beam delivery system for high peak power laser PIV illumination Meas. Sci. Tech., Springer, 1999, 10, 239-245

32. Fiscaletti, D.; Westerweel, J. & Elsinga, G. E. Long range micro-PIV to resolve the small scales in a jet at high Reynolds number *Exp in Fluids*, Springer, 2014, 55, 1812
33. English, R. E.; Halpin, J. M.; House, F. A. & Paris, R. D. Optical design of a high-power fiber-optic coupler SPIE 1527, Current Developments in Optical Design and Optical Engineering, San Diego, CA, 1991
34. Hunter, B.; Leong, K.; Sanders, P.; Miller, C.; Golden, J.; Glesias, R. & Lavery, P. Designing a fiber-optic beam delivery system Argonne National Laboratory, 1997
35. Hsu, P. S.; Jiang, N.; Gord, J. R. & Roy, S. Fiber-coupled, 10 kHz simultaneous OH planar laser-induced fluorescence/particle-image velocimetry *Optics Letters*, Springer, 2013a, 38, 130-132
36. M. Vanella, P. Ra P. Rabenold and E. Balaras. An embedded-boundary method with adaptive mesh refinement for fluid-structure interactions problems. *J. Comput. Phys.*, 229:6427-6449, 2010.
37. Mira at Argonne National Labs. <https://www.alcf.anl.gov/mira>
38. Vanella M. and Balaras E., "A moving least-squares reconstruction procedure for embedded boundary formulations," *J. Comput. Phys.*, Vol. 228(18), pp. 6617-6628 (2009).
39. Kim J., Moin P. and Moser R. D., "Turbulent statistics in fully developed channel flow at low Reynolds number," *J. Fluid Mech.*, Vol. 177, pp. 133-166 (1987).
40. Moser R. D., Kim J. and Mansour N. N., "Direct numerical simulation of turbulent channel flow up to $Re_{\tau} = 590$," *Phys. Fluids*, Vol. 11(4), pp. 943-945 (1999).
41. Mohapatra P., Dubey A., Daley C., Vanella M. and Balaras E. "Parallel Algorithms for Using Lagrangian Markers in Immersed Boundary Method with Adaptive Mesh Refinement in FLASH", Proceedings of SBAC-PAD 2013, Oct. 23-26, Porto de Galinhas, Brazil (2013).
42. Vanella M., EzEldin H., Mohapatra P., Daley C., Dubey A. and Balaras E., "A computational scheme for simulation of dense suspensions of arbitrarily shaped rigid particles," *Bulletin of the American Physical Society, APS-DFD*, November 21-24 (2013).